



**HAL**  
open science

# Design of novel soft materials and understanding how soft networks break using mechano-fluorescence

Victoria Waltz

► **To cite this version:**

Victoria Waltz. Design of novel soft materials and understanding how soft networks break using mechano-fluorescence. Material chemistry. Université Paris sciences et lettres, 2021. English. NNT : 2021UPSL091 . tel-03609230

**HAL Id: tel-03609230**

**<https://pastel.hal.science/tel-03609230>**

Submitted on 15 Mar 2022

**HAL** is a multi-disciplinary open access archive for the deposit and dissemination of scientific research documents, whether they are published or not. The documents may come from teaching and research institutions in France or abroad, or from public or private research centers.

L'archive ouverte pluridisciplinaire **HAL**, est destinée au dépôt et à la diffusion de documents scientifiques de niveau recherche, publiés ou non, émanant des établissements d'enseignement et de recherche français ou étrangers, des laboratoires publics ou privés.



**THÈSE DE DOCTORAT**

**DE L'UNIVERSITÉ PSL**

Préparée à l'Ecole Supérieure de Physique et de Chimie  
Industrielles de la ville de Paris (ESPCI Paris)

**Design of novel soft materials and understanding how  
soft networks break using mechano-fluorescence**

**Conception de nouveaux matériaux mous et compréhension de la  
rupture moléculaire des réseaux à l'aide de la mécano-fluorescence**

Soutenue par

**Victoria WALTZ**

Le 14 décembre 2021

Ecole doctorale n° 397

**Physique et Chimie des  
Matériaux**

Spécialité

**Chimie des Matériaux**

**Composition du jury :**

Min-Hui, LI Directrice de recherche, CNRS/Chimie ParisTech	<i>Présidente</i>
Sylvie, CASTAGNET Directrice de recherche, CNRS/Université de Poitiers	<i>Rapporteuse</i>
José M., ASUA Professor, University of the Basque Country	<i>Rapporteur</i>
Shelby, HUTCHENS Assistant professor, University of Illinois	<i>Examinatrice</i>
Costantino, CRETON Directeur de recherche, CNRS/ESPCI Paris	<i>Directeur de thèse</i>
Jutta, RIEGER Directrice de recherche, CNRS/Sorbonne Université	<i>Co-Directrice de thèse</i>



# Table of contents

List of symbols

List of abbreviations

Acknowledgments/Remerciements

**General introduction and motivation of the project.....1**

**Chapter 1: From the physics of polymer to reinforced elastomers.....7**

Introduction .....	11
1. Introduction to polymer network physics .....	11
1.1. The isolated polymer chain.....	11
1.2. Rubber elasticity .....	14
1.3. The importance of entanglements.....	15
1.4. End of the Gaussian regime.....	17
2. Macroscopic failure .....	18
2.1. LEFM.....	18
2.2. Greensmith approximation .....	20
2.3. Lake and Thomas model.....	22
3. How to reinforce elastomers? .....	23
3.1. General guidelines .....	24
3.2. Delay nucleation .....	24
3.3. Slow down propagation .....	26
3.4. The specifications of elastomers.....	27
3.4.1. Viscoelasticity .....	27

3.4.2. Fillers.....	28
3.4.3. Physical bonds.....	29
3.5. Multiple networks.....	30
3.5.1. Double network hydrogels .....	30
3.5.2. Models for the fracture mechanics of double network hydrogels.....	34
3.5.3. Multiple network elastomers.....	35
Conclusions.....	43
References.....	44

## **Chapter 2: Nanocomposite elastomers filled with soft interpenetrable particles.....53**

Introduction.....	57
1. Results.....	58
1.1. Synthesis and characterization of the materials.....	58
1.1.1. Particles synthesis .....	58
1.1.2. Dispersion and swelling of the particles in ethyl acrylate.....	60
1.1.3. Synthesis of a simple matrix as a reference .....	61
1.1.4. Synthesis of the nanocomposites.....	61
1.2. Mechanical properties of the nanocomposites.....	63
1.2.1. Effect of the volume fraction of filler .....	63
1.2.2. Effect of the degree of crosslinking of the filler particles.....	71
Conclusion.....	78
2. Experimental part.....	79
2.1. Chemicals .....	79
2.2. Synthesis conditions .....	79
2.2.1. Soft “Filler Particles” by emulsion polymerization .....	79
2.2.2. “Reference matrix” by bulk polymerization .....	80

2.2.3. Preparation of the nanocomposite .....	81
2.3. Characterization methods .....	84
2.3.1. Gravimetric analysis.....	84
2.3.2. DLS .....	84
2.3.3. DSC .....	85
2.3.4. Mechanical tests .....	85
References .....	89

## **Chapter 3: Aqueous route to double network particles and characterization of the films therefrom.....91**

Introduction .....	95
1. Results.....	97
1.1. Synthesis.....	97
1.1.1. Synthesis of the “Single latex” (S) by emulsion polymerization .....	97
1.1.2. Swelling of the latex particles in aqueous dispersion by EA .....	98
1.1.3. Synthesis of the “Double latex” (D) by seeded emulsion polymerization.....	102
1.2. Film formation and characterization .....	116
1.2.1. Temperature effect on film formation.....	116
1.2.2. Comparison of D latex with the corresponding constituting single networks .	117
1.2.3. Effect of the crosslinking density in the S seeds on S and D films.....	120
1.3. Connecting particles.....	123
1.3.1. Presentation of the DAAM/ADH system .....	123
1.3.2. Effect of DAAM on S film .....	123
1.3.3. Connecting the particles through the 2nd network.....	128
Conclusion.....	140
2. Experimental part.....	142
2.1. Synthesis.....	142

2.1.1.	Chemicals and reagents .....	142
2.1.2.	Synthesis of the “Single latex” (S) by emulsion polymerization .....	142
2.1.3.	Synthesis of the “Double latex” (D) by seeded emulsion polymerization .....	143
2.1.4.	Drying process.....	145
2.2.	Characterization methods .....	145
2.2.1.	Gravimetric analysis.....	145
2.2.2.	DLS .....	145
2.2.3.	AFM .....	146
2.2.4.	CryoTEM .....	146
2.2.5.	Mechanical tests .....	146
Appendix	.....	147
References	.....	148

## **Chapter 4: Imaging and quantification of bond breakage in elastomers using confocal microscopy.....151**

Introduction	.....	155
1.	Sample synthesis .....	157
1.1.	Single network.....	157
1.2.	Multiple network .....	157
1.3.	Mechanofluorescent single network.....	159
2.	Mechanical test .....	160
3.	Imaging and quantification of bond breakage .....	160
3.1.	Confocal set-up.....	160
3.2.	Image collection .....	162
3.3.	Imaging analysis .....	163
3.3.1.	Calibration of fluorescence .....	164
3.3.2.	Quantification.....	166

4. Representativity of the mechanophore’s activation for chain breakage .....	169
5. Dependence of DACL activation’s on strain rate and temperature .....	171
Conclusions .....	173
References .....	174

## **Chapter 5: Soft network fracture mechanics study using mechano-fluorescence .....175**

Introduction .....	179
1. Fracture of notched samples .....	181
1.1. Crack propagation.....	181
1.1.1. Video analysis .....	182
1.1.2. Effect of notch length.....	189
1.2. Quantification of chain scission on fracture surfaces .....	199
1.3. Discussion.....	200
2. Fracture of unnotched samples .....	205
2.1. Mechanical reproducibility .....	206
2.2. Direct observation.....	207
2.3. Effect of the viscoelasticity .....	212
Conclusion.....	214
Appendix .....	216
References .....	222

## **Chapter 6: Effect of soft networks structures on fracture studied with mechano-fluorescence .....223**

Introduction .....	227
1. Experimental methods .....	229
1.1. Materials .....	229

1.2. Mechanical characterization .....	230
2. Results and discussion .....	230
2.1. Mechanical properties.....	230
2.2. Damage quantification.....	237
Conclusion.....	245
Appendix .....	246
References .....	247

## **Chapter 7: Quantitative study of molecular bond breakage and load transfer during the necking of multiple network elastomer.....249**

Introduction .....	253
1. Materials and methods .....	254
1.1. Chemicals and reagents .....	254
1.2. Single network synthesis .....	255
1.3. Multiple network synthesis.....	255
1.4. Mechano-fluorescent network synthesis .....	256
1.4.1. DAFL incorporation .....	256
1.4.2. SP incorporation.....	257
2. Confocal imaging of stretched samples .....	257
2.1. Home-made tensile test set up .....	258
2.2. Confocal imaging .....	259
2.3. Systematic image analysis .....	260
3. Necking in multiple networks .....	269
3.1. Mechanical characteristics of necking.....	269
3.2. Damage quantification bulk vs neck regions (in the bulk and the matrix).....	271
3.3. Load transfer between the filler and the bulk (SP in the matrix) .....	275

4.	What parameters control the necking process?.....	277
4.1.	Effects of the pre-stretch.....	277
4.2.	Effects of the filler network crosslinking content .....	282
5.	Effect of the connectivity between filler and matrix networks.....	287
5.1.	SNHMA synthesis .....	287
5.2.	Necking in HMA multiple networks .....	289
6.	Discussion.....	293
	Conclusion.....	294
	Appendix .....	296
	References .....	300

## **General conclusion .....303**

	Résumé en français.....	311
--	-------------------------	-----

### **List of symbols**

$C_1$ and $C_2$	constants from Mooney-Rivlin model
$E_x$	contribution of the crosslinks to the Young's modulus
$E_e$	contribution of the entanglements to the Young's modulus
$G$	energy release rate
$W$	strain energy density
$a$	crack length
$\Gamma$	fracture energy
$\Gamma_0$	threshold value of fracture energy from Lake and Thomas model
$G_{\text{damage}}$	damage energy
$\dot{\lambda}$	stretch rate
$\lambda$	deformation
$\sigma$ or $\sigma_N$	nominal stress
$\Sigma_{\text{norm}}$	normalized areal number of broken chains
$\Sigma$	areal number of broken chains
$\nu_x$	chain density
$\Phi$	ratio of activated mecanophores
$\Phi_{\text{filler}}$	fraction of broken chains in the filler network
$\Phi_m$	fraction of activated spiropyran in the matrix
$D_w$	average diameter of particles in water
$Q_V$	swelling factor

$D_{EA}$	average diameter of latex particles in EA
$\Sigma U_{hyst}$	cumulated energy dissipated
$R_{cycle}$	ratio of energy dissipated
$\rho_i$	volumic mass of "i"
R	perfect gaz constant
M	molar mass
T	temperature
t	time
F	force
$\gamma$	interfacial free energy
$k_B$ or k	Boltzmann constant
$\eta$	viscosity
I	fluorescent intensity
$N_a$	Avogadro number

### List of abbreviations

ADH	adipic acid dihydrazide
AFM	Atomic Force Microscope
AIBN	azobisisobutyronitrile
BDA	1,4-butanediol diacrylate
D	double latex
DAAm	diacetone acrylamide
DAcL	Diels Alder adduct Cross Linker
DLS	Dynamic Light Scattering
DN	double network
DSC	Differential Scanning Calorimetry
EA	ethyl acrylate
ERC	European Reasearch Council
FE	finite element
HMP	2-hydroxy-2-methylpropiophenone
IPN	interpenetrated polymer networks
KPS	potassium persulfate
LEFM	Linear Elastic Fracture Mechanics
LIPN	Latex IPN
N	necked region
PDI	polydispersity index
PEA	poly(ethyl acrylate)
PMA	poly(methyl acrylate)
QN	quadruple network
S	single latex
SANS	Small Angle Neutron Scattering
SDS	sodium dodecyl sulfate
SN	single network
SP	spiropyran
$T_g$	glass temperature
TN	triple network
UN	unnecked region

## **Acknowledgments/Remerciements**

I chose to write this personal section in French and am sorry for the non-French speaker who may not understand (if you really want, I advise to use deepl to translate the following part).

Je remercie d'abord les membres du jury, José M. Asua, Sylvie Castagnet, Shelby Hutchens et Min-Hui Li, pour avoir accepté d'évaluer mon travail, pour leur intérêt pour mon projet ainsi que pour leurs remarques et les discussions que nous avons partagé.

Je remercie ensuite mes directeurs de thèse. Merci à Jutta Rieger d'avoir accepté de co-diriger ma thèse. Merci pour tout le temps qu'elle m'a accordée et pour ses conseils que je garde en mémoire et qui m'aideront pour la suite.

Merci également à Costantino Creton de m'avoir accordée ce projet de thèse. Merci pour sa confiance tout au long de ma thèse, sa disponibilité malgré un emploi du temps bien chargé et pour toutes les discussions que nous avons pu partager.

Merci aux membres de mon comité de suivi de thèse, Nadège Pantoustier, Guillaume Miquelard et Christel Laberty-Robert, pour avoir écouté mes présentations, pour leurs questions et leurs perspectives qui ont nourrit mon projet de thèse.

Malgré la crise sanitaire et le doux bruit des travaux, j'ai passé de très bons moments pendant cette thèse et cela je le dois aux personnes qui ont croisé mon chemin.

Merci aux laboratoires SIMM et IPCM (équipe LCP) et à leurs membres.

Merci à Christian Fretigny et Etienne Barthel, directeur successif du laboratoire SIMM de m'avoir accepté sein du laboratoire.

Merci également Matteo Cicotti pour son temps et son point de vue qui a été très utile pour la partie mécanique de mon projet.

Merci à Jean Comtet pour son aide sur l'analyse des images et tout le travail du chapitre 7. J'ai eu beaucoup de chance de pouvoir travailler avec lui et je lui souhaite beaucoup de réussite dans sa carrière de chercheur.

Merci à Nadia qui a travaillé sur le projet des émulsions pendant son stage de 6 mois et qui m'a fait confiance pour être son encadrante de stage.

Merci à Bruno Bresson pour les expériences d'AFM, et pour son aide dans le montage du set-up expérimental de traction sous le microscope confocal qui m'a permis de faire des belles images du necking des réseaux multiples.

Merci à Tetsuharu Narita pour m'avoir formée à utiliser la DLS.

Merci à Mohammed Hanafi pour m'avoir formée à utiliser la DSC et pour son aide et soutien sur les problèmes expérimentaux.

Merci à Freddy Martin d'avoir répondu à mes questions sur la gestion des déchets toxiques, ce qui m'a évité de faire des bêtises.

Merci à Armand Hakopian pour son aide avec l'informatique et pour m'avoir informée sur les process utiles au labo (oui oui il y en a).

Merci aux gestionnaires Mayu Hirano-Courcot, Marie-Thérèse Mendy et Fabienne Decuq qui ont été d'un grand soutien dans tous les process administratifs et surtout pour les déplacements en conférence.

Merci à Jean-Michel Guigner pour les expériences de cryo-TEM.

Merci à Gilles Garnaud pour ses mails qui font toujours sourire et pour la livraison de nos colis jusqu'au bureau.

Merci à Hélène Montès pour sa bonne humeur et les chouquettes.

Et globalement, merci à tous, pour les échanges que nous avons pu avoir au SIMM que ce soit dans les couloirs, pendant une manip, une réunion ou un séminaire, ou même autour d'un déjeuner ou d'une pause « goûter ».

Je tiens à remercier toutes les personnes rencontrées au labo et avec qui j'ai pu discuter et partager des moments au-delà du travail. Ces moments hors du labo (où on parle parfois aussi de sciences) font curieusement partie de ce qui rend le labo si agréable, en particulier quand plus rien ne marche et qu'on est tout déprimé. Que vous ayez participé de près ou de loin à la bonne ambiance du SIMM, merci.

Je voudrais remercier en particulier Juliette, Ludovic, Yinjun, Gabo, Xavier qui étaient là quand j'ai commencé mon projet et qui m'ont formée et lancée dans mes débuts. C'était génial de commencer ma thèse au sein d'une si belle équipe !

Merci aussi à tous ceux qui ont travaillé sur les mécanophores, Jean, Gaëlle, Jianzhu, YuanYuan, Ombeline et Côme.

Merci à mes co-bureau successifs : Valentine, Aude, Anusree, Noushin, Gaétan, Léa, Hao, et Mohammad. Je crois que vous m'avez vu dans tous mes états, alors merci de m'avoir soutenue dans les moments difficiles et merci pour toutes les pauses gâteaux/bananes qu'on a pu faire.

Merci aussi au bureau d'à côté, Pascal, Lucile, Lola, Aaliyah, Gabriel. Pouvoir m'arrêter dans votre bureau et vider mon sac ou prendre une pause thé, c'était comme avoir un deuxième bureau. Et une mention spéciale pour le rire de Lucile qui traverse les murs et est communicatif. Merci à Flora-Maud, Julie pour les bons moments de bavardages. Merci à Maxime pour ton humour...

Merci à tous les participants des fashion lab days (formal monday et very casual friday) et à Gaétan pour cette idée de génie.

Je voudrais remercier ensuite mes amis pour avoir partagé avec moi les expériences d'une thèse (la leur ou la mienne) et pour m'avoir rappelé qu'il y a autre chose dans la vie que le travail.

Je remercie en particulier Anusree. (J'écris en français parce que je suis sûre que tu comprendras.) Merci d'avoir été là. J'ai eu beaucoup de chance de pouvoir partager mon bureau avec une si bonne amie et j'en garderai plein de bons souvenirs.

Merci aussi à ma bibi. Entre confidente et partenaire d'arts plastiques. J'ai beaucoup de chance d'avoir une personne aussi formidable dans ma vie.

Je remercie ensuite ma famille. Merci d'avoir confiance en moi quand je doute. Vous m'avez soutenue au mieux. Votre amour et soutien compte beaucoup pour moi. C'est beaucoup grâce à vous et à votre confiance si j'ai pu en arriver jusque-là.

Enfin je remercie Antoine. Sans toi je ne serai certainement pas là en train d'écrire ces quelques mots, et ce manuscrit ne serait probablement pas là non plus. Cette thèse c'est aussi la tienne tant tu m'as soutenue, accompagnée et aidée pendant ces un peu plus de trois ans, comme si ton seul projet de thèse ne te suffisait pas... Il m'est difficile de réaliser pleinement la chance que j'ai de partager mon quotidien avec toi, tant je suis chanceuse, et encore plus de le décrire avec des mots... Tu m'apportes tellement. Ma vie est meilleure avec toi. À travers les épreuves, tu me donnes la force de me relever et envie d'avancer. J'espère pouvoir te rendre la pareille ou plus encore. Merci d'être dans ma vie.

*À mes grands-mères.*

# **General introduction and motivation of the project**



Elastomers are crosslinked polymer networks reversibly deformable. This characteristic offers them a wide range of applications in the tire industry, sealants, dampers and some new ones in the biomedical field or in high technology. However, in some cases their usage is limited by their low mechanical strength and by the propagation of a crack initiated by a defect. A large number of previous studies has been dedicated to the investigation and understanding of fracture in soft networks as will be reviewed and summarized in chapter 1. Yet, fracture is a complex multi-scale process and many open questions remain, and some will be the focus of the present work

- On the one hand, many new elastomers designs have been developed to improve the material's toughness and stiffness while keeping its high level of reversible extensibility. However, while various strategies have been implemented to enhance stiffness or fracture toughness, none fits all applications.

For example, the most broadly used reinforcement strategy for elastomers is the composite strategy, where hard fillers (in the form of nanometer size particles, or fibers) are dispersed in an elastomer matrix. The composite materials benefit then from both the matrix extensibility and the filler stiffness. However, the dissipative properties of the composite become more rate and temperature dependent, and hence will affect the working temperature range. A second drawback of the composite strategy is the lack of transparency of the material either in the unloaded state (due to the filler opacity) or in the loaded state (known as whitening due to cavitation). Another strategy has been developed at the lab scale which overcomes the previous composites limitations. Developed first on hydrogels by Gong et al. [<sup>1</sup>], then on elastomers by Ducrot et al. [<sup>2</sup>], the multiple network strategy consists in a first highly-crosslinked network which is interpenetrated and pre-stretched by a second loosely crosslinked network. The first network gives the material its stiffness and acts as a sacrificial network that dissipates energy by irreversibly breaking during stretching, while the second network maintains the mechanical integrity of the material. Multiple networks are transparent materials whose main energy dissipation mechanism upon fracture is not much affected by temperature or strain rate (because the scission of sacrificial bonds is not much rate dependent). However, the multiple network synthesis process is not direct. The first bulk network must stay in a bath of excess monomers (with initiator and crosslinker) for the network to swell and reach its swelling equilibrium. This process takes time (at least 2h for a 1 mm thick sample) and limits the shape of the final sample. Therefore, we are interested in developing a new more versatile and eco-friendly route to make materials with a similar multiple network architecture, and which would benefit from the same sacrificial bond dissipation mechanism to delay macroscopic failure.

- On the other hand, it is also of great interest to understand fundamental aspects of fracture, to predict crack initiation and propagation directly from molecular composition or network structure and guide the material's engineer toward a wider range of soft tough materials.

This PhD work is included in a larger program funded by the European Research Council (ERC). The overall objective of the ERC project is to understand the fracture of soft materials by linking the molecular scale with the micro-structure (at 50-100  $\mu\text{m}$  scale) and with the macro scale. Its final goal is to build multi-scale and physically based molecular models predicting the fracture energy of soft polymer based materials based on their molecular architectures.

The fracture of soft materials is a complex process still incompletely understood because it involves several dissipation mechanisms, not only in front of the crack tip, such as friction between monomers, relaxation of pendant polymer chains and fracture of stretched chains by bond scission [3].

The molecular model of Lake and Thomas, currently used, describes fracture of soft materials in conditions where there is no viscoelastic dissipation [4]. It predicts that to create a new surface, bond breakage will be limited to one molecular planar region with a thickness in the order of a mesh size, and each broken bond will release an energy equal to the homolytic dissociation of a C-C bond times the number of C-C bonds in the chain backbone. Though, the model conditions are far from real-life conditions, and its estimation of the broken chain density and the energy dissipated per chain length can be questionable, it still predicts accurately the variations of fracture energy with network structure [5].

Experimentally, energy dissipation was a complete black box until the recent work of J. Slootman [6,7]. In her PhD, she developed a tool to image and quantify bond breakage in soft networks using mechano-chemistry. This tool enables to separate the contribution of bond scission (damage) from the rest of the viscoelastic dissipation mechanisms included in the fracture energy. Her results showed that, to create a new surface, bond scission in soft networks occurs over more than a mesh size, and that the quantity of broken chains varies with viscoelasticity (variation in temperature and strain rate conditions).

Her pioneering work focused mainly on one particular poly(methyl acrylate) (PMA) single network crosslinked by 0.41 mol% of crosslinker. That specific network was chosen for its viscoelastic properties at room temperature which led, once broken, to a fluorescent signal strong enough to be measured with her confocal microscope set-up. Her microscope set-up was not adapted to the imaging of less viscoelastic samples with a very localized bond scission, like the poly(ethyl acrylate) (PEA) single networks. Her first trial to investigate the model of Lake and Thomas was based on two PMA single networks, crosslinked by 0.41 and 0.20 mol%, which were far from the threshold conditions of the model, and her first results did not result in clear conclusions.

Therefore, it was of great interest to continue her pioneering work and use the mechanofluorescent tool, that she developed, but to focus on a confocal microscope with a better spatial resolution. That way, more polymer systems, less viscoelastic (like PEA), with different network structures, could be tested, to revisit old, and up to now inaccessible, questions of soft networks mechanics, and in particular address why the model of Lake and Thomas, that is conceptually too simplistic, predicts such a good scaling of fracture energy with the network molecular structure despite the existence of viscoelastic dissipation.

Direct experimental access to bond scission lets us also revisit some fracture mechanics hypotheses that were implicitly accepted and can help the development of more realistic molecular models to predict the fracture behavior of soft networks.

This manuscript is divided into 7 chapters which can be separated into two parts:

- a first part focusing on material designs inspired by the multiple network architecture and presented in chapters 2 and 3.
- a second part focusing on the use of mechanochemistry to investigate in detail the fracture process of soft networks, which includes the chapters 4 to 7.

Chapter 1 is common to both parts and introduces the basic concepts of polymer mechanics, fracture, and the different strategies to reinforce soft materials. The purpose is to expose some elements that are useful to the understanding of the rest of the manuscript and to discuss the state of the art.

Chapter 2 describes the synthesis of a nanocomposite filled with soft penetrable crosslinked particles, and the characterization of its mechanical properties in uniaxial extension, cyclic loading and crack propagation from a preexisting notch as a function of the volume fraction of fillers and the crosslinking density of the filler particles. This new method to make double network structured materials enables to control precisely the shape of the sample and overcome the limitation of the previous bulk double network process.

Chapter 3 presents an all-aqueous route to make double network particles by emulsion polymerization and describes the mechanical characterization of the films obtained from the controlled drying of the latex. This process enabled us to overcome both the previous limitations of the bulk double network process which are the swelling time and the control of the final shape. The challenges of this process are presented.

Chapter 4 introduces the mechanofluorescent tool, developed by J. Sloopman, coupled with an improved microscope confocal imaging and image analyses process, to quantify bond breakage (in post-mortem) at the crack surface. The question of the representativity of the mechanophore's activation to report for C-C bond breakage and the question of the dependence of the mechanophore's activation with strain rate and temperature, are addressed.

Chapter 5 examines the applicability of the fundamental Linear Elastic Fracture Mechanics (LEFM) relationship between critical energy release rate and critical crack tip stress and strain field, by

quantifying chain scission at the crack tip upon crack propagation in samples with different initial notch lengths. We also investigate fracture of unnotched samples to characterize chain scission upon crack “nucleation” and compare the crack propagation mechanisms.

Chapter 6 uses mechanochemistry to address experimentally the key hypotheses of the model of Lake and Thomas. We worked with PEA samples with various crosslinker contents to vary the network structure, and checked the effect of the network architecture on the variation of the fraction of broken chains at the crack tip with the energy release rate, during crack propagation.

Chapter 7 is finally dedicated to the study of macroscopic necking in multiple network elastomers in uniaxial extension. Using the same mechanofluorescent tool coupled to the confocal microscope and a special homemade tensile set-up (under the confocal), we observe the evolution of sacrificial bond scission during the nucleation of a neck in real-time and quantify the fraction of broken chains in the necked and unnecked region of the stretched sample. Several effects of the material structure are also investigated.

Finally, the main contributions of this work are summarized in a general conclusion.

1. Gong, J. P. Materials both Tough and Soft. *Science* **344**, 161–162 (2014).
2. Ducrot, E., Chen, Y., Bulters, M., Sijbesma, R. P. & Creton, C. Toughening Elastomers with Sacrificial Bonds and Watching Them Break. *Science* **344**, 186–189 (2014).
3. Creton, C. 50th Anniversary Perspective: Networks and Gels: Soft but Dynamic and Tough. *Macromolecules* **50**, 8297–8316 (2017).
4. Lake, G. J. & Thomas, A. G. The Strength of Highly Elastic Materials. *Proceedings of the Royal Society A: Mathematical, Physical and Engineering Sciences* **300**, 108–119 (1967).
5. Zhang, W. *et al.* Fatigue of double-network hydrogels. *Engineering Fracture Mechanics* **187**, 74–93 (2018).
6. Slooman, J. Détection quantitative de l’endommagement moléculaire, par mécano-fluorescence, dans les matériaux mous. (PSL, 2019).
7. Slooman, J. *et al.* Quantifying Rate- and Temperature-Dependent Molecular Damage in Elastomer Fracture. *Phys. Rev. X* **10**, 041045 (2020).

# Chapter 1

## From the physics of polymer to reinforced elastomers



## Table of contents

Introduction .....	11
1. Introduction to polymer network physics.....	11
1.1. The isolated polymer chain.....	11
1.2. Rubber elasticity .....	14
1.3. The importance of entanglements.....	15
1.4. End of the Gaussian regime.....	17
2. Macroscopic failure.....	18
2.1. LEFM.....	18
2.2. Greensmith approximation .....	20
2.3. Lake and Thomas model.....	22
3. How to reinforce elastomers?.....	23
3.1. General guidelines .....	24
3.2. Delay nucleation .....	24
3.3. Slow down propagation .....	26
3.4. The specifications of elastomers.....	27
3.4.1. Viscoelasticity .....	27
3.4.2. Fillers.....	28
3.4.3. Physical bonds.....	29
3.5. Multiple networks.....	30
3.5.1. Double network hydrogels .....	30
3.5.2. Models for the fracture mechanics of double network hydrogels.....	34
3.5.3. Multiple network elastomers.....	35
Conclusions .....	43
References .....	44



## Introduction

Elastomers are very interesting polymeric materials due to their particular ability to deform reversibly. They are naturally soft extensible materials but suffer from intrinsically coupled mechanical properties. For example, conventional polymer networks suffer from a tradeoff between stiffness and toughness.

These materials are used in a wide range of applications, from shoe soles to joints or tires, mainly under modified reinforced forms. There is still a growing demand for stiffer and tougher materials for some specific applications like artificial actuators and soft electronics. This is why it is of interest to develop new designs of elastomers to meet the criteria of such applications.

However, the understanding of soft material fracture is not complete yet. We mainly lack on molecular scale models that bridge the gap between mechanics and chemistry. Better knowledge on the fracture mechanics of simple conventional soft polymer networks would be a great help in the development of better targeted reinforcement strategies to toughen elastomers.

### 1. Introduction to polymer network physics

In this part of the chapter, several models used throughout the years to describe the behavior of polymeric materials (from the molecular point of view) will be presented. They are all covered in a reference textbook from Colby and Rubinstein that has been used in this part of the chapter [1].

#### 1.1. The isolated polymer chain

A polymer chain results from the assembly of monomers and can be modeled as an assembly of  $N$  bonds of length  $l$ . In a situation where all the bonds are aligned, the maximum length of the chain, also known as contour length, corresponds to:

$$R_c = N \times l \quad \text{Eq. 1}$$

In practice, the bonds are not aligned but they each have an angle  $\theta$  with their neighbors. This angle is called valence angle. The maximal length of chain becomes:

$$R_{max} = N \times l \times \cos(\theta) \quad \text{Eq. 2}$$

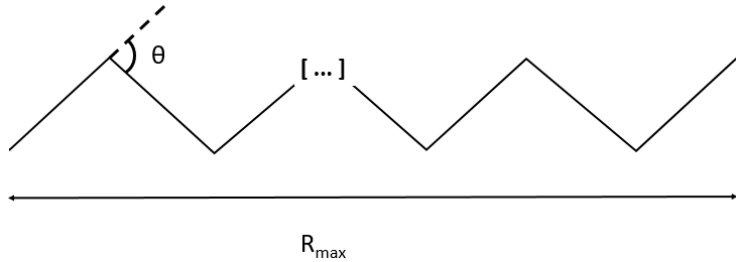


Figure 1 Schematic representation of a polymer chain with  $N$  bonds of length  $l$

In reality, a more representative length of this chain is the average end to end distance. It represents the average chain length at thermodynamic equilibrium. In order to maximize the conformational entropy, the chain is considered a random walk of monomers which means it is composed of randomly linked and oriented segments. An additional parameter called structure factor  $C_\infty$  refines a bit more the model and accounts for the correlation between adjacent monomers that are not randomly oriented in reality. The distance is then given by:

$$R_0^2 = \langle R_{ee}^2 \rangle = C_\infty \times N \times l^2 \tag{Eq. 3}$$

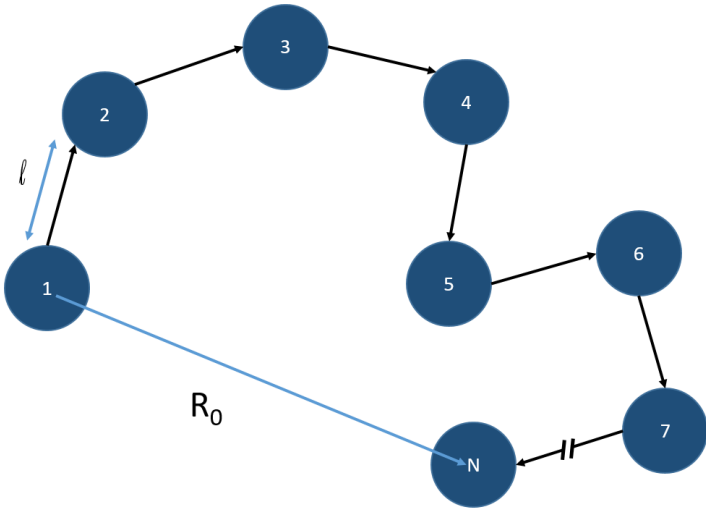


Figure 2 Schematic representation of the maximal size of a polymer chain  $R_{max}$  and the valence angle  $\theta$  between bonds

The real length of a polymer chain is below its maximal length, so the polymer chain is coiled. The chain has access to different conformations but not all are equally accessible. Assuming that the chain is attached at one end at the origin of a cartesian coordinate system, the other end

has a probability to be in the vicinity of a position  $(x,y,z)$ . This probability calculated by Kuhn, and Guth and Mark, corresponds to a Gaussian function [2]. So the chain conformations follow a Gaussian statistic.

In theory, the polymer chain can be extended by applying a force on one of its end up to its maximal extensibility. This means the chain would unfold and change conformations to deform which requires less energy than bond breakage. That explains why compared to crystalline material where deformation implies bond breakage, polymeric materials are easier to deform.

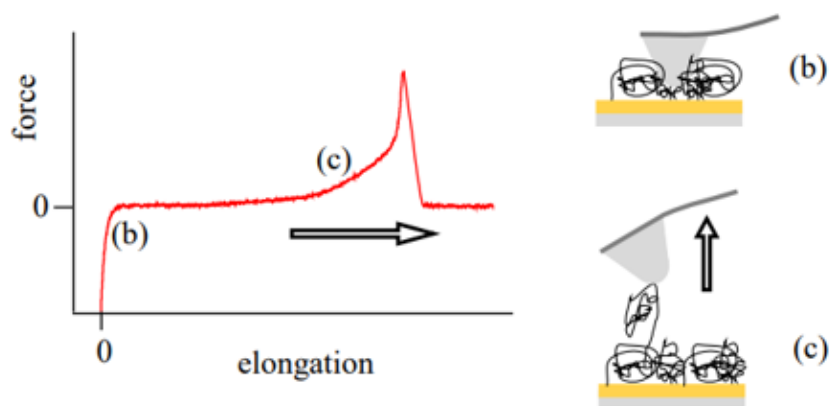


Figure 3 Schematic of a single molecule force spectroscopy experiment. Upon retraction of the cantilever, the polymer chain is stretched while the force and elongation are recorded.

An experimental study done by Oesterhelt et al. [3] on the mechanical characterization of a single polymer chain of poly(ethylene glycol) using an atomic force microscopy (AFM) tip has witnessed two regimes during the stretching of the chain.

At the beginning, the force remains low as the polymer chain unfolds. The response is not representative of the monomer properties but is characteristic of the statistic behavior of the chain. When extending a chain, the loss of accessible conformations decreases the entropy of the system which encourages the chain to return to its original conformation. The force displacement plot is linear.

At a certain deformation, depending on the number of monomers composing the chain or the maximal length of the chain, the force increases non linearly due to non-linear entropic elasticity. When the chain has reached its extended state, further elongation requires the

distortion of the bonds such as the decrease of the valence angle. This regime is enthalpy controlled and depends mainly on the monomer properties.

It is possible to derive the physics of a conventional polymer network above its glass transition temperature ( $T_g$ ) from the isolated chain behavior.

Conventional polymer networks are defined as polymer chains crosslinked via permanent covalent bond into a network, in which entanglements, physical crosslinks and reversible crosslinks of the polymer chains are negligible. The way the chains would interact with each other cannot be neglected in the final mechanical behavior of a real elastomer.

## 1.2. Rubber elasticity

Kuhn and Flory [2] developed the affine model to describe a soft network where there is no physical interaction between chains and friction is negligible.

This model suggests that each individual chain deforms proportionally to the macroscopic deformation of the material. Unless there is bond breakage, in this model, all deformation is fully reversible due to the entropic nature of the elasticity.

Defining  $\lambda_i$  the relative deformation in the direction  $i$ , if the materials deforms in the direction  $x$ ,  $y$  and  $z$ , the affine model defines that the chains deform by the same ratios in the respective directions. Then an expression of the change in free energy  $\Delta F$  can be given as:

$$\Delta F = \frac{nkT}{2}(\lambda_x^2 + \lambda_y^2 + \lambda_z^2 - 3) \quad \text{Eq. 4}$$

Where  $n$  is the number of elastic strands in the network,  $k$  is the Boltzmann constant and  $T$  the temperature.

Assuming that the material is incompressible, we have  $\lambda_x\lambda_y\lambda_z = 1$ . In the case of uniaxial extension in the  $x$  direction, at a stretch  $\lambda$ , we have  $\lambda_x = \lambda$  and  $\lambda_y = \lambda_z = \frac{1}{\sqrt{\lambda}}$ .

The value from the nominal stress  $\sigma_N$  can be derived from Eq. 4, relatively to the uniaxial stretch  $\lambda$ :

$$\sigma_N = \frac{f}{S_0} = \nu_x kT \left( \lambda - \frac{1}{\lambda^2} \right) = G_x \left( \lambda - \frac{1}{\lambda^2} \right) \quad \text{Eq. 5}$$

Where  $f$  is the force,  $S_0$  is the initial cross-section of the material in the transverse direction to the traction direction,  $\nu_x$  is the number density of elastic strands in the network and  $G_x$  is the shear modulus of the material.

The shear modulus is linked to the Young's modulus by:  $E = G_x \times (1 + \nu)$  where  $\nu$  is the Poisson's ratio of the material. In the case of an incompressible material,  $\nu = 0.5$  which gives  $E = 3G_x$ .

The shear modulus can also be expressed as:

$$G_x = \nu_x kT = \frac{\rho RT}{M_x} = \frac{\rho RT}{M_0 N_x} \quad \text{Eq. 6}$$

Where  $\rho$  is the density of the material,  $R$  is the perfect gas constant,  $M_x$  is the molar mass between crosslinks,  $M_0$  is the molar mass of one monomer and  $N_x$  is the number of monomers between two crosslinks.

From Eq. 6 we can see that the stiffness of an elastomer increases with increasing temperature which is the sign of the entropic nature of rubber elasticity. We can also see the dependence with,  $N_x$ , the chain length between two crosslinks. The number of chains per unit volume (equivalent to the number of crosslinks per unit volume, with a prefactor) does affect the modulus. The longer the chain between crosslinks is, the softer the final elastomeric network will be. For temperatures well above  $T_g$ , when friction is negligible, the nature of the chemical bonds does not affect the modulus.

The affine network model supposes that  $\sigma_N / \left( \lambda - \frac{1}{\lambda^2} \right)$  is a constant, equal to  $G_x$ , that only depends on the crosslinking density of the network. But this is without counting on the question of entanglements.

### 1.3. The importance of entanglements

Entanglements are defined as physical interactions between polymer chains that are long enough to constrain one another through knots and loops. These limit the chains motion and add transient rigidity to the material. In fact, the entanglements can slide upon deformation in opposition to chemical crosslinks that are permanent. The effect of entanglements on the modulus is strain dependent and should decrease as the strain increases, which results in the softening of the material.

The simplest way to take entanglements into account is to consider these as transient crosslinks. To do so, we can introduce a density of entanglements  $\nu_e$  and add it to the contribution of the shear modulus  $G = G_e + G_x = (\nu_e + \nu_x) kT$ . However, this does not reflect the strain dependence.

Mooney and Rivlin [4,5] gave an empirical approach to the affine model by considering that the reduced stress  $\sigma_{MR} = \sigma_N / \left(\lambda - \frac{1}{\lambda^2}\right)$  evolves linearly with  $1/\lambda$ :

$$\sigma_{MR} = \frac{\sigma_N}{\left(\lambda - \frac{1}{\lambda^2}\right)} = 2C_1 + \frac{2C_2}{\lambda} = G \quad \text{Eq. 7}$$

Where  $C_1$  and  $C_2$  are two empirical parameters experimentally accessible.

This simple model describes quite well the behavior of crosslinked and entangled materials and gives a fairly simple formula to take into account the softening with increasing strains, typically observed as in Figure 4 [6].

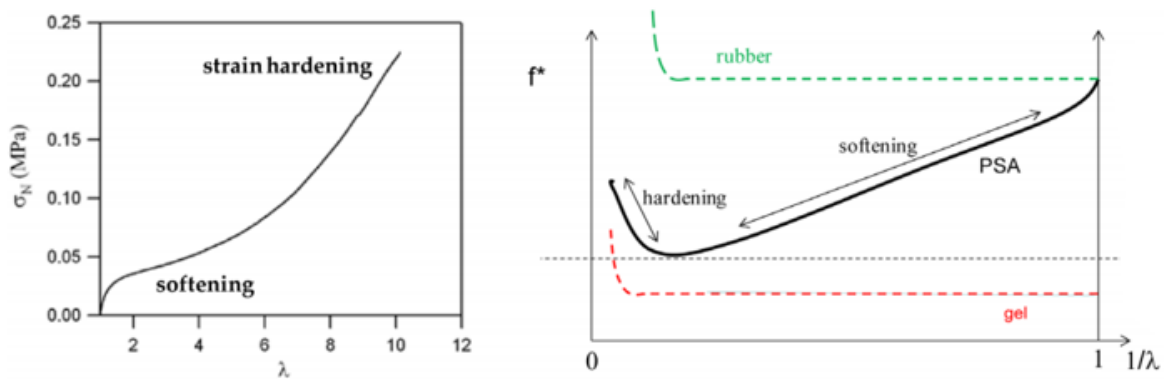


Figure 4 : (a) Typical nominal stress versus uniaxial stretch plot for a PSA and (b) Mooney representation of the same data as a function of  $1/\lambda$  and comparison with an elastic gel and an elastic rubber (reproduced from [6])

Note that, this expression of the model is limited to uniaxial extension, and the parameters  $C_1$  and  $C_2$  aren't representative of any physical characteristic of the material.

Rubinstein and Panuykov [7] proposed more recently a molecular model which takes into account the entanglements. The entanglements are modeled as proposed by Edwards' slip tube model [8]: a potential is applied along the chains and is unfavorable to the movement of monomer perpendicular to the chain. The chain behaves as if constrained in a tube as represented in Figure 5.

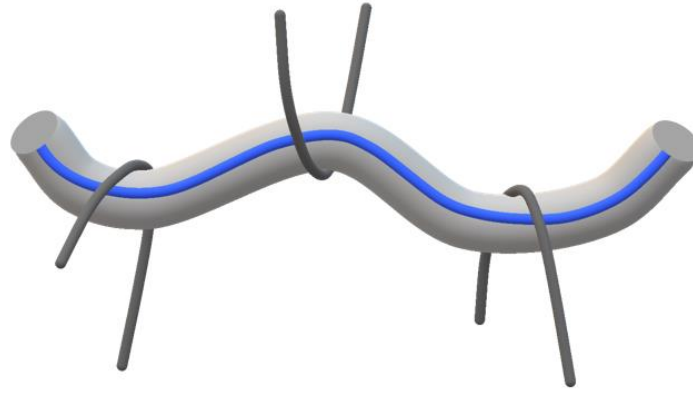


Figure 5 Schematic representation of the slip tube model

Rubinstein and Panuykov precise that the tube fluctuates randomly and that the amplitude of the fluctuation evolves with regards to the strain tensor. In uniaxial extension, their model gives a semi-analytical stress-strain equation:

$$\sigma_{MR} = \frac{\sigma_N}{\left(\lambda - \frac{1}{\lambda^2}\right)} = \frac{1}{3} \left( E_x + \frac{E_e}{0.74\lambda + 0.61\lambda^{-1} - 0.35} \right) \quad \text{Eq. 8}$$

Where  $E_x$  and  $E_e$  are respectively the contribution of the crosslinks and the entanglements to the Young's modulus  $E$  such as  $E = E_x + E_e$ .

This model is very useful to extract the contribution of crosslinks and entanglements from non-linear elastic responses of a polymer network at intermediate stains. This model fits the experimental data in uniaxial extension and compression test.

#### 1.4. End of the Gaussian regime

At large extension, all the previous models become irrelevant as they are all only valid as long as the chains' extension remained well below the contour length.

The number of possible conformations at high strain becomes so limited that the amount of free energy needed to deform the network further becomes very high. This translates by an increase in rigidity when the chains are stretched close to their limit extensibility, which can be observed experimentally as an increase in the local slope of a stress-strain curve: this phenomenon is called strain-hardening.

The stiffening of a single chain is well described by the Langevin function, and can be introduced into the previous model as in Arruda and Boyce's model [9] to take into account the

finite extensibility of the chains. However, the stiffening of an elastic material cannot be predicted easily from only the single chain as stress concentration effects and interactions between chains become important in highly stretched polymer networks.

Gent's constitutive model [10] gives an empirical expression that takes into account the finite extensibility of the chains. In this model, the nominal stress  $\sigma_N$  can be calculated by a fairly simple formula:

$$\sigma_N = \nu_x kT \frac{\left(\lambda - \frac{1}{\lambda^2}\right)}{1 - \frac{J_1 - 3}{J_m}} \quad \text{Eq. 9}$$

where  $J_1$  is the first strain invariant defined by  $J_1 = \lambda_x^2 + \lambda_y^2 + \lambda_z^2$  and  $J_m$  is the maximum allowable value of  $J_1 - 3$ .

This model is in good agreement with experiments as long as the effect of entanglements is not dominant.

Even though the mechanics of soft polymers is well understood, the fracture of these materials remains an active field of research. In reality, the imperfect network chain length distribution is difficult to assess and may affect everything. Some shorter chains may break before others and create defects that can later concentrate stress and lead to cracks. The complexity of real polymer networks makes it particularly difficult to understand and model macroscopic failure. Understanding fracture is fundamental to the development of new polymeric material and their use in cutting edge applications.

## 2. Macroscopic failure

The study of fracture consists usually in determining the energy needed to propagate a crack. This fracture energy is generally noted  $\Gamma$  or  $\Gamma_c$ .

### 2.1. LEFM

In the framework of Linear Elastic Fracture Mechanics (LEFM), the main assumption is that the bulk material remains elastic everywhere except in a small region around the crack tip. This simplifies the approach to localized dissipative phenomenon occurring to propagate a crack, that is the creation of two new surfaces.

The strain energy release rate  $G$  is then defined as the change in total mechanical energy  $W_m$  over the change in surface area  $A$  of a crack.

$$G = \frac{dW_m}{dA} \quad \text{Eq. 10}$$

Griffith [6] proposed that a crack only propagates in a material when  $G$  reaches a critical value  $G_c$ , where  $G_c$  is the minimal energy to create two new surfaces, also known as Dupré energy of adhesion, and the fracture energy is defined as  $\Gamma = G_c$ .

In reality, both the energy to create two new surfaces as well as the energy dissipated during the propagation should be considered in order to propagate a crack.

Irwin [11] refined the model by detailing the stress concentration at the crack tip as a dependence of the stress to the inverse of the square root of the distance to the crack:

$$\sigma(r) = \frac{K}{\sqrt{r}} \quad \text{Eq. 11}$$

Where  $K$  is the stress intensity factor (in  $\text{Pa}\cdot\text{m}^{1/2}$ ).

Then follows a condition to crack propagation: a crack will propagate when  $K \geq K_c$ , with  $K_c$  being a property of the material called material toughness. In LEFM, this condition is equivalent to  $G \geq G_c$ .

These equations are valid in the hypothesis of LEFM. Unfortunately, in the case of highly elastic materials, the way a crack propagates can be very different from what happens in more brittle materials. In particular, non-negligible energy will be dissipated not only at the crack tip, and for more than just new surfaces creation (such as relaxation of pendant chains, friction between monomers, bond breakage).

The measurements of the fracture energy  $\Gamma$  takes into account all these energies.

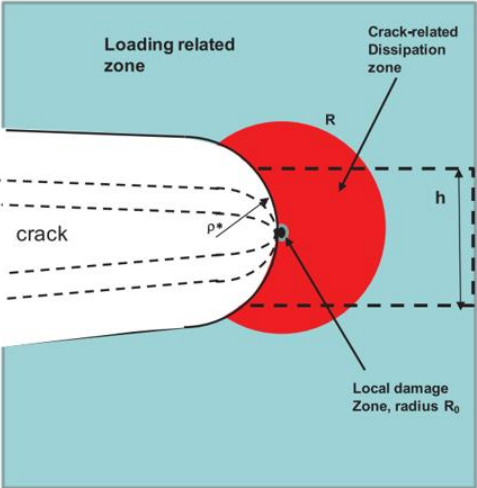


Figure 6 Schematic representation of the different zones where energy may be dissipated during crack propagation. Reproduced from [6]

2.2. Greensmith approximation

The measurement of the fracture toughness has been done through various experimental methods such as pure-shear test and single-notch test as can be seen in Figure 7. They are generally based on the introduction of a notch in the sample followed by the stretching of the material which induces the propagation of the crack.

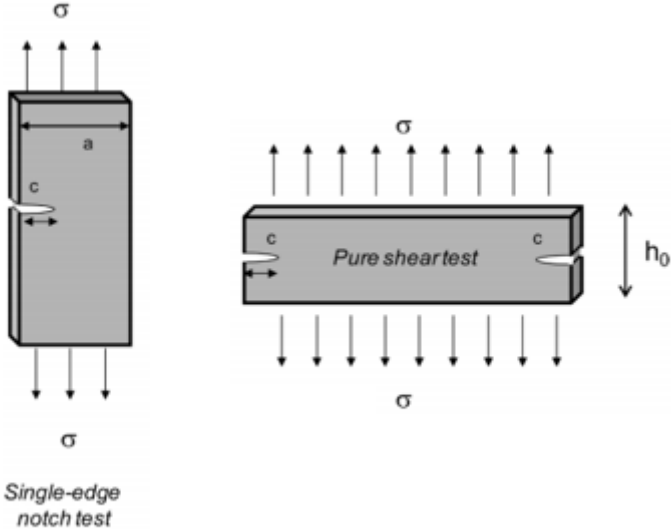


Figure 7 Two possible tests to measure the toughness of soft materials. Reproduced from [6]

Greensmith [12] proposed an empirical expression to quantify the strain energy release rate for neo-Hookean elastomers in a single-notch test:

$$G(\lambda) = \frac{6 c W(\lambda)}{\sqrt{\lambda}} \quad \text{Eq. 12}$$

Where  $c$  is the length of the initial notch,  $W$  is the strain energy density calculated from the stress-strain curve of an un-notched sample  $W(\lambda) = \int \sigma(\lambda) d\lambda$ .

When the sample reaches a critical stretch  $\lambda_c$ , the crack starts to propagate:

$$\Gamma = G(\lambda_c) = \frac{6 c W(\lambda_c)}{\sqrt{\lambda_c}} \quad \text{Eq. 13}$$

In pure shear geometry, where the width  $w$ , the height  $h$  and the thickness  $t$  of the sample respect  $w \gg h \gg t$  and  $c \ll h$ , the strain energy release rate does not depend on the length of the notch:

$$G(\lambda) = W(\lambda) \times h \quad \text{Eq. 14}$$

Gent and Schultz [13] suggested to define two contributions to the fracture toughness to account for:

- the intrinsic fracture energy of the material if there is no dissipation at all,  $\Gamma_0$
- the contribution of the dissipation to toughness,  $\Gamma_D = \Gamma_0 \times f(v, T)$ , where  $f(v, T)$  is function dependent of the strain rate and the temperature, which characterize dissipation during propagation

The fracture toughness is then given by:

$$\Gamma = \Gamma_0 \times (1 + f(v, T)) \quad \text{Eq. 15}$$

Person estimated  $f(v, T)$  from the linear viscoelastic properties of the material. But this estimation did not take into account the non-linear processes happening during crack propagation as these cannot to be easily theoretically calculated yet.

However,  $\Gamma_0$  has been successfully estimated by Lake and Thomas.

### 2.3. Lake and Thomas model

Lake and coworkers showed that in the absence of viscoelastic dissipations (at high temperature far from  $T_g$ ) a minimum amount of energy was required to propagate a crack and so, for a wide range of elastomers.

Lake and Thomas [14] elaborated a molecular model that predicted from simple molecular arguments a rate independent dissipation process: they assumed that when a stretched chain breaks, the total energy stored in each stretched bond of the chain is irreversibly released. Therefore, the minimum energy required to break a chain is proportional to the length of that chain (or the number of C-C bond in the chain  $N_x$ ). Assuming that only the chains crossing the plane of the crack will break, the intrinsic fracture energy for a material can be calculated as:

$$\Gamma_0 = N_x U \Sigma \quad \text{Eq. 16}$$

Where  $\Sigma$  is the areal density of chain crossing the crack plane,  $U$  is the bond energy of a C-C bond (350 kJ/mol).

For a homogeneously crosslinked network:

$$\Sigma \sim \nu_x l N_x^{\frac{1}{2}} C_\infty^{\frac{1}{2}} \quad \text{Eq. 17}$$

Where  $\nu_x$  is the density of crosslinks,  $l$  is the bond length,  $N_x$  is the number of C-C bonds between crosslinks and  $C_\infty$  the characteristic ratio.

Then from the previous equations, one can write:

$$\Gamma_0 \sim U \nu_x l N_x^{\frac{3}{2}} C_\infty^{\frac{1}{2}} \sim \frac{U l \rho}{M_0} C_\infty^{\frac{1}{2}} N_x^{\frac{1}{2}} \quad \text{Eq. 18}$$

Where  $\rho$  is the monomer density and  $M_0$  is the molar mass of the monomer.

This model shows the intrinsic coupling between toughness and the square root number of C-C bonds between crosslinks, which is also related to the inverse stiffness of the material.

In this model, we can question the localization of breakage: a single plane with no other micro-cracks elsewhere than in this crack plane, seems to be an underestimation of damage in highly stretched materials. Also the energy released per C-C bond is assumed to be equal to the homolytic scission energy of the bond and this seems quite overestimated. To release such

energy, just before the breakage of a bond in the chain, the whole chain should be in a conformation where all its bonds are close to their breakage point and capable of breaking.

Craig and coworkers [15] recently suggested that the average energy released by the C-C bonds in the breaking chains during crack propagation may be less than the homolytic scission energy of C-C bonds but closer to 60 kJ/mol.

Even though this model is 50 years old, the order of magnitude and the scaling of  $\Gamma_0$  with  $N_x$  are very relevant [16].

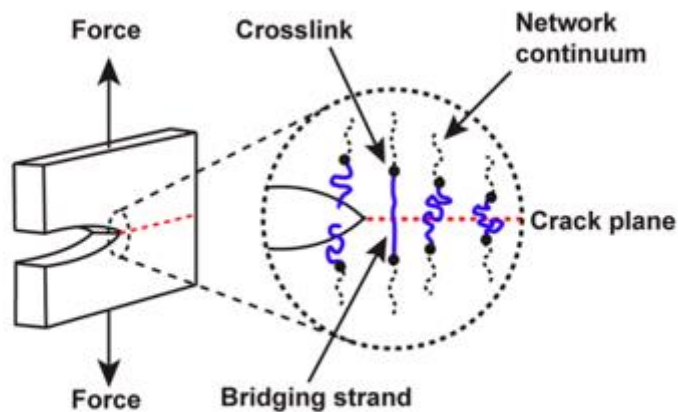


*Figure 8 Schematic representation of the rupture of an elastomer at the molecular scale according to the model of Lake and Thomas (reproduced from [15])*

### 3. How to reinforce elastomers?

Conventional polymer networks are limited by intrinsically coupled material properties based on the chemical nature of a polymer network. The best example is the existing trade-off between stiffness and toughness which both depend on the chain length between crosslinks. Increasing crosslink density, decreases the chain length between crosslinks and increases the low strain modulus. Unfortunately, from the Lake and Thomas model presented above, one can see that increasing crosslink density also inevitably decreases the fracture toughness, which makes it impossible to simply improve both stiffness and toughness of an elastomer.

Though conventional polymer networks are very interesting for the development of general models, the common use of elastomers requires materials' improvements. The following section will aim at describing some of the reinforcement strategies for soft materials.

### 3.1. General guidelines

Various strategies to design tough soft materials are summarized in recent reviews on tough hydrogels [17-19].

Hydrogels are good model materials with growing interest in biomedical applications like artificial tendons or cartilage. They are soft stretchable materials that contains a high proportion of water. Because these materials are swollen networks, their internal friction and entanglements are negligible and they behave as purely elastic materials. Classical hydrogels are very weak and thus very sensitive to any reinforcement. A great variety of hydrogels can be synthesized by tuning the chemical structure based on organic chemistry.

Fracture of a material can be divided into two events: first the nucleation of a defect in the materials that, then, can lead to the second phase which is the propagation of a crack. In order to improve the material resistance to fracture, one can consider to reinforce the material in regards to either of the fracture phases.

### 3.2. Delay nucleation

In this part are presented two ways to delay the fracture nucleation.

The first strategy is to synthesize an ideal polymer network. Such a network is composed of a uniform chain length between crosslinks, a uniform functionality and no defect [18].

Following the pioneer work of Sakai and al. [20], ideal polymer networks have been synthesized using multi-arm macro-monomers in the form of tetra-arm PEG. The arms of adjacent macro-monomers were crosslinked into polymer chains. Uniform chain length, uniform functionality and almost no defect could be achieved because the lengths of the macro-monomer arms were uniform and the reaction efficiency of the crosslinking process was high.

The defect free nature of the ideal polymer network has demonstrated to make the material highly stretchable and resilient [21].

A slideable crosslink is commonly made of two covalently crosslinks polymer rings that connect two polymer chains together. This enables the polymer chains to slide inside the rings [18].

The polymer networks with slideable crosslinks are generally synthesized from cyclodextrin-based polyrotaxanes [22]. Cyclodextrin-based polyrotaxanes are inclusion complexes composed of linear polymer chains that are threaded through the cyclodextrin molecules and then capped by bulky groups at the chain ends. The cyclodextrins can be crosslinked with each other to interconnect the threaded polymer chains and form the polymer network [23,24].

Polymer networks with slideable crosslinks have shown to be both mechanically stable and reconfigurable due to the permanent and slideable nature of the crosslink. Upon deformation, the slideable crosslink tend to reconfigure the polymer network in a way that the reconfigured polymer network approximates an ideal polymer network.

In both these strategies (Figure 9), upon deformation all chains have or tend to have the same length. So the network can be stretched homogeneously without micro-cracks occurring early on the deformation. Micro-cracks usually occur because of shorter chains reaching their limit extensibility and often results in correlated chains breakage and macroscopic failure of the material.

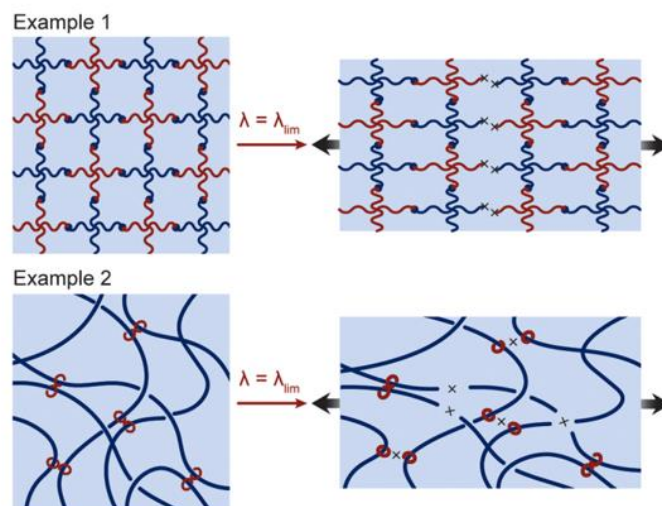


Figure 9 Schematic representation of an ideal polymer network and a network with slideable crosslinks at rest and in a stretched state

Both these strategies delay fracture nucleation but they do not slow down the fracture propagation. So when a defect nucleates in the material, the crack propagates fast and failure is inevitable. The following part will detail some strategies to slow down fracture propagation.

### 3.3. Slow down propagation

In order to slow down crack propagation once it has started, the strategy consists in increasing the amount of energy needed to propagate a crack by dissipating energy in something else than the creation of two new surfaces.

Recent reviews [17,18] which have summarized the different strategies to reinforce hydrogels, agree on a common strategy to reinforce hydrogels which consist in increasing dissipation while maintaining extensibility. For such purpose, at least one component in the hydrogel should maintain a high stretch limit, which means that the network's chains should be long (or should contain a high amount of monomer unit). And at least one component in the hydrogel should dissipate substantial mechanical energy under deformation in a zone close to the crack tip (like the breakage of sacrificial bonds or more generally friction or plasticity mechanisms).

To do so, it is interesting to introduce transient (“physical”) crosslinks to the network as it would enable to dissipate energy when the physical bonds break [25,26]. The physical bonds act as reversible crosslinks.

There exist various types of transient crosslinks which could weaken physical bonds like ionic groups in the network coupled with metal ions [27–29], metal-ligand complexes [30], hydrogen bonds [31] or hydrophobic interactions [32].

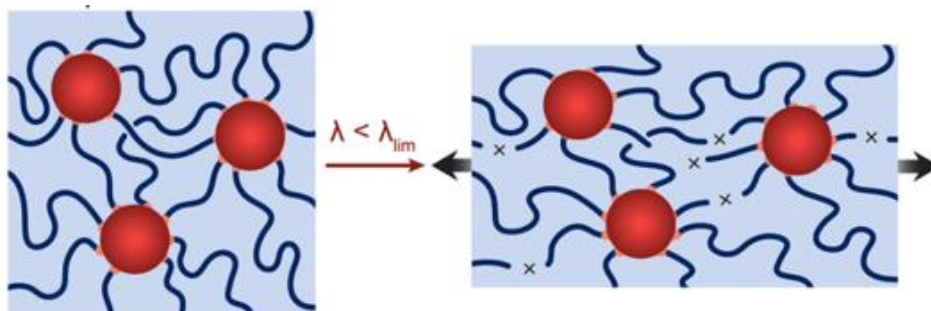


Figure 10 Schematic representation of high functionality crosslinks in a polymer network at rest and in a stretched state

Strong physical crosslinks like crystalline domains and glassy nodules also dissipate more energy by naturally acting as high functionality crosslinks [33].

High functionality crosslinks (Figure 10) correspond to molecular regions where multiple polymer chains bond between two adjacent high functionality crosslink. All the chains between two high functionality crosslinks are rarely the same length. This means that the shorter chains will break or detach from the high functionality crosslink while the longer one maintain the integrity and extensibility of the material as the material is deformed and will dissipate energy. The bonds between the high functionality crosslink and the chains can be permanent, strong or weak physical crosslink or dynamic covalent crosslinks or a combination of the above [34].

Nano/micro fibrous hydrogels also implement the design of tough hydrogels. The reorientation and realignment of the microfibers during stretching can further enhance the stretchability of the material [35,36]. The fracture of the nano/microfibers from the hydrogel matrices dissipates substantial mechanical energy.

### 3.4. The specifications of elastomers

#### 3.4.1. Viscoelasticity

Elastomers are similar to hydrogels in the fact that they are both three dimensional stretchable networks. The main difference is that hydrogels are swollen networks while elastomers are dry. This means that in an elastomer, the chains are closer to each other and friction between chains cannot be neglected during the deformation of the material.

This friction induces some viscoelastic dissipation whose effects have been studied both experimentally and theoretically on fracture. Gent [37] showed for example that bringing an elastomer closer to its  $T_g$  could increase its fracture toughness by two orders of magnitude.

However, using viscoelasticity to improve fracture toughness comes with some major drawbacks. One of them is that viscoelasticity is time and temperature dependent. Which means that the materials properties become very sensitive to the conditions of use. Thus for each type of applications, one would need to prepare a specific material with the adequate  $T_g$ . Also using viscoelasticity as the main source of dissipation reaches a limit for applications with a wide range of temperature use or strain rates. Finally, even in good starting conditions of use, dissipated energy generally produces heat which could also affect the material properties during usage.

### 3.4.2. Fillers

The most common way to reinforce rubbery materials is the introduction of inorganic nanofillers inside the rubbery matrix to obtain a final material called nanocomposite.

Basically inorganic hard nanofillers, like carbon or silica, are dispersed into an elastomer matrix. The combination of a rigid dispersed phase inside a soft phase makes the final material both stiffer and tougher.

The addition of nanofillers comes with some consequences in regards to the mechanical behavior. A strong non linearity of the modulus is observed, that is known as the Payne effect [38]. It corresponds to a decrease in stiffness and an increase in viscous losses observed when the strain increases between 0.1 and 10%. This effect depends strongly on the filler fraction and disappears when the temperature increases or when the strain rate approaches zero which makes it very similar to viscoelasticity.

The other dissipation mechanism is known as the Mullin's effect (Figure 11): it consists in a significant softening at large strain after the first elongation of the material. This softening is accompanied by a residual deformation and can be partially recovered after heating or after rest time [39,40].

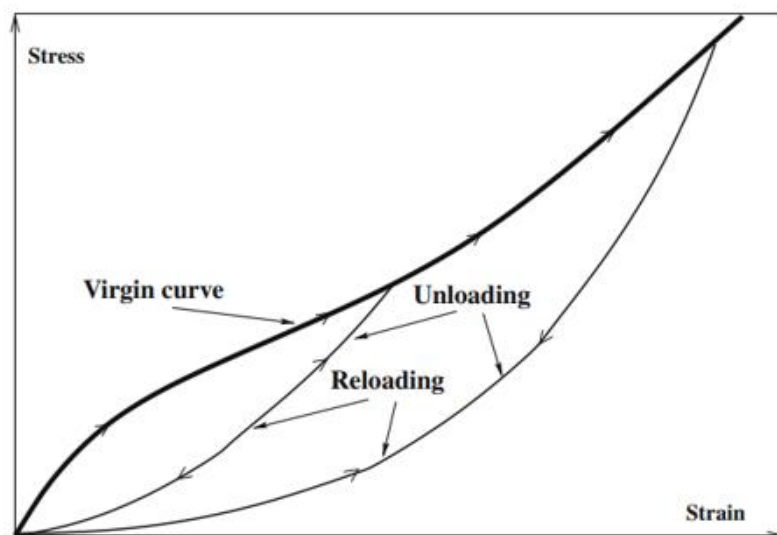


Figure 11 Typical stress-strain plot of the Mullins' effect

A lot of efforts has been made to understand at least qualitatively the reinforcement of fillers in elastomers and the main parameters behind this process. First, greater reinforcement is obtained when the fillers are relatively homogeneously distributed within the matrix and in a sufficient

amount to get a percolating network of filler particles [41]. Then, the surface chemistry of the filler and the interactions with the matrix also play an important role in the reinforcement mechanism [42]. The question of the polymer chains at the surface of the filler particles is a research topic on itself. One way to explain the mechanical properties of filled elastomer is to see it as the consequences of the frozen and bound polymers at the surface of the particles which create glassy domains close to the particles and increase dissipation in the material during deformation [43].

Adding filler to elastic material undoubtedly improves both the stiffness and toughness of the material but it also introduces some complicated dynamic effects. It brings some more complexity to the process as well, as the distribution of the fillers within the matrix is a key parameter to the final material properties. Finally, one major drawback of this material is the loss of transparency that is accompanying the incorporation of filler particles. This is definitely a limitation to some applications.

### 3.4.3. Physical bonds

Similar to what has been presented for hydrogels, it is possible to introduce physical bonds into elastomers in order to dissipate energy by grafting some polar groups to the chains. The main difference here is that elastomers are hydrophobic materials, therefore the polar functions tends to aggregate and form clusters [44]. Shabbir et al. [45] studied ionomer melts and found slower crack propagation which indicates there is some sort of dissipation occurring in materials with physical bonds.

Another strategy again is the one of dynamic covalent bonds, same as for hydrogels, the fracture and recovery of the physical bonds could dissipate energy. This strategy adds an interesting self-healing property to the materials which makes it recyclable. In one study, authors combined covalent crosslinks with transient ones and demonstrated fracture energies up to 13,5 kJ/m<sup>2</sup> [46].

One mechanism that includes strong physical interactions can be mentioned: it is the strain induced crystallization. This is quite a rare behavior, however, natural rubber is one good example of such material [47].

Viscoelasticity, the use of inorganic fillers or the introduction of physical bonds to dissipated energy are three strategies that all introduce strain rate dependence through unconventional

polymer network interactions. Another strategy based only on polymer network architectures has been developed and will be the focus of the following section.

### 3.5. Multiple networks

Interpenetrated polymer networks (IPN) have been used to enhance the mechanical properties of polymer materials. At first, the key of this strategy was the use of two different types of polymer materials with contrasting properties in order to obtain a final material that combines the advantages of both materials, as in conventional nanocomposites. Later on, one particular type of IPN called the double network hydrogel developed by Gong et al. [48].

#### 3.5.1. Double network hydrogels

Gong et al. [48] synthesized their double network hydrogel (Figure 12) in a sequential synthesis where a first hydrogel network made of short chain (highly crosslinked, quite brittle) is first synthesized and then immersed in a solution of water, monomers, initiators and crosslinker to form a second polymer network with long chain entangled with the first network.

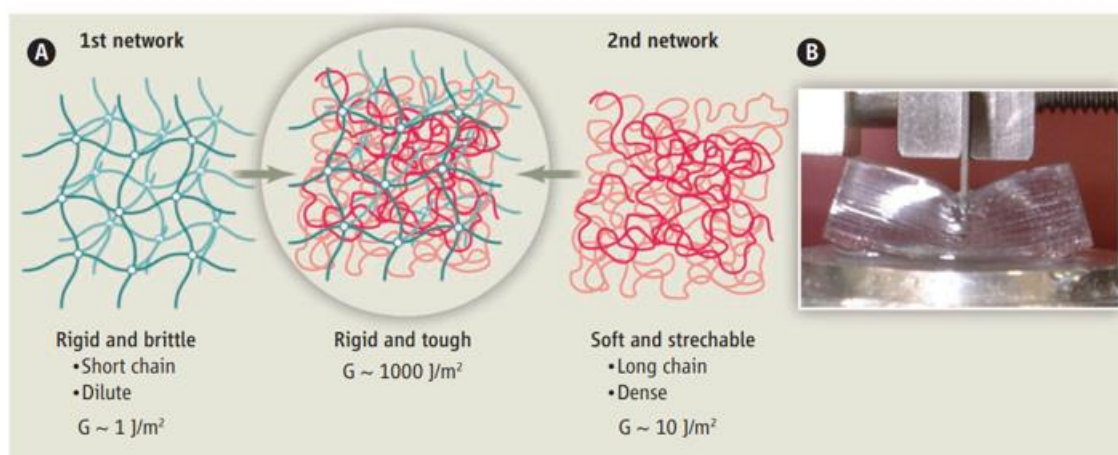


Figure 12 Double network hydrogel

Thanks to this strategy stiffer hydrogels containing between 60 and 90 wt% water with a reinforcement of the fracture toughness from few  $\text{J/m}^2$  for a simple hydrogel, to over  $1000 \text{ J/m}^2$  for double network hydrogel, could be obtained.

Several syntheses were done with different polymers to get information on the criteria to obtain tough double network hydrogels [49].

- One best polymer for making such material appeared to be the polyelectrolyte poly(2-acrylamide-2-methylpropanesulfonic acid) (PAMPS) as the first network and

poly(acrylamide) (PAAm) as the second network. Due to its polyelectrolyte nature, the first gel network swells in the second polymerization step and is highly extended in the final double network hydrogel.

- It was shown that the molar ratio of second network to first network should be between 20 and 30 to reach the best mechanical properties.
- The first and second network crosslink density ratio is an important criterion in the reinforcement as well. The first network should be tight while the second network should have chains long enough to entangle (molecular weight of the chain between crosslink above  $10^6$  g/mol) [50].
- The first and the second network should be interconnected to transfer the strain. Double network hydrogels with no crosslinker in the second network have been synthesized and showed very good mechanical properties. In Nakajima's paper [51], a double network with two completely independent networks was prepared by suppressing all the unreacted carbon-carbon double bonds prior to polymerizing the second network. They demonstrated that in the case of the uncrosslinked second network, the reinforcement mechanism comes mainly from the covalent connection between the first and the second network.

When the material is stretched, the short chains of the first network break randomly within the material as they reach their limiting extensibility sooner and dissipate energy. This phenomenon happens before the macroscopic failure of the material as the second network long chains maintain the integrity of the network. The group of Gong performed Dynamic Light Scattering (DLS) experiment to study the relaxation in double networks [52]. Their results showed the presence of clusters in the deformed state which they interpreted as “crack-stoppers”.

This reinforcement is based on bond breakage thus it is not viscoelastic. This enabled to produce strain rate and temperature independent soft and tough hydrogels. In reality, some fracture energy measurements showed a weak variation of the toughness with crack propagation velocity [53].

The mechanical behavior of double network hydrogel shows characteristic phenomenon like hysteresis and necking [54] (Figure 13). Hysteresis similar to the Mullin's effect has been observed in double network gels [55]. Under step cycle loading, hysteresis could be measured for the first cycle while no hysteresis was measured for the second cycle. The second load was softer than the first one and the softened second cycle was purely elastic.

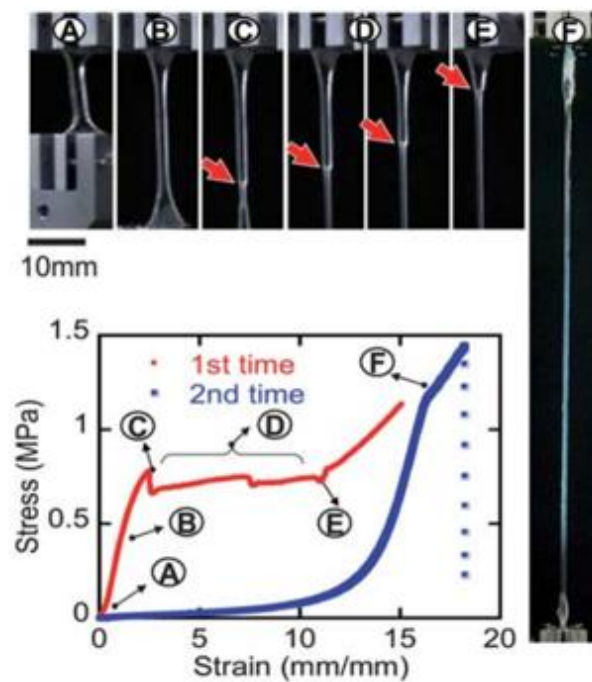


Figure 13 Mechanical behavior of a double network hydrogel and necking

The main difference that can be noticed from the comparison between double networks and filled rubbers is the absence of recovery in the double network material as opposed to the filled elastomers. The bond breakage mechanism is irreversible. The hysteresis signal can be attributed to the bond breakage happening during the load. After the first cycle, all the shorter chains that could break at the reached stretch already dissipated their energy. During the second stretch, no more energy is dissipated from bond breakage, the material is softer and has a purely elastic behavior.

The necking phenomenon is more often observed in metals or semi crystalline or glassy materials. It corresponds to the formation of a stable localized region of higher deformation in the material which propagates along the tensile direction as the sample is being stretched, as can be seen in the figure above. This mechanical instability is due to an unstable softening

followed by a stabilizing hardening. Two different structures of the material coexist at the same nominal stress.

During the neck propagation of double network hydrogel, a plateau value of the tensile stress can be observed. This plateau value is fairly independent on the stretching rate. After the neck propagation, in cyclic loading, it can be seen that the material become very soft. It is a sign that irreversible structural change has happened inside the gel. One explanation is the fragmentation of the first brittle network into small clusters [56,57]. These clusters act as high functionality macro-crosslinker for the second network.

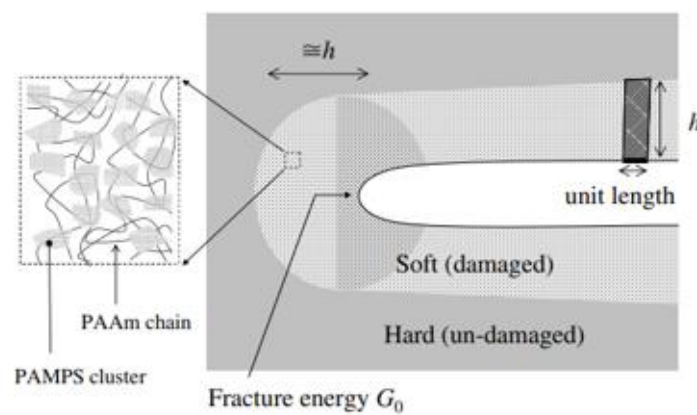


Figure 14 Representation of fracture mechanism in double network hydrogel

One question remains: what is the criteria to know whether or not a material will yield?

Using tetra-PEG homogeneous network as first network, Matsuda et al. [58] synthesized double network gels with a well-controlled structure. The swelling of the first network was enabled by polyelectrolyte chains incorporated in the network structure to work as molecular stent and artificially increase the osmotic pressure. They observed a decrease of the yield stress with increasing chain length and explained it by geometric arguments: the closer the chain to its finite extensibility, the smaller the yield strain. They also obtained a master curve for stress and strain by taking into account the dilution of the chains of the first network.

A recent work by Nakajima et al. has shown that if the second network doesn't affect the mechanical behavior of the double network hydrogel before necking, after necking both networks play a role in the mechanical properties of the necked region [59].

Cyclic fatigue of double network gels has also been studied by Suo et al. [60]. They showed that the fatigue threshold is almost insensitive to the concentration of second network (close to  $400 \text{ J.m}^{-2}$ ). They found that the fatigue crack propagation rate is less sensitive to strain energy release rate in double network hydrogels compared to the single network hydrogels. These materials show relatively good fatigue properties.

### 3.5.2. Models for the fracture mechanics of double network hydrogels

Following the experimental observations, Tanaka [61] and Brown [62] proposed a similar model for the double network hydrogel reinforcing mechanism. The propagation of a crack is described as a two-step process. First the local high strain at the crack tip breaks the first network. This induces the creation of a damage zone around the crack tip that must be crossed during the second step which cost more energy as represented below.

Direct observation of the damage zone via Force Atomic Microscopy (AFM) and laser scanning microscopy, Figure 15, [63,64] confirmed qualitatively the model for gels. However, none of the models explained the reinforcement mechanics in the case of an uncrosslinked second network.

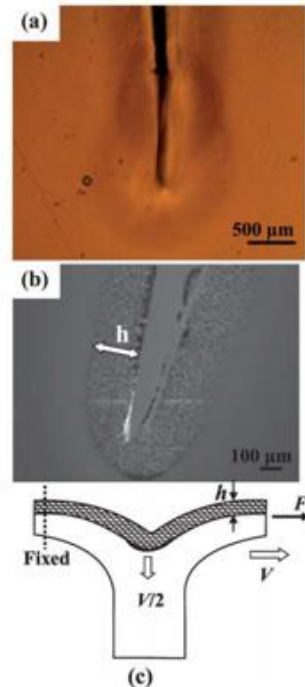


Figure 15 Direct images of the necked region in crack propagated double network hydrogels

New hydrogel designs inspired by the double network strategy are being developed to better understand the mechanics behind tough soft materials [65,66] or to push the reinforcement even further [67,68].

This strategy has been implemented to elastomer in our group by the work of Ducrot [69].

### 3.5.3. Multiple network elastomers

The synthesis of interpenetrated double network elastomers from ethyl acrylate and methyl acrylate was performed first by Ducrot [70]. It is based on the same sequential strategy as the one used for hydrogels. A first network stiff and highly crosslinked is polymerized and diluted in a second network loosely crosslinked and soft. When the material is stretched, the short chains of the first network break randomly while long chains of the second network maintain the integrity of the material and its elasticity. He repeated the swelling polymerization steps and showed that it was possible to get triple and quadruple elastomers which led to the generic term multiple network elastomers. Chain prestretch was experimentally demonstrated using Small Angle Neutron Scattering [71].

Multiple network elastomers are strongly reinforced in both stiffness and toughness compared to single network elastomers. Their low strain modulus could be multiplied by 4 (1 MPa for a single acrylate network elastomer and 4 MPa for a quadruple acrylate network). High toughness were also reached with fracture energies up to 9 kJ.m<sup>-2</sup> (around 100 J.m<sup>-2</sup> for single acrylate network).

The mechanical values of multiple network elastomers are comparable to what can be obtained with filled elastomers without the disadvantages of the filler strategy. Mainly, the multiple network elastomers are transparent which is not a limit anymore to some applications. Also the reinforcement mechanism for multiple network is based on bond breakage which isn't viscoelastic thus, the use of such material is not limited to a certain range of temperature anymore.

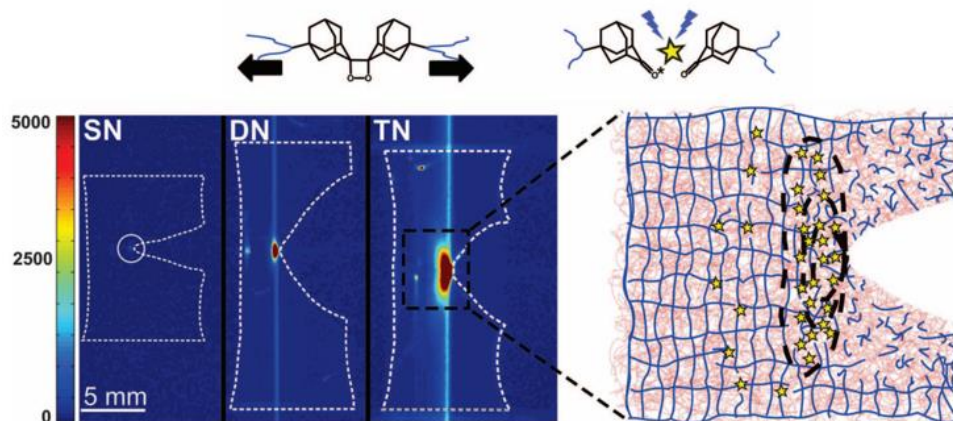


Figure 16 Damage zone and mechanochemistry in SN, DN and TN

Ducrot et al. first proved that bond breakage within the first network was responsible for the improved toughness of the material by using mechanochemistry which stands for the use of a mechanical force to induce a chemical reaction [72]. It is increasingly used in polymer materials as new tools to observe damage. In these cases, the chemical reaction induced comes usually with a modification of the light signal of the molecule which can release a light signal (mechanochemiluminescent molecule) or become fluorescent (mechanofluorescent molecule) or change its visible light absorption spectra (mechanochromic molecule).

Ducrot et al. [69] used mechanoluminescence in the form of dioxetane based molecule [73] incorporated inside the material as a crosslinker. When this molecule breaks, a light signal is emitted. This directly give space and time resolved information on damage within the material. They performed crack propagation tests and could map the intensity of bond breakage into the damage zone around the crack tip.

P. Millereau [74] carried out a systematic study to refine the understanding of the multiple network. He performed numerous synthesis from the same first network, he used a mix of solvent and monomer to tune the prestretch of the chains of the first network. He then performed uniaxial extension and obtained a set of stress strain curve from which he identified four different characteristic mechanical behavior governed by the level of prestretch:

Type 1: prestretch low, no significant reinforcement (range of concentration that correspond to conventional IPN).

Type 2: prestretch between 1.5 and 2 strain hardening is observable but no damage could be measured in the bulk before macroscopic failure.

Type 3: prestretch between 2 and 3, strain-hardening and pseudo Mullins' effect. The bond breakage happening in the first network is sufficient to dissipate energy, as it is visible in the hysteresis in cyclic loading. This bond breakage results as well in the softening of the material.

Type 4: prestretch above 3, necking is observed.

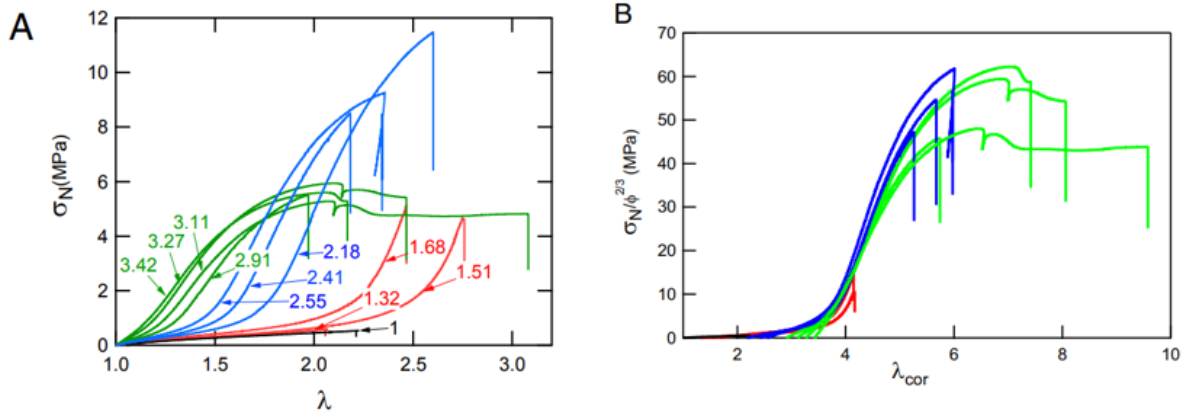


Figure 17 Stress-strain master curve of multiple network elastomer

The work of Millereau et al. [75] demonstrated that the mechanical properties of the multiple network were mainly controlled by two parameters:

1. The prestretch of the first network defined as:

$$\lambda = \frac{L_{total}}{L_{SN}} = \left( \frac{V_{total}}{V_{SN}} \right)^{1/3} \sim \left( \frac{m_{total}}{m_{SN}} \right)^{1/3}$$

Where  $L_{total}$  total and  $L_{SN}$  are a characteristic length (thickness, width or length) of the final material respectively of the multiple network sample and the single network sample.  $V_{total}$  and  $V_{SN}$  are the volume respectively of the multiple network sample and the single network sample.  $m_{total}$  and  $m_{SN}$  are the weight respectively of the multiple network sample and the single network sample.

2. The volume fraction of first network,  $\Phi$ , defined as:

$$\Phi = \frac{V_{SN}}{V_{total}} \sim \frac{m_{SN}}{m_{total}}$$

Only if the two networks have the same density, the volume fraction is equal to the weight fraction. Otherwise density has to be taken into account.

It was possible to plot all the curves on one reduced stress vs. reduced stretch master curve by normalizing stress and deformation by taking into account respectively the dilution of the chains and the prestretch of the chains of the first network.

One can notice that the volume fraction of first network can be deduced from the prestretch  $\Phi = \left(\frac{1}{\lambda}\right)^3$ . Then, only one main parameter controls the large strain mechanical behavior of multiple network, that is the prestretch of the chains of the first network. Note that the fracture point cannot be predicted by the filler network pre-stretch.

P. Millereau also used the mechanoluminescent dioxetane as a crosslinker following the same process as E. Ducrot, he incorporated the probe in a multiple network ( $\lambda=3$ ) to study necking. During the tensile test experiment, for small strains there was no signal at first. Then at higher strains, there was a slight decrease of the local modulus that was accompanied by bond scission all over the sample. At the maximal stress, the signal became a lot less intense and more localized, this was associated with the nucleation of necking. After that strain, there were two localized signal shifting corresponding to the necking front which indicated that the necking process corresponds to a local microscopic damage process that precedes a significant structural change within the material.

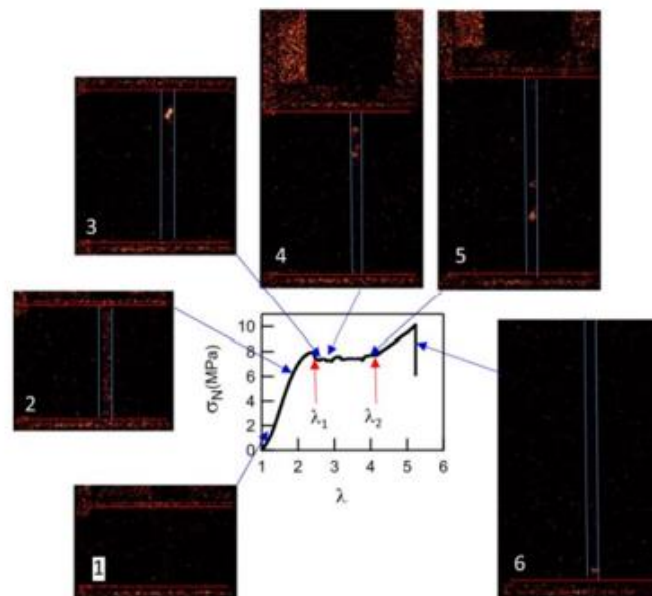


Figure 18 Activation of dioxetane in a triple network elastomer with strain

Y. Chen [76,77] also studied damage in multiple network using mechanochemistry. He used spiropyran, a mechanochromic molecule that change color when it undergoes a force threshold (at 240 pN) [78,79]. Spiropyran when stretched opens to the form merocyanine. This structural change is accompanied by a change in light absorption meaning the molecule change color. The merocyanine form is less stable than the spiropyran, so that after a certain time or with the help of white light, the molecule can go back to its original spiropyran state. The possibility to get a fairly stable signal and to “reset” the molecule, makes spiropyran a particularly interesting tool in the study of local stress within materials.

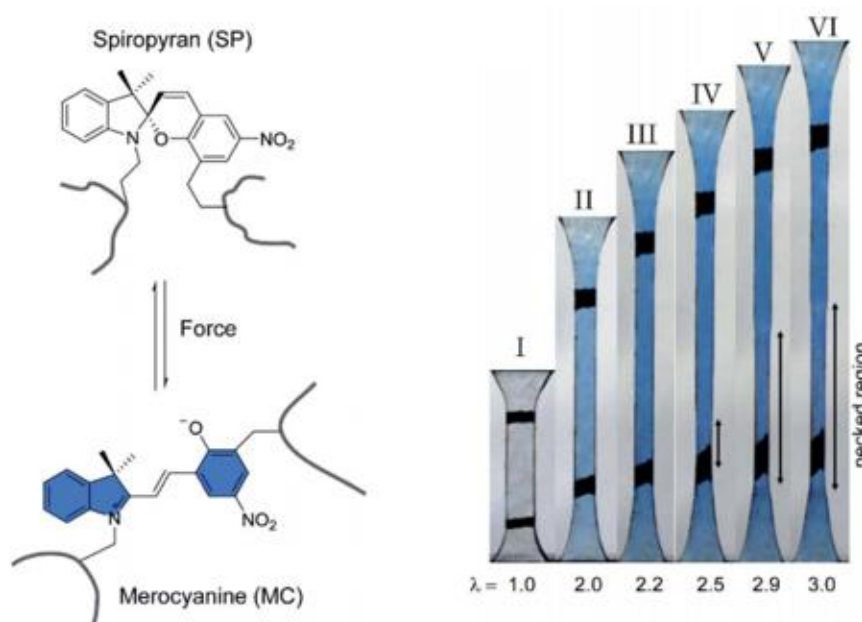


Figure 19 Spiropyran molecule activation into merocyanine and color change during the stretching of a multiple network elastomer with spiropyran in the first network as a function of strain

Y. Chen could incorporate this molecule functionalized di-acrylate as a crosslinker inside either of the networks composing the multiple network to act as a stress sensor. He performed RGB analysis to get a unique space resolved distribution of the stress inside the material [76]. He could map the stress distribution as Ducrot did, but this time in a more cumulative manner as the merocyanine can stay activated for a certain time. He particularly used the variation of color of the merocyanine activated molecule in loaded (blue color) and unloaded state (purple color) [77,80].

He studied necking and found that the breakage of the first network at the yield point was associated with a stress transfer to the second network that could be followed through color change. As previously shown, the activated form of spiropyran, merocyanine, has a color sensitive to relaxation: the stretched form of merocyanine under load in acrylate network is blue while the relaxed form is more purple. Thanks to this sensitivity, he showed that even at the end of the necking process, the stress transfer was not complete and only 9 % of the chains in the first network were unloaded after necking. In fact, the merocyanine doesn't reach its relaxed color which means there is still some load within the first network in the necked region. This means that the first network is still percolating although it is very damaged. This result differs from the double network hydrogel hypothesis of Gong's group that the first network breaks into separated clusters.

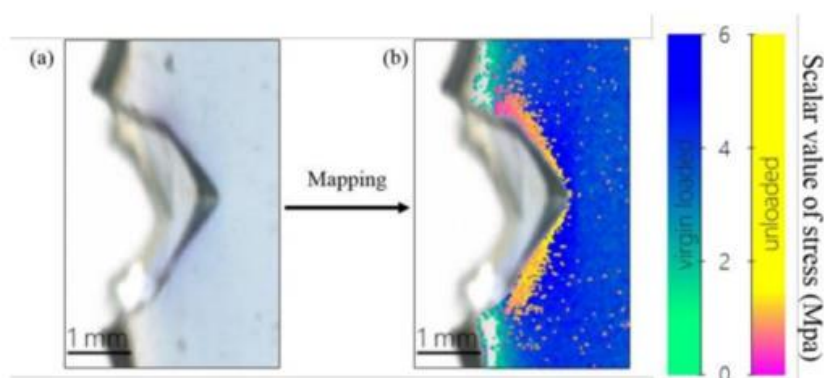


Figure 20 Fracture propagation studied with Spiropyran activation and RGB color analysis

Although the use of mechanochemistry brought new insight to the understanding of damage in multiple network, neither dioxetane nor spiropyran were used as quantification tools. There comes the recent work of J. Slotman, previous PhD student in our lab.

In her work [81], she used a  $\pi$ -extended anthracene maleimide retro Diels-Alder [82]. This molecule is a mechanofluorophore which means that under a force, the molecule undergoes a chemical reaction which leads to a shift in fluorescence.

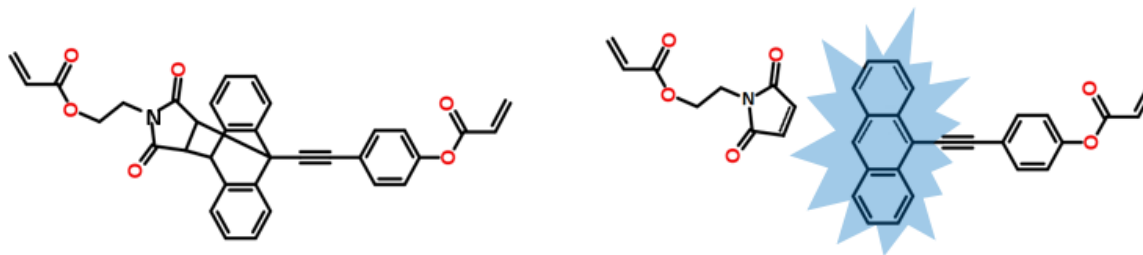


Figure 21 DACL mechanophore

More precisely, the unactivated form of the  $\pi$ -extended anthracene maleimide isn't fluorescent. When the molecule is stretched up to its breaking point, it undergoes a retro Diels-Alder reaction which frees a fluorescent  $\pi$ -extended anthracene moiety. This mechanofluorophore gives a non-reversible stable signal that enabled space resolved post-mortem analysis using confocal imaging. She functionalized the mechanofluorophore into a di-acrylate and used it as a crosslinker (which will be called DACL later on) inside single and multiple network elastomer. Using a confocal microscope, she was able to screen damage in the material in 3D in situ and in post-mortem, at a resolution of approximately 100  $\mu\text{m}$ .

During her work, she developed a way to quantify bond breakage by calibrating the quantity of activated molecules inside the sample. She synthesized the fluorescent moiety of the mechanophore and made calibration samples out of it to convert the intensity of light into a concentration of activated molecules. Thanks to which she could turn back the fluorescent signal she measured in her sample, into a ratio of broken bonds. All of this method will be described in more detail in the corresponding chapter of this manuscript.

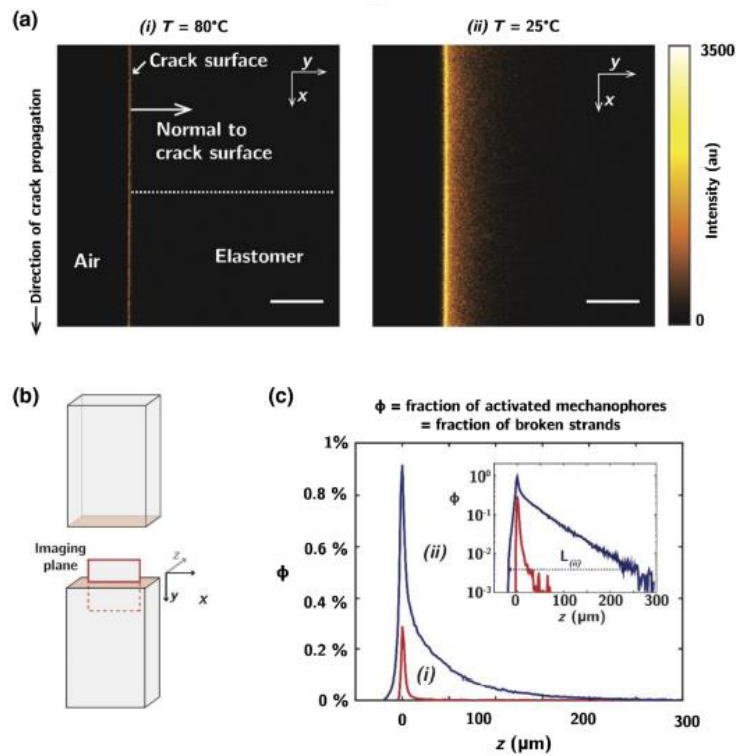


Figure 22 Post mortem characterization of a multiple network elastomer containing DACL using confocal macroscopy

She studied the fracture of single and multiple methyl and ethyl acrylate network materials at different strain rate and temperature to better grasp the evolution of the damage zone and the dependence of fracture on viscoelasticity. She confirmed that the size of the damage zone was highly dependent on the degree of prestretching of the first network with better precision, she found a damage zone over  $180 \mu\text{m}$  away from the crack surface for triple network while the damage zone of double network elastomer reached about  $40 \mu\text{m}$ . She proved that damage in the first network of the multiple network occurred before crack propagation and was higher in the perpendicular direction to the crack propagation.

This led to a new tentative picture to the fracture of multiple network elastomers:

- First random chains of the first network break in the bulk in front of the crack.
- At some point, the breakage very close to the crack tip goes from random to correlated, creating a highly damaged region and stress transfer from the first to the second network
- Finally, the crack propagates in the highly damaged region.

The crack initiation is delayed by the sacrificial bonds but once the crack starts to propagate, the propagation is fast in the necked region.

The understanding of fracture in multiple network isn't complete yet, but her work gave access to a new powerful tool to observe and quantify bond breakage in soft polymer networks.

## Conclusions

Elastomers are very interesting deformable materials. Their everyday use requires some longevity, thus resistance to fracture is a criterion to focus on. Reinforcement strategies exist and are constantly being developed.

The multiple network strategy seems very promising as it leads to transparent tough material with tunable toughness and stiffness based on the prestretch of the first network. It is currently used as a good model material for the study of fracture as the first network prestretch enables to access large chain extension and chain breakage without early macroscopic failure of the sample. However, a more mainstream use would require to develop other fabrication process which would overcome the current limitations of the synthesis, the main one being the macroscopic swelling of a polymer network.

Based on the understanding on the key factors that reinforce the multiple network, one objective of this manuscript will be to develop new designs of materials with similar sacrificial bonds behavior as multiple networks, but with a less restrictive fabrication process.

On another hand, the reinforcement of elastomer remains limited by the understanding of the fracture process itself. The fracture of hard and brittle materials is fairly well described by the linear elastic fracture mechanics. Unfortunately, highly elastic materials don't fit into the previous category. The nucleation and propagation of cracks in soft elastic materials involves a variety of non-linear processes all hidden under the viscoelastic dependence of fracture toughness. No model can yet predict their fracture behavior based on their molecular structure.

Using the mechanoluminescent tools developed to study fracture in multiple network, a part of this project will focus on the study of fracture propagation in soft single network materials. We will experimentally question the LEFM prediction that predicts the relation between the energy release rate and the stress and strain field at the crack tip.

In the fracture process, prior to its propagation, a crack should nucleate within the material. How a defects transforms into a propagated crack remains an open question. Therefore, with mechanochemistry, we will also explore damage distribution in the nucleation process.

The model of Lake and Thomas predicts well the relation between the toughness of a polymer network and its structure (chain length), however, if you look into this molecular model in detail, it seems questionable. Indeed, it suggests that when a material break, only the chain that are crossing the newly created surface break and when a chain breaks, it release the same energy as if all of the bonds broke. This model is supposed to work only when neglecting viscoelasticity, however, even in real life conditions, with some viscoelastic dissipation during propagation, the model still provides a correct scaling. There may be two errors cancelling each other in this model, an underestimation of the number of bonds broken and an overestimation of the amount of energy release by broken chain which compensate each other. Using mechanochemistry as a tool to access quantitatively bond breakage in various polymer materials, a part of this work will aim at understanding why the model of Lake and Thomas works.

Finally, multiple network materials also demonstrate a typical necking behavior. As the presence of a necked phase was observed for double network hydrogels, at the crack tip, during the propagation, even in materials that don't demonstrate this behavior macroscopically; the study of necking and how stress transfer from one network to another during this process will be the focus of one chapter in this manuscript.

## References

1. Rubinstein, M. & Colby, R. H. *Polymer Physics*. (OUP Oxford, 2003).
2. Treloar, L. R. G. *The Physics of Rubber Elasticity*. (Oxford University Press, USA, 1975).
3. Oesterhelt, F., Rief, M. & Gaub, H. E. Single molecule force spectroscopy by AFM indicates helical structure of poly(ethylene-glycol) in water. *New J. Phys.* **1**, 6–6 (1999).
4. Mooney, M. A Theory of Large Elastic Deformation. *Journal of Applied Physics* **11**, 582–592 (1940).

5. Rivlin, R. S. Large Elastic Deformations of Isotropic Materials. IV. Further Developments of the General Theory. *Philosophical Transactions of the Royal Society of London. Series A, Mathematical and Physical Sciences* **241**, 379–397 (1948).
6. Creton, C. & Ciccotti, M. Fracture and adhesion of soft materials: a review. *Rep. Prog. Phys.* **79**, 046601 (2016).
7. Rubinstein, M. & Panyukov, S. Elasticity of Polymer Networks. *Macromolecules* **35**, 6670–6686 (2002).
8. Edwards, S. F. The statistical mechanics of polymerized material. *Proc. Phys. Soc.* **92**, 9–16 (1967).
9. Arruda, E. M. & Boyce, M. C. A three-dimensional constitutive model for the large stretch behavior of rubber elastic materials. *Journal of the Mechanics and Physics of Solids* **41**, 389–412 (1993).
10. Gent, A. N. A New Constitutive Relation for Rubber. *Rubber Chemistry and Technology* **69**, 59–61 (1996).
11. Irwin, G. R. Analysis of Stresses and Strains Near the End of a Crack Traversing a Plate. *Journal of Applied Mechanics* **24**, 361–364 (1957).
12. Greensmith, H. W. Rupture of rubber. X. The change in stored energy on making a small cut in a test piece held in simple extension. *Journal of Applied Polymer Science* **7**, 993–1002 (1963).
13. Gent, A. N. & Schultz, J. Effect of Wetting Liquids on the Strength of Adhesion of Viscoelastic Material. *The Journal of Adhesion* **3**, 281–294 (1972).
14. Lake, G. J. & Thomas, A. G. The Strength of Highly Elastic Materials. *Proceedings of the Royal Society A: Mathematical, Physical and Engineering Sciences* **300**, 108–119 (1967).

15. Wang, S., Panyukov, S., Rubinstein, M. & Craig, S. Quantitative Adjustment to the Molecular Energy Parameter in the Lake–Thomas Theory of Polymer Fracture Energy. *Macromolecules* **52**, (2019).
16. Bhowmick, A. K. Threshold Fracture of Elastomers. *null* **28**, 339–370 (1988).
17. Zhao, X. Multi-scale multi-mechanism design of tough hydrogels: building dissipation into stretchy networks. *Soft Matter* **10**, 672–687 (2014).
18. Zhao, X. *et al.* Soft Materials by Design: Unconventional Polymer Networks Give Extreme Properties. *Chem. Rev.* **121**, 4309–4372 (2021).
19. Creton, C. 50th Anniversary Perspective: Networks and Gels: Soft but Dynamic and Tough. *Macromolecules* **50**, 8297–8316 (2017).
20. Sakai, T. *et al.* Design and Fabrication of a High-Strength Hydrogel with Ideally Homogeneous Network Structure from Tetrahedron-like Macromonomers. *Macromolecules* **41**, 5379–5384 (2008).
21. Matsunaga, T., Sakai, T., Akagi, Y., Chung, U. & Shibayama, M. Structure Characterization of Tetra-PEG Gel by Small-Angle Neutron Scattering. *Macromolecules* **42**, 1344–1351 (2009).
22. Okumura, Y. & Ito, K. The Polyrotaxane Gel: A Topological Gel by Figure-of-Eight Cross-links. 3.
23. Loethen, S., Kim, J. & Thompson, D. H. Biomedical Applications of Cyclodextrin Based Polyrotaxanes. *null* **47**, 383–418 (2007).
24. Mayumi, K. & Ito, K. Structure and dynamics of polyrotaxane and slide-ring materials. *Polymer* **51**, 959–967 (2010).
25. Voorhaar, L. & Hoogenboom, R. Supramolecular polymer networks: hydrogels and bulk materials. *Chem. Soc. Rev.* **45**, 4013–4031 (2016).

26. Wang, W., Zhang, Y. & Liu, W. Bioinspired fabrication of high strength hydrogels from non-covalent interactions. *Progress in Polymer Science* **71**, 1–25 (2017).
27. Lee, K. Y. *et al.* Controlling Mechanical and Swelling Properties of Alginate Hydrogels Independently by Cross-Linker Type and Cross-Linking Density. *Macromolecules* **33**, 4291–4294 (2000).
28. Sun, T. L. *et al.* Physical hydrogels composed of polyampholytes demonstrate high toughness and viscoelasticity. *Nature Mater* **12**, 932–937 (2013).
29. Li, J., Illeperuma, W. R. K., Suo, Z. & Vlassak, J. J. Hybrid Hydrogels with Extremely High Stiffness and Toughness. *ACS Macro Lett.* **3**, 520–523 (2014).
30. Yavvari, P. S. & Srivastava, A. Robust, self-healing hydrogels synthesised from catechol rich polymers. *J. Mater. Chem. B* **3**, 899–910 (2015).
31. Zhang, G., Chen, Y., Deng, Y., Ngai, T. & Wang, C. Dynamic Supramolecular Hydrogels: Regulating Hydrogel Properties through Self-Complementary Quadruple Hydrogen Bonds and Thermo-Switch. *ACS Macro Lett.* **6**, 641–646 (2017).
32. Mihajlovic, M. *et al.* Tough Supramolecular Hydrogel Based on Strong Hydrophobic Interactions in a Multiblock Segmented Copolymer. *Macromolecules* **50**, 3333–3346 (2017).
33. Abe, K. & Yano, H. Cellulose nanofiber-based hydrogels with high mechanical strength. *Cellulose* **19**, 1907–1912 (2012).
34. Fu, J. Strong and tough hydrogels crosslinked by multi-functional polymer colloids. *J. Polym. Sci. Part B: Polym. Phys.* **56**, 1336–1350 (2018).
35. Nakayama, A. *et al.* High Mechanical Strength Double-Network Hydrogel with Bacterial Cellulose. *Advanced Functional Materials* **14**, 1124–1128 (2004).

36. Ye, D. *et al.* Deformation Drives Alignment of Nanofibers in Framework for Inducing Anisotropic Cellulose Hydrogels with High Toughness. *ACS Appl. Mater. Interfaces* **9**, 43154–43162 (2017).
37. Gent, A. N., Lai, S.-M., Nah, C. & Wang, C. Viscoelastic Effects in Cutting and Tearing Rubber. *Rubber Chemistry and Technology* **67**, 610–618 (1994).
38. Payne, A. R. The dynamic properties of carbon black-loaded natural rubber vulcanizates. Part I. *Journal of Applied Polymer Science* **6**, 57–63 (1962).
39. Mullins, L. *Softening of Rubber by Deformation*. (Rubber Division, American Chemical Society, 1969).
40. Diani, J., Fayolle, B. & Gilormini, P. A review on the Mullins effect. *European Polymer Journal* **45**, 601–612 (2009).
41. Pu, Z., Mark, J. E., Jethmalani, J. M. & Ford, W. T. Effects of Dispersion and Aggregation of Silica in the Reinforcement of Poly(methyl acrylate) Elastomers. *Chem. Mater.* **9**, 2442–2447 (1997).
42. Qian, S., Huang, J., Guo, W. & Wu, C. Investigation of Carbon Black Network in Natural Rubber with Different Bound Rubber Contents. *null* **46**, 453–466 (2007).
43. Berriot, J., Montes, H., Lequeux, F., Long, D. & Sotta, P. Evidence for the Shift of the Glass Transition near the Particles in Silica-Filled Elastomers. *Macromolecules* **35**, 9756–9762 (2002).
44. Rukmanikrishnan, B., Chae, J. & Lee, J. Rheological, mechanical, thermal and barrier properties of highly elastic polyurethane/zinc ionomer composite films. *Journal of Thermoplastic Composite Materials* 0892705720939173 (2020)  
doi:10.1177/0892705720939173.
45. Shabbir, A. *et al.* Brittle fracture in associative polymers: the case of ionomer melts. *Soft Matter* **12**, 7606–7612 (2016).

46. Wu, J., Cai, L. & Weitz, D. A. Tough Self-Healing Elastomers by Molecular Enforced Integration of Covalent and Reversible Networks. *Adv. Mater.* **29**, 1702616 (2017).
47. Gent, A. N. & Zhang, L.-Q. Strain-Induced Crystallization and Strength of Rubber. *Rubber Chemistry and Technology* **75**, 923–934 (2002).
48. Gong, J. P., Katsuyama, Y., Kurokawa, T. & Osada, Y. Double-Network Hydrogels with Extremely High Mechanical Strength. *Advanced Materials* **15**, 1155–1158 (2003).
49. Gong, J. P. Why are double network hydrogels so tough? *Soft Matter* **6**, 2583 (2010).
50. Tsukeshiba, H. *et al.* Effect of Polymer Entanglement on the Toughening of Double Network Hydrogels. *J. Phys. Chem. B* **109**, 16304–16309 (2005).
51. Nakajima, T. *et al.* True Chemical Structure of Double Network Hydrogels. *Macromolecules* **42**, 2184–2189 (2009).
52. Na, Y.-H. *et al.* Structural Characteristics of Double Network Gels with Extremely High Mechanical Strength. *Macromolecules* **37**, 5370–5374 (2004).
53. Tanaka, Y. *et al.* Determination of Fracture Energy of High Strength Double Network Hydrogels. *J. Phys. Chem. B* **109**, 11559–11562 (2005).
54. Kawauchi, Y. *et al.* Brittle, ductile, paste-like behaviors and distinct necking of double network gels with enhanced heterogeneity. *Journal of Physics: Conference Series* **184**, 012016 (2009).
55. Webber, R. E., Creton, C., Brown, H. R. & Gong, J. P. Large Strain Hysteresis and Mullins Effect of Tough Double-Network Hydrogels. *Macromolecules* **40**, 2919–2927 (2007).
56. Na, Y.-H. *et al.* Necking Phenomenon of Double-Network Gels. *Macromolecules* **39**, 4641–4645 (2006).

57. Nakajima, T., Kurokawa, T., Ahmed, S., Wu, W. & Gong, J. P. Characterization of internal fracture process of double network hydrogels under uniaxial elongation. *Soft Matter* **9**, 1955–1966 (2013).
58. Matsuda, T. *et al.* Yielding Criteria of Double Network Hydrogels. *Macromolecules* **49**, 1865–1872 (2016).
59. Nakajima, T., Kurokawa, T., Furukawa, H. & Gong, J. P. Effect of the constituent networks of double-network gels on their mechanical properties and energy dissipation process. *Soft Matter* **16**, 8618–8627 (2020).
60. Zhang, W. *et al.* Fatigue of double-network hydrogels. *Engineering Fracture Mechanics* **187**, 74–93 (2018).
61. Tanaka, Y. A local damage model for anomalous high toughness of double-network gels. *EPL* **78**, 56005 (2007).
62. Brown, H. R. A Model of the Fracture of Double Network Gels. *Macromolecules* **40**, 3815–3818 (2007).
63. Yu, Q. M., Tanaka, Y., Furukawa, H., Kurokawa, T. & Gong, J. P. Direct Observation of Damage Zone around Crack Tips in Double-Network Gels. *Macromolecules* **42**, 3852–3855 (2009).
64. Tanaka, Y. *et al.* Localized Yielding Around Crack Tips of Double-Network Gels. *Macromolecular Rapid Communications* **29**, 1514–1520 (2008).
65. Okumura, T., Takahashi, R., Hagita, K., King, D. R. & Gong, J. P. Improving the strength and toughness of macroscale double networks by exploiting Poisson's ratio mismatch. *Sci Rep* **11**, 13280 (2021).
66. King, D. R. *et al.* Anisotropic Double-Network Hydrogels via Controlled Orientation of a Physical Sacrificial Network. *ACS Appl. Polym. Mater.* **2**, 2350–2358 (2020).

67. Matsuda, T., Kawakami, R., Namba, R., Nakajima, T. & Gong, J. P. Mechanoresponsive self-growing hydrogels inspired by muscle training. *Science* **363**, 504–508 (2019).
68. Wang, Z. *et al.* Toughening Hydrogels Through Force-triggered Chemical Reactions that Lengthen Polymer Strands. 19.
69. Ducrot, E., Chen, Y., Bulters, M., Sijbesma, R. P. & Creton, C. Toughening Elastomers with Sacrificial Bonds and Watching Them Break. *Science* **344**, 186–189 (2014).
70. Ducrot, E. Innovative tough elastomers : designed sacrificial bonds in multiple networks. (Paris 6, 2013).
71. Ducrot, E., Montes, H. & Creton, C. Structure of Tough Multiple Network Elastomers by Small Angle Neutron Scattering. *Macromolecules* **48**, 7945–7952 (2015).
72. Chen, Y., Mellot, G., van Luijk, D., Creton, C. & Sijbesma, R. P. Mechanochemical tools for polymer materials. *Chem. Soc. Rev.* **50**, 4100–4140 (2021).
73. Chen, Y. *et al.* Mechanically induced chemiluminescence from polymers incorporating a 1,2-dioxetane unit in the main chain. *Nature Chemistry* **4**, 559–562 (2012).
74. Millereau, P. M. Large Strain and Fracture of Multiple Network Elastomers. (Paris 6, 2017).
75. Millereau, P. *et al.* Mechanics of elastomeric molecular composites. *Proceedings of the National Academy of Sciences* **115**, 9110–9115 (2018).
76. Chen, Y., Yeh, C. J., Qi, Y., Long, R. & Creton, C. From force-responsive molecules to quantifying and mapping stresses in soft materials. *Sci. Adv.* **6**, eaaz5093 (2020).
77. Chen, Y., Sanoja, G. & Creton, C. Mechanochemistry unveils stress transfer during sacrificial bond fracture of tough multiple network elastomers. *Chem. Sci.* 10.1039/D1SC03352B (2021) doi:10.1039/D1SC03352B.
78. Zhang, H. *et al.* Spiropyran as a Mechanochromic Probe in Dual Cross-Linked Elastomers. *Macromolecules* **47**, 6783–6790 (2014).

79. Gossweiler, G. R., Kouznetsova, T. B. & Craig, S. L. Force-Rate Characterization of Two Spiropyran-Based Molecular Force Probes. *J. Am. Chem. Soc.* **137**, 6148–6151 (2015).
80. Chen, Y. Cartographie quantitative de la contrainte dans les matériaux mous par mécanochimie. (PSL, 2018).
81. Slooman, J. Détection quantitative de l'endommagement moléculaire, par mécano-fluorescence, dans les matériaux mous. (PSL, 2019).
82. Göstl, R. & Sijbesma, R. P.  $\pi$ -extended anthracenes as sensitive probes for mechanical stress. *Chemical Science* **7**, 370–375 (2016).

## **Chapter 2**

# **Nanocomposite elastomers filled with soft interpenetrable particles**



## Table of contents

Introduction .....	57
1. Results .....	58
1.1. Synthesis and characterization of the materials.....	58
1.1.1. Particles synthesis.....	58
1.1.2. Dispersion and swelling of the particles in ethyl acrylate .....	60
1.1.3. Synthesis of a simple matrix as a reference.....	61
1.1.4. Synthesis of the nanocomposites .....	61
1.2. Mechanical properties of the nanocomposites .....	63
1.2.1. Effect of the volume fraction of filler.....	63
1.2.2. Effect of the degree of crosslinking of the filler particles .....	71
Conclusion.....	78
2. Experimental part .....	79
2.1. Chemicals .....	79
2.2. Synthesis conditions .....	79
2.2.1. Soft “Filler Particles” by emulsion polymerization.....	79
2.2.2. “Reference matrix” by bulk polymerization.....	80
2.2.3. Preparation of the nanocomposite .....	81
2.3. Characterization methods .....	84
2.3.1. Gravimetric analysis.....	84
2.3.2. DLS .....	84
2.3.3. DSC .....	85
2.3.4. Mechanical tests .....	85
References .....	89



## Introduction

Soft polymer materials like gels and elastomers are interesting materials in particular because of their ability to reversibly deform to large strains. Their softness is a limitation to some applications and their industrial use requires some kind of reinforcement. Conventional soft polymer networks show a tradeoff between stiffness and stretchability/toughness which comes from their molecular network structure: the chain length controls both the small strain modulus and the finite extensibility of the material, which affects its toughness. Therefore, new strategies need to be implemented to design soft materials with improved strength while remaining extensible [<sup>1,2</sup>].

Industrially, the most common strategy to reinforce elastomers is the use of hard nanofillers to form what is called a nanocomposite [<sup>3</sup>]. The contrasting properties of stiff fillers dispersed in a soft elastomer matrix gives to the final material both stiffness and toughness. This reinforcement strategy remains limited to specific temperature ranges, as it depends a lot on viscoelastic dissipation [<sup>4</sup>]. In addition, because hard fillers and matrix material are different materials, their optical indexes are different (carbon black is absorbing, silica has a different refractive index than a polymer matrix), therefore at the common filler concentration industrially used, the composites are non-transparent.

Another strategy that overcomes both previous limitations (viscoelastic dependence and transparency) is the use of a crosslinked first network, composed of short chains, pre-stretched by a second loosely crosslinked network, composed of long chains. This, so called double network [<sup>5</sup>], benefits from the first network stiffness and the second network deformability. Moreover, when the double network is stretched, the shorter chains of the first network will break and randomly dissipate energy before the macroscopic failure of the material, which will enhance the material's toughness. This material has the advantage to be transparent and its reinforcement mechanisms don't vary much with temperature (as they are based on chain scission). Nevertheless, the making of such materials knows some limitations, among which, the first network should remain for hours (for mm sized samples) in a monomer and initiator bath to swell and pre-stretch, this step takes time and requires to use an excess of volatile and toxic chemicals, and needs to be improved.

In a previous work, the group of Gong synthesized double network hydrogels with a microgel reinforced first network [<sup>6</sup>]. The microgel reinforced first network corresponds to a composite of soft microgels embedded in a poly(acrylamide) matrix. It was used as a first network to make double network hydrogels. During the stretching of these double network hydrogels, they could observe the deformation and breakage of these microgels. They found that the double network containing microgels reinforced first network exhibited dramatic enhancement in mechanical strength and toughness, in comparison to the hydrogels with no microgels.

Inspired by this work on hydrogels, Clément Robin, intern at SIMM lab under the supervision of Etienne Ducrot, worked on soft particles reinforced elastomers (similar to the previous microgel reinforced first network). Their work on this material remained unpublished but a patent has been filed. Their material consists in a soft matrix polymerized in and around crosslinked and soft particles of the same chemical nature. This material is similar to a composite filled with soft particles (still stiffer than the matrix but softer than inorganic nanoparticles). It should present the advantages of the double network architecture (at the particle scale) without the excess chemicals, slow swelling and fixed shape limitations of the conventional bulk double network synthesis which means that we expect such soft composite to be transparent and show enhanced strength and toughness whilst being synthesized without excess chemicals.

So in this project we reproduced and complemented the experiments of C. Robin on elastomers filled with soft particles. We synthesized crosslinked nanoparticles by free radical emulsion polymerization, dried them to remove the water and re-dispersed them in monomer and initiator for the particles to swell. Then the mix was injected into a mold and the second network polymerization was UV initiated. Different transparent samples could be obtained by varying the crosslink density of the filler particles and their volume fraction in the composite. The mechanical properties of these samples was characterized in large strain and in terms of resistance to crack propagation in notched samples.

## 1. Results

### 1.1. Synthesis and characterization of the materials

#### 1.1.1. Particles synthesis

The objective is here to understand the effect of the filler particle's softness (crosslinking density) on the reinforcement of the composite (matrix filled with particles). Different latexes with various molar concentration of crosslinker were therefore synthesized by emulsion polymerization (following the same standard procedure described in detail in the experimental section 2.2.1), but varying the concentration of crosslinker. The particles were synthesized by free radical emulsion polymerization in water initiated with potassium persulfate (KPS 0.10 mol%), ethyl acrylate (EA) was used as monomer, 1,4-butanediol diacrylate (BDA between 0.6 and 13 mol%) as crosslinker and sodium dodecyl sulfate (SDS 0.60 mol%) as surfactant.

The resulting synthesized latexes are composed of crosslinked particles dispersed in water, and will then be used as soft fillers in the composite. In the rest of the manuscript they will be named P-**XX** with **XX** the molar concentration of the crosslinker (BDA).

*Notes on synthesis conditions*

During the emulsion polymerization, we generally observed modifications of the reaction medium. Before the reaction, the stirred mixture was a transparent-milky liquid, and the organic and aqueous phases separated when stirring was stopped. During polymerization, rapidly, the reaction medium got some slightly blue reflects, which corresponds to the light diffusion of nanometer sized objects, and indicated the formation of particles. After 1 h of reaction, the mix changed to a quite opaque white color, and phase separation was no longer observed when the stirring was stopped. All latex synthesized are reported in Table 1 below. Very little amount of aggregates (<1%) were collected at the end of each latex's polymerization. Stored in the fridge at 5°C, destabilization of the latex occurred within a week, with the formation of visible aggregates. So the latexes were stored at room temperature, where they remained stable: no visible aggregates could be observed over 2 months in latexes stored at room temperature.

All latexes were characterized by gravimetry to calculate the conversion (conv%) and solid content (solid%) as detailed in section 2.3.1. The monomer conversion was high and close to quantitative independently of the amount of crosslinker used. The results are summarized in Table 1.

Name	BDA mol% <sup>a</sup>	conv% (%)	solid% (%)	D <sub>w</sub> <sup>b</sup> (nm) (PDI)	T <sub>g</sub> (°C)
P-0.6	0.58	100	28.6	140 (0.04)	-13
P-1.7	1.67	96	27.4	146 (0.05)	-6
P-3	3.0	100	28.5	156 (0.04)	-10
P-6	6.0	96	28.5	162 (0.01)	1
P-13	13.0	99	31.3	152 (0.05)	12

Table 1 Summary of the characteristics of the latexes synthesized, characterized by gravimetry, DLS and DSC.<sup>a</sup> the molar concentration of BDA corresponds to the molar quantity of BDA over the molar quantity of monomer BDA mol% =  $n(X)/n(EA)$ . <sup>b</sup>D<sub>w</sub> corresponds to the average diameter of the particles dispersed in water.

The size of the particles in water was determined by Dynamic Light Scattering (DLS). We observed that the average diameter (D<sub>w</sub>) of the particles in water did not depend much on the crosslinking content, and varied between 140 and 162 nm. The formation of aggregates did not vary with the crosslinker concentration either and remained below 1%.

The glass transition temperature (T<sub>g</sub>) was determined by Differential Scanning Calorimetry (DSC) for each latex after drying. Table 1 shows that the dried particles T<sub>g</sub> depends on the crosslinking content and varies from -13 °C for the less crosslinked particles to +12 °C for the more crosslinked ones. Since the crosslinker content is very high, it influences the mobility and this results in higher T<sub>g</sub>, as expected. It

should be emphasized that all particles possess a  $T_g$  below room temperature and are, as such, soft particles.

### 1.1.2. Dispersion and swelling of the particles in ethyl acrylate

The latex were dried at room conditions for 3 days and one night under vacuum at room temperature. The particles could be re-dispersed into a monomer solution from the de-aggregation of the macroscopic film. Indeed, the film made from crosslinked particles is not very cohesive. During the film formation, the crosslinked particles coalesce but the chains cannot interpenetrate because of the highly crosslinked nature of the particles. This and the absence of chemical connection between particles lead to weak interfaces which make the film relatively easy to re-disperse in a good solvent.

In order to evaluate the ability of dried particles to disperse and swell in EA, the dried latexes were mixed with EA and the particles' size was also determined in EA by DLS ( $D_{EA}$ ).

This de-aggregation of the film occurred thanks to a strong stirring overnight. The mix went from an inhomogeneous solution of monomer with macroscopic chunks of films, to a homogeneous slightly white solution with no visible aggregates.

The particles dispersed in monomers can swell with monomer until reaching a swelling equilibrium. The swelling factor ( $Q_v$ ) can then be calculated from the average size of the particles in water and EA (Eq. 1). It corresponds to the average volume of a latex particle in EA  $V_{p-EA}$  over the average volume of a latex particle in water  $V_{p-water}$ .

$$Q_v = \frac{V_{p-EA}}{V_{p-water}} \quad \text{Eq. 1}$$

Whereas the size of the particles in water is hardly affected by the crosslinking content, we can observe that the size of the crosslinked particles in a good solvent, like EA, depends on the concentration of crosslinks. When transferred to EA, the particles swell and reach an equilibrium diameter  $D_{EA}$  defined by the structure of the network, the crosslinker concentration and the quality of the solvent. In our case the swelling ratio  $Q_v$  decreases with increasing crosslink density, as expected by the swelling equilibrium theory of Flory-Rehner [7]. The Flory –Rehner equation predicts that the higher the molar concentration of crosslinks, the shorter are the chains between crosslinks and the more difficult it is for the chains to stretch and for the particle to swell. This interpretation is valid if we assume that the distribution of crosslinking point in the volume of the particles is homogeneous. From the work of Gao [8], we know that in solution, the reactivities of the function acrylate in a diacrylate and an acrylate monomer are equivalent. However, in emulsion, the solubility of the monomer in water also plays a role in the reactivity ratio. We didn't find in the literature, a study that could confirm or reject our assumption.

Nevertheless, from our experimental swelling ratios, the distribution of crosslinker in the particle network seems homogenous.

Name	BDA mol% <sup>a</sup>	D <sub>w</sub> <sup>b</sup> (nm) (PDI)	D <sub>EA</sub> <sup>c</sup> (nm) (PDI)	Q <sub>v</sub> <sup>d</sup>
P-0.6	0.58	140 (0.04)	228 (0.05)	4.3
P-1.7	1.67	146 (0.05)	234 (0.03)	4.1
P-3	3.0	156 (0.04)	232 (0.03)	3.3
P-6	6.0	162 (0.01)	216 (0.09)	2.4
P-13	13.0	152 (0.05)	170 (0.06)	1.4

Table 2 Swelling ratios of the latexes synthesized. <sup>a</sup>the molar concentration of BDA corresponds to the molar quantity of BDA over the molar quantity of monomer BDA mol% = n(X)/n(EA). <sup>b</sup>D<sub>w</sub> and <sup>c</sup>D<sub>EA</sub> correspond respectively to the average diameter of the particles dispersed in water and EA. <sup>d</sup>Q<sub>v</sub> corresponds to the volume swelling factor of the latex particles equal to (D<sub>EA</sub>/D<sub>w</sub>)<sup>3</sup>

### 1.1.3. Synthesis of a simple matrix as a reference

A macroscopic sample of “unfilled” simple matrix was synthesized as a reference with 0.01 mol% of BDA by free radical bulk UV induced polymerization following the procedure detailed in the experimental part in section 2.2.2. EA was used as monomer, 0.01 mol% BDA as crosslinker and 0.01 mol% HMP as UV initiator. The sample obtained was a transparent elastomer with little to no macroscopic defects depending on the quality of the mold surface. The amount of initiator used was low enough to induce a slow and more homogeneous UV polymerization of the sample. After 2 h under UV, the conversions of these polymerizations were always good (>98 %), otherwise the materials were not considered satisfactory.

### 1.1.4. Synthesis of the nanocomposites

We performed various synthesis to understand the effect of filler content and molar concentration of crosslinks in the filler particles on the strength and toughness of the composite.

To obtain a nanocomposite, the film of particles was dispersed in a mix of monomer (EA), crosslinker (BDA 0.01 mol%) and UV initiator (HMP 0.01 mol%) overnight. Then the mix was injected into molds and irradiated with low intensity UV (<10 μW/cm<sup>2</sup>) for 2 h to polymerize the elastomer matrix in and around the filler particles.

In the first series of experiments (series 1), nanocomposites with various weight fractions of P-3 particles were prepared. The solution of particles in EA became more viscous as the weight fraction of particles increased. The maximum weight fraction reached for P-3 in EA was 20 %. A formulation with a filler weight fraction of 25 % was tried but the solution of particles in monomer became too viscous to be

injected into the mold. This can be explained by the high volume fraction of particles. If we consider the dense packing of identical spheres in a square, it leads to a volume fraction of 74 %. Because there is a distribution of particles sizes, this dense packing value could be higher than 74%. However, a weight fraction of particles equal to 25 % should represent, once swollen in monomer, a volume fraction of 84 %, well above the dense packing. This explains the gelification of the solution at 25 wt% particles.

In the second series of experiments, different particles varying in their crosslinking density were used as soft fillers (P-0.6, P-1.7...) while the particle volume fraction was kept constant at 30%. We chose to work at constant volume fraction instead of weight fraction because of the importance of the percolating network in composite materials [9].

The resulting nanocomposites were named  $N_{xx}-(YY)$  with **XX** being the molar concentration of crosslinker in the filler particles and **YY** the volume fraction of filler inside the matrix.

All nanocomposites were synthesized as described in the procedure detailed in section 2.2.3, the formulation of the matrix remained constant (EA, 0.01 mol% BDA, 0.01 mol% HMP). As described in section 1.1.2, all particles could be homogeneously dispersed in EA. The obtained mixture was milky with no macroscopic clumps, and could be injected into the polymerization molds through a needle. After UV polymerization, all samples looked transparent even at high wt%.

The compositions of the composites are summarized in the following Table 3.

Name	filler particles	wt%	vol%
Reference matrix	-	0	0
Series 1			
$N_3-(17)$	P-3	5	17
$N_3-(33)$	P-3	10	33
$N_3-(50)$	P-3	15	50
$N_3-(66)$	P-3	20	66
Series 2			
$N_{0.6}-(30)$	P-0.6	7	30
$N_{1.7}-(29)$	P-1.7	7	29
$N_3-(30)$	P-3	9	30
$N_6-(27)$	P-6	11	27
$N_{13}-(29)$	P-13	21	29

Table 3 Summary of the characteristics of reference matrix and composites

All resulting samples were transparent in their undeformed state, neither the concentration of filler or the particles crosslink density affected the transparency of the samples. There was also no obvious whitening of the samples with stretch.

The  $T_g$  of the composites was determined by DSC (section 2.3.3). For all the composites one single glass transition close to  $-12.5\text{ }^\circ\text{C}$  was measured, which was close to that of the reference sample synthesized in the absence of filler (matrix). The only exception was the sample  $N_{13}\text{-(29)}$ , which contains indeed the particles with the highest crosslinker density (13 mol%). It demonstrated two  $T_g$ , one at  $-12.4\text{ }^\circ\text{C}$  and the second one at  $+11.7\text{ }^\circ\text{C}$ , which correspond respectively to the glass transition temperature of the matrix and the P-13 particles. In contrast to the other samples, for this sample, there is apparently a phase separation between the filler and the matrix phases.

## 1.2. Mechanical properties of the nanocomposites

In this section we test the mechanical properties in large strain and uniaxial tension of nanocomposite elastomers filled with elastomer particles of the same chemical nature as synthesized in the previous section. We assume that the penetrable particles are swollen, and hence their chains are pre-stretched by the matrix polymerized around as well as inside the filler particles. All samples looked macroscopically homogeneous and were transparent. As discussed in the introduction, the introduction of the particles in the composite should ideally stiffen and toughen the samples at the same time and reproduce the properties of continuous fillers.

### 1.2.1. Effect of the volume fraction of filler

In this first series of experiments, we studied the effect of the volume fraction of soft and penetrable fillers in a softer matrix. Series 1, of composites  $N_3\text{-(YY)}$  (Table 3), filled with the same fillers (P-3 particle with 3 mol% crosslinker) at various volume fractions (YY) has been mechanically tested in uniaxial tension (at  $20\text{ }^\circ\text{C}$  and stretch rate  $3.33 \times 10^{-2}\text{ s}^{-1}$  details in 2.3.4).

The stress-stretch (nominal stress  $\sigma$  as a function of stretch  $\lambda$ ) curves of the uniaxial extension tests are represented in Figure 1.

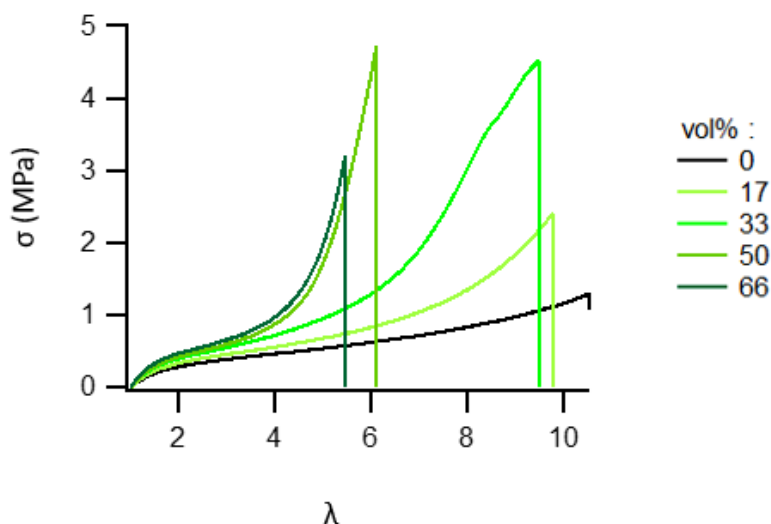


Figure 1 Mechanical behavior (nominal stress and stretch) in uniaxial extension of samples  $N_3$ -(YY) with various volume fraction of fillers

When the volume fraction of filler particles is increased from 0 to 66 %, we observe an increase of the Young's modulus, which increases from 0.53 to 0.95 MPa (a summary of results for all samples' is reported in Table 5). For all volume fractions, the materials remain extensible ( $\lambda > 5.5$ ), even though for higher particle volume fractions the materials break at lower strains. Interestingly, with increasing filler content, comes a clear strain hardening at lower strains. The onset of the hardening phenomenon depends on the volume fraction of particles. Higher fractions of particles result in a strain hardening at lower deformation. The presence of particles seems thus to affect the properties of the material differently at small strains than at high strains. The samples containing a volume fraction of P-3 of 33% shows the best compromise between high deformability and high stress at break.

In conventional composites, the presence of stiff particles enhances the dissipative properties of the material that, in turn, slows down crack propagations. To characterize the dissipative properties of our soft composites, we next performed step cyclic loading tests at increasing values of  $\lambda_{\max}$  on the series 1 to characterize their dissipative properties and the nature of their elasticity. The stress-stretch curves of a step cyclic loading test on the material  $N_3$ -(33) is shown in Figure 2. Each deformation step is represented in a different color.

In general, we observed very little hysteresis even at high deformation and little to no residual deformation. The same behavior was observed for all materials in this series. The Young's modulus at each deformation step and the cumulated irreversibly dissipated energy per deformation step for the series of samples  $N_3$ -(YY) are represented in Figure 4.

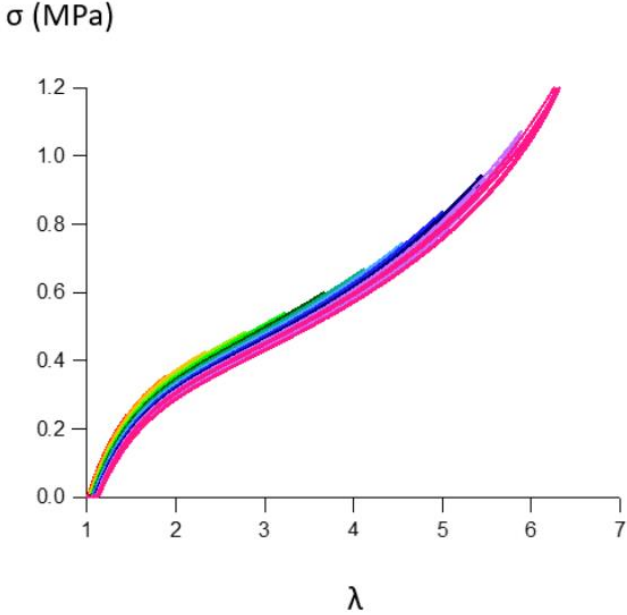


Figure 2 Step-cyclic loading stress-strain curve of sample N<sub>3</sub>-(33)

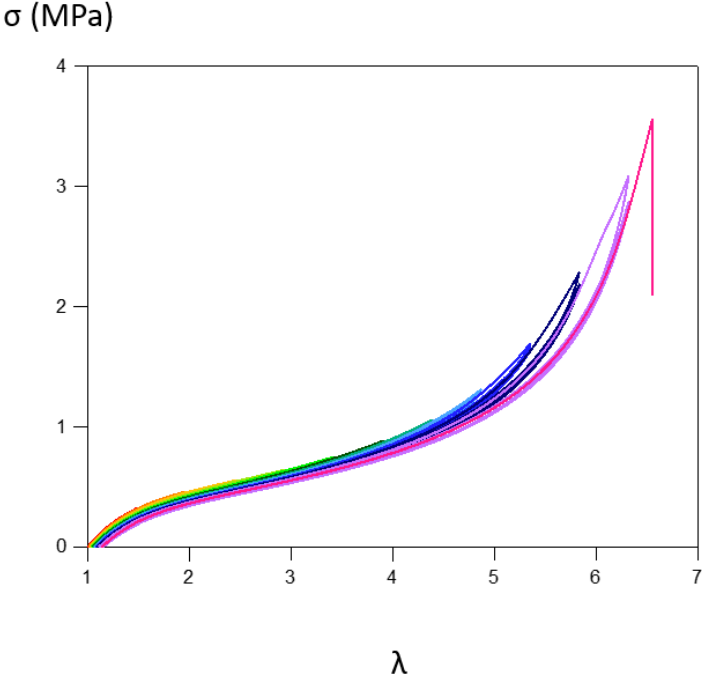


Figure 3 Step-cyclic loading stress-strain curve of sample N<sub>3</sub>-(66)

At each deformation step, the energy dissipated because of permanent damage is calculated from the difference between the first cycle hysteresis and the third cycle hysteresis. The first cycle dissipates energy through viscoelasticity and permanent bond breakage while the third cycle dissipates energy only through viscoelasticity: no more bonds should break when the material is deformed up to the same

stretch level for the third time and the changes in the structure should be reversible. This results in an estimate of the energy lost from permanent damage in the material. We represented in Figure 4 the cumulated energy dissipated from irreversible damage  $\Sigma U_{hyst}$  and the evolution of the Young's modulus  $E$  for each deformation step.

$$\Sigma U_{hyst}(\lambda_n) = \sum_{i=1}^n U_{hyst}(\lambda_i) \quad \text{Eq. 21}$$

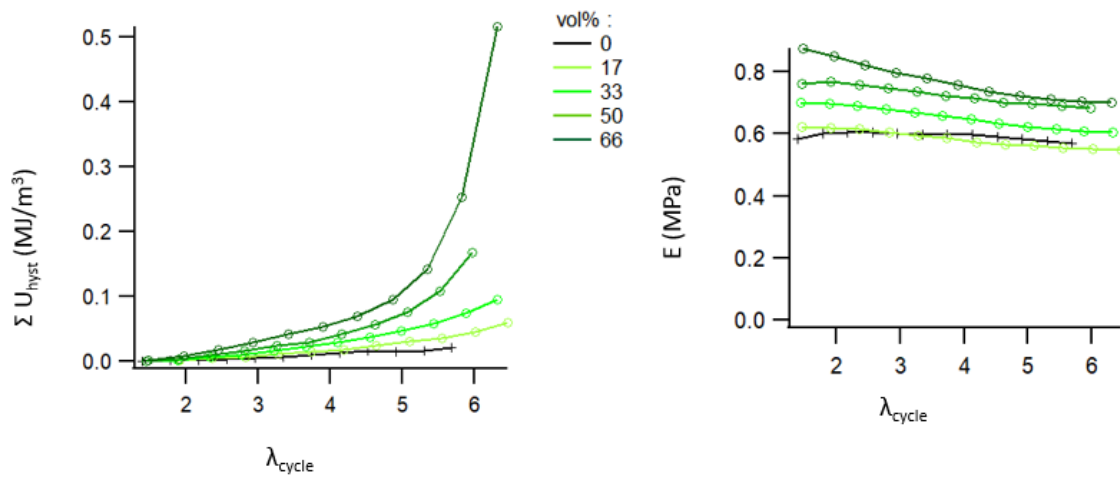


Figure 4 Cumulated dissipated energy (on the left) and Young's modulus (on the right) at each deformation step for the series of sample  $N_3$ -(YY)

To get a better grasp on the amount of energy dissipated as a function of the particles volume fraction, it makes more sense to plot  $R_{cycle}$  given as the ratio of dissipated energy  $\Sigma U_{hyst}$  over total work done  $W(\lambda)$ , as represented in Figure 5.

$$R_{cycle} = \frac{\Sigma U_{hyst}}{W}$$

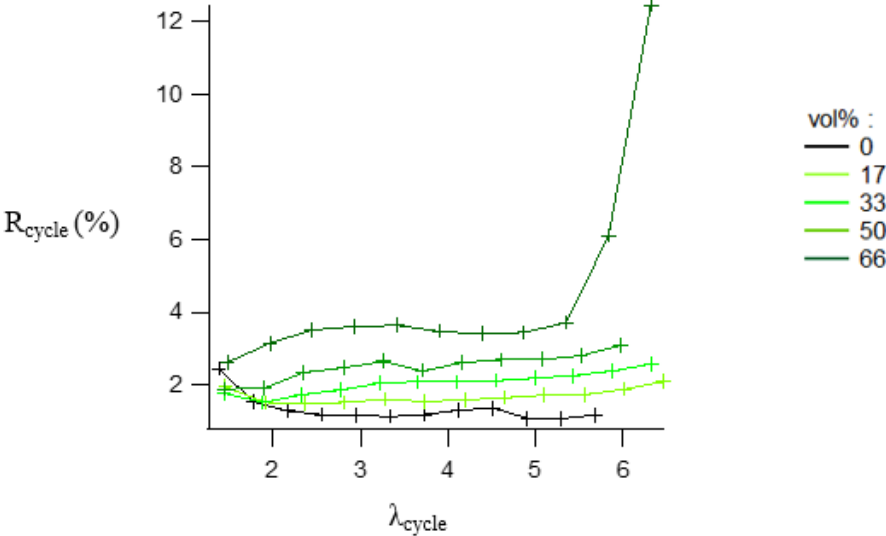


Figure 5 Ratio of dissipated energy due to permanent damage  $\Sigma U_{\text{hyst}}$  over total work done (integral under the loading curve) for each deformation step

It can be seen that the dissipated cumulated energy due to damage at each step of deformation increases with filler content. However, the amount of damage remains low compared to common composites containing hard fillers and the ratio of dissipated energy (Figure 5) remain low and constant for deformation below 5. As the permanent damage within the material is small, the Young’s modulus is hardly affected by the cyclic deformation. The composite material, composed of a matrix filled with soft particles, is highly elastic and presents low viscoelastic dissipation. This is in agreement with the absence of visible residual strain.

The presence of soft particles induces a visible strain hardening in high extension (deformation above 4). We now investigate whether the soft particles will delay the propagation of a crack in the soft composite, thanks to a local strain hardening mechanism at the crack tip, and improve the material’s toughness. To do so, notched samples were subjected to fracture propagation tests (at 20 °C and stretch rate  $3.33 \times 10^{-2} \text{ s}^{-1}$ ) to observe the effect of soft particles on the material toughness (details in section 2.3.4). The results are plotted in Figure 6.

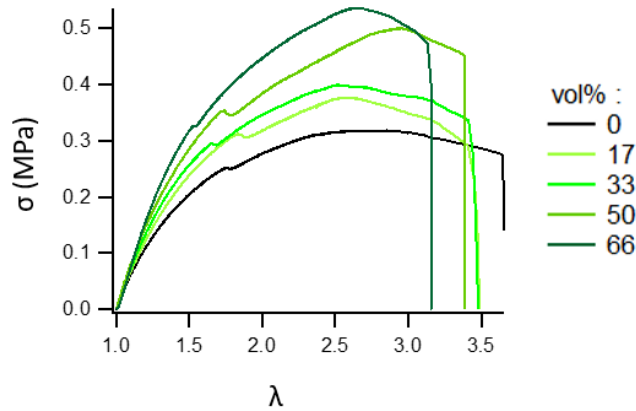


Figure 6 Stress-strain curves of notch propagation test of the samples  $N_3$ -(YY).

Figure 6 shows that the critical strain at break of the material which varies between 2.3 and 2.7 is not affected by the particle volume fraction, (detailed results reported Table 4). However, the maximum stress at break increases with increasing filler fraction from 0.33 to 0.51 MPa. Compared to elastomers reinforced with hard fillers the maximum stress remains however low as could be expected from the previous experiments. The toughness, given by Greensmith's formula (Eq. 22), is slightly improved by an increasing quantity of fillers. The toughness increases from 1.31 kJ/m<sup>2</sup> for the matrix alone to 1.66 kJ/m<sup>2</sup> (Table 4). This means that more energy is needed to propagate a crack and this energy is dissipated during the propagation. Because the material is highly elastic (Figure 1), the dissipated energy may be the result of more bond breakage.

Name	filler particles	wt% (%)	vol% (%)	E (MPa)	$\lambda_{\max}$	$\sigma_{\max}$ (MPa)	$\lambda_c$	$\sigma_c$ (MPa)	$\Gamma$ (kJ/m <sup>2</sup> )
Reference matrix	-	0	0	0.53 $\pm 0.02$	10.1 $\pm 2.8$	1.6 $\pm 0.9$	2.5 $\pm 0.3$	0.33 $\pm 0.04$	1.31 $\pm 0.36$
<i>Series I</i>									
N <sub>3</sub> -(17)	P-3	5	17	0.67 $\pm 0.02$	8.3 $\pm 1.0$	2.3 $\pm 0.1$	2.7 $\pm 0.4$	0.33 $\pm 0.06$	1.70 $\pm 0.50$
N <sub>3</sub> -(33)	P-3	10	33	0.72 $\pm 0.04$	9.0 $\pm 0.9$	4.5 $\pm 0.1$	2.4 $\pm 0.1$	0.37 $\pm 0.04$	1.42 $\pm 0.07$
N <sub>3</sub> -(50)	P-3	15	50	0.82 $\pm 0.01$	5.0 $\pm 0.3$	4.4 $\pm 0.8$	2.3 $\pm 0.2$	0.44 $\pm 0.09$	1.52 $\pm 0.29$
N <sub>3</sub> -(66)	P-3	20	66	0.95 $\pm 0.03$	4.8 $\pm 0.7$	3.2 $\pm 0.7$	2.3 $\pm 0.2$	0.51 $\pm 0.05$	1.66 $\pm 0.37$

Table 4 Summary of the mechanical characterization of the samples from series I. Values averaged over 3 samples for uniaxial extension and 2 samples for notch propagation.

The effect of the soft fillers on the low strain mechanical properties ( $\lambda < 4$ ) is quite limited. However, at the crack tip the difference in strain hardening should be visible. Presumably the lack of damage at high strain may explain the moderate toughening effect (not much chain scission presumably occurs before actual fracture).

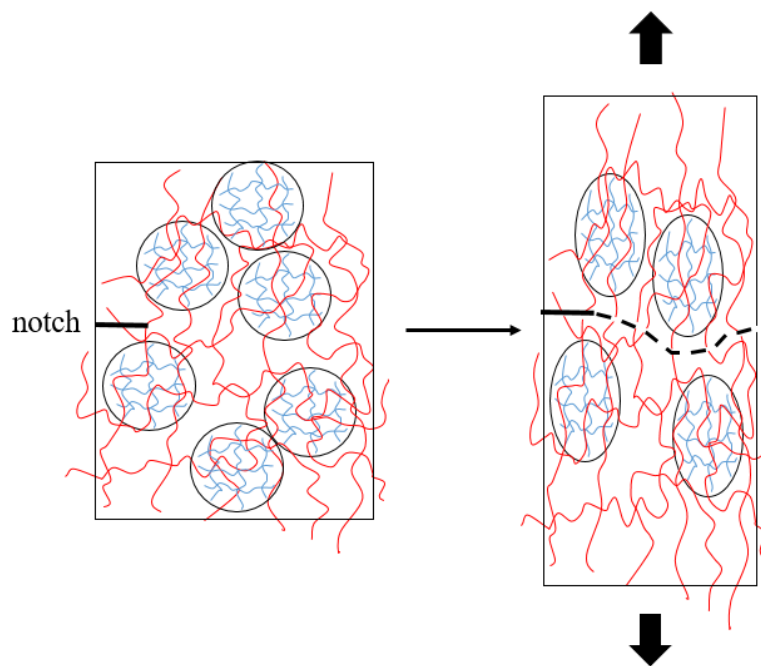


Figure 7 Zoomed schematic representation of a crack propagation in composites filled with soft particles

This result contrasts with the effect of hard fillers that affect a lot both the stiffness and toughness of the material.

The swollen interpenetrated particles may locally act as domains of higher crosslinking content. Thus, when the material is stretched, the softer regions deform first, before the interpenetrated regions deform. This is in agreement with the little effect of the particles at low strains. It is possible that the deformation of the overall sample in one direction brings the particles closer together in the transverse direction which favors their deformation through a compression mechanism [10] as represented in Figure 8. The higher the amount of particles the sooner they will be in contact and then in compression. This compression driven strain hardening would give an explanation to the tunable strain hardening that does not necessarily imply that the strands in the particles reach their limiting extensibility in the tensile direction.

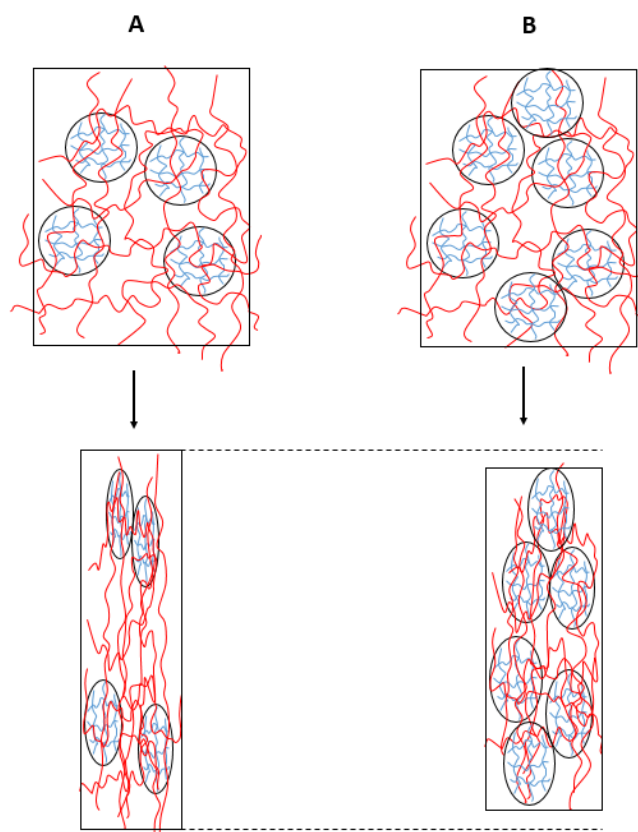


Figure 8 A. and B. Zoomed schematic representation of the composite network structure with respectively a low and a high concentration of particles in the matrix, upon stretching, the particles get into contact at different deformation.

### 1.2.2. Effect of the degree of crosslinking of the filler particles

In conventional bulk double networks, when the first network crosslinker concentration increases, the double network shows a strain hardening at lower stretches. We believe that the degree of crosslinking of the particles should have a positive effect on the composite mechanical behavior as well. In this part, we want to understand the effect of the molar concentration of crosslinks in the filler particle network, on the strength and toughness of the composite. So we synthesized and characterized a series of samples  $N_{xx}$ -(30) with the same filler volume fraction fixed at 30 %, but containing different particles that differ in their crosslinking density (XX corresponds to the molar concentration of BDA).

The stress strain curves from uniaxial extensions at  $3.33 \times 10^{-2} \text{ s}^{-1}$  are represented in Figure 9.

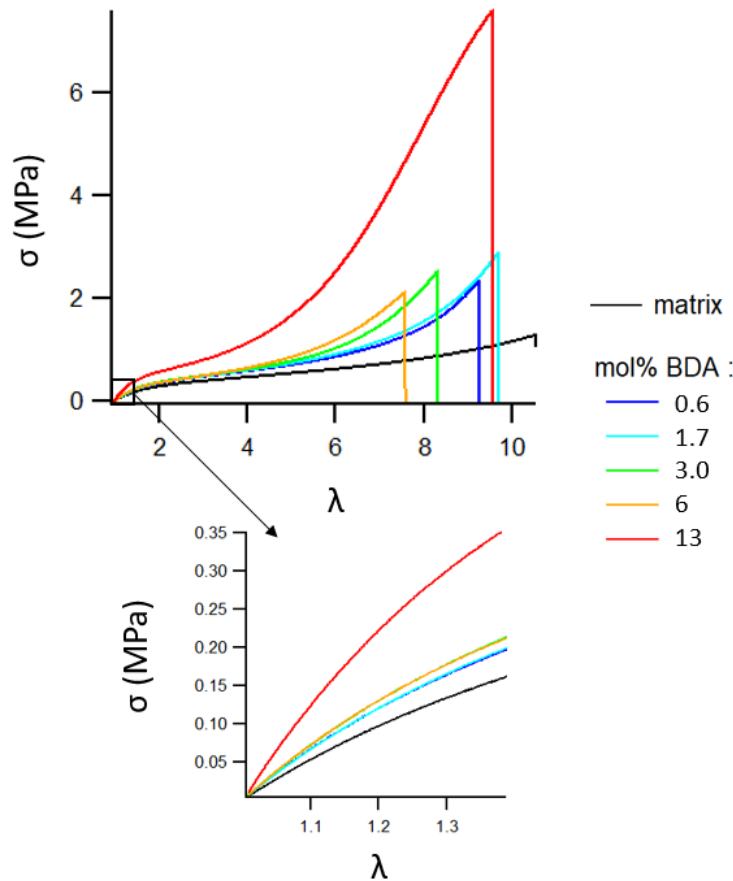


Figure 9 Stress-strain curve of the uniaxial extension of samples  $N_{xx}-(30)$

As shown in Figure 9, at constant volume fraction of filler, the Young's modulus  $E$  increased with increasing crosslinker density of the filler. The Young's modulus varied from 0.53 for the matrix alone to 1.35 MPa for  $N_{13}-(30)$ . One can thus conclude that in the presence of highly crosslinked particles (P-13, 13 mol% BDA with  $T_g = 12^\circ\text{C}$ ), the Young's modulus increases by a factor 2.5.

At that volume fraction of filler, the samples demonstrate some strain hardening at lower stretch when the filler particles are more densely crosslinked.

We can see on the plot that the maximal stretch and stress at break are less affected by the crosslinking density of the particles than by their volume fraction. The stretch at break fluctuates between 5 and 10, while the stress at break varies between 1.6 and 2.9 MPa, except for the sample  $N_{13}-(30)$ , which contains the most crosslinked (less soft) particles and showed as significantly improved stiffness while maintaining the same strain at break of almost  $\lambda = 10$ . Note that this particular sample showed greater nominal stress at break at 7.4 MPa while staying very stretchable with a strain at break around 8.6 and comparable to the other sample filled with less crosslinked particles. Note that in terms of true stress at break ( $\sigma_T = \lambda * \sigma_N$ ) this samples breaks at close to 70 MPa, a remarkably high value for a transparent elastomer made of poly(ethyl acrylate), higher than unfilled natural rubber [11].

Name	filler particles	wt% (%)	vol% (%)	E (MPa)	$\lambda_{\max}$	$\sigma_{\max}$ (MPa)	$\lambda_c$	$\sigma_c$ (MPa)	$\Gamma$ (kJ/m <sup>2</sup> )
Reference matrix	-	0	0	0.53 $\pm 0.02$	10.1 $\pm 2.8$	1.6 $\pm 0.9$	2.5 $\pm 0.3$	0.33 $\pm 0.04$	1.31 $\pm 0.36$
<i>Series 2</i>									
N <sub>0,6</sub> -(30)	P-0.6	7	30	0.67 $\pm 0.03$	8.0 $\pm 0.3$	2.1 $\pm 0.02$	2.7 $\pm 0.5$	0.29 $\pm 0.03$	1.58 $\pm 0.60$
N <sub>1,7</sub> -(29)	P-1.7	7	29	0.72 $\pm 0.01$	8.7 $\pm 0.2$	2.9 $\pm 0.4$	2.5 $\pm 0.6$	0.37 $\pm 0.11$	1.59 $\pm 0.80$
N <sub>3</sub> -(30)	P-3	9	30	0.74 $\pm 0.01$	7.3 $\pm 0.9$	2.5 $\pm 0.3$	3.5 $\pm 0.5$	0.46 $\pm 0.05$	3.03 $\pm 0.73$
N <sub>6</sub> -(27)	P-6	11	27	0.81 $\pm 0.02$	5.3 $\pm 1.1$	2.1 $\pm 0.01$	3.3 $\pm 0.4$	0.47 $\pm 0.02$	2.69 $\pm 0.51$
N <sub>13</sub> -(29)	P-13	21	29	1.35 $\pm 0.03$	8.6 $\pm 0.6$	7.4 $\pm 0.6$	4.1 $\pm 0.1$	1.08 $\pm 0.18$	6.43 $\pm 0.39$

Table 5 Summary of the mechanical characterization of the samples from series 2. Values are averaged over 3 samples for uniaxial extension and 2 samples for notched propagation

Furthermore, step cyclic loading was performed in order to get more insight on the damage within the sample happening during stretching. Most plots showed the same highly elastic low hysteresis behavior as observed for series 1, presented in Figure 2. Increasing the crosslink density in the particle network increased however the hysteresis as shown in the stress-stretch curve of N<sub>6</sub>-(30) and N<sub>13</sub>-(30) in Figure 10.

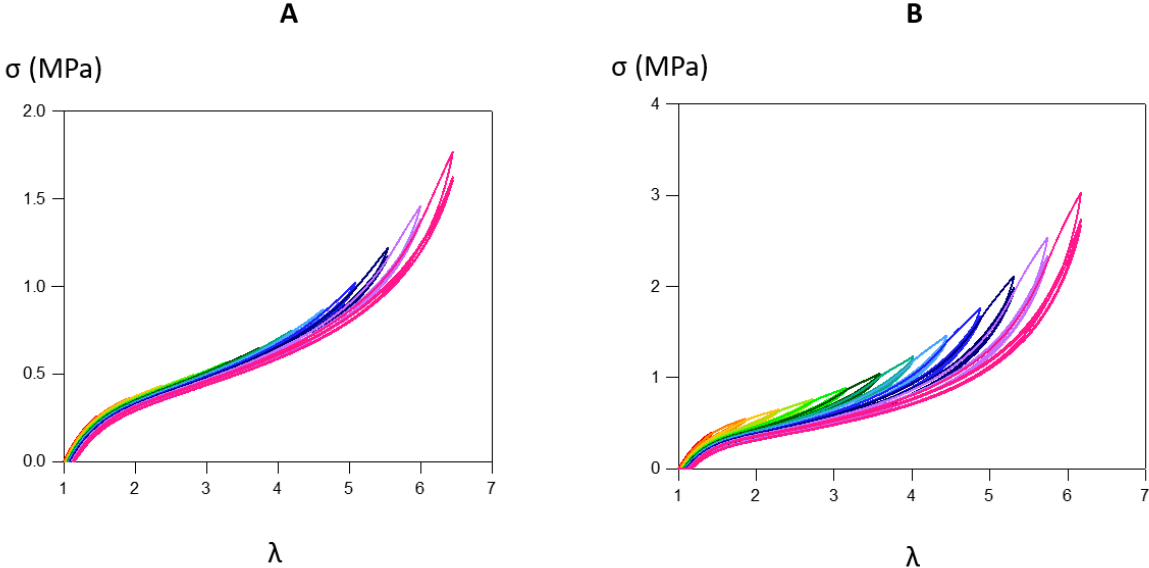


Figure 10 Step-cyclic loading stress-strain curve of **A.** sample  $N_6-(30)$  and **B.**  $N_{13}-(30)$

The cumulated dissipated energy and the Young’s modulus for each deformation step are plotted in Figure 11.

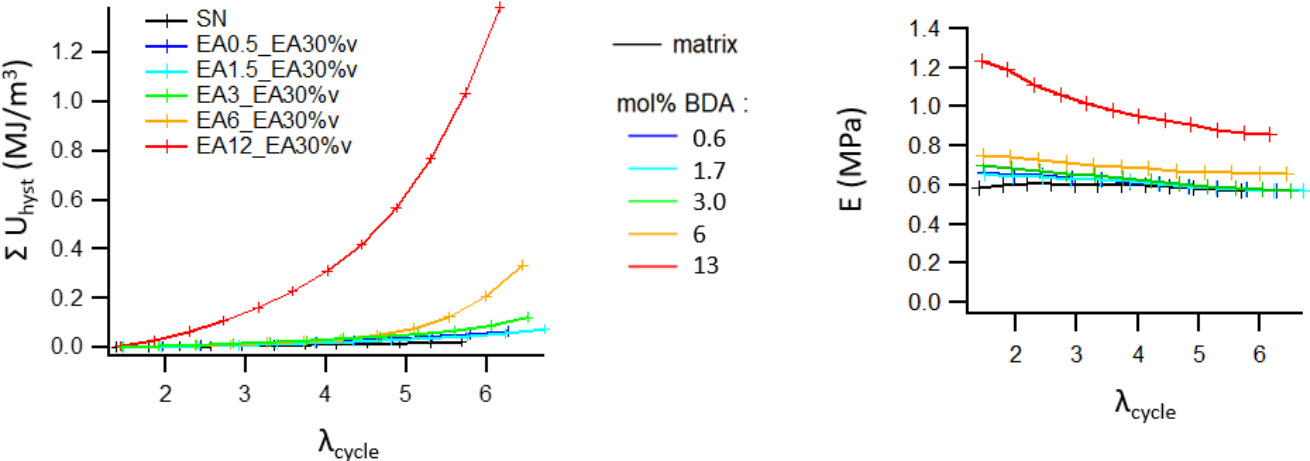


Figure 11 Cumulated energy irreversibly dissipated (on the left) and Young’s modulus (on the right) for each deformation step of the sample  $N_{xx}-(30)$

To get a better grasp on the fraction of energy dissipated as a function of the particles crosslink density, it makes more sense to plot  $R_{cycle}$  given as the ratio of dissipated energy  $\Sigma U_{hyst}$  over total work done  $W(\lambda)$ , as represented in the Figure 12.

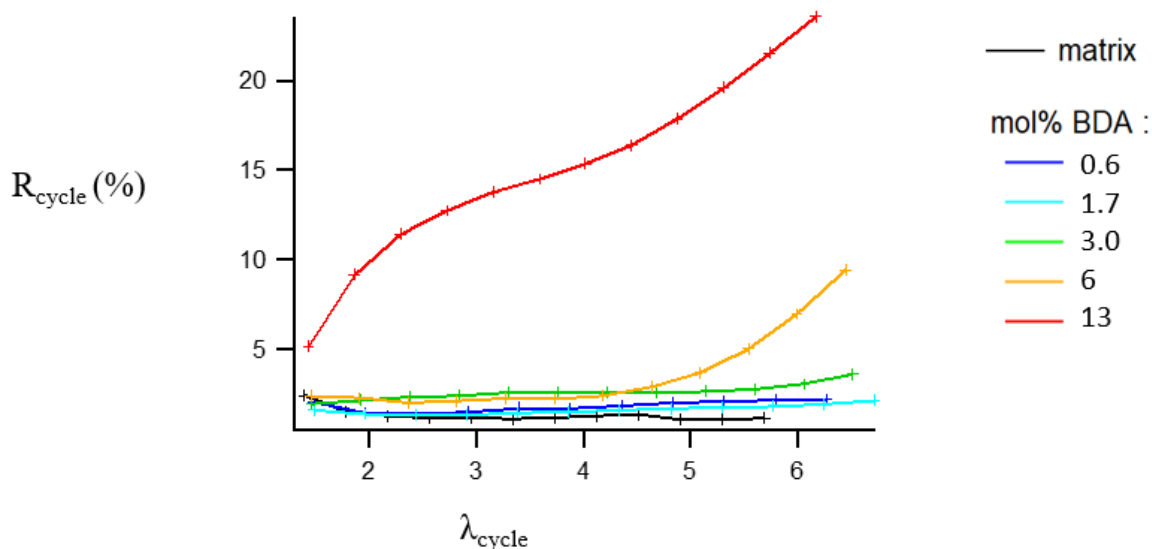


Figure 12 Ratio of dissipated energy due to permanent damage  $\Sigma U_{\text{hyst}}$  over total work done (integral under the loading curve) for each deformation step

Figure 11 shows that the cumulated irreversibly dissipated energy is roughly independent of the crosslinking density of the filler particles except for the more densely crosslinked particles P-13. Figure 12 confirms this observation. Both plots in Figure 11 and Figure 12 show that the samples containing the more crosslinked particles ( $N_6$ -(30) and  $N_{13}$ -(30)) dissipate more energy than the samples with less crosslinked particles.  $N_6$ -(30) demonstrating an increasing dissipative behavior at higher stretches ( $\lambda > 4$ ), while  $N_{13}$ -(30) is always more dissipative than the rest of the samples, and its dissipative behavior increases with increasing stretch.

This transition in the dissipative properties, between  $N_6$ -(30) and  $N_{13}$ -(30), suggests that there is a threshold crosslink density between 6 and 13 mol%, above which the particles and the matrix have a larger contrast and dissipate more energy. Another explanation could be the fillers'  $T_g$ . P-13 have a  $T_g$  closer to the ambient temperature (12 °C), therefore, they are more viscoelastic and dissipate more energy at 25 °C.

Except for the P-13, the Young's modulus of the soft composite is quite unaffected by the step stretching. This observation correlates with the ratio of dissipated energy  $R_{\text{cycle}}$  (Figure 12) which remains low for all samples except the one filled with P-13. This means that very little damage actually occurs in samples filled with particles crosslinked with less than 6 mol% crosslinker, when the material is stretched.

Among all samples,  $N_{13}$ -(30) shows the highest level of cumulated dissipated energy due to damage. The energy dissipated due to damage corresponds to the dissipated energy of the first loading/unloading cycle minus the dissipated energy of the third loading/unloading cycle for the same deformation step

$\lambda_{cycle}$  (Eq. 20). The cumulated energy corresponds to the sum of the energy dissipated for each deformation step up to  $\lambda_{cycle}$  (Eq. 22).

From Figure 11, we can see that almost 7 times more irreversible damage has happened microscopically within the composite N<sub>13</sub>-(30) before failure compared to the other samples of this series. Among all particles, the P-13 particles produce the strongest and most dissipative ( $T_g$  closer to working conditions) material that contrasts the most with the matrix properties, which may be the reason why P-13 reinforce the matrix more.

Finally, we also carried out crack propagation tests on this second series of materials. The results are plotted in Figure 13.

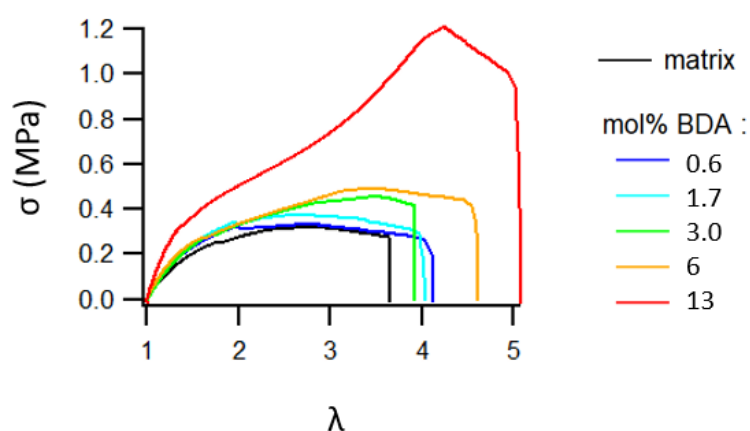


Figure 13 Crack propagation tests stress strain curve of samples N<sub>x</sub>-(30) with a constant volume fraction of filler particles = 30vol%

At the exception of N<sub>13</sub>-(30) filled with the more crosslinked particles P-13, the material's strength and toughness increases slightly with the crosslinking content of the particles. This encourages us to believe that there is a threshold above which the particles crosslinking density plays an important role in the composite mechanics. This toughness and strength enhancements could be the results the viscoelastic properties of the particles (whose  $T_g$  is 12 °C close to 20 °C at which the tests were executed) which leads to more damage or viscoelastic dissipation in the material (Figure 10).

At constant volume fraction of particles, the strain hardening behavior of the soft composite seems to be affected by the particles crosslink density. This strain hardening can be due to chains getting closer to their finite extensibility or to non-interpenetrable particles that come into compression against each other due to the compression of the sample in the transverse directions of traction.

As a first hypothesis, the strain hardening could result from chains reaching their limit extensibility. This can happen when the composite is stretched, the chains deform and the short chains in the crosslinked particles reach their finite extensibility for a lower deformation than the rest of the matrix.

However, in a particle-filled composite the less crosslinked matrix may deform differently than the particles.

C. Robin observed the deformation of the particles in one similar composite by Small Angle Neutron Scattering (SANS), he applied 3 different levels of stretch 1, 2.5 and 5.2, to the composite and analyzed the deformation of the particles. His SANS images are reported in Figure 14.

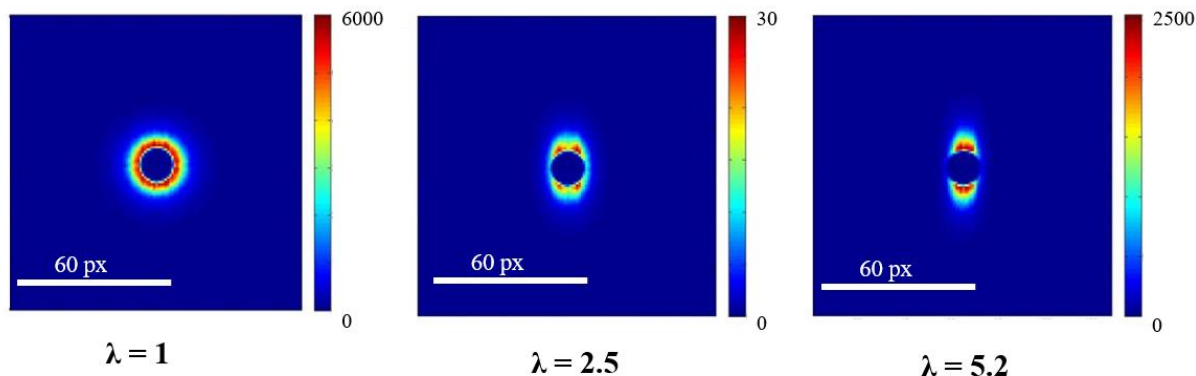


Figure 14 SANS images of a sample  $N_3$ -(33) with deuterated nanoparticles, deformed at  $\lambda = 1, 2.5$  and  $5.2$ .

$\lambda$	$\lambda_{\text{particle}}$
1	1
2.5	1.25
5.2	1.9

Table 6 Deformation applied to the composite and corresponding deformation of the particles within the stretched composite, measured by SANS.

By analyzing the scattering pattern, he could access the deformation of the particles and his results are reported in the Table 6. They show that the particles deform a lot less than the composite. This means that the elastic behavior of the material comes from the soft matrix between the particles. His results suggest that the strain hardening is the result of the short chains in the particles reaching their finite extensibility.

In the second hypothesis, it's the compression of the stiffer particles that trigger a strain hardening. The volume fraction of swollen particles is kept constant. Therefore, they should come into compression approximately at the same stretches. But the modulus of the particles depends on their crosslinking density, therefore, the mechanical response of the highly crosslinked particles will translate in a strain hardening of the composite occurring at lower stretch.

## Conclusion

Nanocomposites filled with soft penetrable particles have been synthesized in a simpler and more versatile process than usual composite or double networks which require respectively particular care for particles dispersion or a two-step process with a long swelling time of a macroscopic sample in bath of excess volatile chemicals, and a poor control of the final shape.

The materials obtained had the advantage of being transparent and experienced no whitening during stretching, as opposed to usual composites with hard fillers [12,13]. This process fabricates materials with a high level of reversible elastic behavior, low hysteresis, low modulus and a tunable strain hardening and fracture energy in a more straightforward way.

The soft particles clearly reinforce the matrix and increase the stress at break compared to the matrix alone. On the other hand, compared to stiff fillers, the Young's modulus is moderately affected by the presence of soft fillers as long as the particles remain soft enough. The same holds for the deformability of the samples, which remains very deformable, almost as the matrix alone, in comparison to conventional composites filled with hard fillers.

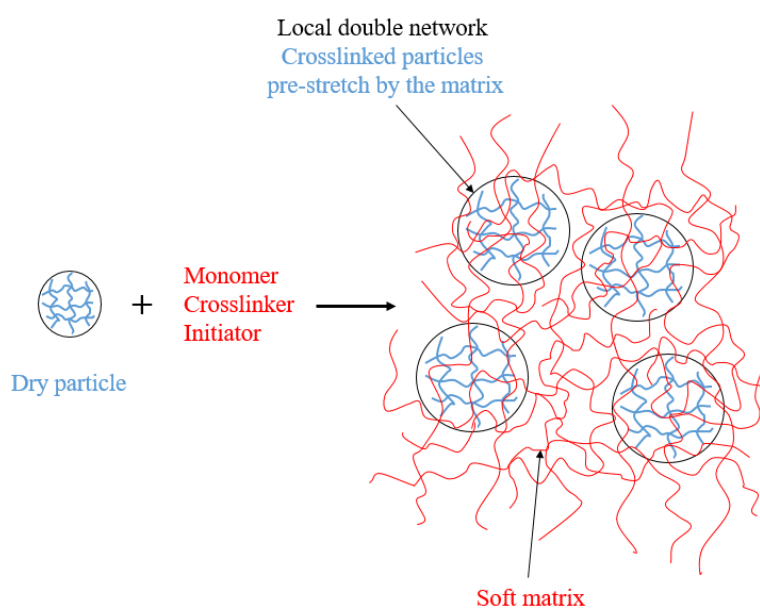


Figure 15 Representation of the composite structure. The particles are pre-stretched by the matrix.

The volume fraction of soft fillers is a key parameter to tune the onset of strain hardening in these materials. The particles are interpenetrated with the soft matrix, which forms local double network structures at the particles scale embedded in a soft matrix as represented in Figure 15. The particles are pre-stretched by the matrix network and the volume fraction of particles in the composite corresponds to the volume of the swollen particles over the total volume of the composite. An optimal volume

fraction of filler particles on the work of extension around 30 % was observed in a series of samples with various volume fraction of particles with constant crosslink density.

This way of making nanocomposite makes it possible to tune the material's strain hardening while keeping its modulus constant and retain a good reversible deformability. The ease of processing and tunability of the properties make this material promising for specific applications that demand strain controlled hardening.

The lack of connectivity between particles (which usually aggregates in conventional composite) may explain the poor toughness enhancement experienced with our samples. The particles could be connected between each other during or after the matrix polymerization step, using dual crosslink functionalization. The lack of large scale damage even at high strains may also explain why the samples are quite notch sensitive, no dissipation mechanism delays or slows down the propagation of a crack.

In future work, we could consider to change the monomer of the matrix network to a non-volatile one to make nanocomposite coatings in the idea of the work of Takahashi et al. [14] who dried a layer of latex before spreading a second monomer to polymerize a continuous matrix. In the same idea, we could dry the latex on complex surfaces then layer the non-volatile second monomer to penetrate the particles prior to polymerizing and forming a continuous matrix. The final coatings would hopefully reach similar mechanical performances as the composites studied in this work.

## 2. Experimental part

### 2.1. Chemicals

Ethyl acrylate (EA, Aldrich, 99%), 1,4-butanediol diacrylate (BDA, Aldrich, 90%), 2-hydroxy-2-methylpropiophenone (HMP, Aldrich, 97%), potassium persulfate (KPS, Aldrich,  $\geq 99\%$ ), sodium dodecyl sulfate (SDS, Aldrich,  $\geq 99\%$ ) were used as reagents. EA and BDA were purified through an alumina column before use. Water was purified and deionized through a MilliQ purification system before use. All polymerizations were carried in the absence of oxygen, in a glovebox, with reagents degassed under nitrogen.

### 2.2. Synthesis conditions

#### 2.2.1. Soft "Filler Particles" by emulsion polymerization

Filler particles of crosslinked poly(ethyl acrylate) (PEA) were synthesized by free radical emulsion polymerization.

The typical procedure for the preparation of particles crosslinked with 3.0 mol%<sup>1</sup> BDA is reported here. In a typical experiment (latex P-3 in Table 1), EA (20.0 g, 0.200 mol, 3.63 mol/L) was used as monomer and BDA (1.1879 g, 5.99 mmol, 3.0 mol%<sup>1</sup>) as crosslinker. Both monomers were mixed in ultrapure water (41.0 g) containing SDS (0.3456 g, 1.2 mmol, 21.8 mmol/L, 0.6 mol%<sup>1</sup>) as surfactant in a sealed round bottom flask. In another sealed vial, an aqueous initiator, KPS (0.0513 g, 3.45 mmol/L, 0.1 mol%<sup>1</sup>), was dissolved in ultrapure water (14.0 g). Both solutions were degassed under nitrogen for 45 min to remove the oxygen. This operation was done in an ice bath to avoid the decomposition of the initiator and the evaporation of the monomer. At the end of the bubbling phase, some monomer may have evaporated even with the use of an ice bath. The loss mass was compensated by degassed EA added at the end. The initiator solution was finally injected to the rest of the mix and the balloon was set in an oil bath at 60 °C under magnetic stirring. The emulsion polymerization was stopped after 3 h of reaction by opening the reactor and the emulsion was stored in a closed vial at room temperature. The solids content (%solid), aggregate content (%agg) and monomer conversion (%conv) were determined by gravimetric analysis and average particle size and its polydispersity (PDI) were determined by light scattering, both methods will be detailed below in section 2.3.1 and 2.3.2. To prepare the films, the latex was dried into a silicone mold at room conditions until the sample went from a white liquid to a transparent solid. Once the transparent film was formed, it was further dried under vacuum overnight at room temperature to make sure all adsorbed water and residual monomers were removed. The dried film obtained was quite cohesive and uniform but brittle.

### 2.2.2. “Reference matrix” by bulk polymerization

The simple single network, called “polymer matrix” in the following, was synthesized as a reference by free radical bulk UV polymerization.

This polymerization was carried out in a glovebox (MBraun Unilab) under nitrogen to avoid any inhibition of the polymerization due to reaction with oxygen. All reactants available in the glovebox were degassed beforehand.

In a typical experiment (Table 3, matrix) EA (4.00 mL, 36.7 mmol) was used as monomer and BDA (6.92 μL, 0.0367 mmol, 0.01 mol%) as crosslinker. HMP (5.59 μL, 0.0367 mmol, 0.01 mol%) was used as organic UV initiator. All reagents were mixed in a vial, then injected into a mold. The latter was composed of two glass plates covered with transparent PET sheets (hydrophobic surface)

---

<sup>1</sup> The mol% ratio of a compound X corresponds to the molar quantity of the compound X over the molar quantity of monomer, as follows:  $mol\% = \frac{n_X}{n_{EA}} \times 100$

separated by a silicone spacer (1 mm) to control the thickness. The whole was held together by a metal frame as shown in Figure 16.

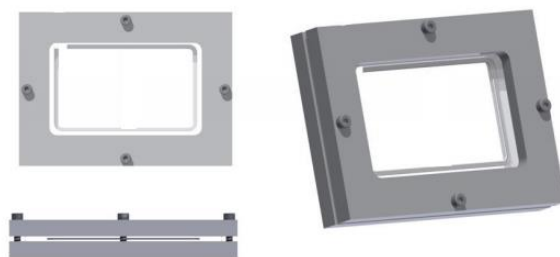


Figure 16 Customized molds for network polymerization

The mold was irradiated under low UV power ( $< 10 \mu\text{W}/\text{cm}^2$ ) for 2 h to enable a slow polymerization, which minimizes the number of simultaneously growing chains.

The reaction is represented Figure 17. After the polymerization, the sample was dried overnight under vacuum at room temperature to remove any unreacted volatile monomer. The sample was weighted before and after vacuum to calculate the monomer conversion as follows:

$$\%conv = \frac{m_f}{m_i} \quad \text{Eq. 2}$$

With  $m_i$  and  $m_f$  respectively the initial mass before vacuum and the final mass after.

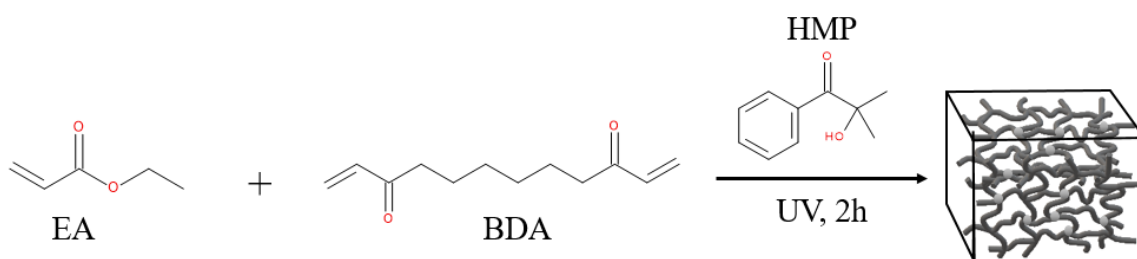


Figure 17 Schematic representation of the single network synthesis

### 2.2.3. Preparation of the nanocomposite

The nanocomposites are composed of the filler particles (their synthesis is presented in section 2.2.1) dispersed in a single network matrix.

A typical synthesis of a composite with 10 wt% of filler particles is detailed below.

Under inert atmosphere, the dried particles (0.9663 g, 10 wt%), in the form of small pieces of film, were put in a vial containing EA (8.6691 g, 86.6 mmol) and sealed. The mixture was vigorously stirred overnight to disperse the particles until the solution became homogeneous and with no visible clumps. Finally, BDA (1.63  $\mu\text{L}$ ,  $8.66 \times 10^{-3}$  mmol, 0.01 mol%) and HMP (1.32  $\mu\text{L}$ ,  $8.66 \times 10^{-3}$  mmol, 0.01 mol%) were added to the solution. Then the mix was injected into the customized molds (Figure 1) using a syringe equipped with a 0.8 mm inner diameter needle.

The mold was exposed to low UV power ( $< 10 \mu\text{W}/\text{cm}^2$ ) for 2 h to enable slow polymerization of the polymer matrix around and inside the particles. During the polymerization, the sample changed from a white solution to a transparent solid.

In the following, various types of nanocomposites were synthesized, to achieve different mechanical properties, by varying mainly two parameters:

- The first parameter is the weight fraction *wt%* or volume fraction *vol%* of fillers in the nanocomposite.

The weight fraction is given by:

$$wt\% = \frac{m_{fillers}}{m_{total}} = \frac{m_{fillers}}{m_{matrix} + m_{fillers}} \quad \text{Eq. 3}$$

Where  $m_{fillers}$ ,  $m_{matrix}$  and  $m_{total}$  are respectively the mass of the dry filler particles, the matrix and the total sample.

The volume fraction corresponds to the volume of the “monomer” swollen filler particles in the matrix:

$$vol\% = \frac{V_{fillers}}{V_{tot}} \quad \text{Eq. 4}$$

For the nanocomposite synthesis, the particles are dispersed in EA before polymerization. During this step, the particles swells with the monomer. Thus  $V_{fillers}$  corresponds to the total volume of the swollen particles inside the matrix equal to:

$$V_{fillers} = m_v \times \rho_{PEA} \times Q_v \quad \text{Eq. 5}$$

And  $V_{tot}$  is the total volume of the sample given by:

$$V_{tot} = V_{matrix} + V_{dry\_fillers} = (m_{matrix} + m_{fillers}) \times \rho_{PEA} \quad \text{Eq. 6}$$

This results in a simple relationship between the weight fraction and the volume fraction:

$$vol\% \approx Q_v \times wt\% \quad \text{Eq. 7}$$

- The second parameter, is the degree of crosslinking of the soft fillers particles:

The softness of the filler particles should decrease with increasing molar concentrations of crosslinks as given by the relationship between the theoretical Young's modulus  $E_{th}$  and the molecular weight between crosslinks  $M_{x,th}$ :

$$E_{th} = \frac{3\rho RT}{M_{x,th}} \quad \text{Eq. 8}$$

Where  $\rho$  is the density of the material ( $\text{kg/m}^3$ ), R the perfect gas constant ( $\text{J/K/mol}$ ) and T the temperature (K).

The molecular weight between crosslinks can be estimated by:

$$M_{x,th} = \frac{M_0}{2 \times mol\%/100} \quad \text{Eq. 9}$$

From the previous estimation, we can directly link the Young's modulus with the molar concentration of crosslinks:

$$E_{th} = \frac{6\rho RT}{M_0} \times \frac{mol\%}{100} \quad \text{Eq. 10}$$

## 2.3. Characterization methods

### 2.3.1. Gravimetric analysis

Gravimetric analyses were performed on the latex to calculate the conversion of the monomer into polymer (conv%), the quantity of aggregates (agg%) formed during the polymerization and the solids content (solid%).

Using a syringe equipped with a needle, a sample of the latex was extracted just before opening the reactor, at the end of the polymerization process. This sample was weighted in a pan right after pouring and after complete drying.

$$solid\% = \frac{m_f - m_p}{m_i - m_p} \quad \text{Eq. 11}$$

Where  $m_p$ ,  $m_i$  and  $m_f$  are respectively the mass of the pan, the wet sample and the dried sample.

$$conv\% = \frac{solid\% - \frac{m_{NV}}{m_{tot}}}{\frac{m_{monomer}}{m_{tot}}} \quad \text{Eq. 12}$$

Where  $m_{NV}$  is the mass of all the non-volatile compounds,  $m_{monomer}$  is the mass of the initially added monomer and  $m_{tot}$  is the total mass of the latex solution (monomer, non-volatile chemicals and water).

The aggregates were collected by filtering the latex on a filter paper of mesh size 0.6  $\mu\text{m}$ .

$$agg\% = \frac{m_{agg}}{m_{tot} \times solid\%} \quad \text{Eq. 13}$$

Where  $m_{agg}$  is the total mass of the aggregates.

### 2.3.2. DLS

The average particle diameter (D) and dispersity factor (PDI) of highly diluted (< 0.01 solid%) aqueous dispersions of particles were measured by dynamic light scattering (DLS) at 25 °C, with an ALV/CGS-3 Compact Goniometer System from ALV-GmbH (90° angle, 22 mW HeNe laser at 632.8 nm).

The highly diluted latexes were placed in glass tubes to fit into the DLS equipment. The measurements were done after 5 min for temperature stabilization, the measurements lasted 120 s and were repeated 3 times.

An estimation of the number of particles per volume of latex can be calculated from the size of the particles as given in the following equation:

$$N(L^{-1}) = \frac{\text{solid}\% \times \rho_{\text{latex}}}{V_{1p} \times \rho_{PEA}} \quad \text{Eq. 14}$$

Where  $\rho_{\text{latex}}$  and  $\rho_{PEA}$  are respectively the latex density (approximately equal to 1) and the polymer density, and  $V_{1p}$  is the average volume of a particle (equal to  $4/3\pi(D/2)^3$ ).

### 2.3.3. DSC

A thermal characterization of the solid sample was done using a Q800 Tzero DSC technology from Thermal Analysis with a temperature ramp of 20 °C/min from -50 to 40 °C. The glass transition temperatures of the synthesized particles could be extracted from the minimum of the derivated heat flow versus temperature.

### 2.3.4. Mechanical tests

All the mechanical tests were performed on an Instron tensile machine, model 5565, equipped with a 100 N load cell and a video extensometer. Two white marks were placed on the samples at a minimum distance of 5 mm for the video extensometer to measure the distance between the marks. Deformation was automatically calculated from the video extensometer data. Measurements errors for force and deformation were less than 0.5 %.

Home-made pneumatic clamps, represented Figure 18, were used to hold the samples during the test. The pressure of the clamps was provided by a line of pressurized air controlled with a manometer.

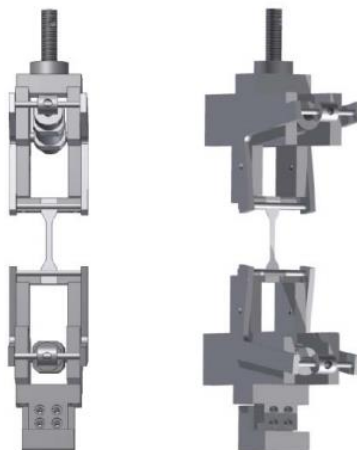


Figure 18 Home-made pneumatic clamps

The machine was equipped with a temperature controlled chamber that enabled tests at controlled temperatures between -5 and 100 °C. A fan inside the chamber ensured a homogeneous temperature inside the chamber.

*Tensile test*

Tensile tests were performed on dumbbell samples cut using a punch. The gauge length was 20 mm, the width was 4 mm and the thickness was approximately 1 mm depending on the sample. A typical dumbbell shaped sample is shown in Figure 19.

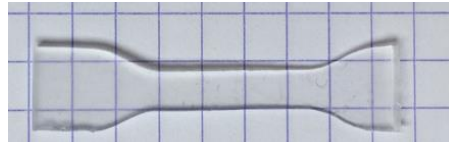


Figure 19 Picture of a dumbbell shaped sample

The machine was displacement controlled and the crosshead speed was set at 500  $\mu\text{m/s}$ , stretch rate  $3.33 \times 10^{-2} \text{ s}^{-1}$ .

Raw data from the tests including time ( $t$ ), force ( $F$ ), position of the crosshead ( $p$ ) and deformation calculated by the video extensometer ( $\epsilon_{\text{ex}}$ ) were further used to analyze the samples.

The strain was calculated as follows:

$$\lambda = \frac{L(t)}{L_0} \quad \text{Eq. 15}$$

Where  $L_0$  and  $L(t)$  are respectively the initial length and the real length at the time  $t$  of the sample.

From the video extensometer data:

$$\lambda = 1 + \epsilon_{\text{ex}} \quad \text{Eq. 16}$$

The nominal stress  $\sigma_N$  was calculated as:

$$\sigma_N = \frac{F(t)}{w_0 e_0} \quad \text{Eq. 17}$$

Where  $w_0$  is the initial width and  $e_0$  is the initial thickness of the sample.

The points corresponding to a pre-load of the sample were manually removed from the experimental plots.

The Young's modulus was measured by fitting the stress deformation curve with an affine fit in the region of linear deformation (between 2 and 8%).

For highly stretchable samples the white marks could become too deformed to be properly detected by the video extensometer. When such thing happened, the deformation was manually calculated from the crosshead position as follows, taking into account the correction from the experimental data of the video extensometer:

$$\varepsilon_{cross} = \left( \frac{p(t) - p_0}{p_0} \right) \times \frac{\alpha_{ex}}{\alpha_{cross}} \quad \text{Eq. 18}$$

Where  $p_0$  is the initial position of the crosshead,  $p(t)$  is the crosshead position at time  $t$ ,  $\alpha_{ex}$  and  $\alpha_{cross}$  are respectively the slope of the affine fit of the strain time curve from the video extensometer and the crosshead position.

$$\lambda_{cross} = 1 + \varepsilon_{cross} \quad \text{Eq. 19}$$

### Step-cyclic loading

Step-cyclic loadings were performed on dumbbell shaped sample as presented for the tensile test.

The test was controlled in displacement, and the crosshead speed was set at 500  $\mu\text{m/s}$  in both loading and unloading. For each deformation step, the sample was stretched up to a maximal position  $\lambda_{cycle}$  and unloaded to its original position 3 times. The nominal stress and the strain were extracted from the raw data as previously explained.

For each deformation step, the area under the curve of each loading and unloading cycle was measured.

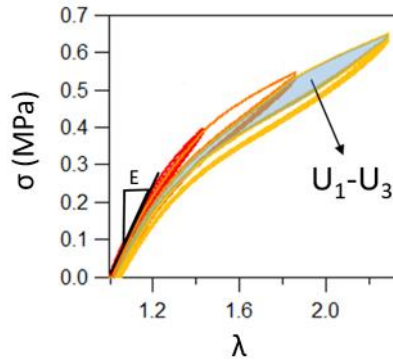


Figure 20 Stress-strain curve of 3 step deformations (red, orange, yellow) with 3 loading/unloading cycles. Area in blue corresponds to energy dissipated in the 1<sup>st</sup> cycle minus the energy dissipated in the 3<sup>rd</sup> cycle.

During the first sample loading/unloading, the hysteresis corresponds to energy dissipated by both permanent damage and viscoelasticity. We assumed that the second loading up to the same deformation step did not cause additional damage as conventionally done for filled elastomers [15], so the hysteresis measured during the second cycle should be only the result of viscoelastic dissipation. A third loading/unloading cycle was performed to the same deformation step just to make sure the previous assumption was correct.

From the hysteresis area of the first cycle  $U_1$  and the third cycle  $U_3$ , could be calculated the energy irreversibly dissipated due to permanent damage in the material  $U_{hyst}$ , by cutting the energy dissipated by viscoelasticity from the first hysteresis:

$$U_{hyst} = U_1 - U_3 \quad \text{Eq. 20}$$

The cumulated dissipated energy from permanent damage was calculated as the sum of the energy irreversibly dissipated for each maximal position,  $\Sigma U_{hyst}$ .

$$\Sigma U_{hyst}(\lambda_n) = \sum_{i=1}^n U_{hyst}(\lambda_i) \quad \text{Eq. 21}$$

It was also possible to follow the evolution of the Young's modulus as a function of the maximal deformation applied. Considering that the modulus at low strain is representative of the number of elastically active chains in the material, damage within the material could affect the modulus at low strains.

#### *Crack propagation test*

Crack propagation tests were performed on rectangular samples, 15 mm long, 5 mm wide, approximately 1 mm thick depending on the sample. A 1 mm notch was made at the border the sample using a new razor blade each time to make sure the razor blade had the same sharpness and would cut the sample in a reproducible manner.

The measurement was controlled in displacement and the speed was set at 500  $\mu\text{m/s}$ .

The maximal deformation and maximal stress before crack propagation could be extracted from the stress-strain curve of the notch propagation test.

Toughness of the material could be calculated using the Greensmith's formula:

$$\Gamma = 6 \times \frac{a \times W(\lambda_c)}{\sqrt{\lambda_c}} \quad \text{Eq. 22}$$

Where  $W(\lambda_c)$  is the strain energy which corresponds to the area under the stress-strain curve of the unnotched sample up to the critical deformation  $\lambda_c$  and  $a$  is the initial notch size.

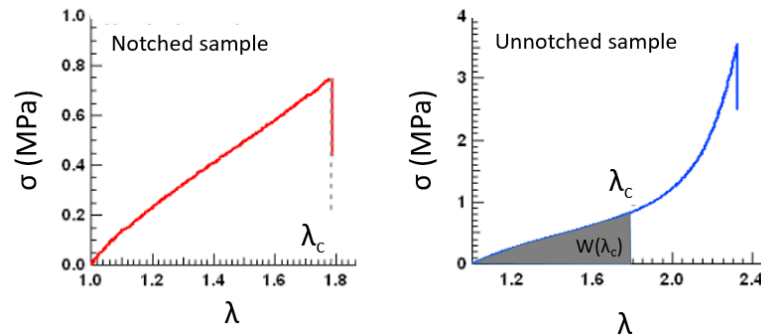


Figure 21 Notched and unnotched samples stress-strain curve.  $\lambda_c$  corresponds to the critical deformation at which the crack starts to propagate.  $W(\lambda_c)$  is the area under the curve of the unnotched sample stress-strain curve up to  $\lambda_c$ .

## References

1. Zhao, X. Multi-scale multi-mechanism design of tough hydrogels: building dissipation into stretchy networks. *Soft Matter* **10**, 672–687 (2014).
2. Zhao, X. *et al.* Soft Materials by Design: Unconventional Polymer Networks Give Extreme Properties. *Chem. Rev.* **121**, 4309–4372 (2021).
3. Heinrich, G., Klüppel, M. & Vilgis, T. A. Reinforcement of elastomers. *Current Opinion in Solid State and Materials Science* **6**, 195–203 (2002).
4. Berriot, J., Montes, H., Lequeux, F., Long, D. & Sotta, P. Evidence for the Shift of the Glass Transition near the Particles in Silica-Filled Elastomers. *Macromolecules* **35**, 9756–9762 (2002).
5. Ducrot, E., Chen, Y., Bulters, M., Sijbesma, R. P. & Creton, C. Toughening Elastomers with Sacrificial Bonds and Watching Them Break. *Science* **344**, 186–189 (2014).
6. Hu, J. *et al.* Microgel-Reinforced Hydrogel Films with High Mechanical Strength and Their Visible Mesoscale Fracture Structure. *Macromolecules* **44**, 7775–7781 (2011).

7. Flory, P. J. & Rehner, J. Statistical Mechanics of Cross-Linked Polymer Networks II. Swelling. *The Journal of Chemical Physics* **11**, 521–526 (1943).
8. Gao, H., Min, K. & Matyjaszewski, K. Determination of Gel Point during Atom Transfer Radical Copolymerization with Cross-Linker. *Macromolecules* **40**, 7763–7770 (2007).
9. Wang, Z., Liu, J., Wu, S., Wang, W. & Zhang, L. Novel percolation phenomena and mechanism of strengthening elastomers by nanofillers. *Physical Chemistry Chemical Physics* **12**, 3014–3030 (2010).
10. Witten, T. A., Rubinstein, M. & Colby, R. H. Reinforcement of rubber by fractal aggregates. *J. Phys. II France* **3**, 367–383 (1993).
11. Zhang, H. *et al.* Strain induced nanocavitation and crystallization in natural rubber probed by real time small and wide angle X-ray scattering. *Journal of Polymer Science Part B: Polymer Physics* **51**, 1125–1138 (2013).
12. Zhang, H. *et al.* Cavitation, crazing and bond scission in chemically cross-linked polymer nanocomposites. *Soft Matter* **15**, 9195–9204 (2019).
13. Ramier, J. *et al.* In situ SALS and volume variation measurements during deformation of treated silica filled SBR. *J Mater Sci* **42**, 8130–8138 (2007).
14. Takahashi, R. *et al.* Tough Particle-Based Double Network Hydrogels for Functional Solid Surface Coatings. *Adv. Mater. Interfaces* **5**, 1801018 (2018).
15. Clough, J. M., Creton, C., Craig, S. L. & Sijbesma, R. P. Covalent Bond Scission in the Mullins Effect of a Filled Elastomer: Real-Time Visualization with Mechanoluminescence. *Advanced Functional Materials* **26**, 9063–9074 (2016).

## **Chapter 3**

# **Aqueous route to double network particles and characterization of the films therefrom**



## Table of contents

Introduction .....	95
1. Results .....	97
1.1. Synthesis.....	97
1.1.1. Synthesis of the “Single latex” (S) by emulsion polymerization .....	97
1.1.2. Swelling of the latex particles in aqueous dispersion by EA.....	98
1.1.3. Synthesis of the “Double latex” (D) by seeded emulsion polymerization .....	102
1.2. Film formation and characterization .....	116
1.2.1. Temperature effect on film formation .....	116
1.2.2. Comparison of D latex with the corresponding constituting single networks .....	117
1.2.3. Effect of the crosslinking density in the S seeds on S and D films .....	120
1.3. Connecting particles .....	123
1.3.1. Presentation of the DAAM/ADH system.....	123
1.3.2. Effect of DAAM on S film .....	123
1.3.3. Connecting the particles through the 2 <sup>nd</sup> network .....	128
Conclusion.....	141
2. Experimental part .....	143
2.1. Synthesis.....	143
2.1.1. Chemicals and reagents .....	143
2.1.2. Synthesis of the “Single latex” (S) by emulsion polymerization .....	143
2.1.3. Synthesis of the “Double latex” (D) by seeded emulsion polymerization .....	144
2.1.4. Drying process.....	146
2.2. Characterization methods .....	146
2.2.1. Gravimetric analysis.....	146
2.2.2. DLS .....	146
2.2.3. AFM .....	146
2.2.4. CryoTEM.....	147
2.2.5. Mechanical tests .....	147
Appendix .....	148
References .....	149



## Introduction

*Elastomers are an important class of material, characterized by their unique ability to deform reversibly up to several times their initial length. Conventional elastomers are soft polymer networks with fairly low resistance to crack propagation. Therefore, their industrial use requires some reinforcements. The most famous examples of reinforced elastomers are composite materials, in which stiff particles are dispersed in a soft elastomer matrix. Though, this strategy is widely used, it has its limitations and new elastomer designs are being developed to meet the needs of future applications like soft actuators or flexible electronics.*

*One promising strategy consists in the pre-stretching of a first polymer slightly crosslinked network followed by the polymerization of a 2<sup>nd</sup> network embedded in the first one, which freezes the pre-stretch. Such obtained materials are known as ‘double networks’<sup>[1-4]</sup>. This interpenetrated network system shows enhanced strength and toughness depending on the pre-stretch level of the 1<sup>st</sup> network while keeping a good extensibility. When the double network is stretched, both networks deform but the pre-stretched shorter chains of the 1<sup>st</sup> network tend to reach their limit extensibility prior to the rest of the sample and breakage of so called sacrificial bonds happens randomly in the sample. This phenomenon dissipates energy and delays the macroscopic failure of the material.*

Traditionally, a double network is obtained from the swelling of a crosslinked 1<sup>st</sup> network in a bath of excess monomer (and initiator, crosslinker and sometimes solvent) until equilibrium followed by the polymerization of the entrapped monomers <sup>[3,4]</sup>. This process has some limitations: the swelling step takes time and uses an excess of volatile monomers (toxicity and ecological limit), the swelling limits the shape of the sample (whose size shouldn’t exceed the bath size), the control of this shape (complex shapes will be difficult to get because of the 1<sup>st</sup> network deformation), and the 1<sup>st</sup> network’s shape determines the double network’s shape.

In the previous chapter, we successfully synthesized soft composites reinforced by a local double network architecture within soft filler nanoparticles embedded in a soft continuous matrix. To make these composites, we used crosslinked soft nanoparticles dispersed overnight in a monomer, crosslinker and initiator mixture that was then injected into molds and polymerized under UV. This process overcame some limitations of the previous bulk process: no excess monomer was used to make the sample and the use of a first network in the form of nanometric particles allows more flexibility concerning the double network’s shape, which is only determined by the synthesis of the second network. However, the swelling step is still time-consuming and the process was not adapted for coatings. Nevertheless, these resulting materials demonstrated strain-hardening, tunable with the concentration of filler particles, and good extensibility. However, the process to obtain macroscopic samples limits the concentration of fillers to ~66 % in volume, which is close to the maximal packing

for monodisperse particles\*. In the process, the particle/monomer mixture is injected into the molds through a syringe, which further limits the maximal filler concentration as the mixture viscosity increases with filler content.

In this project, we work on a novel approach to overcome the previous limitations. We aim at producing interpenetrated ‘double network’ particles through an aqueous emulsion polymerization process and dry them into films of “double network” particles.

Latex IPN (LIPN) have been mainly studied for their internal phase separation giving rise to microstructuration and non-spherical morphologies [5]. LIPN are complex systems even when only one monomer is used. Morphologies that can be generated using two-stage sequential emulsion polymerization depend on the polymerA-monomerB compatibility, the degree of seed crosslinking and can include core-shell, inverted core-shell [6], raspberry-like [7,8], crescent moon like or half-moon like [9] and dumbbell structure [10]. Most of the former studies focused on different particle morphologies and internal microphase separation. LIPN have found application as coatings, adhesives, resins, sealable films and applied as additives in paints or toners [11].

While the IPN strategy has been extended to prestretched ‘double networks’, the current project is determined to extend the LIPN strategy to nanoparticles composed of a pretretched ‘double network’.

In our project, we want to use water-born particles as first crosslinked network and swell these particles dispersed in water with the same monomer used in the 1<sup>st</sup> network to obtain double network particles. The first particles are polymerized by a free radical emulsion polymerization, and then used as seed particles for the polymerization of the 2<sup>nd</sup> network.

Compared to the bulk or composite process, this all-water process is more ecofriendly as no excess monomer nor chemical solvent is needed. In addition, we expect the swelling of the particles to be faster thanks to their nanometric size. Finally, the film formation step should be much more versatile, and compatible with various and complex shapes as well as coatings.

In our study, we will perform a two-step sequential emulsion polymerization of the same monomer and play with the quantity of added monomer in the second polymerization to pre-stretch differently the 1<sup>st</sup> network and mimic thereby the behavior of a macroscopic double network at the particle scale. The latex of double network particles (called double latex “D” in the following) is then dried into films in order to study their mechanical properties, as represented in Figure 1.

---

\* For monodispers spheres, the densest packing uses approximately 74% of the volume. A random packing of equal spheres has generally a density around 64%.

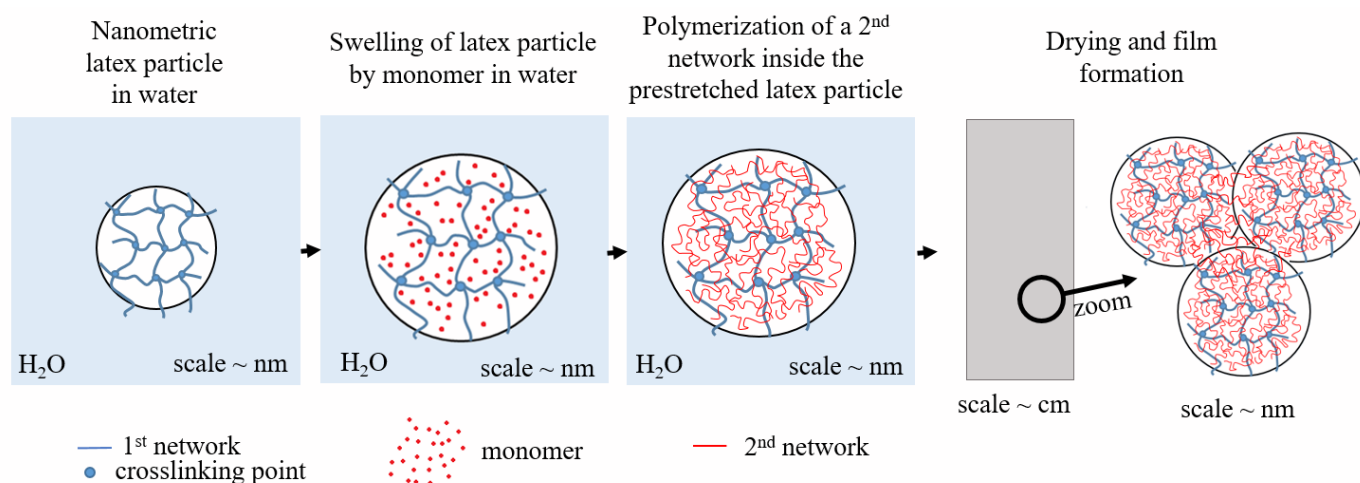


Figure 1 Representation of the double latex polymerization process, from the single latex to the dried double latex.

The work presented in this chapter has been realized with the help of Nadia Belhot during her M2 internship.

The first part will discuss the synthesis and optimizations of the simple and double latexes. Thereafter, we move on to the characterization of the mechanical properties of films formed from the previously synthesized “single latex” (S) and “double latex” (D). Finally, we will describe the strategies used to connect the particles and strengthen the film’s cohesion, and characterize the mechanical behavior of these films in uniaxial extension.

The second part will focus on the experimental methods.

## 1. Results

### 1.1. Synthesis

#### 1.1.1. Synthesis of the “Single latex” (S) by emulsion polymerization

First, lightly cross-linked single latexes were prepared through established emulsion polymerization protocols [12], using ethyl acrylate (EA) as a model monomer, 1,4-butanediol diacrylate (BDA) as a crosslinker, KPS as an initiator, and SDS as a surfactant in a concentration. The concentration  $C(\text{SDS})$  of surfactant was modified from the established protocol and decreased so that  $C(\text{SDS})$  is below the critical micellar concentration ( $C(\text{SDS}) = 3.63 \text{ mmol/L}$ ,  $C(\text{CMC}) = 7 \text{ mmol/L}$ ). The polymerization were performed at 25 % solids at 60 °C following the protocol detailed in section 2.1.2. Keeping all other parameters constant, we varied the amount of crosslinker from 0 to 0.8 mol% (see Table 1), in order to understand the effect of the crosslink density in the seed on the synthesis of the double latex (D), and

more precisely the swelling and pre-stretch of the single particles (S), and their effect on the films' mechanical properties. We chose to work with such concentration of crosslinker to compare our mechanical results with the conventional bulk double networks that contained these concentrations of crosslinker [13].

The resulting latexes were labeled “S $\mathbf{x}$ ”, where S stands for single latex and  $\mathbf{x}$  corresponds to the molar percentage of crosslinker relative to the monomer. For example, a simple latex with 0.5 mol% crosslinker is labeled S0.5. If another simple latex was synthesized in the same conditions, but in a separate batch, it was labeled S0.5bis.

The latexes were characterized with gravimetry in order to determine the monomer conversion and final solids. DLS (as detailed in 2.2.2 and 2.2.1) was used to determine the average hydrodynamic radius of the particles. The results are summarized in Table 1.

Table 1 Synthesis of single latexes by emulsion polymerization of EA at 60 °C using KPS as initiator and SDS as a surfactant and BDA as crosslinker.<sup>#</sup>

Name	Synthesis conditions	Characterization				
	mol% <sub>BDA</sub> <sup>a</sup>	%conv	%agg	%solids	R <sup>b</sup> (nm)	PDI
S0	0	100	1.0	26	114	0.01
S0.3	0.3	100	4.8	27	105	0.03
S0.5	0.5	100	2.1	27	109	0.03
S0.5bis	0.5	100	2.7	26	118	0.04
S0.8	0.8	100	1.9	27	116	0.03

<sup>#</sup> c(KPS) = 3.63 mmol/L; c(SDS) = 3.63 mmol/L; monomer = 0.200 mol. <sup>a</sup> molar percentage of BDA = n(BDA)/n(EA). <sup>b</sup> averaged radius of the latex particles.

The results show that varying the crosslinker concentration did not affect much the latex polymerization. In all cases, the monomer conversion was quantitative and latexes with radius around 110 nm were obtained, with no significant variation caused by the variation of the crosslinker between 0 and 0.8 mol%. The creation of aggregates remains below 5 % for all polymerizations.

### 1.1.2. Swelling of the latex particles in aqueous dispersion by EA

The swelling step is crucial in double network architectures, to activate the sacrificial bonds dissipation mechanism. The 1<sup>st</sup> network pre-stretch results from its swelling that it “frozen” by the polymerization of the 2<sup>nd</sup> network (within the 1<sup>st</sup> network). When the material is stretched, the 1<sup>st</sup> network's chains reach their limit extensibility before the chains of the 2<sup>nd</sup> network and randomly break in the material which dissipates energy before the sample macroscopic failure, and enhances the material's fracture toughness.

Swelling of the S particles is also crucial in our emulsion polymerization system, not only to pre-stretch the 1<sup>st</sup> network and generate the sacrificial bonds in the double network architecture, but also to ensure that the 2<sup>nd</sup> polymerization step occurs inside the seed particle while avoiding secondary nucleation.

Compared to the swelling of the particles in a monomer bath described in Chapter 2, here the swelling step is done directly in the diluted seed latex, *i.e.* on nanometer-sized polymer particles surrounded by water. The size, the chemical environment of the particles and the polymer-monomer interactions will greatly affect their swelling process because of thermodynamic considerations, including surface energies at the monomer swollen particle/ water interface.

In a three component system, composed of crosslinked polymer particles dispersed in water and a solvent (in our case the monomer), which is a good solvent for the polymer and partially miscible with water, the chemical potential,  $\Delta G_{m,p}$ , of the monomer in the crosslinked latex particles can be written as:

$$\Delta G_{m,p} = \Delta G_m + \Delta G_{el} + \Delta G_s \quad \text{Eq. 1}$$

Where  $\Delta G_m$ ,  $\Delta G_{el}$ , and  $\Delta G_s$  are respectively the contributions of the monomer-polymer mixing force, the contribution of the polymer network elastic restrictive force and the contribution of the particle-water interfacial tension force.

$$\Delta G_m = RT [\ln(1 - \Phi_p) + \Phi_p + \chi_{m,p}(\Phi_p)^2] \quad \text{Eq. 2}$$

Where R is the gas constant, T is the temperature,  $\Phi_p$  is the polymer volume fraction and  $\chi_{m,p}$  is a monomer-polymer interaction parameter.

$\Delta G_m$  encourages the particle swelling when the polymer volume fraction is close to 1 (so when little amounts of monomer diffuses into the particle).

$$\Delta G_{el} = \frac{RTV_m d_p}{M_c} * (\Phi_p^{1/3} - \Phi_p/2) \quad \text{Eq. 3}$$

Where  $V_m$  is the molar volume of the monomer,  $d_p$  is the polymer density and  $M_c$  is the molecular weight between crosslinks.

$\Delta G_{el}$  is a restrictive contribution to the particle swelling, which increases with the particle crosslink density.

$$\Delta G_s = \frac{2V_m\gamma}{r} \quad \text{Eq. 4}$$

Where  $\gamma$  is the interfacial free energy.

$\Delta G_s$  is a restrictive contribution to the particle swelling which increases with decreasing particle radius.

From the thermodynamic model, the swelling of the particles is affected by:

- the quantity of monomer in the particles. Lower quantities of monomer drastically affect the contribution of the monomer-polymer mixing force and encourage particle swelling.
- the crosslink density. Less crosslinked particles show lower contribution of the elastic restrictive forces.
- the size. Bigger particles show lower contribution of the interfaces and facilitate swelling.

While for particle swelling in monomer the interfacial consideration can be neglected, surface tensions will restrict the particle swelling in water.

In a “water/good solvent for polymer” system, crosslinked nanometric particles swell due to the free energy of mixing; but the maximum swelling is restricted by the network structure and by the interfacial tension forces. This leads to a saturation concentration of monomer in latex particles and a maximum swelling equilibrium that is lower than the one in pure monomer [14].

Taking into account these considerations, we wanted to estimate the maximal swelling of our seed latex particles dispersed in water by EA. To study the swelling, we estimated the averaged hydrodynamic particle radius by DLS at different time intervals. In more details, we added monomer (EA) in excess to S0.5 latex diluted in water to 0.01 wt%, and followed the S0.5 particle swelling as a function of time. The monomer phase separates on top of the water phase until equilibrium is reached (saturation concentration (EA) in water = 0.15 g/L). The monomer diffuses into the PEA polymer particles until equilibrium is reached. EA in excess serves as a stock phase, so that the monomer concentration in the water phase will remain at the saturation concentration.

From the initial particle size and the swollen size at  $t$ , it is possible to calculate a size ratio  $\lambda$  equal to:

$$\lambda = \frac{R_{swollen}(t)}{R_i} \quad \text{Eq. 5}$$

Where  $R_i$  is the initial averaged radius of the particles and  $R_{swollen}(t)$  is the averaged radius measured at the time  $t$ .

$\lambda$  is equivalent to the deformation of the chains in the 1<sup>st</sup> network, it corresponds thus to the 1<sup>st</sup> network's pre-stretch.

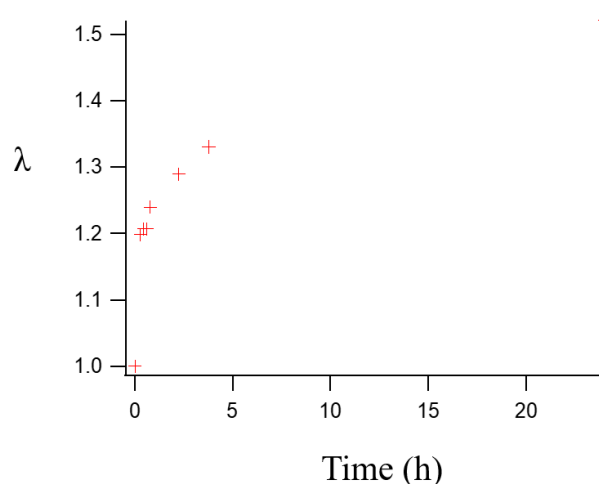


Figure 2 Evolution of the size ratio of latex particles S0.5 in water saturated with EA measured by DLS (0.01 % solids content).

Figure 2 shows that crosslinked latex particles, in EA saturated water, swell rapidly to  $\lambda = 1.2$  after 15 minutes, then slowly swell up to  $\lambda = 1.5$  after 20 h (which we considered maximum), following a Fickian diffusion [15].

The maximum swelling of S0.5 particles surrounded by monomer saturated water was  $\lambda = 1.5$ , which is considerably lower than the maximum swelling measured for comparable crosslinked particles (with BDA = 0.5 mol%) surrounded by monomer only, where  $\lambda = 1.6$ . However, both values are quite close to each other: the water-polymer interface does not restrict much the equilibrium swelling.

For bulk samples, the double network architecture showed an enhancement of the material's toughness starting from  $\lambda = 1.6$  (this value corresponds to a double network of PEA, with a 1<sup>st</sup> network containing 0.5 mol% of crosslinker). The maximal pre-stretch value obtained with the aqueous system ( $\lambda = 1.5$ ) may thus be sufficient to improve the final particles' network toughness, once the double network created and the film formed.

### 1.1.3. Synthesis of the “Double latex” (D) by seeded emulsion polymerization

In order to create the double latex (D) containing a pre-stretched first crosslinked network, the first single latex (S) was used as a seed latex. The second polymerization step consists then in the seeded polymerization of EA (in the presence of the crosslinked S prepared before) and in the absence of crosslinker, in order to allow interparticle chain diffusion during film formation yielding in connection of particles and high deformability of the final film. Each individual particle contains a 1<sup>st</sup> network, which will be swollen and upon polymerization become a double network particle. These supposed dispersion of double network particles will be called double latex (D) in the following. We might note here that despite the absence of crosslinker in the second polymerization step, the 2<sup>nd</sup> PEA network might be lightly crosslinked and partially covalently linked to the 1<sup>st</sup> network due to transfer reactions occurring within the 2<sup>nd</sup> network or on the first network. Actually, in the polymerization of bulk double network [3], un-controlled transfer reactions were proven to be sufficient to connect the 2<sup>nd</sup> network to the first one [16].

Our aim is to make D particles whose 1<sup>st</sup> network is pre-stretched as much as possible, in order to favor strain hardening in the final films. The 1<sup>st</sup> network pre-stretch directly depends on the 1<sup>st</sup> network swelling and therefore on the quantity of 2<sup>nd</sup> network polymerized.

$$\lambda^3 = \frac{V_{tot}}{V_1} = \frac{V_1 + V_2}{V_1} = 1 + \frac{V_2}{V_1} \quad \text{Eq. 6}$$

Where  $V_{tot}$ ,  $V_1$  and  $V_2$  are respectively the total volume of the D particle, the volume of the first network and the volume of the second network.

As the polymer in the first and second network are the same, we can write:

$$\lambda^3 = 1 + \frac{m_2}{m_1} \quad \text{Eq. 7}$$

$$m_2 = m_1(\lambda^3 - 1) \quad \text{Eq. 8}$$

Where  $m_1$  and  $m_2$  are respectively the mass of polymer in the first network and second network.

So to reach high pre-stretch as  $\lambda = 1.5$ , it is required to polymerize 2.4 times more monomer (in weight) in the second polymerization step than in the first one. However, it is important that the latex remains stable during the polymerization, to minimize product loss through the formation of large aggregates

that precipitate. Moreover, the locus of the second polymerization (desired inside the seed particles) is fundamental for the 1<sup>st</sup> network pre-stretch, and in fine the film's mechanical properties. To optimize the 1<sup>st</sup> network pre-stretch, the second polymerization should occur within the seed particles and secondary nucleation should be prevented.

We therefore used AIBN - instead of KPS - as an organo-soluble initiator (at 1.0 mol %) in the second polymerization step to encourage the second polymerization to occur inside the 1<sup>st</sup> network particles. The good solubility in EA and the limited solubility of AIBN in water should reduce the number of initiator-derived free radicals in the aqueous phase, which could initiate the polymerization of the small fraction of monomer soluble in the aqueous phase leading to the formation of new particles (secondary nucleation).

In addition, the final solid contents below 30 % were targeted to prevent latex destabilization. Therefore, the seed latex synthesized at 25 % solids was diluted to 8 % solids before the second polymerization step. It is important to note that all seeded polymerizations were performed with a surfactant concentration below the critical micellar concentration: no surfactant was added in the second polymerization step. So the surfactant in the emulsion was only due to the surfactant introduced in the first polymerization, which was diluted by water addition to 1.21 mmol/L. The absence of micelles should avoid the stabilization of monomer droplets in micelles and prevent secondary nucleation.

### ***Batch polymerization***

In a first series of experiments, we performed seeded polymerizations in simple batch conditions, *i.e.* adding the total amount of monomer at once, at the beginning of the polymerization. The monomer and seed emulsion mix was kept in the fridge overnight (> 10 h) before polymerization to let time for the monomer to diffuse in the seed particles until equilibrium is reached.

As summarized in Table 2, we used single latex S0.5 as seed particles and varied the ratio of added monomer (added at once) over the initial mass of polymer particles ( $r$ ):

$$r = \frac{m_{added}}{m_{ip}} \quad \text{Eq. 9}$$

Where  $m_{ip}$  is the initial mass of latex particles and  $m_{added}$  is the total final mass of monomer added.

Table 2 Synthesis of the double latex particles synthesized by seeded emulsion polymerization through a batch process. Effect of added monomer quantity  $r$ .

Name	Synthesis parameters		Characterization								
	seed latex	$r^a$	%conv	%agg	% solids	R (nm)	PDI	$\lambda_{th}$	$\lambda$	$N_p$ (m <sup>-3</sup> )	$\Delta N_p$
S0.5 <i>diluted</i>	-	-	-	-	9	109	0.03	-	-	1.48E+19	-
Db-r0.3	S0.5	0.3	84	0.4	11	120	0.04	1.1	1.1	1.36E+19	-8%
Db-r0.7	S0.5	0.7	97	0.1	14	129	0.02	1.2	1.2	1.39E+19	-6%
Db-r1.0	S0.5	1	87	1.0	16	133	0.02	1.3	1.2	1.64E+19	-1%
Db-r2.5	S0.5	$\geq 2.5$	-	latex not stable			-	-	-	-	-

<sup>a</sup> $r = m(\text{monomer})/m(\text{latex particles})$ . The surfactant and initiator concentration, polymerization time and temperature were kept constant.  $c(\text{SDS}) = 1.21 \text{ mmol/L}$ ;  $\%(\text{AIBN}) = 1.0 \text{ mol}\%$ ;

From the particle sizes measured by DLS, we could estimate a number of particles  $N_p$  per volume unit:

$$N_p (/m^3 \text{ latex}) = \frac{m_{ptot}}{m_{1p}} = \frac{\text{solids}}{\frac{4}{3}\pi R^3 \rho_{PEA}} \quad \text{Eq. 10}$$

Where  $m_{ptot}$  and  $m_{1p}$  are respectively the total polymer mass per volume unit of the latex and the averaged mass of one particle, *solids* is the solid content (in  $\text{g/cm}^3_{\text{latex}}$ ) measured by gravimetry,  $\rho_{PEA}$  is the polymer density ( $1.12 \text{ g/mL}$ ) and  $R$  is the averaged particles radius.

However, the error from the DLS measurements affects a lot the precision of the estimated number of particles. Therefore, the following discussions and conclusions based on the evolution of the number of particles shouldn't be much considered.

In order to estimate, whether secondary aggregation happened or not during the second polymerization step, we generally compared the initial  $N_p$  after dilution with the  $N_p$  after the second polymerization step. In case, a considerably amount of aggregates was formed during this 2<sup>nd</sup> polymerization step, the wt% of aggregates was estimated by weighing. As the formation of aggregates naturally decreases the

$N_p$ , we estimated a ‘theoretical  $N_p$ ’ taking into account the  $N_p$  lost by aggregation, in order to assess whether secondary nucleation took place or not. The theoretical  $N_p$  was then calculated as:

$$N_{p,th}(/m^3) = \frac{m_{ptot}}{m_{1p}} = \frac{solids (1 + \%agg/100)}{\frac{4}{3}\pi R^3 \rho_{PEA}} \quad \text{Eq. 11}$$

Where  $\%agg$  is the amount of solid aggregated during the polymerization.

From the evolution of  $N_p$  from the first to the second polymerization, we could estimate the creation of secondary particles  $\Delta N_p$  given as:

$$\Delta N_p = \frac{N_p(2) - N_p(1)}{N_p(1)} \quad \text{Eq. 12}$$

Where  $N_p(1)$  and  $N_p(2)$  are respectively the number of particles in the first and second polymerization steps.

The results are reported in Table 2.

The double latex (D) obtained with the batch method were labeled Db-r**X** where Db refers to “double latex” (D) prepared in batch conditions (b) and **X** refers to the mass ratio (r) of added monomer over the initial mass of polymer seed particles in the latex.

The polymerizations were obtained following the process detailed in section 2.1.3, and the weight fraction of added monomer relative to the initial polymer was varied from 0.3 to 2.5. After 3 h of polymerization, the polymerizations were quenched and the resulting latexes were characterized by gravimetry, to determine the monomer conversion and the solids content, and by DLS to determine the size of the particles (methods detailed in the experimental section 2.2.1 and 2.2.2).

From the sizes of the S and D particles, it is possible to express a size ratio as  $\lambda$ :

$$\lambda = \frac{R_D}{R_S} \quad \text{Eq. 13}$$

Where  $R_S$  and  $R_D$  are respectively the average radius of the S particles and D particles.

The size ratio and the ratio of added monomer  $r$  are theoretically related by:

$$\lambda_{th} = (r + 1)^{\frac{1}{3}} \quad \text{Eq. 14}$$

Where  $\lambda_{th}$  corresponds to the size ratio expected if 100 % of the monomer exclusively polymerizes inside of the particles and no additional particles are generated through a secondary nucleation mechanism.

If we make the assumption that the 2<sup>nd</sup> network polymerizes exclusively inside the 1<sup>st</sup> network (without forming excrescences), then  $\lambda$  (and  $\lambda_{th}$ ) corresponds to the pre-stretch of the 1<sup>st</sup> network like in a conventional macroscopic double network (where 2<sup>nd</sup> network is synthesized in homogeneous conditions).

In bulk double networks, a mechanical effect of the network architecture is observed starting from  $\lambda \geq 1.6$  (for a first PEA network crosslinked with 0.5 mol% BDA) [17].

The results for this series of experiments are summarized in the Table 2. The experimental  $\lambda$  values reached in our seeded batch emulsion polymerization matched the maximal theoretical  $\lambda_{th}$  (Table 2), but remained below the useful range of  $\lambda \geq 1.6$ , at least according to our previous results. We can observe that increasing  $r$  from 0.3 to 1, has no significant impact on the monomer conversion, which is above 84% in all cases. Furthermore, the amount of aggregates created was negligible as long as the amount of monomer added was  $r \leq 1$ . When the ratio of added monomer over initial mass of polymer particles was equal to 2.5, after one night without stirring (to let the monomer diffuse into the particles) we observed the presence of an organic monomer layer at the top of the flask). Phase separation happens, as the amount of monomer exceeds the amount that can swell the particles (maximum  $r$  calculated in section 1.1.2 :  $r_{max} = 2.4$ ). Therefore, using AIBN as an organo-soluble initiator, it becomes impossible to avoid the formation of macroscopic aggregates generated through droplet nucleation or nucleation within the top monomer layer (which might be observed during polymerization, although the reaction medium is stirred).

To avoid this phase separation, the ratio of added monomer over initial polymer content should remain below a critical value (equal to 2.4 for S0.5, calculated from  $\lambda$  at the maximum swelling in water). This limits however the pre-stretch of the particle that can be reached in one batch polymerization. In order to reach higher  $\lambda$ ,  $r$  needs to be increased. This might be possible through a multiple step polymerization

process by doing several successive batch polymerizations. This process resembles the process used to produce multiple networks, where swelling and polymerization steps are repeated with the same sample in order to go from a single, to a double, to a triple... to a multiple network, which reaches every time higher pre-stretch. Such a multi-step process is however time consuming, in particular when the latex particles are swelled overnight between each polymerization step.

An alternative to multiple swelling steps might be a semi-continuous process, which seem more straightforward and should also allow to increase the overall pre-stretch  $\lambda$ . We will investigate this method in the following section.

### *Semi-batch polymerizations*

As explained above, a seeded *semi-batch* polymerization method, where the monomer is continuously added in the polymerization medium might be a solution to reach higher  $\lambda$ . Again, we increased progressively the total amount of monomer added relative to the initial mass of polymer in the feed ( $r$ ). The initiator added during the second polymerization step remained AIBN (1 mol% relative to EA). It was introduced dissolved in a fraction of EA added as an initial shot prior to the polymerization, during which the residual amount of EA was continuously fed to the polymerization medium.

In addition, in order to reach the best compromise between high pre-stretch and polymerization “control” (in the sense of particle stability, low amount of aggregates), other parameters can be modified to tune the seeded semi-batch process:

- amount of initially added monomer (i.a.m.) expressed as a mass ratio of added monomer over initial polymer

$$r_{i.a.m.} = \frac{m_{i.a.m.}}{m_{ip}} \quad \text{Eq. 15}$$

Where  $m_{ip}$  and  $m_{i.a.m.}$  are respectively the mass of the polymer particles initially present in the seed latex and the mass of the initially added monomer just before initiation

- feed rate ( $f$ ) at which the monomer is added

The surfactant concentration and the organic initiator molar percentage,  $\text{mol\%}(\text{AIBN}) = 1 \text{ mol\%}$  with respect to amount of initially added monomer ( $n_{i.a.m.}$ ), were kept constant. We chose to keep the amount of initially added monomer  $r_{i.a.m.}$  equal to 0.35, *i.e.* 35 wt% of the mass of polymer particles initially present in the latex, because this parameter was already investigated in the previous batch polymerization work, and this specific quantity shouldn't result in phase separation. We let the mix

equilibrate for 20 minutes before initiating the polymerization. The rest of the monomer was added, at different rates, to the polymerization using an automatic syringe pump as detailed in the experimental section 2.1.3.

Double latexes (D) polymerized following the semi-batch polymerization process will be named:

**D $\mathbf{x}$ -f $\mathbf{y}$ -r $\mathbf{z}$**

Where  $\mathbf{x}$  refers to the crosslinker (BDA) concentration in the seed latex  $S\mathbf{x}$ ,  $\mathbf{y}$  corresponds to the feed rate in mL/h and  $\mathbf{z}$  corresponds to the mass ratio of monomer added in total until the end of the polymerization with respect to the initial amount of polymer in the latex.

For example, a double latex obtained from the seed latex S0.5 a feed rate of 1.5 mL/h and a ratio of monomer added in total over initial amount of polymer particles equal to 2, will be name D(0.5)-f1.5-r2.

In order to reach a targeted pre-stretch  $\lambda$ , we have to reach the related total amount of monomer  $r$ . This can be done more or less quickly by adding monomer at different rates. High feed rates would enable to reach higher pre-stretch faster. We checked separately the effect of feed rate and pre-stretch.

- **Effect of feed rate**

We investigated first the effect of feed rate keeping constant the total amount of monomer added ( $r = \text{const.}$ ). A first set of experiment was performed with a seed latex containing 0.5 mol% of crosslinker (S0.5 and S0.5bis). We carried out 4 polymerizations with increasing feed rates from 1 mL/h to 2.5 mL/h, all other parameters remained constant (seed latex composition, surfactant and monomer concentrations,  $r_{i.a.m.}$ ,  $r$ ). The latexes were characterized by gravimetry and DLS. Compositions and the results of the characterizations are reported in Table 3.

Table 3 Synthesis of the double latex particles by seeded emulsion polymerization through a semi-continuous process. Effect of feed rate.

Name	Synthesis parameters			Characterization								
	seed latex	r	f (mL/h)	%conv	%agg	%solid	R (nm)	PDI	$\lambda_{th}$	$\lambda$	$N_p$ (m <sup>-3</sup> )	$\Delta N_p$ †
S0.5 diluted	-	-	-	100	-	8	109	0.03	-	-	1.48E+19	-
S0.5bis diluted	-	-	-	100	-	8	118	0.04	-	-	1.12E+19	-
D(0.5)-f1-r1.4	S0.5	1.4	1	88	3.5	17	143	0.03	1.1	1.2	1.28E+19	-13%
D(0.5bis)-f1.5-r1.3	S0.5bis	1.3	1.5	91	1.2	17	147	0.01	1.2	1.2	1.15E+19	3%
D(0.5bis)-f2-r1.4	S0.5bis	1.4	2	85	3.5	17	146	0.01	1.2	1.2	1.21E+19	7%
D(0.5bis)-f2.5-r1.4	S0.5bis	1.4	2.5	85	1.2	17	148	0.03	1.3	1.3	1.13E+19	1%

Seed latex formulation,  $r_{i,a,m}^a$ , and  $r^b$ , surfactant and initiator concentrations, and polymerization temperature were kept constant.  $r_{i,a,m}=35\%$ ;  $r=1.4$ ;  $c(\text{SDS})=1.21$  mmol/L;  $\%(\text{AIBN})=1$  mol%.

<sup>a</sup>  $r_{i,a,m} = m(\text{monomer before initiation})/m(\text{latex particles})$ . <sup>b</sup>  $r = m(\text{monomer})/m(\text{latex particles})$ .

From Table 3, it occurs that changing the feed rate from 1 mL/h to 2.5 mL/h does not have any significant impact on neither the monomer conversion nor the formation of aggregates. The results on the secondary nucleation appear to be quite puzzling. Although the percentage of aggregates was taken into account in the estimation of particles concentrations, Table 3 shows that at a feed rate of 1 mL/h, the number of particles concentration is lower in the D latex than in the S latex, and 13 % of particles were lost. This result could be explained by some experimental errors:

- The particles concentration in the S latex was estimated (by gravimetry and DLS) once right after the polymerization. Errors on the particles concentration due to sedimentation of the particles or water evaporation over time are possible and weren't verified before by gravimetry right before the second polymerization step.
- The seed latex dilution to 8 wt% is also a source of errors in the estimation of the particles concentration, and the solids were not double-checked after dilution.

† The error from the particles size measurements affects a lot the precision of the estimated number of particles. Therefore, the following discussions and conclusions based on the evolution of the number of particles shouldn't be much considered.

- The percentage of aggregates measured at the end of the second polymerization step could be underestimated because of the method of filtration (use of filter paper) and weighted.

All these experimental errors may explain such values reported in Table 3. It remains difficult to clearly conclude on the effect of feed rates on the creation of secondary particles.

It should be noted yet that the first experiment with a feed rate of 1 mL/h was the only one made with seed latex S0.5, the following three experiments – revealing no loss of particles - were performed with seed latex S0.5bis. Therefore, it seems reasonable to neglect the first experiments' s  $N_p$  results and to conclude that secondary nucleation remains very limited in the selected conditions.

These results show that it is possible to play with the feed rate. Nevertheless, for the following polymerizations, we generally chose feed rates of 1 mL/h to encourage starved polymerization conditions.

- **Effect of 2<sup>nd</sup> network weight fraction ( $r$ )**

In order to reach higher  $\lambda$ , it is necessary to increase  $r$  as both values are theoretically linked. Keeping all other parameters constant (seed latex composition,  $r_{i.a.m.}$ , feed rate), we investigated the effect of  $r$  on the polymerization. Because the feed rate was set constant here, we increased progressively the polymerization duration in order to add more monomer and increase thereby  $r$ . The latexes were characterized by gravimetry and DLS. Composition and results are reported in the table below.

From Table 4, we can see that polymerizing more monomer in the second step tends to increase significantly the quantity of aggregates, while the monomer conversion seems not affected by  $r$ . The prestretch  $\lambda$  increased with  $r$  as expected.

Here again, it is difficult to conclude on the creation of secondary nanoparticles, due to the same experimental errors discussed above.

Table 4 Synthesis of the double latex particles synthesized by seeded emulsion polymerization through a semi-continuous process. Effect of added monomer quantity  $r$ .

Synthesis parameters		Characterization								
Name	$r^a$	%conv	%agg	%solid	R (nm)	PDI	$\lambda_{th}$	$\lambda$	$N_p$ (m <sup>-3</sup> )	$\Delta N_p^\ddagger$
S0.5 diluted	-	-	-	8	108	0.03			1.48E+19	-
D(0.5)-f1-r1.4	1.4	88	3.5	17	143	0.03	1.1	1.2	1.28E+19	-13%
D(0.5)-f1-r3.4	3.4	99	16.6	29	167	0.03	1.6	1.5	1.55E+19	4%

Seed latex, feed rate,  $r_{i.a.m}^b$ , surfactant and initiator concentrations, and polymerization temperature were kept constant.  $f=1$  mL/h;  $r_{i.a.m}=35\%$ ;  $c(SDS)=1.21$  mmol/L;  $\%(AIBN)=1$  mol%

<sup>a</sup>  $r = m(\text{monomer})/m(\text{latex particles})$ . <sup>b</sup>  $r_{i.a.m} = m(\text{monomer before initiation})/m(\text{latex particles})$ .

- **Direct observations**

The polymerization of latex IPN can lead to anisotropic, snowman or raspberry like morphologies due to phase separation between the 1<sup>st</sup> and the 2<sup>nd</sup> network. Aiming to observe the morphology of a D latex particle in water, we performed cryoTEM, as detailed in the experimental section 2.2.4, on D(0.5)-f1-r3.4. To be able to compare the morphology of the D latex particle with the seed latex particle, we also performed cryoTEM on the corresponding seed latex S0.5.

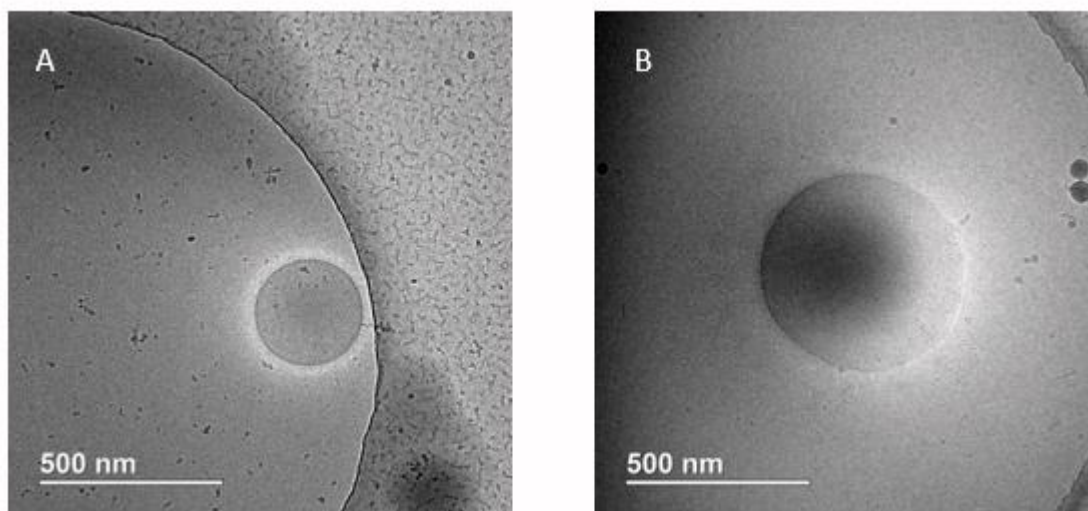


Figure 3 CryoTEM images of S0.5 (A) and D(0.5)-f1-r3.4 (B)

<sup>‡</sup> The error from the particles size measurements affects a lot the precision of the estimated number of particles. Therefore, the following discussions and conclusions based on the evolution of the number of particles shouldn't be much considered.

We can see on the Figure 3 that the morphology of S0.5 and D(0.5)-f1-r3.4 are both spherical. The swelling of the D latex happened thus isotropically.

However, the characterization method does not enable us to distinguish the 1<sup>st</sup> network and 2<sup>nd</sup> network within one particle. Thus, we cannot clearly conclude whether or not the polymerization of the 2<sup>nd</sup> network occurred completely inside, at the interface or around the particle, which would give rise to a 'core-shell' structure.

- **Effect of the seed latex crosslinking density**

Up to now, all the D latex polymerizations were done with the same seed latex, namely S0.5 containing 0.5 mol% of crosslinker. However, we know that the crosslinking content in a conventional network affects its softness. We also know from previous work that the 1<sup>st</sup> network composition also affects the mechanical properties of the double network [17]. A more crosslinked network present shorter chains that will get closer to their limit extensibility for lower pre-stretch, hence demonstrate strain-hardening at lower elongations. In contrast, in our process, densely crosslinked particles may be more difficult to swell in water due to their elastic energy.

In a third series of experiments, we therefore used different single latexes (S) containing 0.3, 0.5 or 0.8 mol% of BDA, namely S0.3, S0.5 and S0.8, as seeds for the synthesis of the D latex. All other parameters ( $r_{i.a.m.}$ , feed rate,  $r$ ) remained constant. Again, the resulting latexes were characterized by gravimetry and DLS (details in the experimental section 2.2.1 and 2.2.2) and the results are reported in Table 5.

Table 5 shows that, at constant  $r$ , we reach higher  $\lambda$  for lower crosslink content in the seed latex. This observation is disputable, if we further take a look at the conversion of D(0.8)-f1-r1.3, which is lower (70%) than the two others, presumably due to oxygen contamination during the polymerization. The theoretical pre-stretch was calculated as if the conversion was 100 %. If we consider the experimental conversion at 70 % for D(0.8)-f1-r1.3, then  $\lambda_{th,conv}$  becomes equal to 1.3, which is closer. If less monomer is converted into polymer, the prestretch  $\lambda$  is consequently lower than targeted; and the difference between the theoretical value and the experimental value diminishes.

As a conclusion, varying the crosslinker concentration from 0.3 to 0.8 mol% in the seed particles did not allow us to vary the prestretch in the particles.

Considering the creation of secondary nanoparticles, despite the experimental errors discussed earlier, the results presented in Table 3 clearly show that more particles were created during the polymerization of D(0.8)-f1-r1.3 which had the highest crosslinked seed particles.

Based on these result, in the following experiments, the crosslinking density of the seed latex will be kept constant at 0.5 mol%.

Table 5 Synthesis of the double latex particles synthesized by seeded emulsion polymerization through a semi-continuous process. Effect of the crosslinker density in the seed latex.

Name	Synthesis parameters	characterization								
	seed latex	%conv	%agg	%solid	R (nm)	PDI	$\lambda_{th}$	$\lambda_{th, conv}$	$\lambda$	...
S0.3	-	-	-	8	105	0.03	-	-	-	...
S0.5	-	-	-	8	109	0.03	-	-	-	...
S0.8	-	-	-	8	116	0.03	-	-	-	...
D(0.3)-f1-r1.3	S0.3	99	2.1	19	141	0.03	1.3	1.3	1.3	...
D(0.5)-f1-r1.4	S0.5	88	3.5	17	143	0.03	1.3	1.3	1.2	...
D(0.8)-f1-r1.3	S0.8	70	2.5	16	136	0.04	1.4	1.2	1.2	...

Name	Synthesis parameters	Characterization		
	seed latex	...	$N_p$ (m <sup>-3</sup> )	$\Delta N_p$ <sup>§</sup>
S0.3	-	...	1.66E+19	-
S0.5	-	...	1.48E+19	-
S0.8	-	...	1.23E+19	-
D(0.3)-f1-r1.3	S0.3	...	1.47E+19	-11%
D(0.5)-f1-r1.4	S0.5	...	1.28E+19	-13%
D(0.8)-f1-r1.3	S0.8	...	1.39E+19	13%

Feed rate,  $r_{i,a,m}$ <sup>a</sup>,  $r$ <sup>b</sup>, surfactant and initiator concentrations, polymerization time and temperature were kept constant.  $f=1$  mL/h;  $r_{i,a,m}=35\%$ ;  $r=1.4$ ;  $c(SDS)=1.21$  mmol/L;  $\%(AIBN)=1$  mol%

<sup>a</sup>  $r_{i,a,m} = m(\text{monomer before initiation})/m(\text{latex particles})$ . <sup>b</sup>  $r = m(\text{monomer})/m(\text{latex particles})$ .

<sup>§</sup> The error from the particles size measurements affects a lot the precision of the estimated number of particles. Therefore, the following discussions and conclusions based on the evolution of the number of particles shouldn't be much considered.

- **D particles morphology**

We have previously seen by cryoTEM that the swelling was isotropic, but we couldn't differentiate the first and 2<sup>nd</sup> network with this technique. Not only the particle morphology, but also the internal structure of D particles can be quite complex and is considered crucial for the expected double network reinforcement.

In a simple worst scenario, all monomer of the 2<sup>nd</sup> network polymerized around the particles and did not connect to the particles. So when a D particle is dried on a substrate, the 2<sup>nd</sup> network spread around onto the substrate and the D particle look like a “fried egg”.

In an ideal scenario, all monomer polymerized within the particles, and transfer reactions connected the two networks together, so that upon drying, the majority of the chains of the 2<sup>nd</sup> network remain stuck inside the particle. In this situation, the D particle should spread less onto the substrate than the original S particle (thanks to the enhanced stiffness of the 1<sup>st</sup> network in its pre-stretched state).

However, it is possible that the real situation lies between the worst and the ideal ones, meaning the linear chains of the 2<sup>nd</sup> network may be partially stuck inside the pre-stretched 1<sup>st</sup> network and partially free to move outside of the particles up to a certain extent (few nanometers). Looking at the dried D particles cross-section, and comparing them to the S particles cross-section and their contact angle, we may grasp some understanding on the morphology of the D particles.

In order to get a better understanding of the morphology of the D particles (homogeneous or core shell) and the effect of the seed particles on this morphology, we performed AFM (as detailed in the experimental section 2.2.3). The S latex particles and D latex particles were highly diluted before drying in order to prepare sample with isolated dried particles. AFM images are reported in Appendix.

We measured the cross section of the flattened particles by AFM following a method represented in Figure 4. In order to compare the samples, we plotted their height profile, centered on their maximum and with a baseline shifted to 0. Figure 5 summarized the height profiles of the different single latex prepared with different amount of crosslinker and the double latex prepared with S0.5. We can see that the cross section decreases with crosslink content. This can be understood, as more crosslink content in S particles makes them less soft and less spreadable.

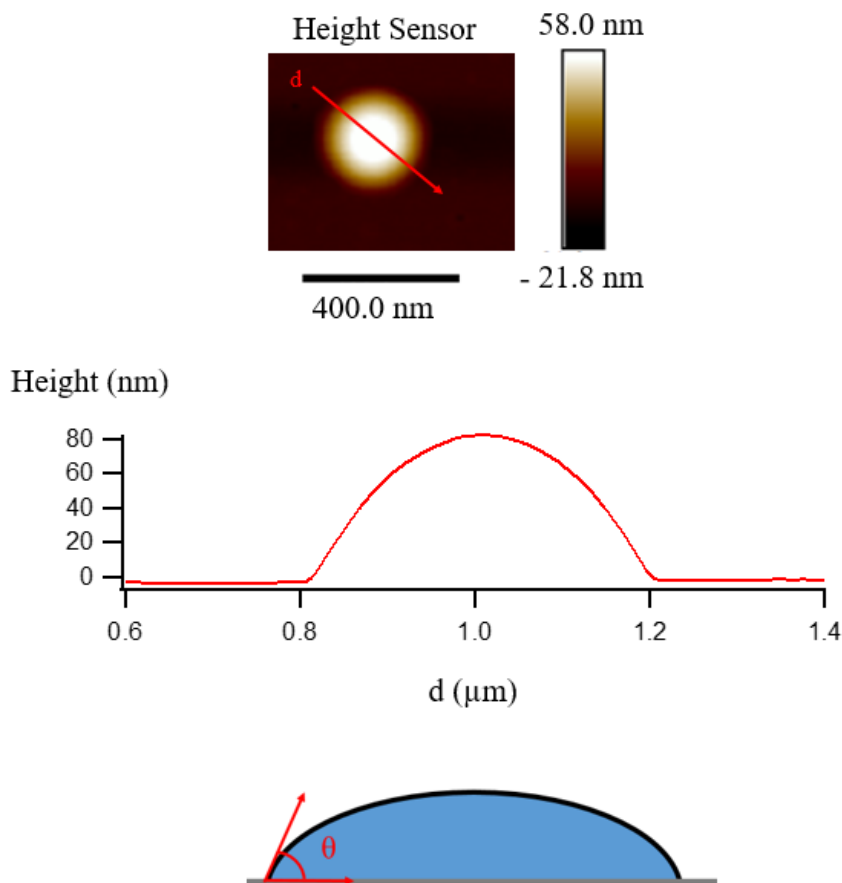


Figure 4 AFM image analyses from the image, to the height profile, to the contact angle.

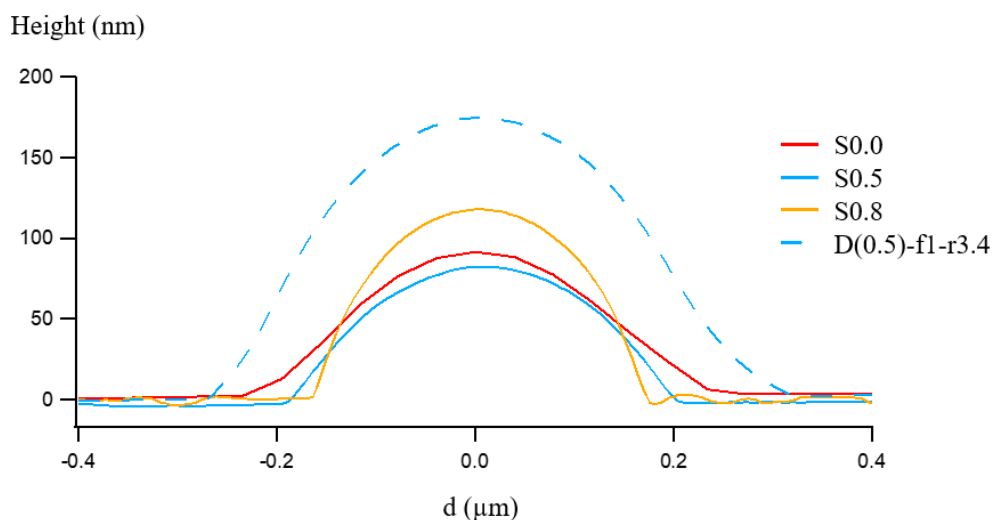


Figure 5 AFM height profiles of the dried particles S0.0, S0.5, S0.8 and D(0.5)-f1-r3.4

From Figure 5 we can estimate the contact angle of each particle on the surface. The results are reported in Table 6. It shows that the contact angle decreases with decreasing crosslinker molar percentage in the S particles, which is logical as the particles can spread more on a substrate when there is less crosslinker

in the network. The D particle's contact angle does not look as sharp as its seed particle S0.5 contact angle. It encourages us to believe that the D particle's structure is partially interpenetrated and some of the 2<sup>nd</sup> network, in the D particle, can diffuse through the 1<sup>st</sup> network on tens of nanometers.

*Table 6 Contact angle measured from AFM profiles*

Sample	Contact angle (°)
S0	16
S0.5	35
S0.8	59
D(0.5)-f1-r3.4	16

Only a few AFM images were taken for each samples. Because the latex particles can be quite polydisperse, it would be important to complete this work taking and analyzing a large quantity of images in order to confirm these observations.

## 1.2. Film formation and characterization

Macroscopically, the bulk double networks have been mechanically characterized and showed enhanced Young's modulus and strain hardening due to the random breakage of sacrificial bonds when the 1<sup>st</sup> network's pre-stretch was above 1.6. We can wonder whether D latex films benefit from the mechanical properties of each individual D particle (with the pre-stretched 1<sup>st</sup> network architecture). In the following section, we study the mechanical behavior of D latex particles assembly in the form of latex films.

### 1.2.1. Temperature effect on film formation

Before setting up the mechanical experiments, we had to find optimized conditions for the film formation. Indeed, the film formation is crucial for the future film's mechanical properties. It has been shown that the temperature can have an influence on the particles organization in the film [18]. In this section, we check the effect of temperature on the film drying process using D latex.

Generally, after slow evaporation for 3 days, at room temperature, transparent films were obtained. In order to finish the drying step, D(0.3)-f1-r1.3 presented in section 1.1.3 (Table 5) was dried following 2 methods (detailed in the experimental section 2.1.4): one pristine film was the dried under vacuum at room temperature for 10h, another one was dried for the same period of time under vacuum at 100 °C. The samples were then tested in uniaxial extension (detailed in the experimental section 2.2.5) and the results are plotted in the Figure 6.

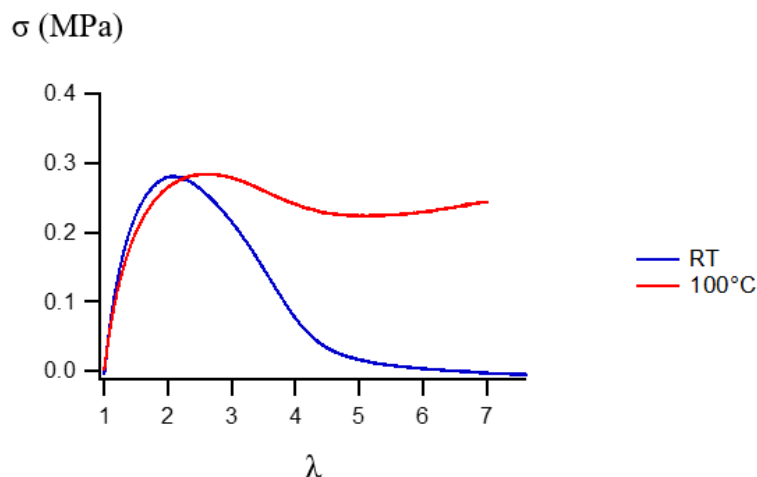


Figure 6 Effect of the drying temperature on the film's mechanical response

Figure 6 shows that at low deformation, the stress/modulus are not affected by the drying temperature. However, at higher deformation, there is a significant difference: the sample dried at 100°C (under vacuum) showed less softening than the sample dried (under vacuum) at room temperature. The temperature seems to improve the cohesion of the particles in the final film. This could be due to the effect of temperature on chain dynamics that improves inter-particles chain diffusion. At 100°C, the chains are more encouraged to diffuse from one particle to another leading to stronger interfaces between particles.

Therefore, in the following experiments for the film formation, drying at 100 °C was used as the standard method for all samples.

### 1.2.2. Comparison of D latex with the corresponding constituting single networks

Secondly, we want to understand the effect of the network architecture on the mechanical response of a double latex (D) particles assembly. To do so, we compared a classical D film with the single latex used as seed in its synthesis. In addition, we also used particles synthesized in the absence of BDA as reference as they should represent the properties of the second network alone. Both reference networks (first and second) were synthesized and dried separately, as represented in Figure 7.

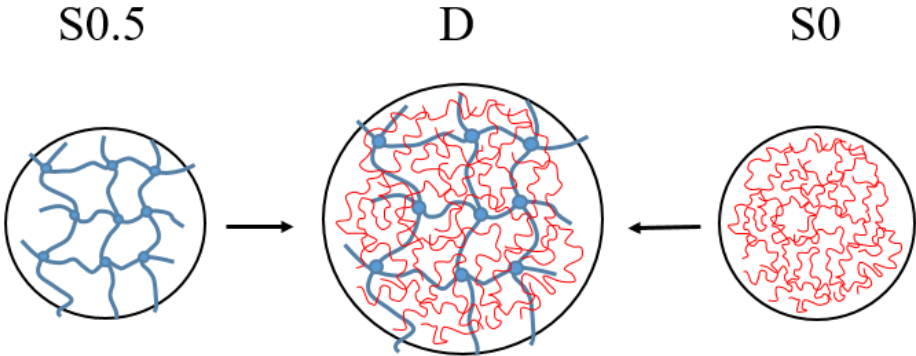


Figure 7 Schematic representation of the first single crosslinked network (S0.5 particle) and 2<sup>nd</sup> network alone (S0 particle) composing together a double latex (D) particle

We used the D(0.5)-f1-r1.4 latex film system (Table 3) and its 1<sup>st</sup> network S0.5, and we synthesized separately the 2<sup>nd</sup> network S0 by emulsion polymerization (see Table 1). All latexes were dried separately into macroscopic films. The films were tested mechanically with a tensile test machine following the process detailed section 2.2.5. Results are represented in Figure 8.

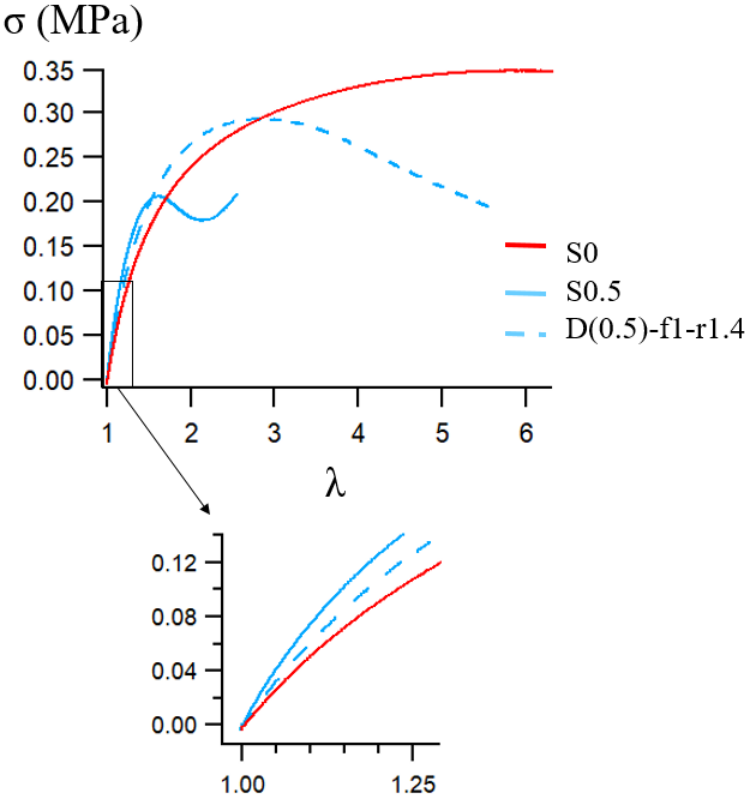


Figure 8 Stress-stretch curve of rectangular samples S0.5 (full line blue), D(0.5)-f1-r1.4 (dotted line blue) and S0 (red)

The D latex film shows a higher Young's modulus than the 2<sup>nd</sup> network S0 alone and higher extensibility than the seed latex S0.5 alone.

In order to verify the importance of structure within the D latex particle on the mechanical properties of the film, we mixed the matrix latex S0 with the seed latex S0.5 in the same ratio as in D(0.5)-f1-r1.4 (in a sample labeled S0.5/S0). This sample has a particular structure where all the 'matrix' is out of the seed particles and no connection exists between the 1<sup>st</sup> and the 2<sup>nd</sup> network. The results of the uniaxial extension test are reported in Figure 9.

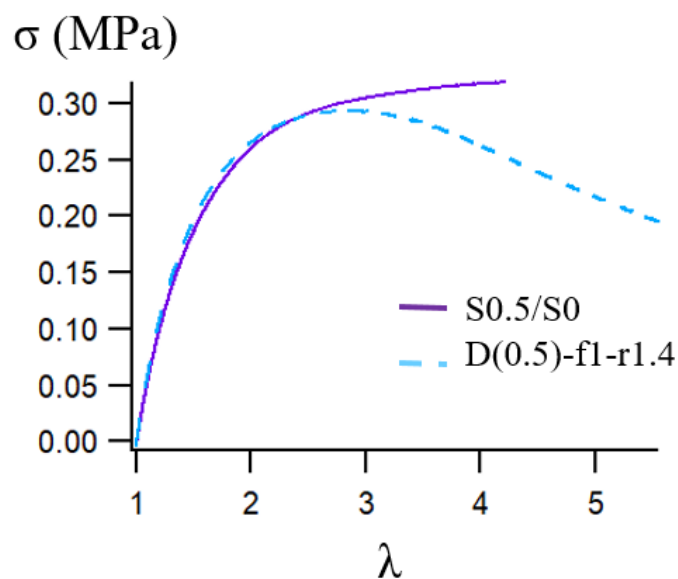


Figure 9 Effect of structure on the stress-stretch curve of dried D latex D(0.5)-f1-r1.4 (in blue) and a dried mix of seed latex and matrix S0.5/S0 (in purple)

The D latex film is less cohesive than in the 'worst case' scenario where all the 2<sup>nd</sup> network is outside of the 1<sup>st</sup> network, represented by the mix S0.5/S0. At higher extension, the D latex film softens whereas S0.5/S0 does not. This difference in behavior proves that the D latex, as it was synthesized, dries in a different structure than S0.5/S0. This shows that not all the 2<sup>nd</sup> network has polymerized outside of the seed particles in the D latex, and that the two networks should be interpenetrated in the particles.

However, Figure 9 shows that the D latex film does not demonstrate a higher Young's modulus than S0.5/S0. This was expected considering the ratio of 2<sup>nd</sup> network over the 1<sup>st</sup> network in the D latex (with  $r = 1.4$ ). This ratio is certainly too low to activate mechanical reinforcement, due to sacrificial bonds behavior observed in classical double network. The absence of toughening could also be a result of the soft particles interfaces: the particles are hardly interconnected because of the limited diffusion of chains between particles. Therefore, when the film is stretched, the soft chains in between particles will stretch first.

### 1.2.3. Effect of the crosslinking density in the S seeds on S and D films

As discussed before, the crosslinking density of a conventional polymer network has a strong impact on its mechanical properties mainly due to the variation of chain lengths between crosslinking points. We suppose that the mechanical behavior of single particles should follow the one of the conventional network, at the particle scale. However, we can wonder how the crosslink content in the S particles will affect the mechanical properties of the particles' film composed of a multitude of individual particles. Therefore, it is interesting to investigate the impact of the S crosslinking density effect on the D films mechanical properties, and to compare them to the corresponding films of S particles as references.

In order to study the effect of S crosslinking density on the mechanical properties of the S and D films, the latex S0.3, S0.5 and S0.8 and the latex D(0.3)-f1-r1.3, D(0.5)-f1-r1.4 and D(0.8)-f1-r1.3 (presented in 1.1.3) were dried following our standard drying process (as detailed in the experimental section 2.1.4) and then tested in uniaxial extension. Stress-stretch curves are represented Figure 10.

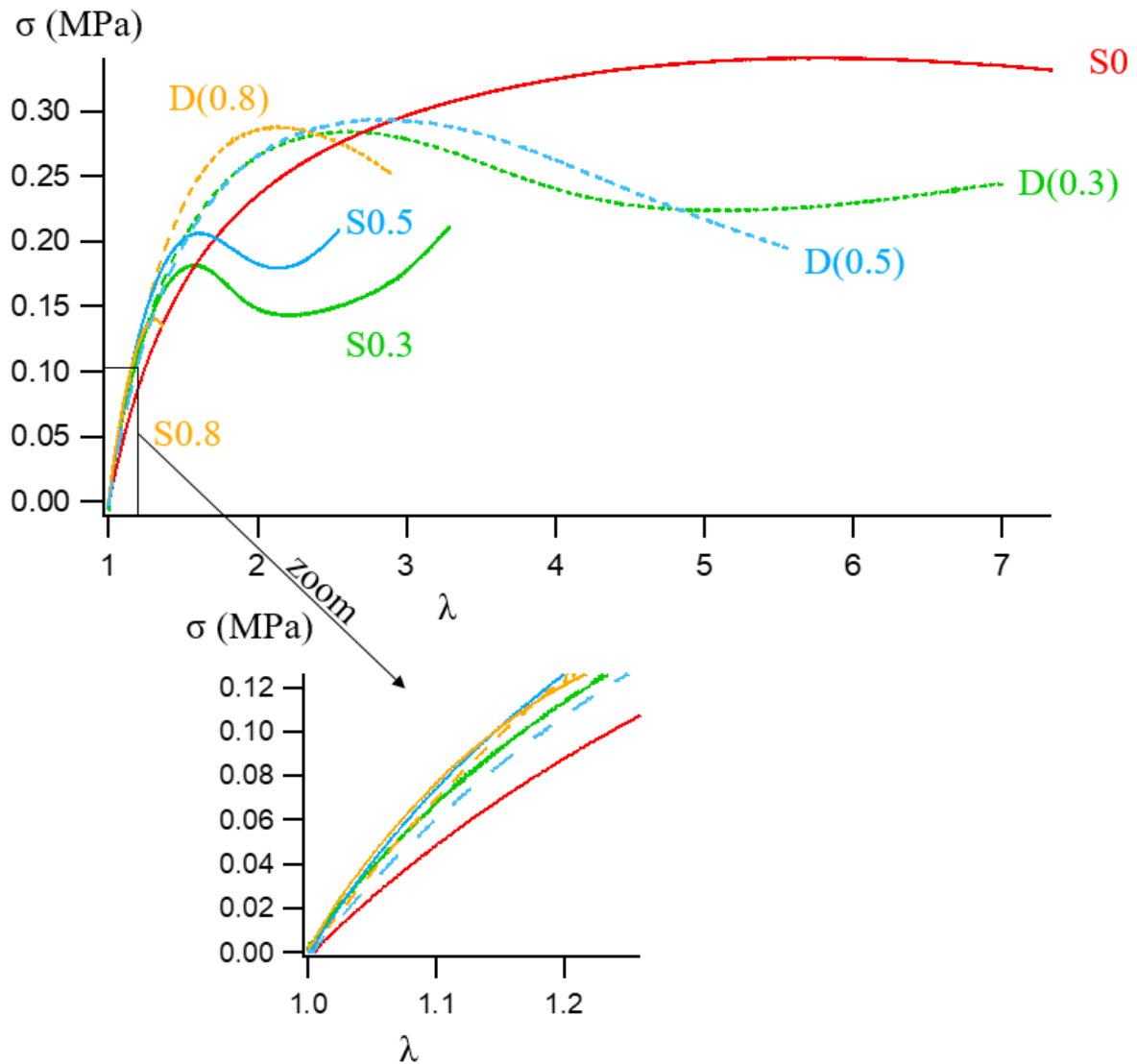


Figure 10 Uniaxial extension stress-stretch curve of rectangular sample cut from films of single latex in plain line S0 (red), S0.3 (green), S0.5 (blue), S0.8 (yellow) and their corresponding double latex D(0.3)-f1-r1.3, D(0.5)-f1-r1.4 and D(0.8)-f1-r1.3 in dotted line DL-1

From the Figure 10, we can see that increasing the crosslinking content in S improves slightly the S film Young's modulus. This behavior relates to the particles low strain stiffness, that increases with crosslink density.

In contrast, there is only little effect of the seed particles' crosslink density on the D films Young's modulus. All D films show a maximal stress followed by a softening that corresponds macroscopically to an inhomogeneous thinning of the material. This inhomogeneous deformation was not observed in S film with uncrosslinked particles, which deforms homogeneously even at high stretches. In this latter case, the particles' chains can interpenetrate fully forming a homogeneous network as almost no connection limits their diffusion. On the contrary, in the film formed from crosslinked S particles

(although lightly crosslinked), the particles come into contact with each other, but they cannot fully interpenetrate each other because of the crosslinking points. This leads to the creation of weaker interfaces between particles. Then during deformation, the particles deform first, before the dislocation of the film happens from the particles' interfaces.

The cartoon in Figure 11 illustrates the film formation and supposed structure of the D films. The crosslinked nature of the 1<sup>st</sup> network makes the particles non-interpenetrable. Upon drying, the particles get closer to each other. Then the chains of the second networks can diffuse, but only over a limited range because they are supposed to be connected to the rest of the network (through transfer reactions).

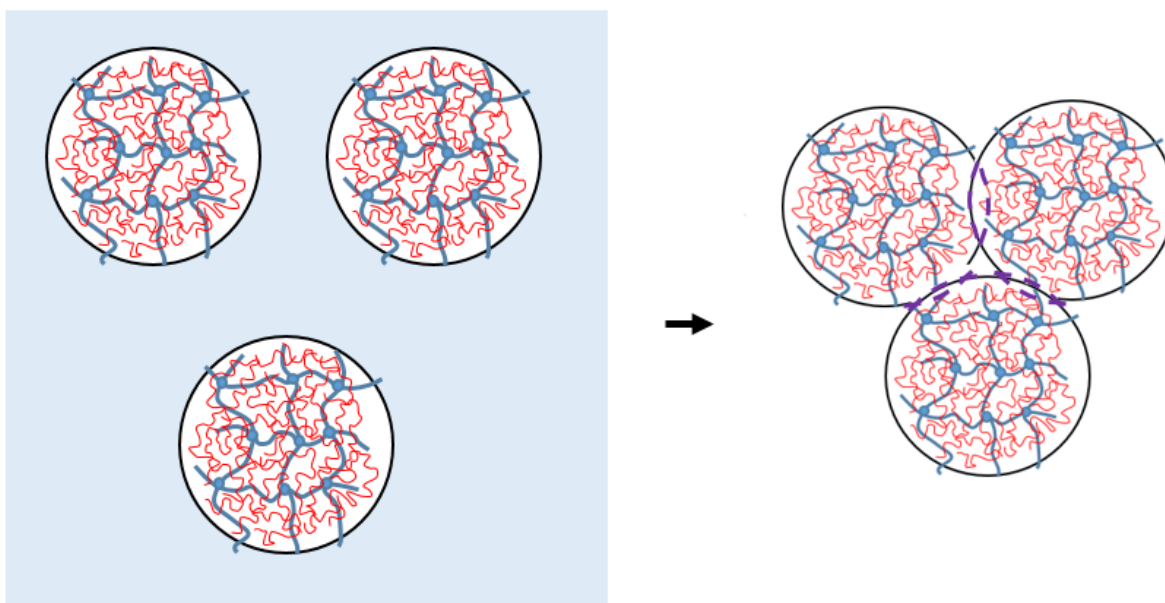


Figure 11 Schematic representation of the latex particles dispersed in water and compacted in the dry film. Weak interfaces between particles are represented in dotted purple lines.

Concerning the D films, we have seen from our previous experiments that the presence of a second uncrosslinked network polymerized within a first lightly crosslinked seed particles network does not give enough cohesion to the final material. The sample fails because of weak interfaces. That prompted us to search for strategies to reinforce the interfaces between individual particles in the film. One promising strategy to reinforce interface relies on the introduction of reactive co-monomers that allow to crosslink the particles after the drying step [19].

### 1.3. Connecting particles

#### 1.3.1. Presentation of the DAAM/ADH system

Diacetone acrylamide (DAAM) was selected as a co-monomer because it will introduce reactive ketone function groups in the particle network. Two ketone functions can be connected during the drying step by the addition of a bifunctional reactant, namely adipic acid dihydrazide (ADH) as shown in Figure 12, [20,21]. This can connect either two chains within the same particles or two chains in two different particles, thereby connecting the particles through hydrazone bonds, which should in fine lead to better cohesion in the film.

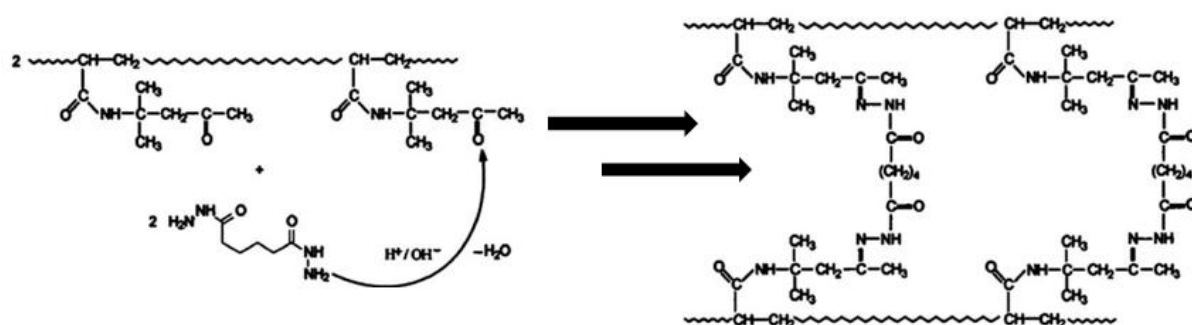


Figure 12 Schematic representation of the reaction between DAAM incorporated in a polymer chain with ADH in solution. Reproduced from [17]

#### 1.3.2. Effect of DAAM on S film

Before jumping to the functionalization of D particles with DAAM, we verified first the impact of the DAAM functionalization in simple S film. We therefore synthesized S particles containing low percentages of DAAM through the copolymerization of EA with DAAM in unseeded batch condition. We checked whether the introduction of DAAM affected the polymerization. Furthermore, we studied the films properties and in particular compared the mechanical behavior without and with the addition of ADH.

The S particles containing DAAM will be labeled as follows:



Where **x** corresponds to the mol% of BDA and **Y** corresponds to the mol% of DAAM

If a latex does not contain DAAM, the labeling system stays similar to the one used in the previous section of this chapter, that is **S<sub>x</sub>**, where **x** corresponds to the mol% of BDA.

Various S were synthesized following the process detailed in the experimental section 2.1.2, with 0.05 to 0.3 mol% DAAM added prior to the thermal initiation. The monomer composition (EA, DAAM and crosslinker ) can be found in the Table 7 below, all other reactants remained constant.

Table 7 Summary of synthesis parameters and characterization results of single latex, effect of DAAM molar concentration.

Name	Synthesis parameters		Characterization					
	mol% BDA	mol% DAAM	%conv	%agg	%solid	R (nm)	PDI	$N_p$ (m <sup>-3</sup> )
S0	0	0	100	0.8	26	113	0.01	3.84E+19
S0DAAM0.3	0	0.3	100	1.9	27	105	0.03	4.97E+19
S0.5ter	0.5	0	100	2.1	27	109	0.03	4.44E+19
S0.5DAAM0.05	0.5	0.05	100	0.7	27	122	0.02	3.17E+19
S0.5DAAM0.15	0.5	0.15	100	1.5	27	116	0.01	3.69E+19
S0.5DAAM0.3	0.5	0.3	96	3.1	26	102	0.02	5.22E+19

c(KPS) = 3.63 mmol/L; c(SDS) = 3.63 mmol/L; monomer = 0.200 mol; T = 60°C; t = 3h

The results in the Table 7 show that the molar percent of DAAM does not significantly affect the synthesis of the S. In all cases, monomer conversions close to quantitative were obtained and the particle diameter ranged from 210 nm to 244 nm, which no clear trend concerning the content of DAAM.

The latexes were dried into films following our standard drying process (described in the experimental section 2.1.4). Then, tensile tests were performed on rectangular samples cut from the dried film using a punch.

We tested first the effect of DAAM in a film of un-crosslinked S particles (0% BDA) dried with or without ADH. The stress-stretch behavior of a S film with 0.3 mol% of DAAM (S0DAAM0.3) dried with or without ADH (0.5 molar equivalent<sup>\*\*</sup>) and a reference S film without DAAM (S0) are reported in Figure 13.

<sup>\*\*</sup> Molar equivalent (eq.) with respect to the molar number of DAAM: X eq. = n(DAAM)/n(ADH)

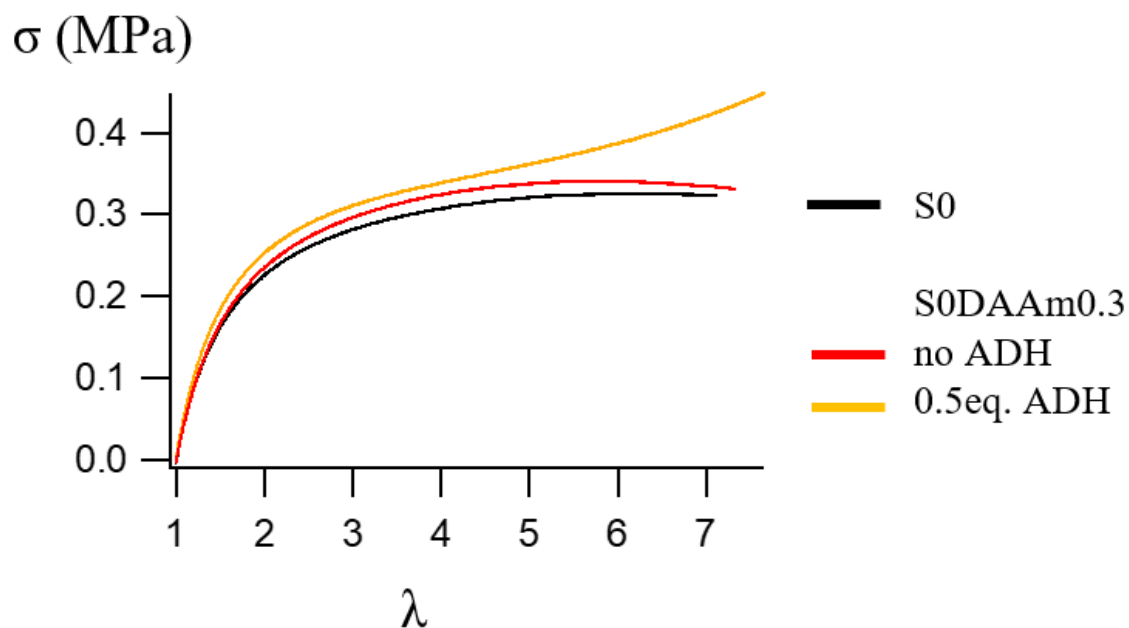


Figure 13 Stress-stretch curve of S0 (black), S0DAAm0.3 without ADH (red) and with ADH (yellow)

As can be seen on the stress-stretch plots in the Figure 13, the addition of 0.3 mol% of DAAM without ADH does not affect the mechanical behavior of the film, as was expected. When 0.5 eq. ADH were added, increased mechanical properties can be noticed at higher extension: While the film softens at high stretches in the absence of ADH, in the presence of ADH, a slight strain hardening is observed at high extension, which indicates that covalent bonds were introduced between individual chains through the connection of DAAM units by ADH, as desired.

In addition, we also varied the quantity of DAAM in crosslinked S particles and dried the films without ADH or with ADH (0.5 eq.). The results of the tensile tests are presented in Figure 14.

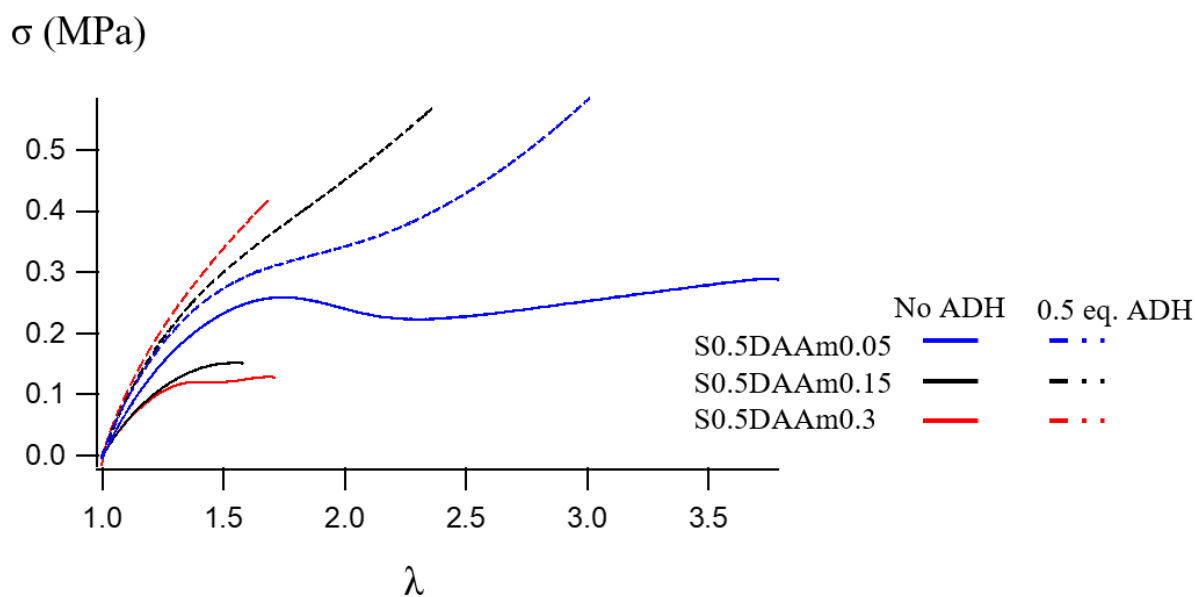


Figure 14 Stress-stretch curve of S0.5DAAm0.05 (blue), S0.5DAAm0.15 (black) and S0.5DAAm0.3 (red) without ADH (full line) and with ADH (dotted line).

Surprisingly, the molar percentage of DAAM has an effect on the mechanical properties of the crosslinked S particles films dried without ADH. They show different stress/stretch behavior and demonstrate different stress/stretch at break, despite the absence of connection between DAAM functions. Concerning the films without ADH, S0.5DAAm0.05 is much more deformable than S0.5DAAm0.15 and S0.5DAAm0.3, containing 0.15 and 0.3 mol% of DAAM respectively. Therefore, we may conclude that the presence of DAAM, even in very low amount, seems to affect the mechanical properties of crosslinked S particles films even without adding ADH during the drying step.

In the presence of ADH, independently of the amount of DAAM, the S films do not longer soften at high stretch, neither do they present early breakage. The modulus at low strain increases with the quantity of DAAM while the stretch at break decreases with the quantity of DAAM. Their mechanical behavior resembles the one of a conventional crosslinked elastomer network. Connections must therefore have been created between particles due to the reaction of DAAM with ADH.

Until then, the added quantity of ADH was kept constant at 0.5 eq. with respect to DAAM. We finally checked the effect of the variation of the number of equivalent of ADH relative to DAAM on the mechanical properties of a S0.5DAAm0.15 film. The results of the uniaxial extension tests are presented in Figure 15.

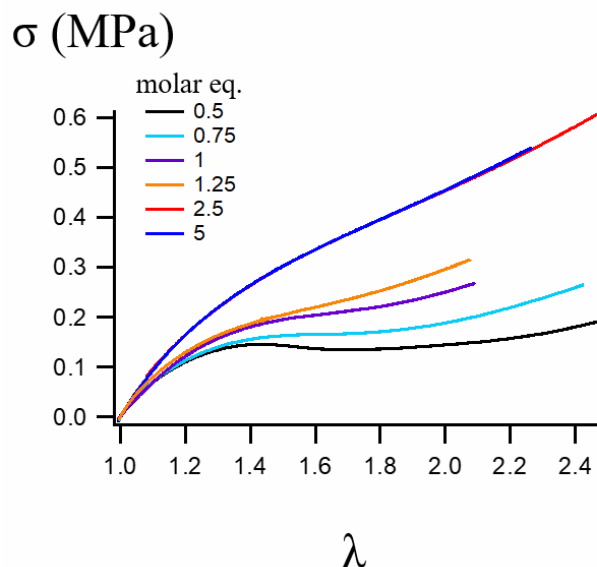


Figure 15 Stress-stretch curve of S0.5DAAm0.15 dried with varying quantity of ADH from 0.5 to 5 molar equivalent.

Figure 15 shows that increasing the amount of ADH strengthened the films (made of S particles with 0.15 mol% of DAAM), up to an optimal stress-stretch behavior, which was reached between 1.25 and 2.5 eq. ADH). Nevertheless, we noticed that the dried films became less transparent and whitened as the molar equivalent of ADH was increased above 1.25. Therefore, despite the positive effect on the mechanical properties in the presence of high quantities of ADH, we decided to dry the samples containing DAAM with the 0.5 eq. of ADH, which actually corresponds to the mole number which is theoretically necessary to connect all DAAM units.

It should be reminded here, that - in order to connect the D particles - it is possible to introduce DAAM as a co-monomer in the 1<sup>st</sup> network or in the 2<sup>nd</sup> network. The following section will successively present the results for both approaches.

It is not excluded that DAAM in the seed particles is preferentially present at the surface of the particle because of the high water solubility of DAAM [22]. This possible heterogeneous distribution of DAAM in the particles may affect the swelling of the particles during the second polymerization step. In order to simplify the system, we will present first the situation where DAAM is introduced in the 2<sup>nd</sup> network. Then, we will study D films with DAAM in the seed particles.

1.3.3. Connecting the particles through the 2<sup>nd</sup> network

- **DAAm in the 2<sup>nd</sup> network**

Figure 16 is a schematic representation of the introduction of the DAAm during the seeded emulsion polymerization to functionalize the 2<sup>nd</sup> network. It starts with (i) the synthesis of the crosslinked seed particle (1<sup>st</sup> network in blue), followed by (ii) the swelling of the particle with EA (in red) and DAAm (in green), and (iii) the polymerization of the EA and DAAm. Finally, (iv) the D particles functionalized with DAAm are dried in the presence of ADH, which creates hydrazine bonds between the particles' 2<sup>nd</sup> networks (light green).

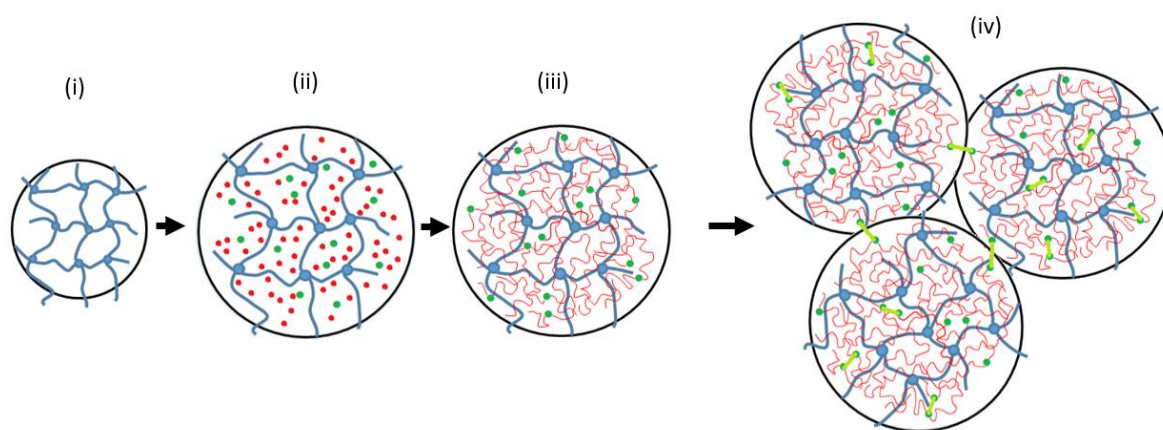


Figure 16 Schematic representation of DAAm (green dots) in double latex during the second polymerization step and the possible connections of DAAm with ADH (n light green) intra and inter-particles.

The sample will be labeled as follows:

$$D(\mathbf{x})\text{-f}\mathbf{y}\text{-r}\mathbf{z}\text{-(m)}$$

Where  $\mathbf{x}$  corresponds to the molar percentage of the crosslinker in the seed latex ( $S\mathbf{x}$ ),  $\mathbf{y}$  corresponds to the feed rate in mL/h,  $\mathbf{z}$  represents the mass ratio of added monomer (in total) over the initial mass of polymer seed particles in the latex, and  $\mathbf{m}$  refers to the composition of the 2<sup>nd</sup> network (which will be labeled  $S\mathbf{m}$ , when it was synthesized separately, *i.e.* without the seeds).

Four different D latex D(0.5)-f1-r1.4-(0DAAmX) were synthesized following the process reported in the experimental section 2.1.3, where increasing amounts of DAAm - from 0.07 to 3.0 mol% - were added in the water phase prior to initiation. Composition and characterization results can be found in Table 8.

Table 8 Summary of synthesis parameters and characterization results on double latexes where the 2<sup>nd</sup> network is functionalized by DAAM

Name	Synthesis parameters	Characterization								
	%mol <sub>DAAM</sub>	%conv	%agg	%solid	R (nm)	PDI	$\lambda_{th}$	$\lambda$	$N_p$ (m <sup>-3</sup> )	$\Delta N_p^{\dagger\dagger}$
S0.5ter diluted				9	109	0.03			1.48E+19	
D(0.5)-f1-r1.4	0	88	3.5	17	143	0.03	1.1	1.2	1.35E+19	-13%
D(0.5)-f1-r1.4-(0DAAM0.07)	0.07	91	4.7	17	141	0.02	1.3	1.2	1.45E+19	-9%
D(0.5)-f1-r1.4-(0DAAM0.3)	0.3	93	1.7	18	139	0.02	1.3	1.2	1.39E+19	-2%
D(0.5)-f1-r1.4-(0DAAM1.0)	1	96	10.6	18	145	0.01	1.3	1.3	1.28E+19	-6%
D(0.5)-f1-r1.4-(0DAAM3.0)	3	83	5.9	17	144	0.11	1.3	1.3	1.35E+19	-13%

Seed latex, feed rate,  $r_{i,a,m}^a$ ,  $r^b$ , surfactant and initiator concentrations, polymerization time and temperature were kept constant.

<sup>a</sup>  $r_{i,a,m} = m(\text{monomer before initiation})/m(\text{latex particles})$ . <sup>b</sup>  $r = m(\text{monomer})/m(\text{latex particles})$ .

$r_{i,a,m} = 35\%$ ;  $r = 1.4$ ;  $f = 1\text{ mL/h}$ ;  $T = 65\text{ }^\circ\text{C}$ ;  $t = 3.5\text{ h}$ ;  $C(\text{SDS}) = 1.21\text{ mmol/L}$ ;  $(\text{AIBN}) = 1\text{ mol\%}$

From Table 8, we notice that the presence of DAAM in the second polymerization step can exacerbate the formation of aggregates during the polymerization of the 2<sup>nd</sup> network. Up to 10.6 % of aggregates were formed, which is more than two times the percentage of aggregates in a D latex without DAAM. The size of the particles was very similar for all experiments and did not vary with the DAAM content. It seems that the presence of DAAM does not affect the creation of secondary nanoparticles. The results are all quite puzzling, because even if the percentage of aggregates was taken into account in the estimation of the number of particles, the values remain negative, meaning that particles were lost during the second polymerization step. As presented in section 1.1.3, this can be the result of experimental errors.

After polymerization we dried a standard latex D(0.5)-f1-r1.4-(0DAAM0.3) with 0.5 eq. ADH (relative to the molar content of DAAM) and performed tensile tests on rectangular pieces cut from the film. The comparison of the results with two references, first, an uncrosslinked S latex containing the same amount

<sup>††</sup> The error from the particles size measurements affects a lot the precision of the estimated number of particles. Therefore, the following discussions and conclusions based on the evolution of the number of particles shouldn't be much considered.

of DAAM - S0DAAM0.3 (Table 7) which is similar to the 2<sup>nd</sup> network alone, and, second, S0.5ter (Table 7), similar to the 1<sup>st</sup> network alone, are represented in the Figure 17 below. Compared to either of the two reference samples, which represent either the corresponding 1<sup>st</sup> or the 2<sup>nd</sup> network alone, we can observe that D(0.5)-f1-r1.4-(0DAAM0.3) shows improved mechanical behavior with a strain hardening at deformations above 3 (Figure 17).

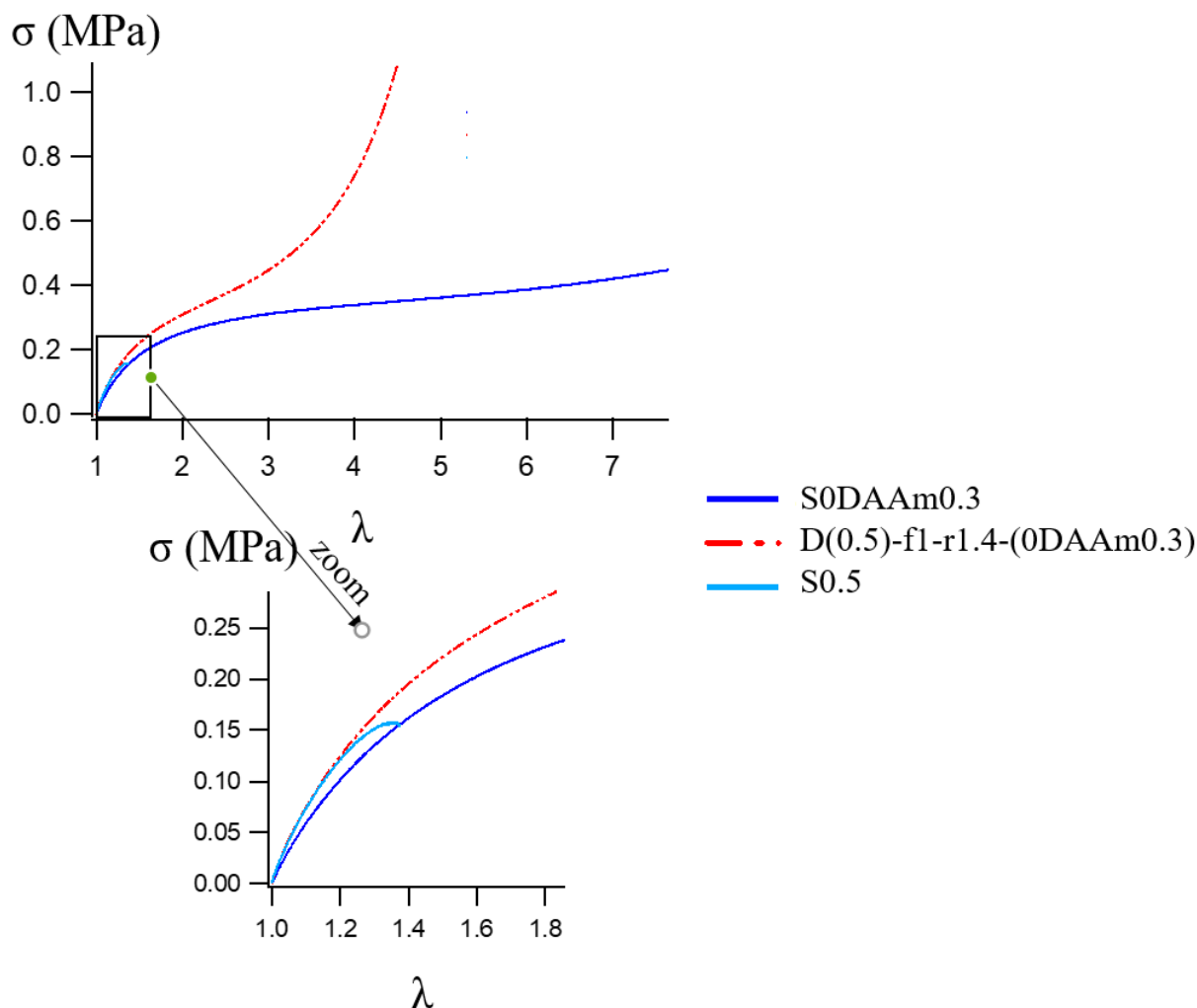
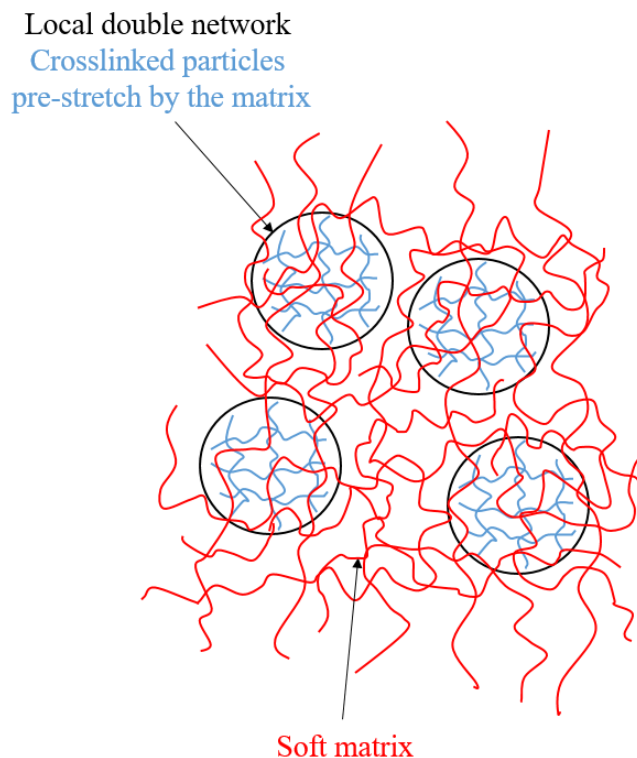


Figure 17 Effect of network structure. Uniaxial extension tests on a D(0.5)-f1-r1.4-(0DAAM0.3) film dried with ADH (red) compared to the 2<sup>nd</sup> network alone corresponding to S0DAAM0.3 dried with ADH (dark blue) and the 1<sup>st</sup> network alone corresponding to S0.5ter (light blue)

This behavior resembles to that of the nanocomposites discussed in Chapter 2 reinforced by soft particles, which corresponds to the association of crosslinked particles embedded in a crosslinked matrix as schematized in Figure 18. However, within the D films, the concentration of 1<sup>st</sup> network particles in the 2<sup>nd</sup> network can reach higher ratios than with the previous process developed in Chapter 2 (that was limited by the gelation of monomers and particles mix involved in the second polymerization step).



*Figure 18 Schematic representation of nanocomposite filled with soft particles.*

In order to assess the impact of the quantity of DAAM in the 2<sup>nd</sup> network, we progressively increased the quantity of DAAM from 0.03 mol% to 3 mol% in the D, following the same polymerization process and characterized the D films mechanical properties by uniaxial tensile tests (at 20 °C and a strain rate of  $3.33 \times 10^{-2} \text{ s}^{-1}$  details in section 2.2.5). The results are presented in Figure 19.

Figure 19 shows that the D film functionalized with DAAM in the 2<sup>nd</sup> network does not soften as the former D(0.5)-f1-r1.4, but on the contrary, the sample strain hardens, presumably thanks to the presence of connections between particles created by the reaction between DAAM ketone groups and ADH.

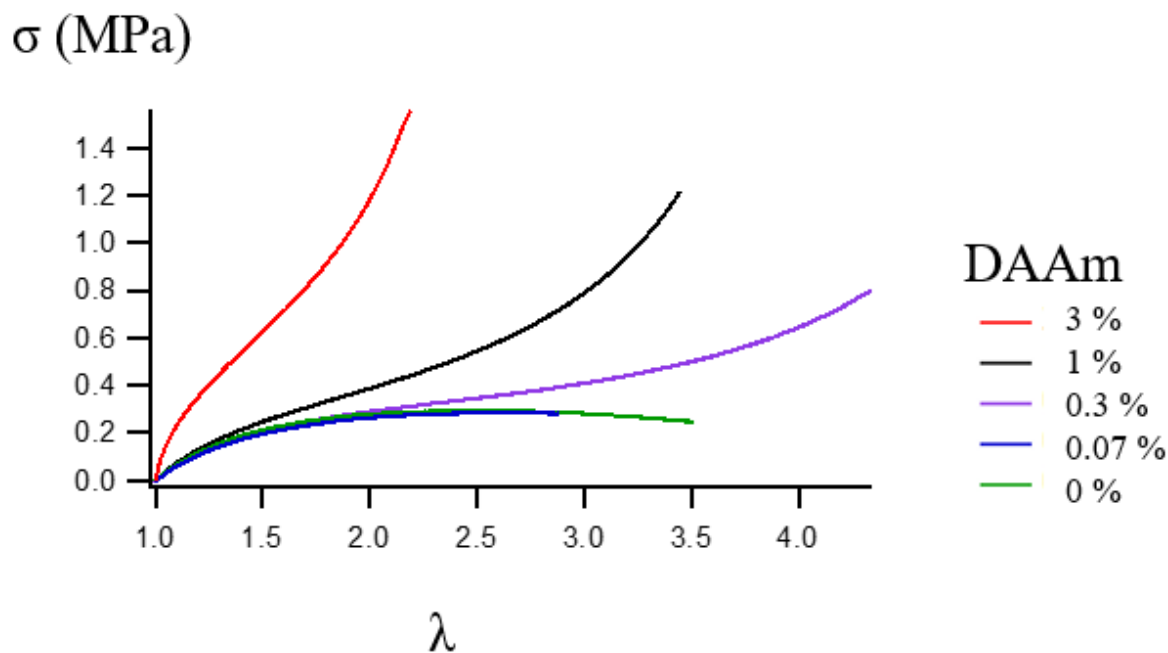


Figure 19 Effect of DAAm quantity (X) in the 2<sup>nd</sup> network of D(0.5)-f1-r1.4-(0DAAmX) films dried with ADH (0.5 eq.)

For the samples containing the lowest quantity of DAAm (0.05 mol%), no effect was observed compared to the DAAm-free sample. Increasing the amount of DAAm from 0.3 to 3 mol% results in a strain-hardening occurring for lower extension together with a slight increase in the Young's modulus.

In order to understand whether or not D films behave similarly to bulk double networks [17], we varied the pre-stretch of the 1<sup>st</sup> network by varying the ratio between the 2<sup>nd</sup> and the 1<sup>st</sup> network,  $r$ . To increase the amount of monomer added, we adapted the polymerization process, and added a higher total amount of monomers (EA and DAAm) during the second polymerization step by increasing the feed rate, keeping all other parameters constant.

Table 9 Summary of synthesis parameters and characterization results of double latex D(0.5)-f<sub>x</sub>-r<sub>y</sub>-(0DAAm1.0)

Name	Synthesis parameters		Characterization								
	f (mL/h)	r	%conv	%agg	%solid	R (nm)	PDI	λ <sub>th</sub>	λ	N <sub>p</sub> (m <sup>-3</sup> )	ΔN <sub>p</sub> <sup>‡</sup>
S0.5ter diluted					9	109	0.03			1.48E+19	
D(0.5)-f1-r1.4-(0DAAm1.0)	1	1.4	96	10.6	18	145	0.01	1.3	1.3	1.39E+19	-6%
D(0.5)-f2-r3.1-(0DAAm1.0)	2	3.1	85	32.4	25	163	0.03	1.6	1.4	1.63E+19	10%

The seed latex S0.5 and the composition of the 2<sup>nd</sup> network S0DAAm1.0, initiator and surfactant concentrations, polymerization time and temperature were kept constant:

C(SDS) = 1.21 mmol/L ; %(AIBN) = 1 mol% ; T = 65 °C ; t = 3.5 h

The results are summarized in Table 9. Increasing the ratio (r) of 2<sup>nd</sup> network over 1<sup>st</sup> network, from 1.4 to 3.1, led to the formation of a high amount of aggregates (32.4 % instead of 10.6 %). This was expected, as in the former results (without DAAM) a significant effect of the ratio of 2<sup>nd</sup> network over 1<sup>st</sup> network (r) was observed on the formation of aggregates (section 1.1.3).

In these latter experiments, the calculated pre-stretch was only increased from 1.3 to 1.4. The pre-stretches reached are not very different because of the high number of aggregates combined to the low conversion reached in D(0.5)-f2-r3.1-(0DAAm1.0) (the theoretical pre-stretch is given as if the conversion was equal to 100 %). If we take into account the conversion, then the theoretical pre-stretch becomes 1.4 and equals the experimental value. Nonetheless, we prepared films from the D reported in Table 9, and measured their mechanical properties by uniaxial extension (at 20 °C and strain rate  $3.33 \times 10^{-2} \text{ s}^{-1}$ ) (shown in Figure 22).

<sup>‡‡</sup> The error from the particles size measurements affects a lot the precision of the estimated number of particles. Therefore, the following discussions and conclusions based on the evolution of the number of particles shouldn't be much considered.

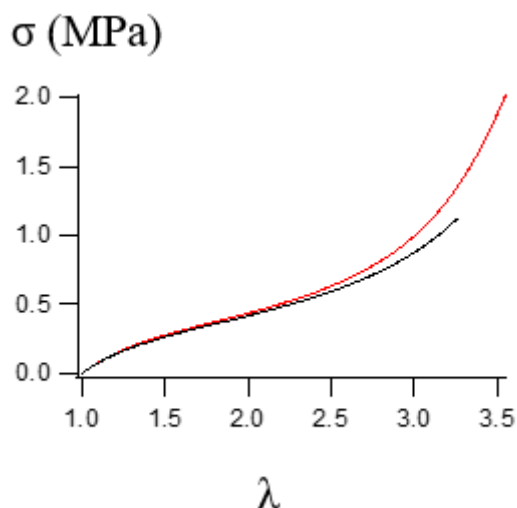


Figure 20 Effect of the pre-stretch on D(0.5)-fx-y-(0DAAm1.0). The red curve corresponds to the D(0.5)-f1-r3.1-(0DAAm1.0) which  $\lambda = 1.4$  and the black curve corresponds to the D(0.5)-f1-r1.4-(0DAAm1.0) with  $\lambda = 1.3$ .

Figure 22 shows that the stress-stretch are very similar between the two samples, the Young's moduli are equivalent but there is a slightly earlier strain hardening for the D latex with the highest seed network pre-stretched. The similarities can be due to the similar experimental pre-stretch of the 1<sup>st</sup> network in the particles.

Both samples pre-stretches remain below the values, for which the pre-stretch had a noticeable positive effect on bulk double networks stress-stretch behavior (expected to be at  $\lambda=1.5$ ). Nevertheless, there is a visible reinforcement of the D films compared to D films without DAAM.

- **DAAm in the 1<sup>st</sup> network**

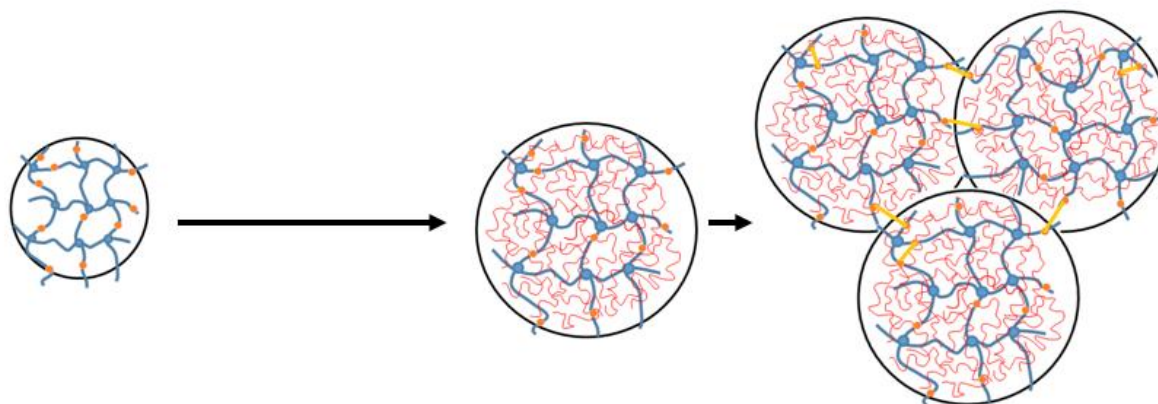


Figure 21 Schematic representation of DAAM (orange dots) in double latex added during the first polymerization step and the possible inter-particles connections of DAAM with ADH (in yellow).

In this second series of experiments, DAAM was introduced as a co-monomer in the 1<sup>st</sup> network during the synthesis of the seed particles. It should be kept in mind that:

- DAAM is highly water-soluble and much more hydrophilic than EA (DAAM is very soluble in water up to 5.92 mol/L and EA is soluble only at 0.0015 mol/L [22]) and might therefore be preferentially localized at the surface of the seed particle rather than in their core. The resulting inhomogeneous distribution of DAAM units in the latex particles might actually be favorable for the crosslinking step and favor interparticle-crosslinking compared to intraparticle crosslinking (occurring within individual particles).
- According to the small quantities of DAAM present in the 1<sup>st</sup> network, we do not expect that the introduction of DAAM will change much how the monomer diffuses inside the particles and how the particle swells during the second polymerization step.

In the final D, the DAAM units in the 1<sup>st</sup> networks should be able to interconnect the particles while the 2<sup>nd</sup> networks (in each particles) should still be able to diffuse in between particles, as represented in Figure 21. If successful, the resulting film should present a higher Young's modulus and result in a stronger film than the ones without DAAM and the ones with DAAM in the 2<sup>nd</sup> networks.

First, we used the S functionalized with 0.05 and 3 mol% of DAAM as seed latex (synthesized as already reported in section 1.3.2):

Table 10 Summary of synthesis parameters and characterization results on single latex functionalized with DAAM. Effect of DAAM molar concentration.

Name	Synthesis parameters	Characterization					
	%mol <sub>DAAM</sub>	%conv	%agg	%solid	R (nm)	PDI	N <sub>p</sub> (m <sup>-3</sup> )
S0.5DAAM0.05	0.05	100	0.7	27	122	0.02	3.16E+19
S0.5DAAM3	3	100	0.7	27	90	0.01	7.89E+19

T = 65 °C ; t = 3.5 h ; n(EA) = 0.200 mol ; %(BDA) = 0.50 mol% ; c(KPS) = 3.63 mmol/L; c(SDS) = 3.63 mmol/L

From these seed latexes, D were obtained following the standard process (detailed in section 2.1.3). The latex composition and the characterization results are summarized in Table 11.

Compared to the D synthesis without DAAM, the presence of DAAM in the seed latex slightly increased the percentage of aggregates from 3.5 % (without DAAM) to 5-6 % (with DAAM, values in Table 11). The conversion of the monomer in the second polymerization, D(0.5DAAM0.05)-f1-r1.4-(0), was lower than for the two other samples, probably only due to experimental error or oxygen contamination in the reactor.

No effect of DAAM was observed on the pre-stretch ( $\lambda$ ). This confirms that  $\lambda$  is controlled by the weight fraction of 2<sup>nd</sup> network ( $r$ ) and not by the seed network functionalization, as expected.

Table 11 Summary of synthesis parameters and characterization parameters of D(0.5DAAMX)-f1-r1.4(0). Effect of DAAM molar concentration in the 1<sup>st</sup> network.

Name	Synthesis parameters	Characterization								
	seed latex	%conv	%agg	%solid	R (nm)	PDI	$\lambda_{th}$	$\lambda$	$N_p$ (m <sup>-3</sup> )	$\Delta N_p$ <sup>§§</sup>
S0.5				9	109	0.03			1.48E+19	
S0.5DAAM0.05				9	122	0.02			1.06E+19	
S0.5DAAM3				9	90	0.01			2.63E+19	
D(0.5)-f1-r1.4-(0)	S0.5	88	3.5	17	143	0.03	1.1	1.2	1.28E+19	-13%
D(0.5DAAM0.05)-f1-r1.4-(0)	S0.5DAAM0.05	66	5	16	145	0.03	1.3	1.2	1.17E+19	11%
D(0.5DAAM3)-f1-r1.4-(0)	S0.5DAAM3	100	5.8	19	114	0.02	1.3	1.3	2.89E+19	10%

Feed rate,  $r_{i.a.m}^a$ ,  $r^b$ , formulation of the 2<sup>nd</sup> network, initiator and surfactant concentrations, polymerization temperature and time were kept constant.

<sup>a</sup>  $r_{i.a.m}$  = m(monomer before initiation)/m(latex particles). <sup>b</sup>  $r$  = m(monomer)/m(latex particles).

$r_{i.a.m}$  = 35 %;  $r$  = 1.4;  $f$  = 1mL/h;  $T$  = 65 °C;  $t$  = 3.5 h;  $C(SDS)$  = 1.21 mmol/L; (AIBN) = 1 mol%

The latex were dried with 0.5 eq. ADH and tested mechanically as detailed in the experimental section 2.2.5. The stress-stretch curves are reported in Figure 22.

Figure 24 shows that a low DAAM concentrations of 0.05 mol% in the seed network does not affect the mechanical behavior of D film compared to a standard film prepared without DAAM. This result goes against the effect observed in Figure 14, where we saw that 0.05 mol% of DAAM in a single latex dried with ADH showed enhanced stress and modulus. The absence of effect of the presence of DAAM in the 1<sup>st</sup> network in the case of D particles film, should be due to the 2<sup>nd</sup> network in between particles that makes the connection between two DAAM less likely to happen.

In contrast, the presence of 3 mol% DAAM in the seed network brings more cohesion to the final material, with a higher Young's modulus and higher stress at break compared to samples without DAAM.

<sup>§§</sup> The error from the particles size measurements affects a lot the precision of the estimated number of particles. Therefore, the following discussions and conclusions based on the evolution of the number of particles shouldn't be much considered.

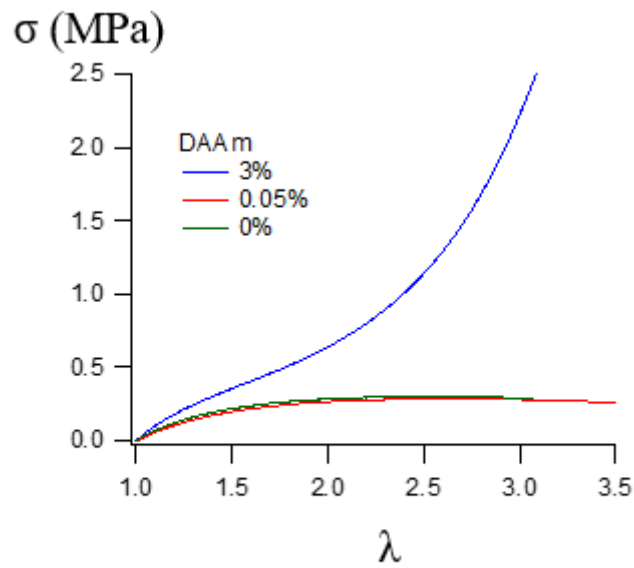


Figure 22 Effect of the quantity of DAAm in the 1<sup>st</sup> network of double latex dried with ADH 0.5 eq.

In order to increase the pre-stretch of the 1<sup>st</sup> network, a third latex was synthesized targeting a higher weight fraction ( $r$ ) of the 2<sup>nd</sup> network. We therefore increased the monomer feed rate to reach higher weight fraction of 2<sup>nd</sup> network in the same amount of time.

The synthesis parameters and the characterization results are reported in Table 12.

Table 12 Effect of pre-stretch on double latex film functionalized with DAAM in the seed latex.

Name	Synthesis parameters		
	seed latex	f (mL/h)	r <sup>a</sup>
D(0.5DAAM3)-f1-r1.4-(0)	S0.5DAAM3	1	1.4
D(0.5DAAM3)-f2-r2.9-(0)	S0.5DAAM3	2	2.9

Name	Characterization								
	%conv	%agg	%solid	R (nm)	PDI	$\lambda_{th}$	$\lambda$	$N_p$ (m <sup>-3</sup> )	$\Delta N_p^{***}$
D(0.5DAAM3)-f1-r1.4-(0)	100	5.8	19	114	0.02	1.3	1.3	2.89E+19	10%
D(0.5DAAM3)-f2-r2.9-(0)	80	9.1	23	126	0.03	1.6	1.4	2.67E+19	2%

Seed latex,  $r_{i.a.m}^b$ , 2<sup>nd</sup> network formulation and polymerization time and temperature remain constant.

<sup>a</sup>  $r = m(\text{monomer})/m(\text{latex particles})$ . <sup>b</sup>  $r_{i.a.m} = m(\text{monomer before initiation})/m(\text{latex particles})$ .

T = 65 °C ; t = 3.5 h ; C(SDS) = 1.21 mmol/L ; (AIBN) = 1 mol%

From the Table 12, we notice that the percentage of aggregates is higher for D(0.5DAAM3)-f2-r2.9-(0) than for D(0.5DAAM3)-f1-r1.4-(0). For these two samples, both the weight fraction of 2<sup>nd</sup> network and the feed rate were modified. However, we saw, in the section 1.1.3, that increasing feed rates did not cause the creation of aggregates in the seeded emulsion polymerization (Table 3). In addition, we also learned that increasing the weight fraction of 2<sup>nd</sup> network increased the amount of aggregates (at constant feed rate, Table 4). Therefore, we believe that the increase in aggregates can be explained here again by the increased weight fraction of 2<sup>nd</sup> network. We can however not exclude that the polymerization kinetics are much slower than then the monomer feed rate and swelling kinetics.

Unfortunately, the experimental pre-stretch reached for D(0.5DAAM3)-f2-r2.9-(0) did not meet the theoretical values (expected for %conv = 100 %), and the pre-stretch for both samples was similar ( $\lambda = 1.3$  or 1.4, see Table 12).

\*\*\* The error from the particles size measurements affects a lot the precision of the estimated number of particles. Therefore, the following discussions and conclusions based on the evolution of the number of particles shouldn't be much considered.

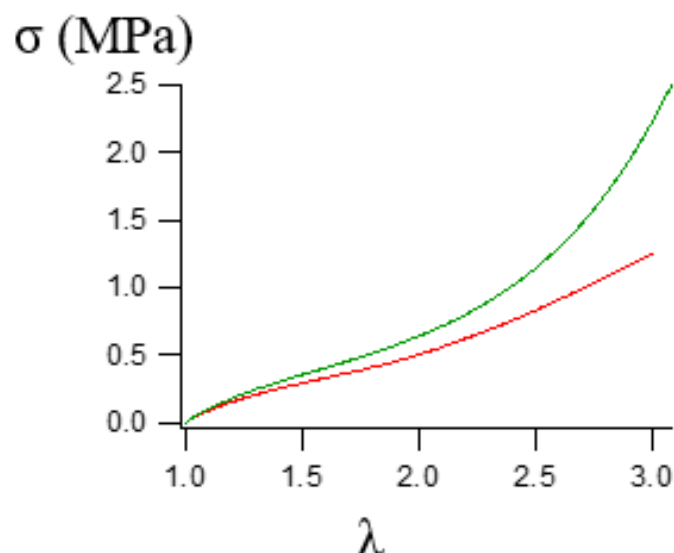


Figure 23 Effect of the prestretch. Red curve  $D(0.5DAAm3)-f2-r2.9-(0)$  with  $\lambda = 1.4$ , and green curve  $D(0.5DAAm3)-f1-r1.4-(0)$  with  $\lambda = 1.3$ .

The samples from Table 12 were tested in uniaxial extension (as described in the experimental part section 2.2.5). The results are presented in Figure 23.

They show that the Young's moduli are not much affected by the pre-stretch of the seed network. On the other hand, the weight fraction of the 2<sup>nd</sup> network seems to affect the mechanical behavior at high stretches: The strain hardening happens for higher stretches in the sample with the highest quantity of added 2<sup>nd</sup> network, and the stress at break is also lower for this sample. This indicates that a higher fraction of the 2<sup>nd</sup> network in D latex makes the film softer. This behavior is actually the opposite to what is expected from the conventional bulk double network, where increasing proportion of 2<sup>nd</sup> network leads to stiffer material. A possible explanation may come from modifications at the particles interfaces. For example, increasing weight fractions of 2<sup>nd</sup> network, increase the risk of polymerizing outside of the particles. If the layer of soft network around the particle grows, then it becomes more difficult to bridge two particles together because of thicker layer between particles as represented in Figure 24.

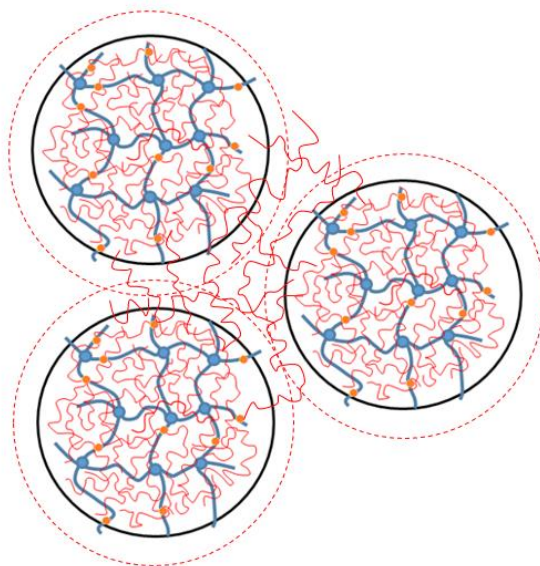


Figure 24 Representation of the potential layer of 2<sup>nd</sup> network

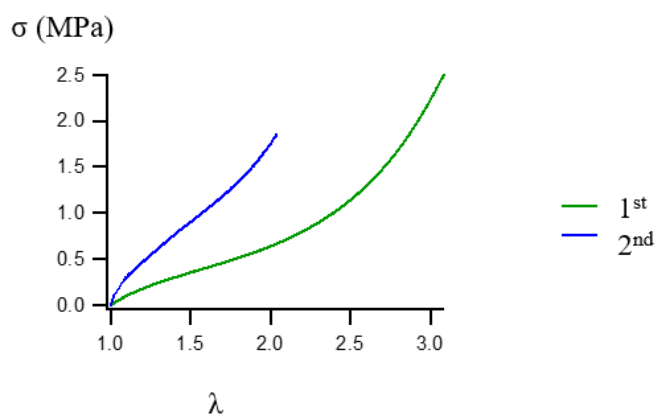


Figure 25 Comparison of D latex functionalized with DAAM in their 1<sup>st</sup> network (green)  $D(0.5DAAM3)-f1-r1.4-(0)$  or 2<sup>nd</sup> network (blue)  $D(0.5)-f1-r1.4-(0DAAM3)$  dried with 0.5 eq. ADH

Finally, we compared the mechanical properties of D latex functionalized by 3 mol% of DAAM either in the 1<sup>st</sup> network or in the 2<sup>nd</sup> network as represented in Figure 25. It shows that connecting the 2<sup>nd</sup> network leads to higher Young's modulus and strain hardening at lower stretches. This result was unexpected, as we expected that connecting the strongest network would make the film stronger. However, as presented in Figure 24, a layer of soft un-functionalized matrix may be sitting around the particles, which presumably limits the possibility of connecting the seed networks.

## Conclusion

In this work, we looked for a new aqueous route for the synthesis of soft materials with a double network structure within each particles.

We studied the synthesis of latex IPN through two different processes (a batch and a semi-batch) with the aim to make D particles with the same structure as conventional bulk double networks. This implies that a first crosslinked network should be pre-stretched by a second (loosely crosslinked or uncrosslinked) network, with high proportion of 2<sup>nd</sup> network.

Making such interpenetrated particles with a great volume fraction of 2<sup>nd</sup> network in emulsion polymerization is difficult, mainly because the monomer swelling is limited in particles surrounded by water due to elastic forces and the second polymerization has the risk to occur outside of the particles: either (i) around the particle, which would result in a core-shell structure instead of an interpenetrated double network, or (ii) in the water phase, resulting in formation of new (un-crosslinked) particles in the aqueous phase.

We have found that to reach a high fraction of the 2<sup>nd</sup> network, the simple seeded *batch* polymerization process is limited due to the saturation concentration of monomer within crosslinked particles in water. Therefore, to reach higher volume fractions of the 2<sup>nd</sup> network, we switched to a *semi-continuous* seeded emulsion polymerization and investigated the effect of the feed rate, the weight fraction of the 2<sup>nd</sup> network and the crosslinking density of the 1<sup>st</sup> network on the synthesis of D particles.

We have found little to no effect of the feed rates between 1 mL/h and 2.5 mL/h. Increasing the fraction of the 2<sup>nd</sup> network tends to destabilize our emulsion system and lead to aggregates, while increasing the crosslinking density from 0.3 to 0.8 mol% in the seed particles led to pronounced undesired secondary nucleation.

We dried the latex into films of D particles to study their mechanical properties and found that the interfaces between particles in D films were stronger than in a crosslinked S films but still needed some reinforcements to activate the double network sacrificial bond mechanism.

Therefore, we functionalized the D particles either in the 1<sup>st</sup> or 2<sup>nd</sup> network by DAAM in order to introduce ketone groups that could be crosslinked by reaction with dihydrazides during the drying of the latex. By adding ADH, a dihydrazide, in the latex before drying, we could connect the DAAM functions, and therefore, connect chains between particles through the formation of hydrazone linkages. The D particles functionalized with DAAM and connected by ADH showed enhanced mechanical properties, no softening at higher extensions and even a strain hardening behavior at higher extensions.

When DAAM is introduced into the 2<sup>nd</sup> network, the structure of the film and its mechanical behavior actually resemble to the one of the previous nanocomposite system presented in Chapter 2. Nevertheless,

this new polymerization process is more ecofriendly, safer and faster than the previous bulk process as it all happens in water, the swelling and the polymerization occur at the same time. In addition, it is fully compatible with common processes used in the industry to prepare coatings.

Finally, aggregations and secondary nucleation observed for the addition of higher 2<sup>nd</sup> network contents limits the pre-stretch of the 1<sup>st</sup> network. Successive semi-continuous or successive batch polymerization could solve these limitations, but this could also exacerbate the presence of a soft 2<sup>nd</sup> network layer around the particles because this layer would swell more easily than the rest of the particles, enhancing a sort of semi core-shell structure. Increasing the concentration of surfactant continuously during the semi-continuous polymerization process through continuous SDS addition together with the monomer, should help stabilizing the newly created particle surfaces and prevent particle aggregations.

## 2. Experimental part

### 2.1. Synthesis

#### 2.1.1. Chemicals and reagents

Ethyl acrylate (EA, Aldrich, 99%), 1,4-butanediol diacrylate (BDA, Aldrich, 90%), potassium persulfate (KPS, Aldrich,  $\geq 99\%$ ), azobisisobutyronitrile (AIBN, Aldrich, 98%), sodium dodecyl sulfate (SDS, Aldrich,  $\geq 99\%$ ), diacetone acrylamide (DAAm, Aldrich, 99%), adipic acid dihydrazide (ADH, Aldrich, 98%) were used as reagents. EA and BDA were purified through an alumina column before use. Water was purified and deionized before use.

All the synthesis described were performed under nitrogen atmosphere because oxygen could inhibit the radical polymerization. To that purpose, all reactant and reaction mixture were bubbled with nitrogen before use.

#### 2.1.2. Synthesis of the “Single latex” (S) by emulsion polymerization

The first step of the fabrication of a double network (D) latex consists in the polymerization of the 1<sup>st</sup> network called single latex (S). The single latexes are obtained in a free radical emulsion polymerization as described in Chapter 2 section 2.2.1 using again KPS as initiator, BDA as crosslinker, but a lower concentration of surfactant (SDS).

Typically (latex S0.5), in a 100 mL sealed round bottom flask, EA (20.00 g, 3.63 mol/L) and BDA (0.198 g, 18.2 mmol/L, 0.5 mol%<sup>†††</sup>) as crosslinker were mixed in ultrapure water (55.00 g) containing dissolved SDS (0.0576 g, 3.63 mmol/L, 0.1 mol%1) and an aqueous initiator KPS (0.0540 g, 3.63 mmol/L, 0.1 mol%1). The mix was stirred by magnetic stirring, during 3h at 60 °C.

The polymerization was quenched by opening the reactor and the latex was stored at room temperature.

---

<sup>†††</sup> The mol% ratio of a compound X corresponds to the molar quantity of the compound X over the molar quantity of monomer, as follows:  $mol\% = \frac{n_X}{n_{EA}} \times 100$

### 2.1.3. Synthesis of the “Double latex” (D) by seeded emulsion polymerization

In order to synthesize the double network latex (D), the seed latex (S) was diluted (1 volume of latex in 2 added volumes of water) and then swollen with the monomer containing an organic initiator (AIBN). The polymerization of these monomers occurs inside of the swollen network.

The polymerization step was then performed in two different ways, either in a batch or in a semi-continuous process, which are detailed below

#### *Seeded batch emulsion polymerization*

In the seeded batch process, the total amount of the monomer was added at once, prior to the initiation of the polymerization. The process is represented in a scheme in Figure 26. As a first step, the seed latex is diluted to keep the final targeted solid content below 30% during all the next steps. The second step corresponds to the addition of the monomer and initiator. At this step, we let the mix at rest for 10 h for the monomer to diffuse into the particles. The third step consists in the thermal initiation of the polymerization at 65 °C. The initiation was only done when all monomer no monomer could be observed as a separate phase.

The formulation of a typical batch polymerization is described below (Sample D(0.5)b1.0):

In a 100 mL sealed round bottom flask, a mixture of EA (2.5 g, 25.0 mmol) with AIBN (1 mol%, 0.25 mmol, 41.0 mg) was added to the seed latex (10 g; 26% solids) diluted in water (20 g). The mix was stirred for 30 min to homogenize to mix and let to rest overnight to let the monomer diffuse into the seed particles. Then the solution was heated to 65 °C under magnetic stirring at approximately 1000 rpm for 3h. The polymerization was quenched by opening of the reactor and the latex was stored in at room temperature.

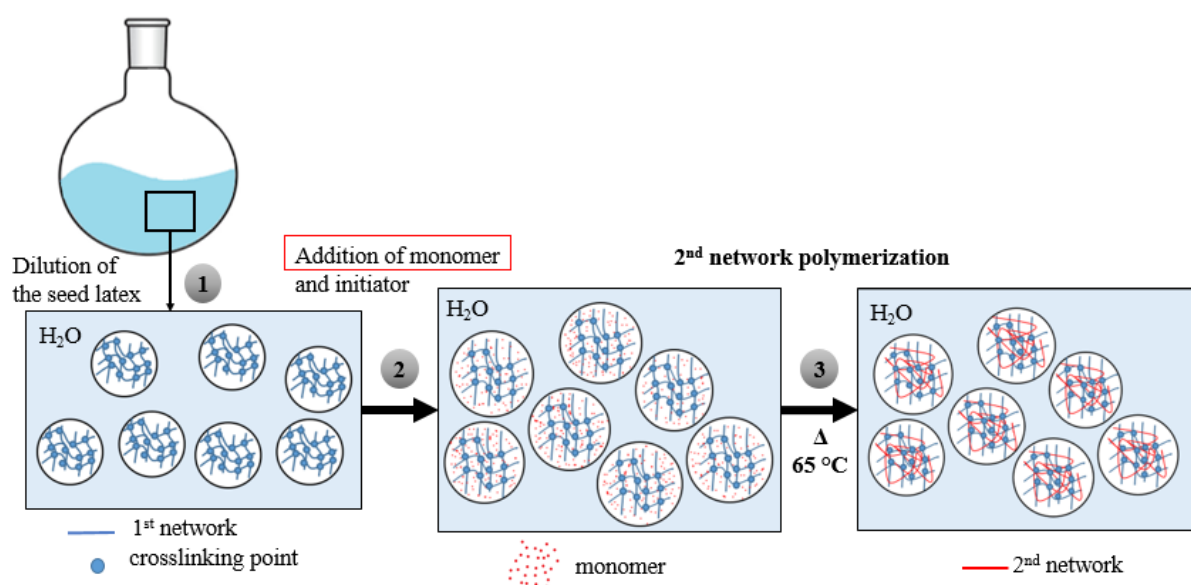


Figure 26 Schematic representation of the batch polymerization process for the synthesis of the double latex particles.

*Seeded semi-continuous emulsion polymerization*

Double network particles were also synthesized via a seeded semi-continuous process, which consist in the continuous addition once the polymerization has been initiated in particles containing an initially small quantity of monomer and initiator. The process is schematically represented Figure 27. In a first step (as for the batch process), the seed latex is diluted to prevent the solid content to overpass 30% at the end of the process. In a second step, a small quantity of monomer and initiator is added to the mix and 20 min are let for the monomer to diffuse into the particles. This step is important to encourage this initiation to occur in the organic phase inside the particles. In a third step, the polymerization is thermally initiated at 65 °C. After 10 min, when the temperature is stabilized, a monomer feed is injected continuously inside the reactor using an automatic syringe pump. In a final fifth step, once enough monomer has been added to polymerize the 2<sup>nd</sup> network, the pump is stopped.

A typical formulation of double latex (latex D(0.5)-f1-r1.3 in section 1.1.3) obtained following a seeded semi-continuous emulsion polymerization is detailed below:

In a 100 mL sealed round bottom flask, the seed latex (10.00 g) was diluted in water (20.00 g). A solution of EA (1.00 mL, 10.9 mmol) and AIBN (0.109 mmol, 17.9 mg) was added to the diluted seed latex. The mix was stirred for 20 min to let the monomer diffuse into the particles. Then it was set in an oil bath at 65 °C. After 10 min, 3.0 mL EA was continuously added to the sealed reactor using an automatic syringe pump at the feed rate of 1 mL/h for 3 h. The reaction medium was stirred by magnetic stirring at approximately 1000 rpm. After the pump has been stopped, the polymerization continued for 20 min before opening of the sealed flask. The latex was stored in a closed vial at room temperature.

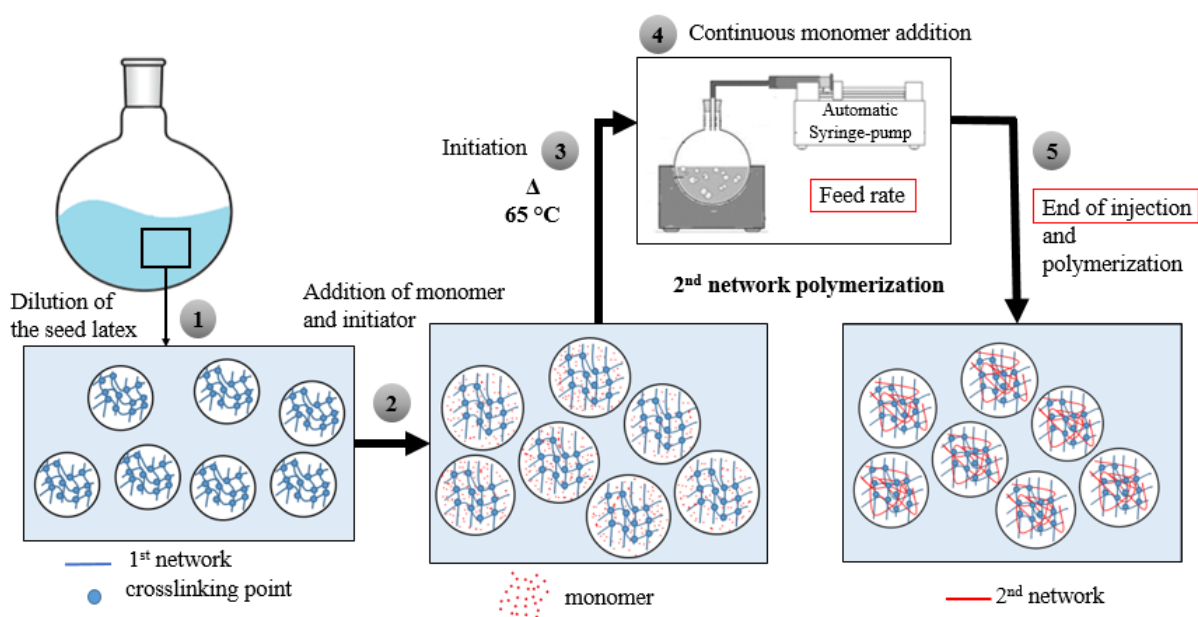


Figure 27 Schematic representation of the semi-continuous polymerization process of double latex

#### 2.1.4. Drying process

In order to be able to test the mechanical properties of a macroscopic sample, the latex were dried into films of thickness around 1 mm.

To do so, 10 mL of latex were dried in rectangular silicone molds (2.8 cm wide by 7 cm long) at room conditions until the sample turned from a white liquid to a transparent solid. The sample was further dried under vacuum overnight at room temperature or at 100 °C to fully remove any traces of adsorbed water (or residual monomer).

### 2.2. Characterization methods

#### 2.2.1. Gravimetric analysis

Refer to Chapter 2 section 2.3.1.

#### 2.2.2. DLS

Refer to Chapter 2 section 2.3.2.

DLS is used to determine the size distribution profile of small particles in suspension based on their Brownian motion. A laser beam hits the moving particles in suspension and the light is scattered. This light speckle is recorded as a function of time. From Brownian motion induced by thermal agitation, the light interferences can be analyzed by an autocorrelation function. A characteristic decay time of the autocorrelation function can be extracted. The relaxation time (inverse of the characteristic decay time  $\tau$ ) is related to the diffusion coefficient  $D$  and the wave vector  $q$  as:

$$\frac{1}{\tau} = 2Dq^2$$

And finally, the Stokes-Einstein equation gives the particles averaged hydrodynamic radius  $R_H$ :

$$R_H = \frac{k_B T}{6\pi\eta_S D}$$

Where  $k_B$  is the Boltzmann constant and  $\eta_S$  is the solution viscosity, and  $T$  is temperature at which the measurement was done.

#### 2.2.3. AFM

Highly diluted latexes were dried on glass slide, then rinsed with ultrapure water and dried again with nitrogen. AFM tests were performed with an ICON Dimension microscope, Nanoscope V, equipped with a tap300 AFM tip from Nanoandmore of frequency 300 kHz and rigidity 40 N/m, in tapping mode.

AFM images were taken with the help of Bruno Bresson at SIMM lab.

#### 2.2.4. CryoTEM

4  $\mu\text{L}$  of diluted latex (1 wt%) was deposited onto a carbon copper grid and blotted before being instantly frozen in liquid ethane. Images were taken at  $-180\text{ }^{\circ}\text{C}$  with a transmission electron microscope (TEM) JEOL JEM 2100 LaB6 operating at 200 keV. The digital images were collected with a Gatan Ultrascan 1000 CCD camera.

#### 2.2.5. Mechanical tests

Tensile tests were performed as presented in Chapter 2 section 2.3.4 with a difference on the sample shape. To optimize material economy, tensile tests were performed on rectangular sample. This should be kept in mind in the discussion as stress concentrates under the clamps and rectangular samples have a tendency to break under the clamp at lower stress and strain than dumbbell shaped samples for the same material.

## Appendix

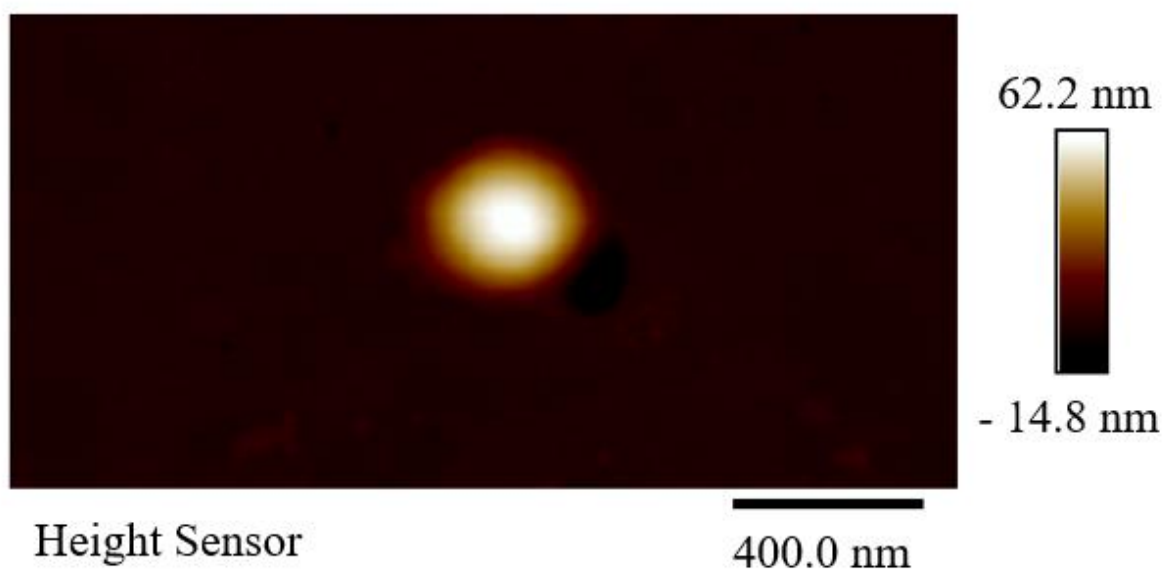


Figure 28 AFM image of a S0.0 dried particle

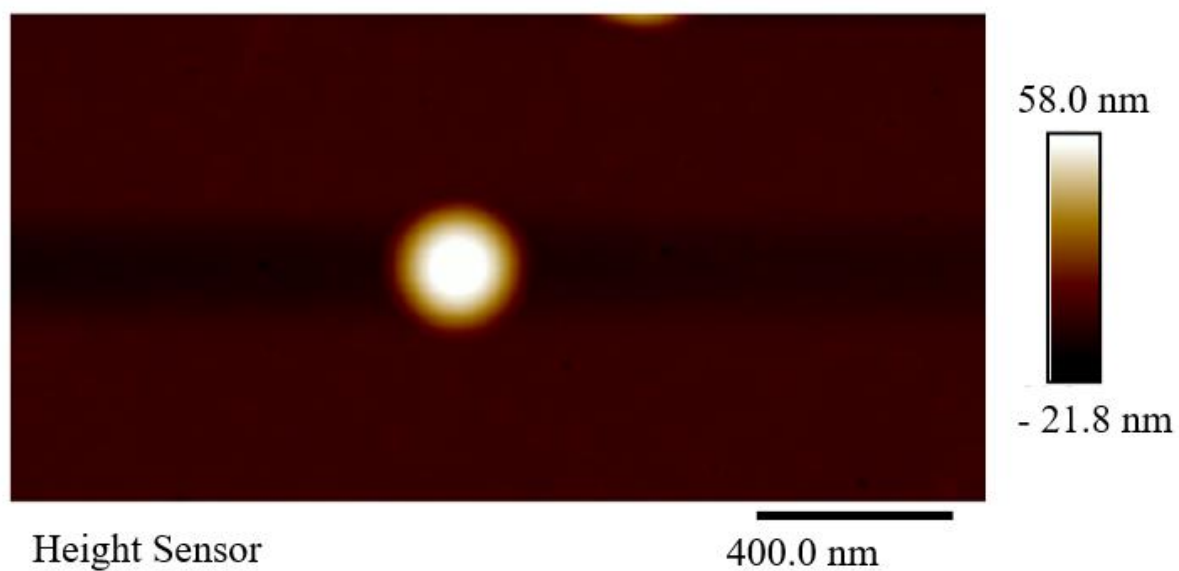


Figure 29 AFM image of a S0.5 dried particle

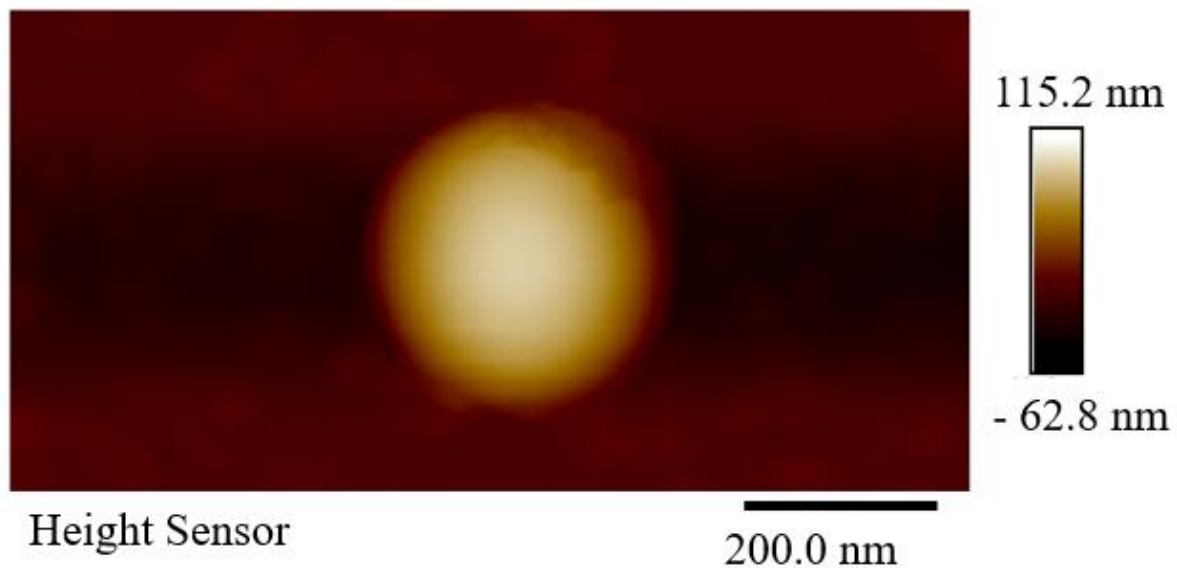


Figure 30 AFM image of a S0.8 dried particle

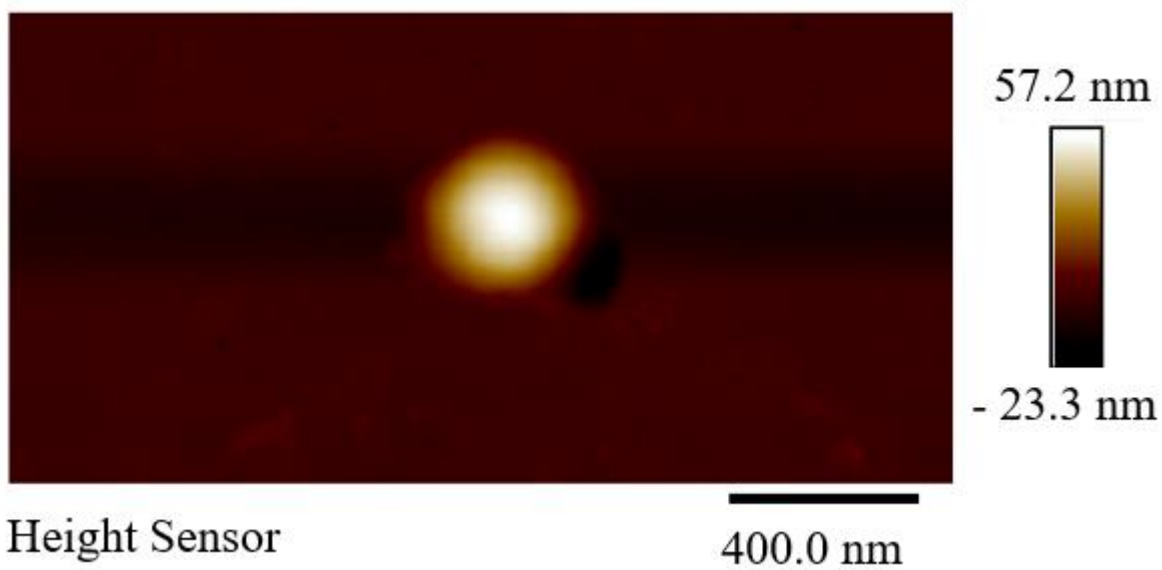


Figure 31 AFM image of a D(0.5)-f1-r3.4 dried particle

## References

1. Gong, J. P., Katsuyama, Y., Kurokawa, T. & Osada, Y. Double-Network Hydrogels with Extremely High Mechanical Strength. *Advanced Materials* **15**, 1155–1158 (2003).
2. Gong, J. P. Why are double network hydrogels so tough? *Soft Matter* **6**, 2583 (2010).

3. Ducrot, E., Chen, Y., Bulters, M., Sijbesma, R. P. & Creton, C. Toughening Elastomers with Sacrificial Bonds and Watching Them Break. *Science* **344**, 186–189 (2014).
4. Gong, J. P. Materials both Tough and Soft. *Science* **344**, 161–162 (2014).
5. Lipatov, Y. S. & Alekseeva, T. T. Phase-Separated Interpenetrating Polymer Networks. in *Phase-Separated Interpenetrating Polymer Networks* vol. 208 1–227 (Springer Berlin Heidelberg, 2007).
6. Muroi, S., Hashimoto, H. & Hosoi, K. MORPHOLOGY OF CORE-SHELL LATEX PARTICLES. *Journal of polymer science. Part A-1, Polymer chemistry* **22**, 1365–1372 (1984).
7. Okubo, M., Yamada, A. & Matsumoto, T. Estimation of morphology of composite polymer emulsion particles by the soap titration method. *J. Polym. Sci. Polym. Chem. Ed.* **18**, 3219–3228 (1980).
8. Okubo, M., Katsuta, Y. & Matsumoto, T. STUDIES ON SUSPENSION AND EMULSION. LI. PECULIAR MORPHOLOGY OF COMPOSITE POLYMER PARTICLES PRODUCED BY SEEDED EMULSION POLYMERIZATION. *Journal of polymer science. Part B, Polymer letters* **20**, 45–51 (1982).
9. Cho, I. & Lee, K. -W. Morphology of latex particles formed by poly(methyl methacrylate)-seeded emulsion polymerization of styrene. *Journal of Applied Polymer Science* **30**, 1903–1926 (1985).
10. Min, T. I., Klein, A., El-Aasser, M. S. & Vanderhoff, J. W. MORPHOLOGY AND GRAFTING IN POLYBUTYLACRYLATE-POLYSTYRENE CORE-SHELL EMULSION POLYMERIZATION. *Journal of polymer science. Part A-1, Polymer chemistry* **21**, 2845–2861 (1983).
11. Silverstein, M. S. Interpenetrating polymer networks: So happy together? *Polymer* **207**, 122929 (2020).
12. Limpanichpakdee, P. T. Synthesis and mechanical properties of elastomers made by sequential-IPNs.
13. Millereau, P. M. Large Strain and Fracture of Multiple Network Elastomers. (Paris 6, 2017).
14. Sheu, H. R., El-Aasser, M. S. & Vanderhoff, J. W. Phase separation in polystyrene latex interpenetrating polymer networks. *J. Polym. Sci. A Polym. Chem.* **28**, 629–651 (1990).
15. Fick, A. V. On liquid diffusion. *null* **10**, 30–39 (1855).

16. Ducrot, E. Innovative tough elastomers : designed sacrificial bonds in multiple networks. (Paris 6, 2013).
17. Millereau, P. *et al.* Mechanics of elastomeric molecular composites. *Proceedings of the National Academy of Sciences* **115**, 9110–9115 (2018).
18. Zhao, C. L., Wang, Y., Hruska, Z. & Winnik, M. A. Molecular aspects of latex film formation: an energy-transfer study. *Macromolecules* **23**, 4082–4087 (1990).
19. Lesage de la Haye, J. *et al.* Hydrophilic MacroRAFT-Mediated Emulsion Polymerization: Synthesis of Latexes for Cross-Linked and Surfactant-Free Films. *Macromolecules* **50**, 9315–9328 (2017).
20. Kessel, N., Illsley, D. R. & Keddie, J. L. The diacetone acrylamide crosslinking reaction and its influence on the film formation of an acrylic latex. *J Coat Technol Res* **5**, 285–297 (2008).
21. Zhang, X., Liu, Y., Huang, H., Li, Y. & Chen, H. The diacetone acrylamide crosslinking reaction and its control of core-shell polyacrylate latices at ambient temperature. *Journal of Applied Polymer Science* **123**, 1822–1832 (2012).
22. Yalkowsky, S. H., He, Y. & Jain, P. *Handbook of Aqueous Solubility Data*. (2010).

#

## **Chapter 4**

# **Imaging and quantification of bond breakage in elastomers using confocal microscopy**



## Table of contents

Introduction .....	155
1. Sample synthesis .....	157
1.1. Single network.....	157
1.2. Multiple network .....	157
1.3. Mechanofluorescent single network.....	159
2. Mechanical test.....	160
3. Imaging and quantification of bond breakage .....	160
3.1. Confocal set-up.....	160
3.2. Image collection .....	162
3.3. Imaging analysis.....	163
3.3.1. Calibration of fluorescence.....	164
3.3.2. Quantification.....	166
4. Representativity of the mechanophore's activation for chain breakage .....	169
5. Dependence of DACL activation's on strain rate and temperature .....	171
Conclusions .....	173
References .....	174



## Introduction

*Elastomers are widely used materials due to their ability to deform reversibly without damage. They find applications in the tire industry, seals and even soft adhesives. However, future applications require elastomers with a higher level of mechanical strength while staying fully reversible without permanent damage.*

*The reversible deformability of elastomers comes mainly from their structure. Conventional elastomer networks consist of chemically or physically connected networks of flexible and mobile polymeric chains that change entropy upon deformation reversibly.*

Unfortunately, the reversible deformability is limited by the macroscopic failure of the material which starts from the nucleation of a crack and then propagates through the material. Elastomer fracture is a multi-scale complex process still poorly understood because of the complexity of the soft polymer network. Its fracture involves localized large viscoelastic deformations, molecular damage and very heterogeneous stresses all dissipating energy during the propagation of a crack. The fracture energy of soft materials can be measured experimentally by crack propagation tests. However the underlying reason accounting for the energy dissipated upon propagation englobes all the dissipative mechanisms like friction between monomers, relaxation of pendant polymer chains and fracture of stretched chains by bond scission. Many questions remain open on the fracture of soft materials. Understanding their fracture process could give new guidelines for the material chemists to design and control dissipative bond scission processes in new fracture resistant elastomers.

Fracture of elastomers has already been investigated by mechanochemistry in our lab. The term mechanochemistry accounts for a chemical reaction that can be triggered by a mechanical stimuli. It is particularly interesting for the study of fracture in elastomers when the chemical reactions induce a visible change (in color, fluorescence or light emission), such molecules are called mechanophores. First, Etienne Ducrot incorporated a dioxetane mechanophore that emitted light upon breakage [1] into multiple network elastomers. His method led to time resolved information on bond breakage in multiple network elastomers during crack propagation. Though an attempt to calibrate the level of dioxetane scission by heating the sample (and hence activating all dioxetane into emitting light) was done by Clough et al. [2], the signal emitted from this mechanophore is very unstable, low and hard to measure, making it difficult to obtain absolute quantitative information and hence to compare different materials. The low level and transient nature of the signal limited also the practical spatial resolution that could be achieved, as the whole width of the sample (5 mm) should be in the picture frame to track the crack propagation.

In a more recent work [3,4], J. Slootman, used a mechanosensitive fluorescent molecule embedded in the elastomer to image and quantify bond breakage in single networks and multiple networks. She used a

pi-extended anthracene mechanofluorescent molecule developed by Göstl et al. [5]. The pi-extended anthracene presents the advantage of giving a stable fluorescent signal that can be imaged quite simply by confocal imaging, even a long time after it has been activated, and thus the spatial resolution can be highly increased compared to dioxetane. She functionalized the molecule to incorporate it inside the polymer network as a crosslinker, in a simple one-step photo-induced free radical polymerization [4]. She could calibrate the concentration of activated mechanophores from the intensity measured using calibration samples.

To quantify bond breakage with the calibrated mechanophores's activation, two main assumptions have to be made:

- the mechanophore crosslinker was homogeneously and randomly incorporated within the material
- the fraction of activated mechanophore is the same as the fraction of chain scission

Her work opened the way to visualize previously inaccessible bond breakage information. It gave information at the micrometer scale, and demonstrate that rupture didn't occur only in the plane of the newly created interface (at the mesh size level) but over a much larger volume at the crack tip. The contribution of molecular damage to the fracture energy could be identified and separated from the overall fracture energy. Her results showed unambiguously that the contribution of molecular damage to the fracture energy varied with strain rate and temperature [4].

The method developed by J. Slotman will be applied in the following chapters, to investigate bond breakage in different polymer systems. As the method is new and non-trivial, this chapter will focus on presenting the updated method from samples synthesis to imaging and quantifying bond breakage in soft polymer networks tagged with pi-extended anthracene mechanofluorescent molecules. Finally, the pi-extended anthracene's ability to quantitatively report for chain breakage will be discussed.

## 1. Sample synthesis

Conventional crosslinked poly(ethyl acrylate) (PEA) networks were chosen as standard samples because they are good basic model elastomer material with a  $T_g$  well below room temperature and were previously studied [3,6].

### 1.1. Single network

PEA single networks (SN) were synthesized, as first shown by Y. Chen [6], in a free radical bulk polymerization following the process described in Chapter 2 section 2.2.2, with a modified formulation:

EA (4.00 mL, 36.7 mmol) was used as monomer, BDA (34.59  $\mu$ L, 0.0183 mmol, 0.50 mol%<sup>1</sup>) as crosslinker and HMP (64.86  $\mu$ L, 0.4250 mmol, 1.16 mol%<sup>1</sup>) as organic UV initiator.

After the polymerization, the single network (SN) is dried under vacuum overnight to remove all unreacted volatile monomer and to estimate the degree of conversion of the polymerization, *conv%*, calculated as:

$$conv\% = \frac{m_1}{m_f} \quad \text{Eq. 1}$$

Where  $m_1$  and  $m_f$  are respectively the sample mass at the end of the polymerization before and after vacuum drying.

### 1.2. Multiple network

Interpenetrated polymer networks, in the specific form of multiple network elastomers (MNE), were polymerized as described in the work of P. Millereau [7]. The material's structure enables the first network to reach high extensibility without macroscopic failure of the whole material. These multiple networks also present the advantage of being transparent.

These materials consist in a first crosslinked network, called filler network, pre-stretched by a less crosslinked network, called matrix. The filler and matrix are polymerized in successive steps of swelling and polymerization, as represented in Figure 1, to obtain a double network (DN). The material is dried under vacuum to ensure that all volatile unreacted monomers have been removed from the samples.

---

<sup>1</sup> The mol% ratio of a compound X corresponds to the molar quantity of the compound X over the molar quantity of monomer, as follows:  $mol\% = \frac{n_X}{n_{EA}} \times 100$

Using the DN as a first network, these swelling and polymerization steps can be repeated to obtain a triple network (TN). And so on, for a quadruple network (QN).

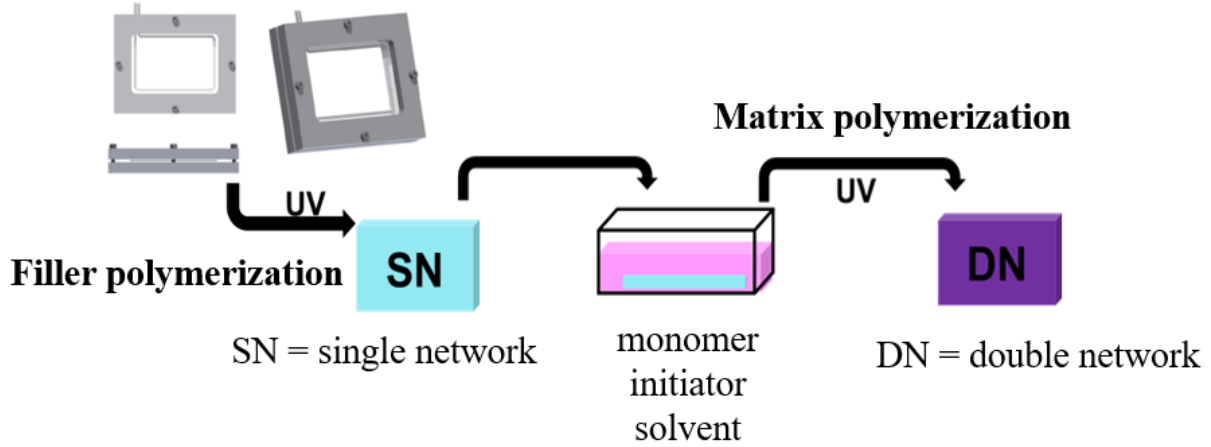


Figure 1 Schematic representation of the double network polymerization process

The SN is obtained as described previously in section 1.1. It was used in smaller rectangular pieces of size 2 cm x 3 cm, to foresee the swelling in the limited sized bath.

The bath formulation is detailed below:

EA (19.00 mL, 174.2 mmol) was used as monomer, BDA (3.29  $\mu$ L, 0.0174 mmol, 0.01 mol%) as crosslinker and HMP (2.66  $\mu$ L, 0.0174 mmol, 0.01 mol%) as organic UV initiator.

In multiple networks, previous works have demonstrated the importance of the filler network's prestretch  $\lambda_0$  [7], it is possible to estimate  $\lambda_0$  by:

$$\lambda_0 = \frac{L_{DN}}{L_{SN}} = \left( \frac{V_{DN}}{V_{SN}} \right)^{\frac{1}{3}} = \left( \frac{m_{DN}}{m_{SN}} \right)^{\frac{1}{3}} \quad \text{Eq. 2}$$

Where  $L_{DN}$  and  $L_{SN}$  are respectively a characteristic length of the DN and SN sample (thickness, width, length),  $V_{DN}$  and  $V_{SN}$  are respectively the DN and SN volume, and  $m_{DN}$  and  $m_{SN}$  are respectively the DN and SN mass, SN being, here, only the piece used to make the DN.

For a TN and a QN:  $\lambda_0 = \left( \frac{m_{TN}}{m_{SN}} \right)^{\frac{1}{3}}$  and  $\lambda_0 = \left( \frac{m_{QN}}{m_{SN}} \right)^{\frac{1}{3}}$ . During a uniaxial test the stretch level of the filler network can be obtained by multiplying the measured stretch by the prestretch, i.e  $\lambda_{1st} = \lambda \cdot \lambda_0$ .

### 1.3. Mechanofluorescent single network

The networks can be tagged with a mechanofluorescent molecule which reports for bond breakage.

R. Göstl et al. synthesized a mechanophore molecule based on a Diels-Alder adduct of a  $\pi$ -extended anthracene. Their molecule presents the advantage to fluoresce stably and sensitively upon force-induced bond scission, which makes it a great candidate to report for chain breakage in polymer networks [5].

The molecule was successfully synthesized and incorporated in acrylate networks at SIMM lab by J. Sloopman [3,4]. The  $\pi$ -extended anthracene maleimide mechano-fluorescent molecule, also called Diels Alder adduct CrossLinker (DACL), represented in Figure 2, was incorporated as a mechano-fluorescent crosslinker in PEA networks.

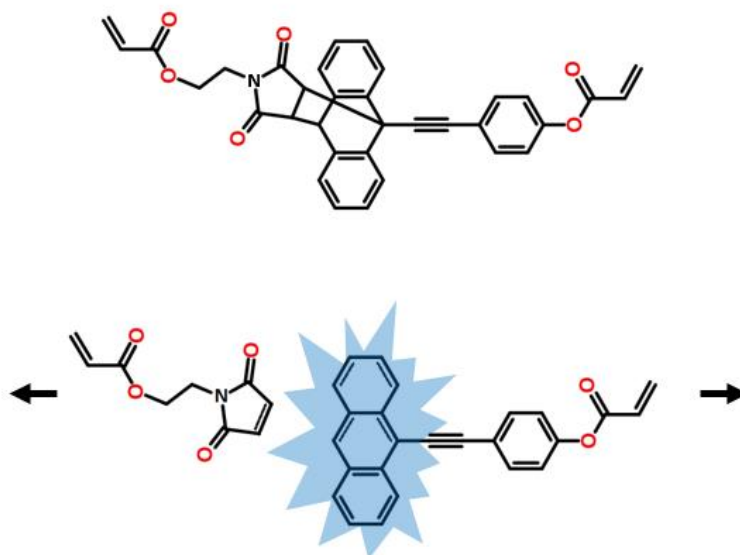


Figure 2 Schematic representation of the mechanophore crosslinker DACL

Upon deformation, the non-fluorescent molecule is stretched and undergoes a force that induces a retro Diels-Alder reaction. This breaks the molecule into two parts, one being a fluorescent anthracene moiety. Only half of the activated form of DACL becomes fluorescent.

For all our samples, we chose to tag SN only because it is the network that will undergo the greatest deformation and is more likely to break and activate the mechanophore. We also chose to keep the DACL concentration in the SN constant, to 0.02 mol %, in order to work with the same volume concentration of mechanophores between samples. The formulation of a typical SN containing DACL (noted DASN) is described as follows:

EA (4.00 mL, 36.7 mmol) was used as monomer, BDA (33.20  $\mu\text{L}$ , 0.0176 mmol, 0.48 mol%) and DACL (7.34  $\times 10^{-3}$  mmol, 0.02 mol%) as crosslinkers and HMP (64.86  $\mu\text{L}$ , 0.425 mmol, 1.16 mol%) as organic UV initiator.

SN containing DACL will be labeled DASN $x$ , where  $x$  is the total molar concentration of crosslinker.

## 2. Mechanical test

The synthesized samples were then mechanically tested in uniaxial extension tests, to measure their mechanical behavior (stress as a function of stretch), to induce damage in the samples and to activate the mechanophores. So in the end, the mechanophore's activation can be analyzed in regards to the mechanical results.

Tensile test and notch propagation tests were performed as described in Chapter 2 section 2.3.4 (same tensile test machine, identical sample shapes and sizes depending on the test type) with modified crosshead speed.

To minimize viscoelastic dissipation during the mechanical tests, all tests were done at a constant crosshead speed of 50  $\mu\text{m/s}$ , which resulted in a stretch rate of  $3.33 \times 10^{-3} \text{ s}^{-1}$ .

### *Notch cutting*

The way the notch is initially made is particularly important when mechanophores are involved because mechanophores can already get activated from cutting. In order to get a reproducible notch with the least amount of activation from the cutting process, each time, a new sharp razor blade was used in a push-cut motion to create a 1 mm length notch in the sample.

## 3. Imaging and quantification of bond breakage

### 3.1. Confocal set-up

Now that the samples have been tagged with mechanofluorescent molecules which have been activated in mechanical tests, we need a way to measure the fluorescent information in the samples. To do so, we used confocal microscopy.

Confocal imaging is a powerful technique built to precisely image materials in 3D. It is commonly used in biology to image living tissues tagged with fluorescent markers. As represented in Figure 3, in the confocal set-up, the sample to be imaged is scanned at a specific depth, using a laser at a precise wavelength that should excite the fluorescent probe. The fluorescent molecule absorbs part of the light and re-emits a luminescent signal. The emission rays are filtered by a pinhole in the confocal head, to select only the rays coming from one specific plane to be recorded. It is thus possible to image the

sample in volume, one plane at a time. Furthermore, by imaging and stacking each plane, it is possible to reconstruct a 3D image of the sample. So confocal imaging does not only give us access to the intensity of activated mechanophores, but it also enables us to get information on the localization of these activations.

For our project, we could use either a confocal macroscope or a confocal microscope. The macroscope set-up illuminates a wider field of view and is adapted to observe millimeter sized samples. This set-up is of interest in live-imaging of crack growth or more generally to correlate bond breakage quantification to a macroscopic transformation (crack growth or necking). For example, J. Slotman used the confocal macroscope to observe growing cracks in multiple network samples [3]. However, a macroscope's resolution is low compared to what can be reached with a microscope and so is the light collection efficiency.

In her work [4], J. Slotman imaged the broken samples after the notch propagated (called post-mortem) with the confocal macroscope. However, post-mortem imaging doesn't require a wide field of view. Therefore, a confocal microscope setup could be used to image samples at higher resolutions and improve significantly the measurement of very low and localized signals (that were lost in the noise with the confocal macroscope set-up).

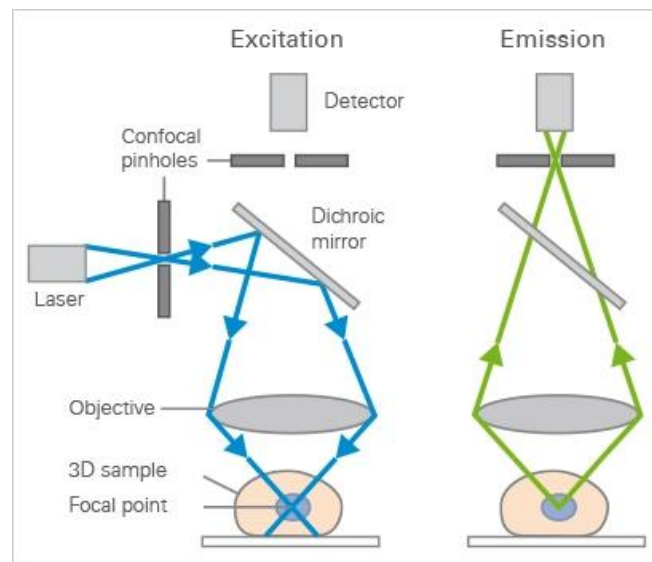


Figure 3 Schematic representation of a confocal set-up

### *Macroscope*

The confocal macroscope was a customized Nikon AZ-100/C2+ equipped with an AZ Plan Fluor 5x objective, with a focal length of 15 mm. The objective is upright and can zoom from 1x to 8x.

### *Microscope*

Mechanophores activation was imaged using a Leica confocal TCS SP8, equipped with an inverted x63 oil immersion objective. Image size was 184.7 x 184.7  $\mu\text{m}$  (1024 x 1024 px).

For both setups, the laser excitation wavelength was set at 405 nm and the emission rays were recorded between 450 and 550 nm with both confocal set-ups.

## 3.2. Image collection

For comparison purposes, the same method was used for each sample to acquire the images. It is presented in this section.

In all samples, the fluorescent signal was found to be homogeneous throughout the thickness (if we correct the measured intensities by the material absorbance which is a function of depth). The 3D nature of the process could then be simplified to a 2D analysis. The surface of the sample was taken as the depth position (z position) where the sample showed the highest intensity (due to light scattering from optical index differences). Images of samples were taken at 100  $\mu\text{m}$  below this surface, to compare images without having to correct intensities with depth.

In post-mortem imaging of broken samples, single optical sections were recorded where the crack has propagated. In post-mortem imaging, the images were taken perpendicularly to the crack surface as represented in Figure 4 A and B.

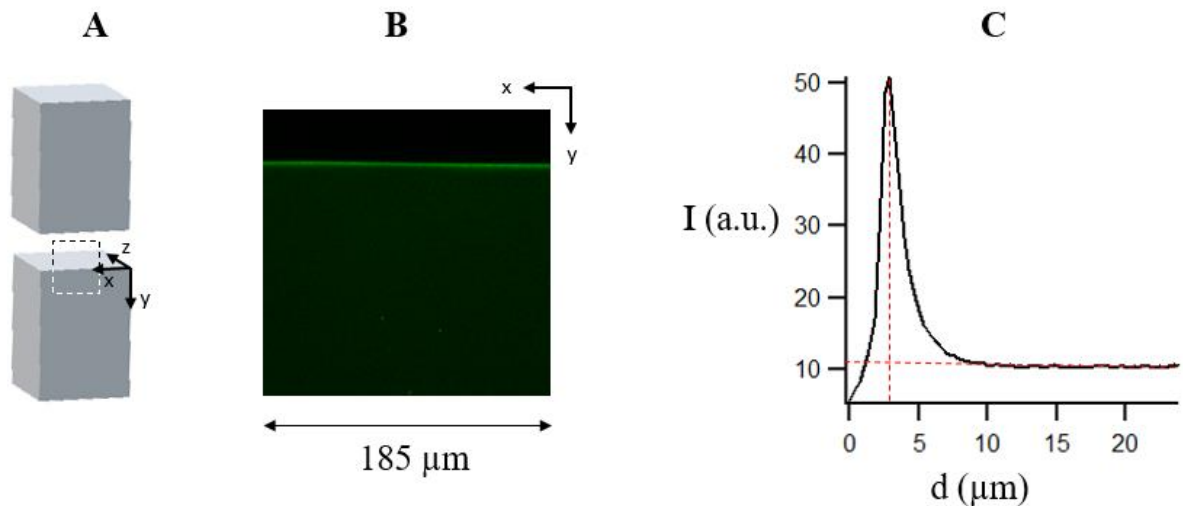


Figure 4 (A) Schematic representation of a broken sample and zone imaged with the confocal, (B) typical image observed at 100 μm inside the sample and (C) intensity measured in the traverse direction to the crack surface

The activation intensity was measured along the perpendicular direction to the crack surface (y direction) and averaged along the crack path (x direction). We could then plot the measured intensity as a function of distance, as shown in Figure 4 C. In order to compare all the measurements, some corrections were done to these raw data, they will be detailed in the following section.

### 3.3. Imaging analysis

To compare samples, all images were processed in the same way.

All signals recorded have background noise which can vary from one sample to another. The background was defined as the plateau in the intensity distance plot, as represented in Figure 5 A. The noise from the bulk sample was not taken into account as activation and was cut off from the intensity measured.

During a depth scan, the crack surface was very likely to present the highest intensity because most breakage should logically happen where the new surface is created and the difference in optical index at the surface may scatter light even more. So the maximum of intensity was taken as the crack surface position. And all distances were shifted to center the pic of intensity to zero, as shown in Figure 5 B.

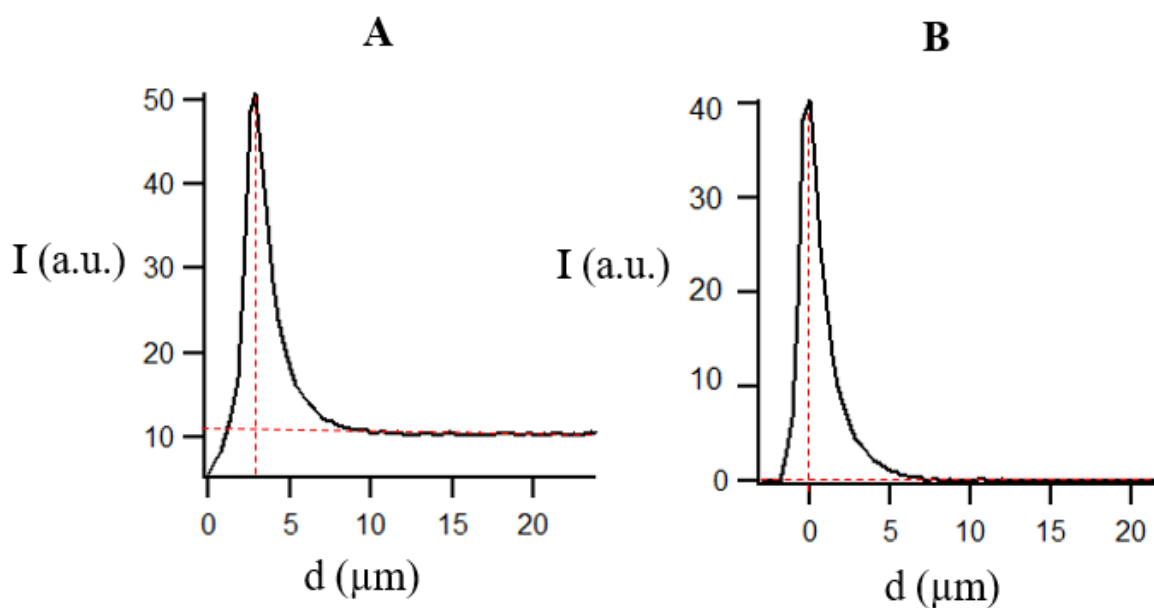


Figure 5 Intensity along the perpendicular direction to the crack surface (A) before correction and (B) after correction of the noise and distance from the crack surface

### 3.3.1. Calibration of fluorescence

The previous sections have shown that we can image, map and measure the intensity from the mechanophore's activation. Next, we want to transform this intensity into an absolute concentration of activated molecules, to report for a fraction of activated mechanophores in the sample and compare materials from different synthesis and having different network structures.

In her work, J. Slotman developed a method to calibrate the concentration of activated mechanophores in the samples from the intensities measured with the confocal microscope [3,4].

[9-((4-anisyl)ethynyl)anthracene] was used as a calibration molecule because it is an equivalent to the DACL activated moiety (Figure 6) [5], so this molecule should have the same fluorescent behavior as activated DACL.

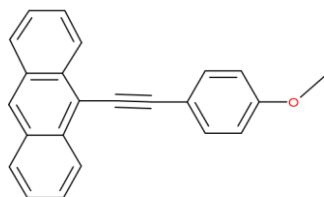


Figure 6 [9-((4-anisyl)ethynyl)anthracene]

The calibration molecule was dissolved in linear PEA ( $M_w \sim 95.000$  g/mol in toluene from Sigma Aldrich) at different known concentrations to make calibration samples. The solutions were cast in small containers for the macroscope set-up or on thin glass plates for the microscope set-up. The samples were dried under a hood for one day and under vacuum overnight to evaporate the solvent. These samples were imaged in the same conditions (zoom, laser, gain) as the rest of the samples. Since the calibration molecule has the same fluorescent signal as the activated DACL, the concentration of activated DACL can be estimated from the known concentration of calibrated molecules. Varying the concentration of calibration molecules in PEA leads to a calibration curve of fluorescent intensity  $I$  (a.u.) as a function of activated fluorescent molecules' concentration  $C$  ( $\text{mol}/\text{m}^3$ ) (Figure 7):

$$I = \alpha \times C + \beta \quad \text{Eq. 3}$$

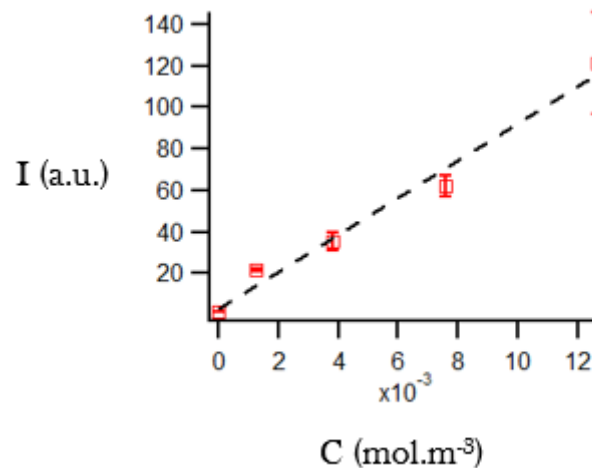


Figure 7 Calibration curve of the activated equivalent of DACL in linear PEA

A new calibration curve should be plotted every time a setting is changed (excitation or emission wavelengths, laser power, detector gain or depth in the material).

Because of pinhole misalignment, the laser intensity can decrease from one day to another. One calibration sample should be imaged before every set of experiments, and if the measured intensity doesn't fall on the calibration curve, a new one should be plotted.

The intensity measured in the broken sample can be converted into a concentration of activated molecules.

### 3.3.2. Quantification

The previous sections have shown that we have access to the concentration of activated mechanophores in the samples. However, our method aims to get information on chain breakage in a network. This section will discuss how we can convert the mechanophores' activation to a quantification of chain breakage within the network.

From the calibration of the mechanophore's activation, J. Sloopman suggested a way to quantify the ratio of broken bonds in samples functionalized with DAAC. To do so, she assumed that:

- The mechanophore molecule is dispersed homogeneously inside the network and reacts like any other monomer
- The fraction of activated mechanophore crosslinker is the same as the fraction of regular crosslinker scission

Though the first assumption can't be verified, it seems plausible. The molecule (in powder form) dissolves well in the monomer. And the acrylate functions at both ends should have the same reactivity ratios as any other acrylate functions in the mix.

The second assumption can be more questionable, particularly because the mechanophore's activation is due to a retro Diels-Alder reaction. This reaction is different from the homolytic dissociation of a C-C bond, thus the energy required to break a mechanophore is different from the energy required to break a C-C bond. To complexify the system, the effect of stretch rate and temperature on both activation energy barriers may enhance the difference between C-C bond breakage and the retro Diels-Alder reaction, especially as the retro Diels-Alder can be thermally induced. Therefore, we can wonder if a retro Diels-Alder reaction can represent well the homolytic dissociation of a C-C bond during chain breakage. Let's put aside the effects of stretch rate and temperature on mechanophore's activation for now, as they will be discussed in a separate section.

Polymer networks made by free radical polymerization of blends of monomers and crosslinkers have a considerable degree of randomness. The distance between crosslink points is random and the conformation of a strand between crosslinks follows Gaussian statistics. As a result there is a quite wide distribution of forces on individual bonds along the chain and at the crosslinking point. In our experiment we introduce a weaker bond (approximately 245 kJ/mol [8] instead of 350 kJ/mol) but it is randomly positioned. Then because the force-stretch curve of single strands is highly non linear, the mechanophore will break preferentially when the strands along the loading path are close to full extension. Therefore we can assume that the activation of the mechanophore should report for the fraction of chains reaching close to full extension and should be representative of all chains reaching full extension.

In summary these previous considerations encourage us to believe that the mechanophore breaks similarly to any other C-C bond that composes the network chains. So the fraction of broken mechanophores should be equivalent to the fraction of broken chains within the network.

Knowing the total concentration of mechanophores incorporated inside the material  $C_{tot}$  and the concentration of activated mechanophores  $C$  (from the measured intensity), it is possible to express a ratio of activation  $\Phi_{act}$  equal to:

$$\Phi_{act} = \frac{C}{C_{tot}} \quad \text{Eq. 4}$$

Then the area under the curve of the fraction of broken chains as a function of distance  $\int \Phi_{act}(y) dy$  corresponds to the fraction of broken chains over a damage zone characteristic of the crack propagation. This would only be true if the probability of scission of the mechanophore in the network is the same or nearly the same as that of the ordinary crosslinker.

In a single network, the average number of elastic strands per unit volume can be estimated from the affine network model by:

$$\nu_x = \frac{E_x}{3kT} \quad \text{Eq. 5}$$

Where  $E_x$  is the crosslinks' contribution to the Young's modulus of the material (in MPa),  $k$  is the Boltzmann constant (in J/K) and  $T$  is the temperature (in K).

In multiple network, the filler network is diluted by a factor  $\Phi_{SN} = \frac{1}{\lambda^3}$ . The average number of elastic strands per cubic meter is then defined by:

$$\nu_x = \Phi_{SN} \frac{E_{x,SN}}{3kT} \quad \text{Eq. 6}$$

Where  $E_{x,SN}$  is the crosslink's contribution to the Young's modulus of the filler network alone (before swelling and polymerization of the matrix).

This leads to the estimation of an experimental areal density of broken chains  $\Sigma_{exp}$  equal to the fraction of broken chains integrated along the y direction, times the volume density of chains:

$$\Sigma_{exp} = 2 \times v_x \times \int \Phi_{act}(y) dy \quad \text{Eq. 7}$$

The factor 2 stands for the specificity of the DACL mechanophore to free only one fluorescent moiety upon activation.

We can note here, that the estimated areal density of broken,  $\Sigma_{exp}$ , is in fact integrated over a volume and then projected to a surface.

To have a comparison, it is possible to estimate the areal number of broken chains of a randomly crosslinked single network with a crosslinker functionality of four by:

$$\Sigma = \frac{v_x \langle R_0^2 \rangle^{1/2}}{2} \quad \text{Eq. 8}$$

Where  $\langle R_0^2 \rangle^{1/2}$  is the average distance between crosslinking points.

From Gaussian statistics:

$$\Sigma = \frac{E}{6kT} l_{cc} \sqrt{C_\infty N_x} \quad \text{Eq. 9}$$

Where  $l_{cc}$  is the length of a C-C bond,  $C_\infty$  is the polymer characteristic ratio and  $N_x$  is the number of carbon bonds between crosslinks.

Finally,  $\Sigma$  can be estimated by:

$$\Sigma = l_{cc} \sqrt{\frac{C_\infty E \rho N_a}{6kT M_0}} \quad \text{Eq. 10}$$

Where  $\rho$  is the material density,  $N_a$  is the Avogadro constant and  $M_0$  is the monomer molecular weight.

We then define  $\Sigma_{norm}$  as the normalized value of the experimental areal number of broken chains over the theoretical areal number of chains:

$$\Sigma_{norm} = \frac{\Sigma_{exp}}{\Sigma} \quad \text{Eq. 11}$$

In the model of Lake and Thomas, the intrinsic fracture energy comes from a number of broken strands equal to the areal density of strands. In the case of a single network, the normalized  $\Sigma_{norm}$  can be seen as a comparison between our experimental results and the model of Lake and Thomas.

#### 4. Representativity of the mechanophore's activation for chain breakage

For a mechanophore to report bond breakage, it should activate in every loaded strand and shouldn't activate in unloaded or partially loaded strands. If the mechanophore is stronger than a conventional C-C bond, it would however never or very randomly activate. In order to activate in any loaded strands, the mechanophore should be weaker than any other of the bonds composing the chain. However, this reasoning has its limits: the mechanophore shouldn't be too weak, else it would activate preferentially even in partially loaded strands and will on the one hand modify the mechanical properties of the network and on the other hand break preferentially and hence in a non representative way. This hypothesis needs to be tested experimentally.

We already know that the barrier energy of the retro Diels-Alder reaction is lower than that of the homolytic dissociation of a C-C bond. Thus, when a chain containing the mechanophore will break, it should break at its weakest point, which is the retro Diels-Alder reaction and free the fluorescent mechanophore moiety. However, we can wonder if this activation of the mechanophore molecule represents well or overestimate chain scission.

If the DACL activation overestimates chain scission, a small variation of the concentration of mechanophore in samples with the same overall crosslinking concentration should affect the ratio of activated DACL.

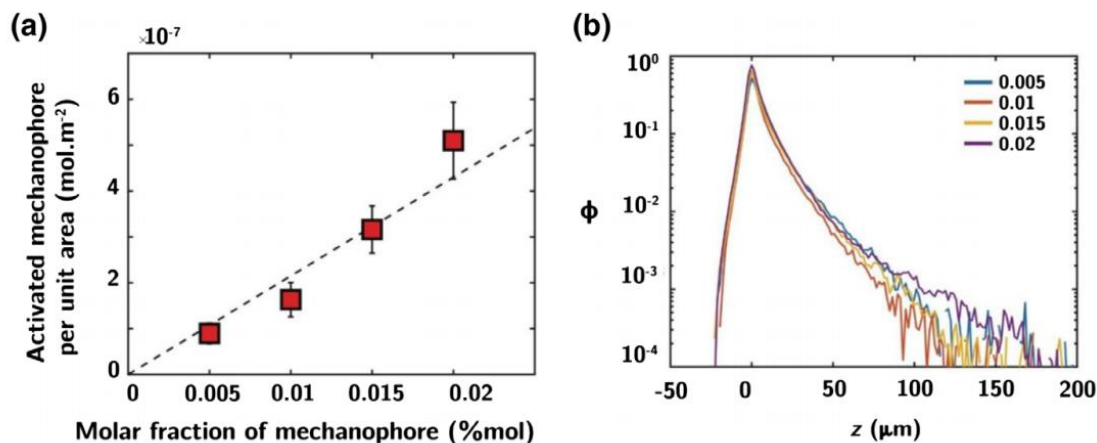


Figure 8 Dependence of DACL activation with DACL concentration. (a) Molar concentration of activated molecule per unit area as a function of the molar concentration of DACL. (b) Damage profiles  $\Phi(z)$  for various initial molar concentrations of DACL in samples with identical total crosslinker concentration.

In order to verify that the mechanophore activation reports correctly for chain scission in a polymer network, four SN samples with a constant concentration of overall crosslinker (0.41 mol%) but different concentrations of DACL (from 0.005 to 0.02 mol%) were synthesized following the procedure described in section 1.1. The monomer used was methyl acrylate to obtain more viscoelastic networks with a higher level of detected bond scission, the crosslinker was BDA, and the initiator was HMP (1.16 mol%).

Rectangular samples (20 mm x 5 mm) with a single edge notch of 1 mm were stretched at a stretch rate of  $3 \times 10^{-3} \text{ s}^{-1}$ . After breakage, the surfaces of the samples were imaged with a confocal microscope. The fraction of activated mechanophore per unit area of crack was measured for each sample and results are shown in Figure 8.

Figure 8 (a) shows that the relation between the molar concentration of activated mechanophores as a function of the total concentration of mechanophores for samples with the same mechanical behavior is nearly linear. The curve is best fitted by a power law function with  $Ax^p$  with  $p=1.5$ .

If we compare the damage profile, Figure 8 (b) shows that the profiles aren't affected by the concentration of DACL in the network and are constant.

So the DACL mechanophores overestimate chain breakage slightly enough to break first in any broken chain while at the same time being consistent with the concentration of molecule that is inside the material. This important result was recently published [4].

## 5. Dependence of DACL activation's on strain rate and temperature

In her work, J. Slotman studied the dependence on temperature and strain rate of the fracture behavior of acrylate soft networks labeled with DACL and found significant differences in levels of activation [4]. In principle these differences could be due to an intrinsic behavior of the DACL with rate or temperature, i.e. various temperatures or stretch rate conditions may exacerbate the difference between C-C bond homolytic dissociation and retro Diels-Alder reaction. Or the differences could be due to different strain fields present at the crack tip for propagation occurring at different T and strain rates, causing therefore different probabilities of bond scission

In this section, we address the effect of stretch rate and temperature on the probability of activation of individual mechanophores embedded into polymer networks.

To investigate this effect, we synthesized TN of poly(methyl acrylate) ( $\lambda_0=2.3$ ) labeled with DACL in the first network as described in section 1.2. In such samples large strains can be applied to the first network (containing DACL) before macroscopic breakage of the sample occurs, and DACL activation can be detected easily before failure for identical strain fields (homogeneous strain).

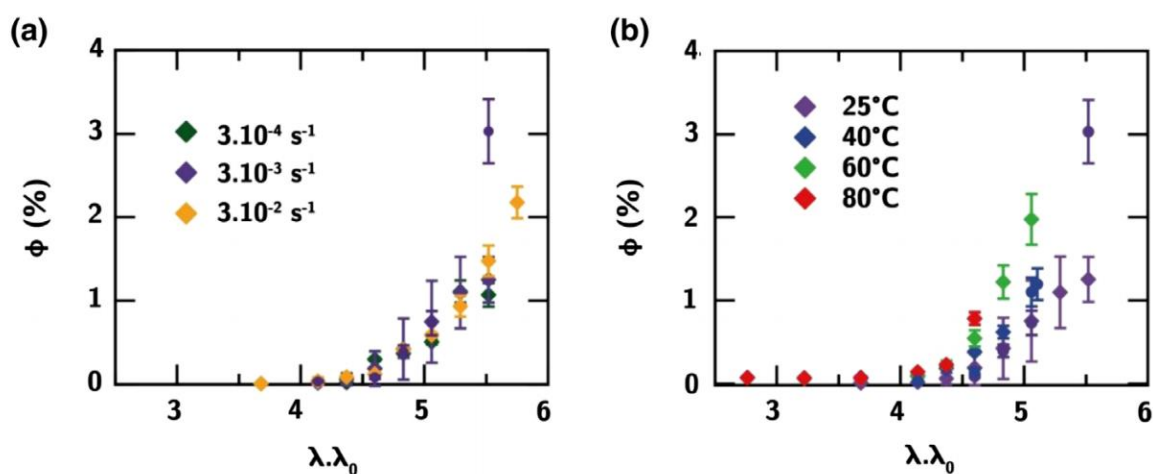


Figure 9 Bulk fraction of activated DACL mechanophore as a function of first network strain in various a) strain rate conditions at 25°C or b) at various temperature conditions and fixed strain rate  $\dot{\lambda}=3 \cdot 10^{-3} \text{ s}^{-1}$ . One sample was used for each condition and imaged at different (x,y) positions in the bulk.

Some samples underwent step extension either at constant temperature 25 °C but three different stretch rates ( $\dot{\lambda}= 3 \cdot 10^{-2}, 3 \cdot 10^{-3}, 3 \cdot 10^{-4} \text{ s}^{-1}$ ) Figure 9 (a); or at four different temperatures (25, 40, 60, 80 °C) but at a constant stretch rate ( $\dot{\lambda}= 3 \cdot 10^{-3} \text{ s}^{-1}$ ) Figure 9 (b). At each deformation step  $\lambda$ , the samples' bulk were unloaded and imaged, with a confocal microscope, at constant depth (100  $\mu\text{m}$ ), to measure the concentration of activated mechanophores in the bulk for that given stretch, and the ratio of activated

mechanophores  $\Phi$ . Figure 9 represents the bulk activation as a function of the stretch of the filler network in the tensile direction  $\lambda/\lambda_0$  for each deformation step.

Figure 9 (a) shows that within experimental error, varying stretch rates didn't affect the level of activation mechanophores activation in the bulk of the sample. The retro Diels-Alder is not sensitive to the stretch rate conditions applied.

For the dependence with temperature, Figure 9 shows a little increase in the probability of activation when the temperature is increased. This should be the result of the dependence of DACL's activation with temperature. It is known that the retro Diels-Alder reaction can spontaneously occur at high temperature ( $> 150$  °C) which means that the energy barrier of the retro Diels-Alder reaction depends on temperature. This effect could lead to the overestimation of damage with increasing temperature. However, in her work [4], J. Slootman found a large decrease in mechanophores' activation with increasing temperatures. Such a slight overestimation at higher temperatures doesn't affect her conclusions.

## Conclusions

In this chapter, the methodology relying on fluorescence activation to map molecular damage in polymer networks was presented.

Mechanofluorescent samples were synthesized and mechanically tested to activate the mechanofluorescent probe and correlate its activation with the mechanical information.

Then we used a laser scanning confocal set-up (either macroscope or microscope) to image the activated mechanophores in the samples. Crack propagation could be observed post-mortem at higher magnification and better resolution by imaging with a confocal microscope at different positions along the fracture path.

The images were then processed to compare samples on the same basis (noise to zero and intensity profile starting from their maximum). The intensity of activation was also successfully calibrated to convert the measured intensity into a concentration of activated mechanophores.

The representativity of the mechanophore to report for chain breakage was discussed as the mechanophore's activation relies on a retro Diels-Alder reaction which is different from the homolytic dissociation of a C-C bond. The lower energy barrier of the mechanophore is necessary to activate preferably the mechanophore in a broken strand. Though the mechanophore activates at a lower force threshold than the homolytic dissociation of a C-C bond, its activation is only triggered close to the chain limit extensibility. And within the (low) working concentration of mechanophore, results show that the mechanophore doesn't over-activate much. Former mechanical characterization [4] have proven that there was no differences in the mechanical behavior between samples without and with mecanophores (at 0.02 mol%). And this remains true at the low working concentrations of our study (between 0.005 and 0.02 mol%).

Finally, the effect of stretch rate and temperature on the mechanophores' activation were investigated and results demonstrate little to no effect of stretch rate and temperature on the mechanophore activation, in the conditions of the tests.

These confirmed our assumption that, whatever the conditions of the mechanical test, the mechanophores report accurately for chain breakage.

## References

1. Ducrot, E., Chen, Y., Bulters, M., Sijbesma, R. P. & Creton, C. Toughening Elastomers with Sacrificial Bonds and Watching Them Break. *Science* **344**, 186–189 (2014).
2. Clough, J. M., Creton, C., Craig, S. L. & Sijbesma, R. P. Covalent Bond Scission in the Mullins Effect of a Filled Elastomer: Real-Time Visualization with Mechanoluminescence. *Advanced Functional Materials* **26**, 9063–9074 (2016).
3. Sloomman, J. Détection quantitative de l'endommagement moléculaire, par mécano-fluorescence, dans les matériaux mous. (PSL, 2019).
4. Sloomman, J. *et al.* Quantifying Rate- and Temperature-Dependent Molecular Damage in Elastomer Fracture. *Phys. Rev. X* **10**, 041045 (2020).
5. Göstl, R. & Sijbesma, R. P.  $\pi$ -extended anthracenes as sensitive probes for mechanical stress. *Chemical Science* **7**, 370–375 (2016).
6. Chen, Y. Cartographie quantitative de la contrainte dans les matériaux mous par mécano-chimie. (PSL, 2018).
7. Millereau, P. *et al.* Mechanics of elastomeric molecular composites. *Proceedings of the National Academy of Sciences* **115**, 9110–9115 (2018).
8. Baba, T., Ishii, M., Kikuchi, Y. & Nakai, H. Application of Bond Energy Density Analysis (Bond-EDA) to Diels–Alder Reaction. *Chem. Lett.* **36**, 616–617 (2007).

# **Chapter 5**

## **Soft network fracture mechanics study using mechano-fluorescence**



## Table of contents

Introduction .....	179
1. Fracture of notched samples .....	181
1.1. Crack propagation .....	181
1.1.1. Video analysis .....	182
1.1.2. Effect of notch length .....	189
1.2. Quantification of chain scission on fracture surfaces .....	199
1.3. Discussion .....	200
2. Fracture of unnotched samples .....	205
2.1. Mechanical reproducibility .....	206
2.2. Direct observation .....	207
2.3. Effect of the viscoelasticity .....	212
Conclusion .....	214
Appendix .....	216
References .....	222



## Introduction

In elastic solids, the driving force for crack growth is the energy release rate  $G$  which is the mechanical energy available for growing a crack per unit area. The resistance to fracture is usually characterized by the fracture toughness  $\Gamma$  which is defined as the critical energy release rate for a pre-existing crack to grow [1]. While the fracture toughness is a material property, the energy release rate  $G$  depends on the loading conditions and the sample geometry.  $\Gamma$  is experimentally determined by stretching a notched sample and computing its energy release rate  $G$  as a function of load and geometry. When crack growth occurs  $G$  equals to  $\Gamma$ .

Although expressions of  $G$  for single edge notched samples can be found in the literature [2], they are mainly based on linear elastic fracture mechanics (LEFM) and can lead to large errors when applied to soft samples subjected to large deformation. The only available expression for  $G$  which accounts for large deformation is given by Rivlin and Thomas [3]:  $G = 2KWa$ . Where  $a$  is the crack length,  $W$  is the strain energy density and  $K$  is a numerical factor which depends on the sample geometry, it was empirically determined by Greensmith on vulcanized rubber for a single edge notch sample [4] for stretch ratios between 1.05 and 2.

More recently, Z. Liu et al. performed a series of finite element simulations to obtain accurate approximations of  $G$  for single edge notch samples that are valid for a larger range of crack lengths and strain levels (between 1.5 and 8) [5].

During fracture propagation, LEFM links the energy release rate to the deformation field at the crack tip and to the local stress. One rupture criterion that determines fracture is molecular, as bonds have to break to create a new surface. At the molecular scale, bond fracture happens at a same local stress threshold.

This project aims to confirm, or not, the importance of the energy release rate  $G$  on chain breakage induced at the crack tip during crack growth, over other parameters like stress or stretch. By varying the initial notch lengths in identical single network sample, crack propagation should occur for different levels of stress and stretch but similar energy release rates  $\Gamma$  as the fracture toughness  $\Gamma$  is a material's property. Note that this macroscopic result has been obtained recently by Suo et al. in their seminal paper on notch sensitivity in soft materials [6].

Assuming that crack growth depends on chain breakage, by extension, we can wonder if chain breakage is more affected by geometric parameters like macroscopic stretch or governed by the energy release rate  $G$ .

Fracture toughness, deduced from  $G$ , takes into account all the energies dissipated to grow the crack (monomer friction, relaxation of pendant chains and fracture of stretched chains by bond breakage). Gent and Schultz [7] suggested to define two separate contributions to account for the intrinsic fracture

energy of the material when there is no dissipation at all, noted  $\Gamma_0$  due to chain breakage; and the contribution of the dissipation to the toughness  $\Gamma_D = \Gamma_0 \times f(v, T)$  where  $f$  is a function of strain rate,  $v$ , and temperature,  $T$ , which characterizes dissipation during propagation.

With the mechanochemistry tool presented in Chapter 4, we can experimentally estimate  $\Gamma_0$ , the contribution of chain breakage in the fracture energy, in post mortem samples, at different positions along the crack path which correspond to previous crack tip position during crack propagation.

With the estimation of energy release rate calculated from the mechanical tests, we can then compare the chain breakage with the energy release rate, and experimentally verify for the first time the effect of estimated energy release rate  $G$  on the extent of chain breakage during crack propagation in soft networks.

Fracture occurs in two stages: nucleation and propagation. Nucleation is poorly understood due to the lack of tools available to assess what is happening at the molecular scale inside the material and the complexity of the mechanism. Conventional microscopy is limited to post-mortem characterization of the surface. If we picture nucleation as a local transition of random chain breakage to correlated catastrophic chain breakage. It is possible to think that clusters of broken chains may grow at the same time in different regions of the sample before stress (or stretch) exceeds a critical value and a crack starts propagating. It is therefore interesting to look for zones in the material where chains were broken but no propagation occurred.

Propagation and nucleation will be investigated in a crosslinked single network elastomer tagged with a mechanofluorescent crosslinker, pi-extended anthracene (DAFL). The samples will be first mechanically tested, then chain breakage will be quantified from confocal imaging. In a first part, crack propagation will be initiated from three different initial lengths of single edge notch to reach different levels of macroscopic far field stress and stretch at propagation, but a similar energy release rates  $G$ . We aim to verify the basic hypothesis of fracture mechanics, that the applied  $G$  controls crack tip stresses and hence probability of chain breakage at the crack tip, rather than other mechanical quantities such as macroscopic stretch. In a second part, no notch will be introduced in the samples to study “natural” nucleation.

## 1. Fracture of notched samples

To correlate the stress and strain data with quantitative molecular chain scission during crack propagation, as shown in Figure 1, we need to investigate mechanically crack propagation first, prior to performing confocal imaging and chain breakage quantification.

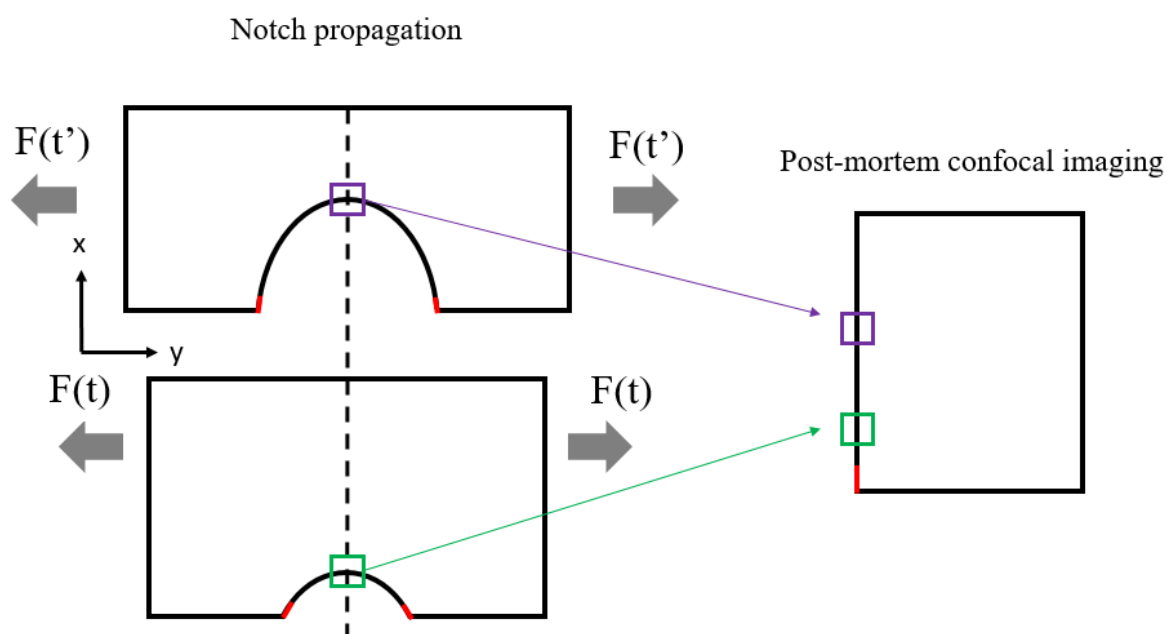


Figure 1 Representation of the relation between the notch propagation test (at a continuous loading rate) at time  $t$  and  $t'$ , and the post-mortem confocal imaging on the broken sample to report for chain breakage which happened at  $t$  (green) and  $t'$  (purple).

During this study, we will work with the same standard sample: a crosslinked single network DASN0.5, composed of PEA chains, functionalized with DACL mechanophore crosslinker (0.02 mol%) and crosslinked with BDA and DACL (0.5 mol%), as described in Chapter 4 section 1.3. We will introduce manually different initial notches (by changing the length) as we know this will initiate the crack propagation at different critical stresses and stretches, and record the mechanical information (macroscopic stretch, crack profile, crack propagation speed, energy release rate).

### 1.1. Crack propagation

To propagate a crack in a controlled and reproducible way, we performed single edge notch propagation tests (on DASN0.5 presented above).

Crack propagation was performed with an Instron tensile test machine equipped with a video extensometer, at a constant stretch rate  $\dot{\lambda} = 3.3 \times 10^{-3} \text{ s}^{-1}$  and temperature  $22 \text{ }^\circ\text{C}$ , on rectangular DASN0.5 samples (20 mm x 5 mm) as detailed in Chapter 2 section 2.3.4. For reproducibility and to minimize DACL activation, the initial notch was introduced in the sample using a new sharp razor blade for each notch as described in Chapter 4 section 2. The notch lengths varied between 0.5 mm and 2 mm.

### 1.1.1. Video analysis

#### *Image processing*

To extract the evolution of the crack profile and notch length during the mechanical test, images of the sample were recorded by the video extensometer at 0.22 s/frame. Some processing needed to be done on the images to obtain the targeted information (crack length, notch profile). This section details the method applied to analyze the videos.

The images, composing the video, were first binarized in order to extract the contours of the sample as represented in Figure 2.

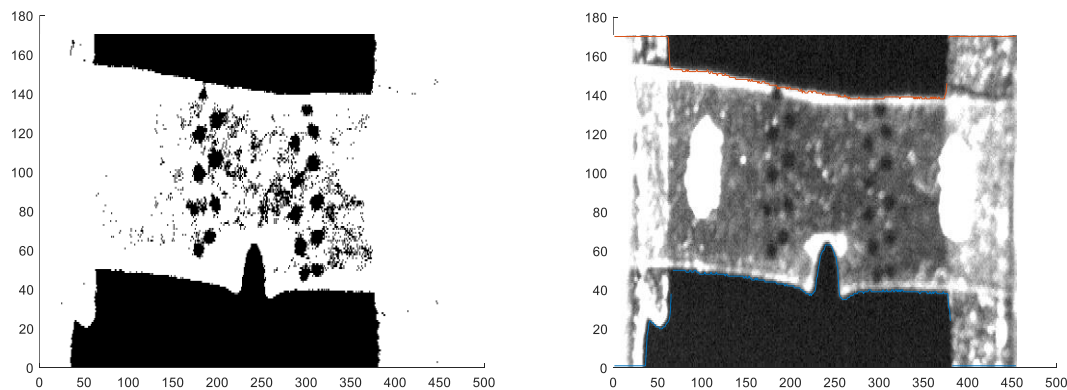


Figure 2 Binarized image of a notched sample during a crack propagation test (left image) and contour extracted in blue and orange on the real caption (right image)

#### *Average deformation vs local deformation*

The first objective of the video analysis is to measure the crack length at any time of the crack propagation test, as it will serve as reference point in the confocal imaging coordinate system.

From the contours, the crack tip position corresponding to the local extremum  $O(x,y)$  of the notched contour could be extracted (Figure 3). The length of the remaining filament of sample along the crack propagation axis called  $b_d(t)$  in the deformed state was calculated as the difference between  $O(x,y)$  and  $O'(x,y')$  the point of the other contour in the same vertical direction.

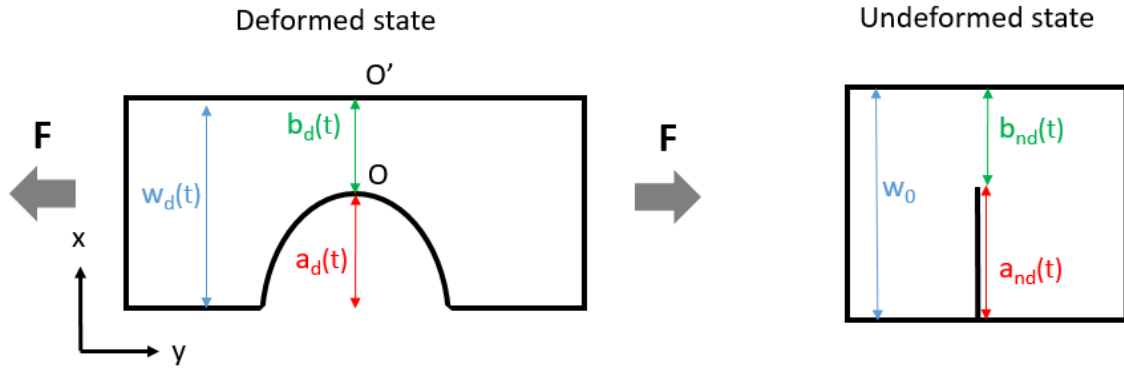


Figure 3 Width, crack and filament length in the deformed state (on the left) and undeformed state (on the right)

Then the length of the crack in the deformed state could be calculated as:

$$a_d(t) = w_d(t) - b_d(t) \quad \text{Eq. 1}$$

Where  $w_d(t)$  is the width of the sample in the deformed state.

Most of the polymer mechanics formulae describe the undeformed state, so the crack length in the deformed state needs to be converted into the crack length in the undeformed state.

$$a_{nd}(t) = a_d(t) \times \sqrt{\lambda_{loc}(t)} \quad \text{Eq. 2}$$

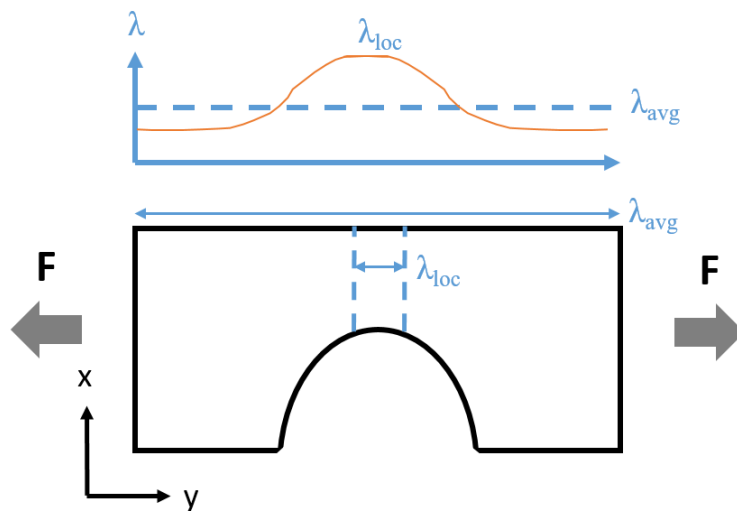


Figure 4 Comparing average deformation with local deformation along the  $x$  axis in a notched sample

We know that the sample is under the same loading force everywhere despite the cross section. At the crack tip, the cross section is reduced, therefore the stress concentrates and the local deformation in front of the crack tip (averaged along the x direction) is greater than the macroscopic deformation in the sample bulk far from the crack tip (far field, Figure 4) where the cross section is larger. Unfortunately, having access to a numeric estimation of the local deformation field during propagation is quite complex (as we didn't perform digital image correlation). There are two possibilities to estimate the local deformation.

- First, we can accept to neglect the error between the local deformation at the crack tip and the far field deformation so:  $\lambda_{loc}(t) = \lambda_{avg}(t)$ .

But we expect this approximation to underestimate the local deformation.

- Second, we can try to estimate an average value of the local deformation using models.
  - With the model of linear elasticity:

This model gives a simple picture of what is happening with crack growth. It considers that the loss of force during crack propagation is due to the crack growth (or the reduction in the section that remains loaded) and translates it linearly as:

$$b_{nd} = w_0 \times \frac{F}{F_{max}} \quad \text{Eq. 3}$$

Where  $F$  is the force still sustained by the sample and  $F_{max}$  is the critical force at which the crack starts to propagate (as shown in the Figure 5),  $b_{nd}$  is the width (in the undeformed configuration) of the remaining ligament when the crack has propagated, and  $w_0 = b_{nd}(t = 0)$  is the initial width of the intact part of the sample before a crack has propagated.

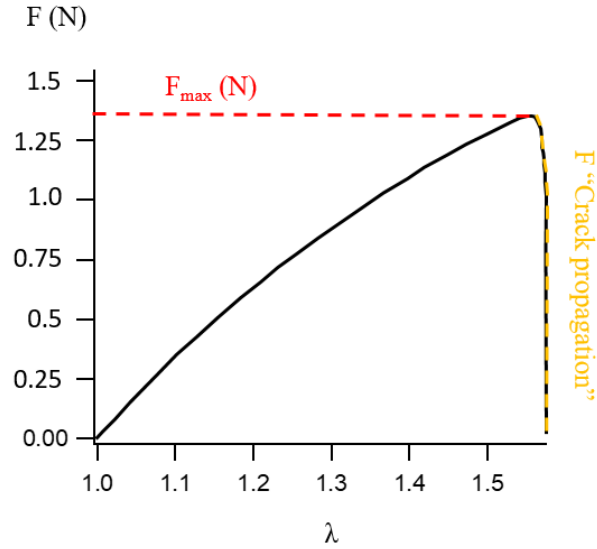


Figure 5 Evolution of the force as a function of the deformation for a notched sample. The crack starts to propagate when  $F=F_{max}$  (red). During the crack propagation, the force decreases (yellow).

Then assuming the network incompressibility, we can write:

$$\frac{b_d}{b_{nd}} = \frac{1}{\sqrt{\lambda_{loc}}} \quad \text{Eq. 4}$$

$$\sqrt{\lambda_{loc}} = \frac{w_0}{b_d} \times \frac{F}{F_{max}} \quad \text{Eq. 5}$$

- With the model of Mooney-Rivlin:

This model, a variation of the neo-Hookean model, takes empirically into account the contribution of the entanglements in the softening of entangled polymer networks at higher stretches. It is more refined than the linear model.

The Mooney-Rivlin formula gives us access to the local stress as a function of the local deformation:

$$\sigma(\lambda_{loc}) = 2 \left( C_1 + \frac{C_2}{\lambda_{loc}} \right) \left( \lambda_{loc} - \frac{1}{\lambda_{loc}^2} \right) \quad \text{Eq. 6}$$

Where  $C_1$  and  $C_2$  are parameters experimentally accessible from the Mooney-Rivlin model's fit on stress-stretch curve of the unnotched sample.

Then the stress can also be expressed as a function of force over section:

$$\sigma(\lambda_{loc}) = \frac{F}{S_{loc}} = \frac{F}{e_{nd} \times b_{nd}} \quad \text{Eq. 7}$$

Where  $F$  is the local force in the remaining section in front of the crack tip, which is equal to the force in the overall sample due to force transmission through the sample.  $S_{loc}$  is the local section, and is equal to the local thickness in the undeformed state  $e_{nd}$  and the length of the remaining filament in the undeformed state  $b_{nd}$ .

$e_{nd}$  can be approximated as  $e_0$  the initial thickness. And  $b_{nd}$  is linked to  $b_d$  the length of the remaining filament in the deformed state by the local deformation  $\lambda_{loc}$ .

Then, from the material incompressibility and Eq. 7:

$$\sigma(\lambda_{loc}) = \frac{F}{e_0 \times b_d \times \sqrt{\lambda_{loc}}} \quad \text{Eq. 8}$$

This simplifies in an equation with only one variable  $\lambda_{loc}$ :

$$\begin{aligned} 4C_1^2 \lambda_{loc}^8 + 8C_1 C_2 \lambda_{loc}^7 + 4C_2^2 \lambda_{loc}^6 - \left(8 + \left(\frac{F}{e_0 b_d}\right)^2\right) \lambda_{loc}^5 \\ - 16C_1 C_2 \lambda_{loc}^4 - 8C_2^2 \lambda_{loc}^3 + 4C_1^2 \lambda_{loc}^2 \\ + 8C_1 C_2 \lambda_{loc} + 4C_2^2 = 0 \end{aligned} \quad \text{Eq. 9}$$

This equation can be solved (knowing  $C_1$ ,  $C_2$ ,  $F$ ,  $e_0$  and  $b_d$ ); it has multiple solutions but only the solution above 1 was considered as the local deformation.

We looked at the differences between the far field deformation  $\lambda_{avg}$  and the local deformations  $\lambda_{loc}$  from the linear model and the Mooney-Rivlin model in the Appendix. As expected, the far field deformation  $\lambda_{avg}$  doesn't take into account the crack propagation and increasingly underestimates the local deformation as the crack propagation, so it will not be considered in the rest of this study.

*Crack length*

From the previously calculated deformations, we can get an estimation of the crack length, in the unloaded state, at any time during the propagation.

In the undeformed state, the total width of the sample where the crack is propagating  $w_{nd_{loc}}$  is equivalent to the averaged width of the sample  $w_{nd_{avg}}$  (because the sample, at rest, should get back to its original shape if the deformation is fully elastic):  $w_{nd_{loc}}(t) = w_{nd_{avg}}(t) = w_0$ .

Where  $w_0$  is the initial sample width.

Then, the crack length in the undeformed state, can be written:

$$a_{nd}(t) = w_0 - b_{nd}(t) \quad \text{Eq. 10}$$

$$a_{nd}(t) = w_0 - b_d(t) \times \sqrt{\lambda_i(t)} \quad \text{Eq. 11}$$

Where  $\lambda_i(t)$  can represents either the local deformation calculated with the model of linear elasticity or with the model of Mooney-Rivlin.

We looked at the differences between the crack length estimated from the linear model and from the Mooney-Rivlin model, it is reported in the Appendix. Though the variation of the estimated crack length with time are comparable between the methods, the local deformation calculated from the Mooney-Rivlin leads to an estimation of the crack length that takes into account the initial notch length: with this method, the estimated initial crack length before propagation is equal to the initial notch length introduced manually. This is an advantage compared to the value from the linear elastic model where the estimated initial crack length before propagation is equal to zero, and therefore, the values need to be shifted by the initial notch length. So for the rest of the study, we decided to use the local deformation calculated by Eq. 9 to estimate the crack length.

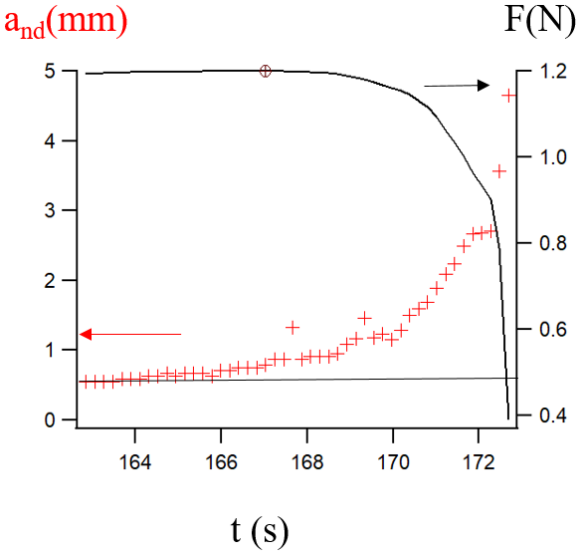


Figure 6 Crack length in the unloaded state  $a_{nd}$  (left axis, red markers) and force  $F$  (right axis, black full line) as a function of time). The black horizontal line corresponds to the length of the initial notch in the sample 0.5 mm. The red round marker refers to the maximum force.

The force and crack length are plotted as a function of time in the Figure 6. It shows that the estimation of crack length before the start of crack propagation (red mark on the force curve) is close to the real value of 0.5 mm when the local deformation was used to estimate crack length (plotted in red).

Figure 6 shows that the crack length increases first slowly, while the force plateaus and decreases slightly. When the crack length increases faster, the force drops. The slope of the crack length plot as a function of time, can be used to extract a crack propagation velocity represented in Figure 7.

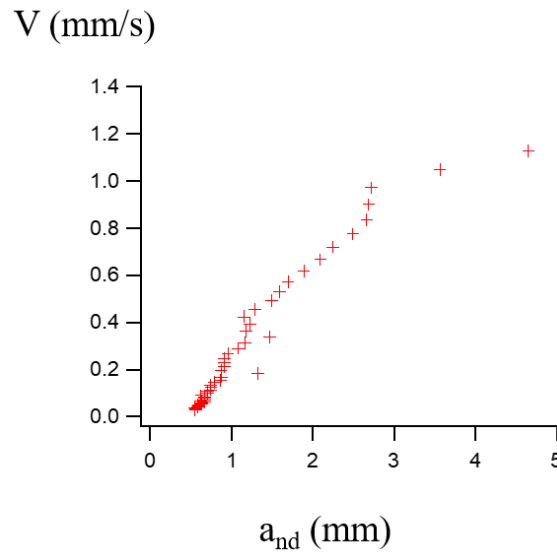


Figure 7 Crack propagation speed as a function of crack length (initial notch length 0.5 mm)

As the crack propagates, the crack length increases and the length of the remaining filament under load decreases, which can lead to an acceleration of the crack propagation. So it makes sense to plot the crack propagation speed  $V$  as a function of the crack length as in the Figure 7.

Figure 7 shows the evolution of crack speed extracted from the image analysis as a function of crack length. We can clearly see that as expected, the crack speed is low at the beginning of crack propagation and accelerates as the crack length increases. The crack speed increases almost linearly with crack length after a first slow propagation step, suggesting a fairly constant acceleration.

The crack speed will affect the viscoelastic dissipation ahead of the crack tip, (which will affect the energy required to propagate the crack and then the local deformation) and finally the ratio of broken chain along the crack path [8].

### 1.1.2. Effect of notch length

Once the video analysis method is well established, we can verify the effect of initial notch length on crack propagation in DASN0.5. From fracture mechanics, we expect to propagate the crack at similar levels of energy release rates for the same network, but at different values of critical nominal stress and stretch.

To verify these statements, crack propagation tests were performed on DASN0.5 rectangular samples with three different initial notch sizes (0.5, 1.0 and 1.8 mm), at a constant stretch rate  $3.33 \times 10^{-3} \text{ s}^{-1}$ . The stress-stretch plots are represented in the Figure 8.

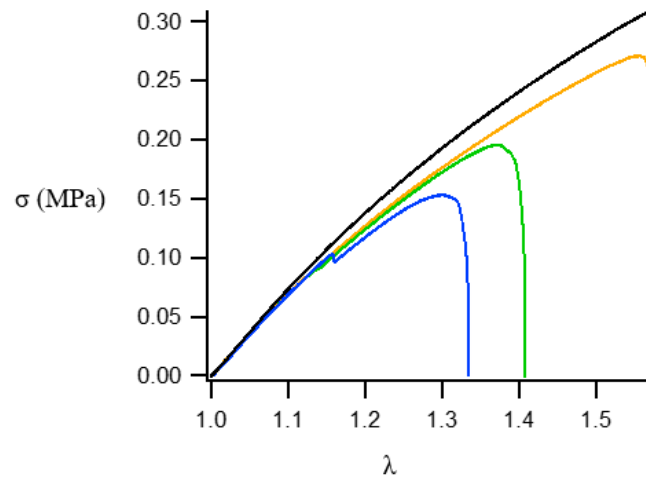


Figure 8 Nominal stress as a function of stretch for notch propagation test on samples with different initial notch sizes: blue 1.8 mm, green 1.0 mm, yellow 0.5 mm, and black uniaxial extension of an unnotched sample

Figure 8 confirms that increasing notch lengths decreases the critical stretch at which the crack starts to propagate, as well as the critical nominal stress. It also affects the averaged deformation of the sample. The deformation is higher in the notch plane, this results in a slight shift of the averaged deformation to higher values, which explains the difference between the unnotched sample (in black) and the notched samples (colored) plots.

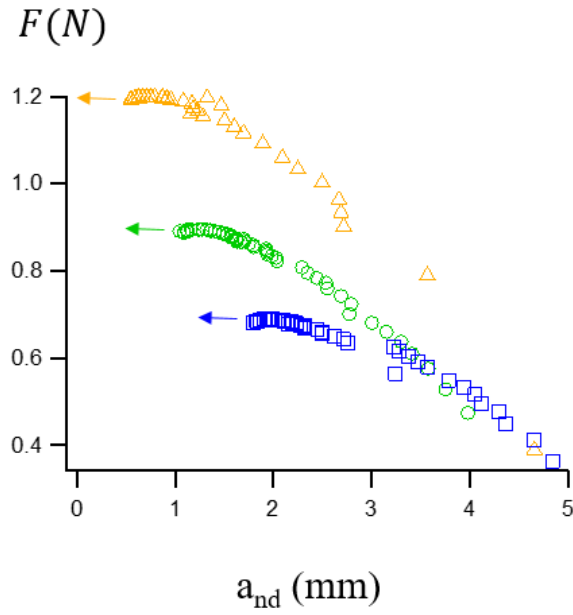


Figure 9 Effect of initial notch length on the evolution of force with crack length for samples (initial notch length: blue 1.8 mm, green 1.0 mm, yellow 0.5 mm)

Figure 9 shows how the force decreases when the crack propagates from different initial notch lengths. The smaller initial cross-section, where the crack propagates, is the weakest and it affects the most the force seen by the sample. When the crack propagates, the smaller section under load reduces and with it, the force. It makes sense to take the crack propagation start at the time corresponding to the maximum force. Smaller initial notch lengths make the force decrease faster.

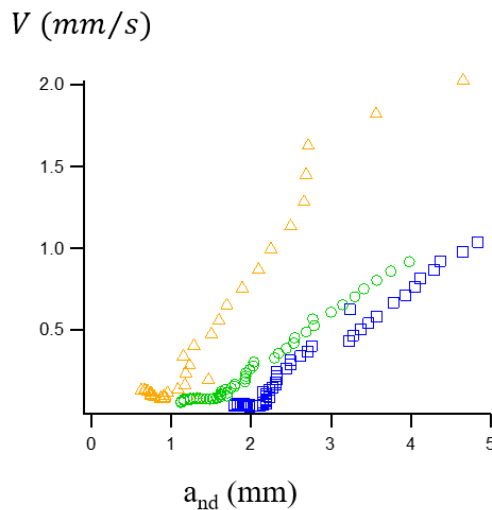


Figure 10 Crack speed as a function of crack length. The slope of the curve gives 0.60 (yellow), 0.32 (green) and 0.35  $s^{-1}$  (blue) (initial notch length: blue 1.8 mm, green 1.0 mm, yellow 0.5 mm)

Figure 10 confirms that the crack propagation speed depends on the initial notch length. This is due to the elastic strain energy density  $W$  which is more important for shorter cracks as they start to propagate at higher stretch.

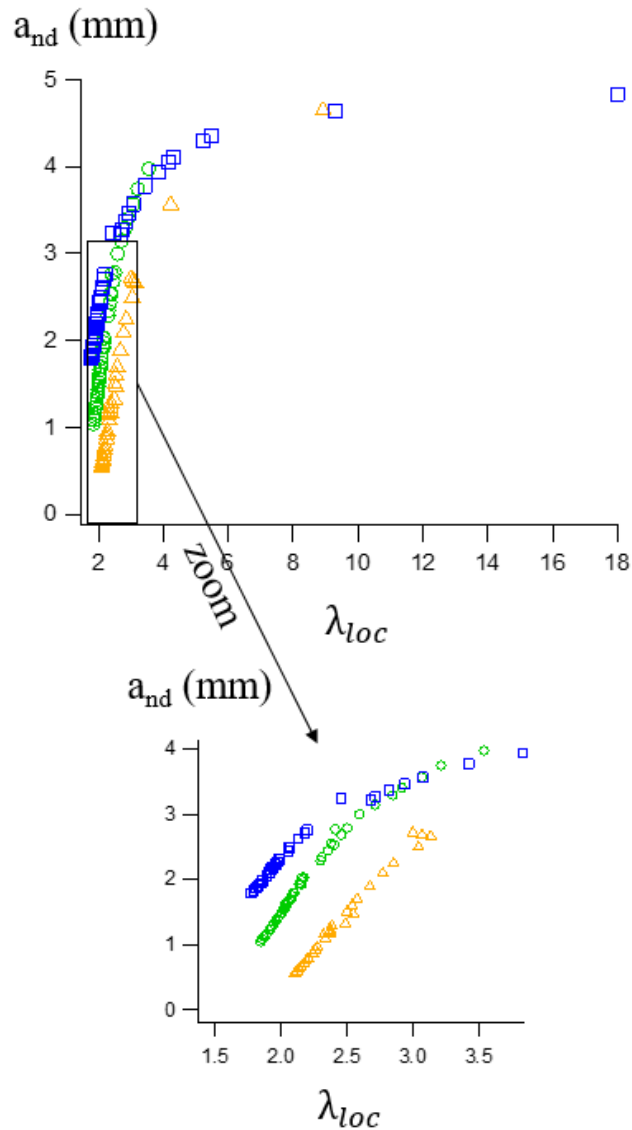


Figure 11 Effect of the local deformation on crack propagation (initial notch length: blue 1.8 mm, green 1.0 mm, yellow 0.5 mm)

Figure 11 represents the crack length as a function of the calculated local deformation for samples with three different initial notch lengths. And results show that there is a shift in the averaged local deformation at which the crack starts to propagate but the difference diminishes as the crack grows.

### *Crack profile*

To further investigate the crack tip zone, the videos of the tests, recorded from the video extensometer, were analyzed to extract the crack opening profile for the different initial notch sizes corresponding to the onset of propagation. We hypothesized that the opening profile would be a good variable to correlate with the local deformation at the crack tip as an alternative to our estimate of  $\lambda_{loc}$ . We expect chain scission to occur at the crack tip when the polymer strands of the network reach their limit of extensibility, therefore the local deformation  $\lambda_{loc}$  and by extension the shape of the profile are of interest. Because the chains' maximal extensibility is an intrinsic parameter of the polymer network, it shouldn't be affected by the initial notch length. So the crack profile at which the propagation starts (a local parameter) shouldn't depend on the initial notch length even though the critical nominal stretch at the onset of crack propagation will increase with decreasing initial notch lengths.

The start of crack propagation was taken as the time at which the force reaches its maximum. The image corresponding to that time were processed (as described in section 1.1.1) and the notched contour was modeled with a parabolic fit as shown in the Figure 12. This led to the crack profile parameter represented in Figure 13, as a function of initial notch length.

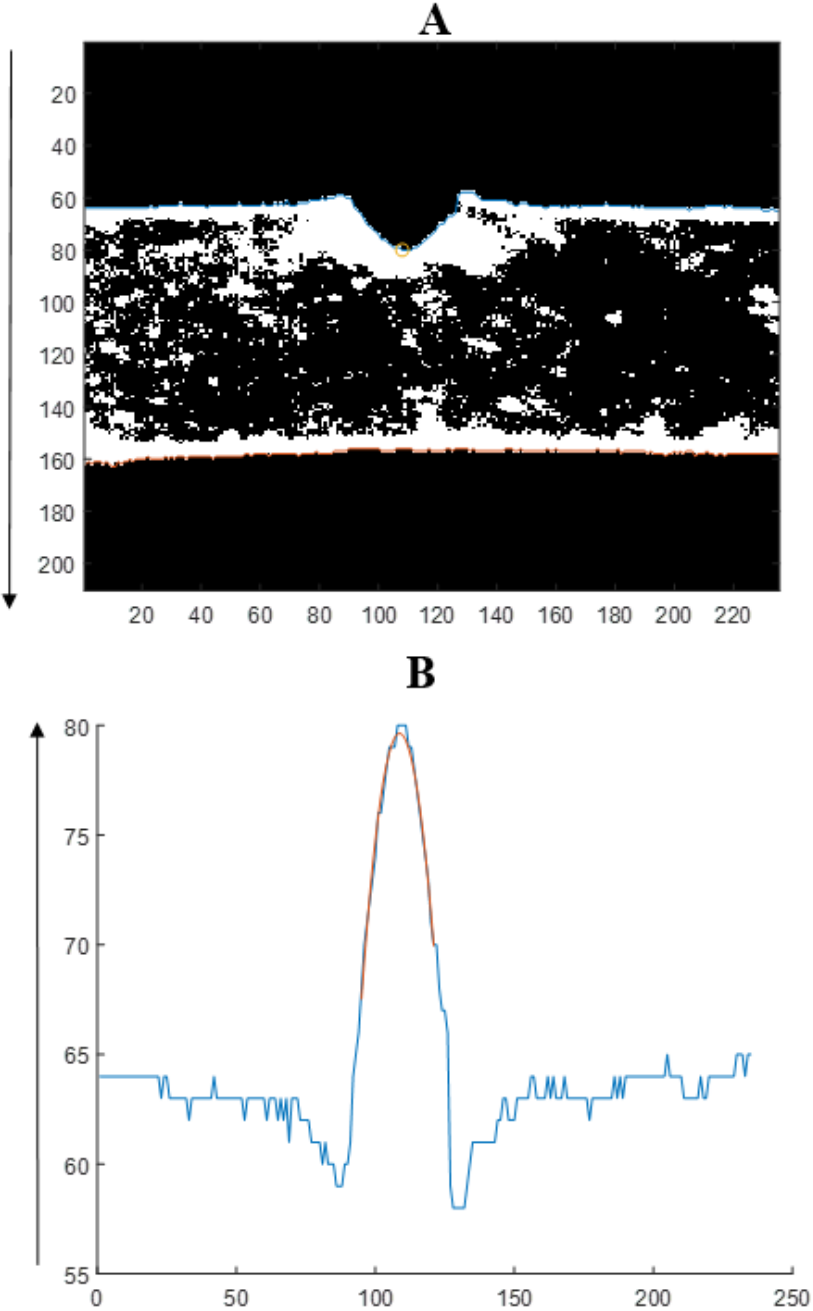


Figure 12 Example of (A) the image processing and (B) parabolic fit of the notched contour for a DASN0.5 sample with an initial notch size of 0.5 mm

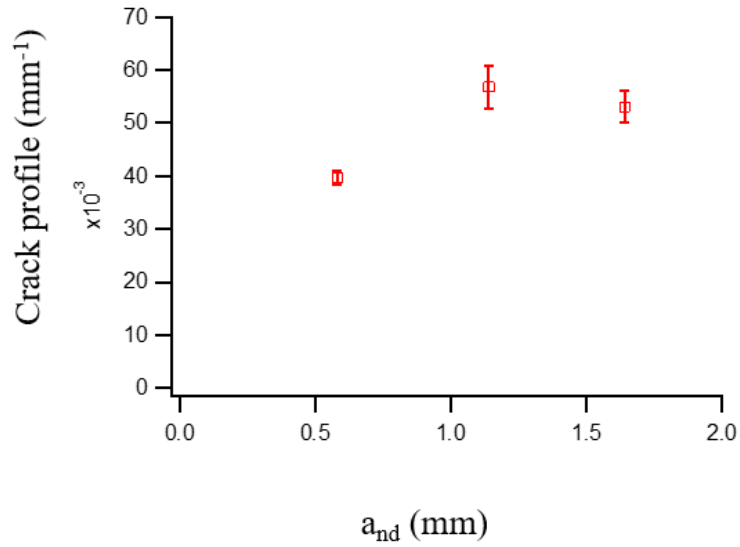


Figure 13 Crack profile at the start of propagation for different samples with various initial notch sizes

A low crack profile parameter describes a very opened notch and the higher the crack profile parameter is, the narrower is the notch. Figure 13 shows that the crack profile parameter, corresponding to the beginning of propagation, seems to vary slightly with initial notch size. Especially, the smaller notch seems to open more before crack growth.

We also followed the crack profile as a function of crack length during the propagation. The results are reported in the Appendix.

#### Fracture energy

The fracture energy can be calculated from the energy release rate at which the crack starts to grow. There are different ways to estimate the energy release rate. Two models fit for soft extensible materials.

- The model of Rivlin and Thomas:

In their model, the energy release rate is estimated as [3]:

$$G = 2 \times K \times W(\lambda) \times a \quad \text{Eq. 12}$$

Where  $a$  is the crack length,  $W$  is the elastic strain energy density, and  $K$  is a numerical factor which was empirically determined by Greensmith for single edge notched samples at stretch ratios between 1.05 and 2 [4].

Fracture toughness is experimentally determined using the critical strain  $\lambda_c$  which corresponds to the deformation of highest stress, and the strain energy  $W$  which corresponds to the area under the curve of the unnotched sample up to the critical strain:

$$\Gamma = 6 \times \frac{a \times W(\lambda_c)}{\sqrt{\lambda_c}} \quad \text{Eq. 13}$$

Toughness as a function of notch size calculated from Eq. 13 is reported in Figure 14. Three different batches were tested to check the reproducibility of our synthesis. Results show that there is some variability in fracture toughness between elastomers made during different synthesis batches. For each elastomer batch, three rectangular samples were cut and notched at different initial lengths.

Some variations in fracture toughness could be observed within the same batch for varying notch length. However, these variations with notch length don't follow the same trends: for one batch, fracture toughness slightly decreases with increasing notch length, while for the two other batches,  $\Gamma$  increases with notch length. So we can assume that these variations are within experimental error and that the initial notch size doesn't affect much the fracture toughness. One more sample was tested in the same conditions as a previous one (same batch and same notch length) to verify the reproducibility of our method. Results show that at identical conditions, the measured  $\Gamma$  are very close to each other.

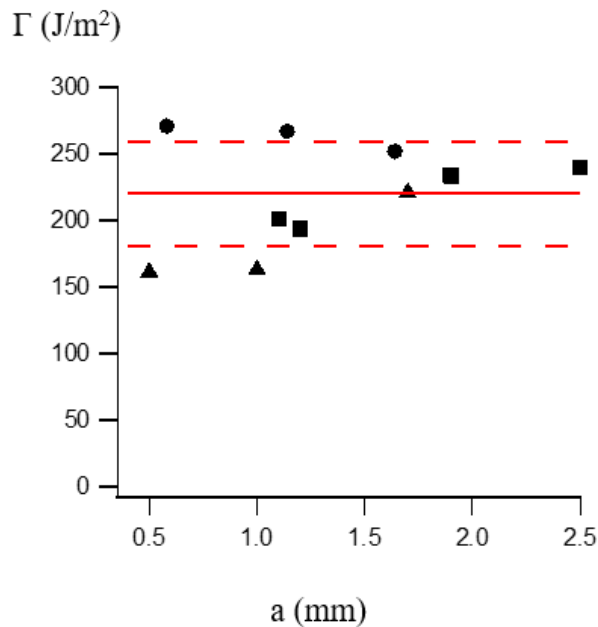


Figure 14 Toughness calculated with the Greensmith formula for samples with various initial notch sizes, the red line corresponds to the mean value 220 J/m<sup>2</sup>, dotted lines are the average standard deviation to the mean value (40 J/m<sup>2</sup>)

- The model of Liu et al. [5]:

Liu et al. carried out finite element (FE) simulations to verify the validity of Greensmith's approximation (for three different material's model: neo-Hookean, Mooney-Rivlin and Arruda-Boyce) and found that it underestimates the energy release rate for  $\lambda < 1.5$ . They also proposed an analytical expression to approximate the energy release rate that they obtained with their FE simulations.

$$G = (2 \times W(\lambda) \times a) \times K(\lambda) \times f\left(\frac{a}{w}\right) \quad \text{Eq. 14}$$

Where  $\lambda$  is the nominal applied stretch,  $f$  is a function that takes into account the notch length over width ratio.

$$f\left(\frac{a}{w}\right) = 0.9997 \exp\left(0.1028 \times \frac{a}{w}\right) + 0.0003 \exp\left(9.007 \times \frac{a}{w}\right) \quad \text{Eq. 15}$$

$K$  is a numerical factor depending on the sample deformation:

$$K(\lambda) = \frac{1.476 \times \lambda + 0.2111}{\lambda - 0.5804} \quad \text{Eq. 16}$$

Experimentally, we will consider  $\lambda$  as the nominal stretch of the sample to estimate  $W$  and  $K$ .

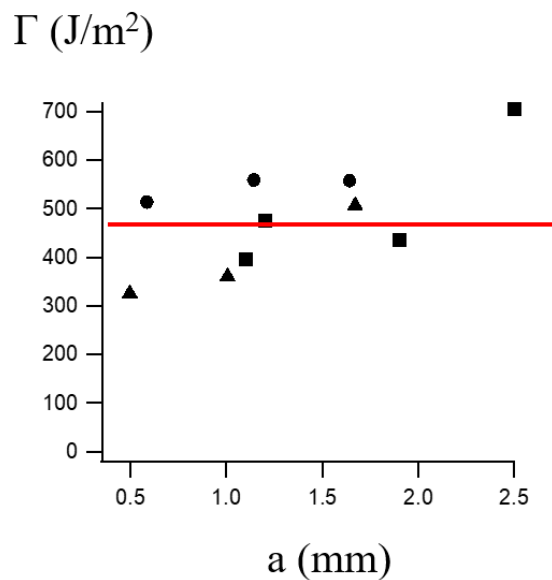


Figure 15 Toughness calculated with the Liu et al. formula of  $G$  for samples with various initial notch sizes, the red line corresponds to the mean value 483 J/m<sup>2</sup>.

The fracture toughness from Liu et al. formula is almost twice the value found with the Greensmith formula. The formula of Liu et al. is more accurate than the formula of Greensmith (as shown by their FE simulations).

Additionally, using this better approximation, the fracture energy seems to slightly increase with notch length. This may be an artefact due to the limitations of the model which is supposed to be valid only for short initial notches. Overall, the notch length doesn't affect the calculated fracture energy, in the following we will calculate the strain energy release rate  $G$  with the formula given by Liu et al.

*Strain energy release rate*

The strain energy release rate could be calculated from the model of Liu et al. not only at the start of crack propagation, as for the fracture energy, but also during the crack propagation (as we have access to all the parameters of the model and especially the crack length  $a_{nd}$  from the video analysis during the crack propagation).

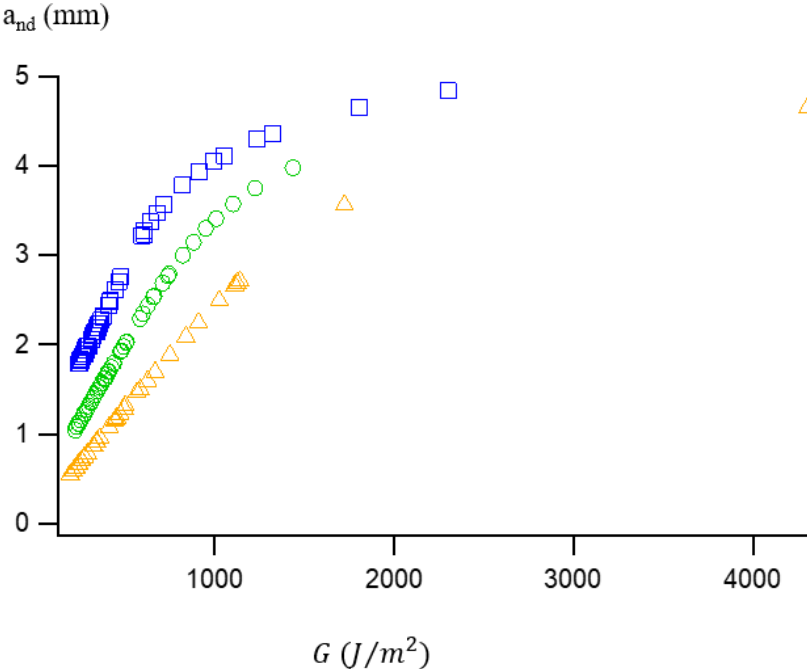


Figure 16 Effect of the initial notch length on the crack length as a function of the energy release rate for samples (initial notch length: blue 1.8 mm, green 1.0 mm, yellow 0.5 mm)

Figure 16 shows the crack length as a function of the energy release rate during crack propagation obtained from Eq. 14. Because of the difference in local deformation and stress, the shorter the initial crack length is, the higher the energy release rate will be for the same crack length during propagation.

## 1.2. Quantification of chain scission on fracture surfaces

We can describe fracture at the molecular scale simply as being driven by molecular arguments, which predicts that breakage of bonds is required to create a new surface. Bond breakage at the crack tip should be the consequence of a local deformation (or a local stress) overpassing a threshold value. In the picture where molecular arguments prevail, this threshold deformation (or stress) should only depend on the chemical nature of the chain, and not on the initial notch size. However, initial notch length determines the critical stress and stretch at which the crack propagation will start. We can wonder if the nominal stress and stretch of the notched sample in the far field will affect the chain breakage happening at the crack tip.

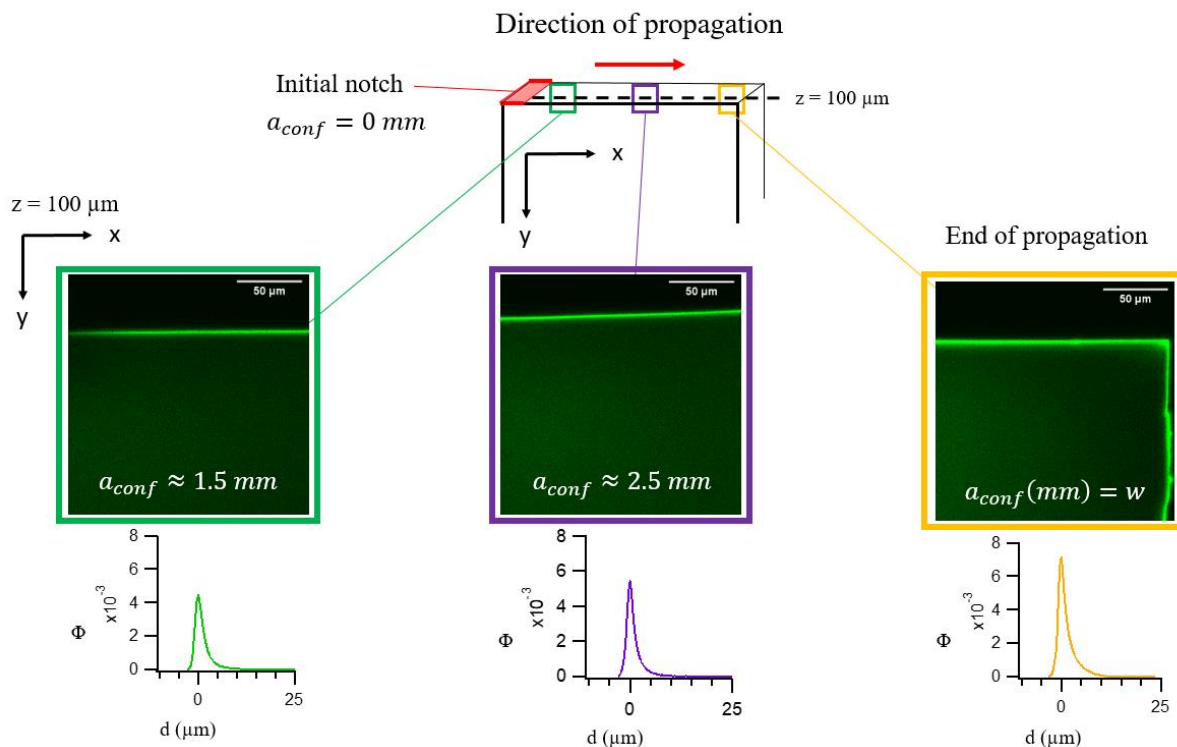


Figure 17 Representation of the post-mortem analysis. Confocal imaging is performed in the plane normal to the crack surface, at  $100 \mu\text{m}$  below the sample surface. Ratio of activated mechanophores as a function of the distance from the crack surface

We performed confocal imaging on DASN0.5 samples with three different initial notch lengths (0.5, 1.0 and 1.8 mm). Images are taken along the crack propagation surface as represented in Figure 17, in a

plane normal to the surface, at 100  $\mu\text{m}$  in depth. The confocal images recorded are processed as described in Chapter 4 section 3, and a normalized areal number of broken strands can be determined, these are represented in Figure 18.

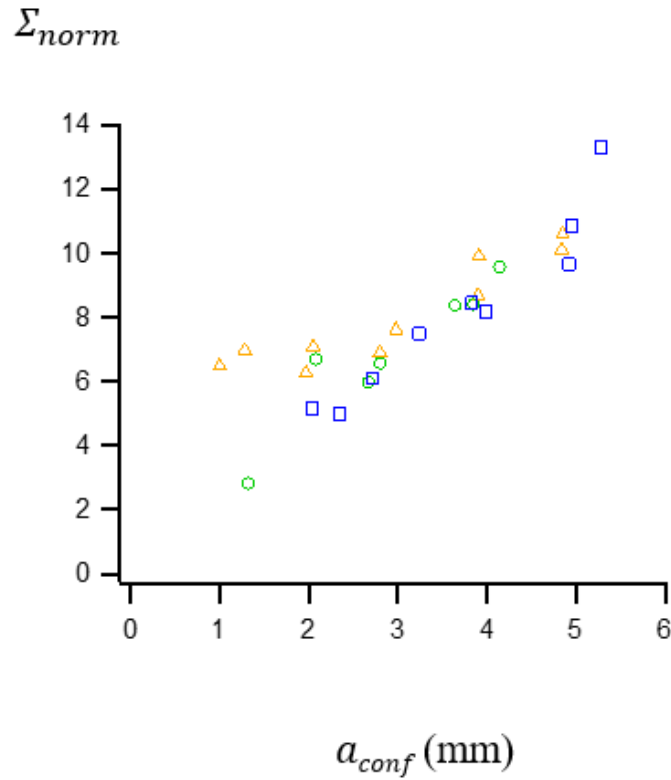


Figure 18 Post-mortem analysis of bond breakage along the crack path reported as a normalized areal number of broken chains  $\Sigma_{norm}$  as a function of the crack length  $a_{conf}$  for samples with different initial notch sizes (blue 1.8 mm, green 1.0, yellow 0.5), filled and unfilled markers corresponds to different series of experiments

### 1.3. Discussion

The classic fracture mechanics continuum vision of soft network fracture [3] states that crack propagation is governed and driven by the energy release rate. This description takes into account all the energy dissipation mechanisms that can be involved in the high deformations reached in soft network fracture.

The molecular vision of fracture requires that in order to propagate a crack (equivalent to creating a new surface) at least all the chains crossing the crack surface need to be broken.

The description of Gent and Schultz merged the two visions by separating the contributions to the fracture energy: the molecular damage energy and the dissipated energy from other mechanisms. Assuming that we can generalize the original description of Gent and Schultz, we would expect:

$$\Gamma = \Gamma_0(1 + f(v, T))$$

Where  $\Gamma_0$  is the energy from chain scission and  $f$  a function of crack velocity  $v$  and temperature  $T$ .

The energy from chain scission can be described as the energy released by the breakage of a chain times the number of broken chains.

We verify this description experimentally: at a constant strain rate and temperature, regardless of the initial notch size,  $\Gamma_0$  should be proportional to the areal density of broken chains  $\Sigma_{conf}$  or (normalized value  $\Sigma_{norm}$ ) that we can measure with the confocal imaging and a quantification process.

Assuming that the crack moves quasi-statically, we estimate  $\Gamma$  at each moment during the crack propagation as  $\Gamma = G$  by saying that all the released elastic energy is dissipated to propagate the crack (no kinetic energy of propagating crack).

To compare the energy release rate  $G$  obtained from the mechanical data/image analysis and the normalized areal number of broken strands  $\Sigma_{norm}$  quantified from the confocal images, we need to find the position at which the confocal image was taken which corresponds to the crack length from mechanical data/video processing, as shown in the Figure 19. So that we can use the position along the crack surface (which is the crack length) as reference and compare  $G(a_{nd})$  and  $\Sigma_{norm}(a_{nd})$ .

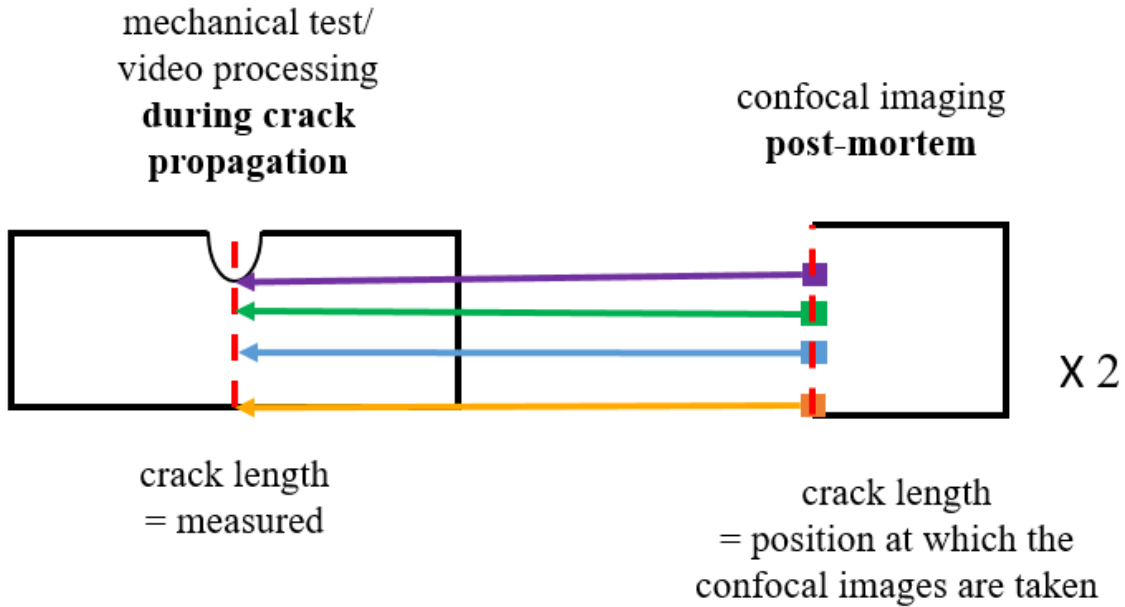


Figure 19 schematic representation of the crack length measured during crack propagation compared to the crack length at which the confocal images are taken post-mortem.

It is possible that the crack length at which the confocal image was taken corresponds to a value in between two crack lengths estimated in two adjacent images of the crack propagation video. When this happened, the closest crack length value from the video analysis was selected to compare  $G(a_{nd})$  and  $\Sigma_{norm}(a_{nd})$ .

The comparison between the crack length extracted from the video analysis and the crack length at which the confocal images were taken is reported in the Appendix.

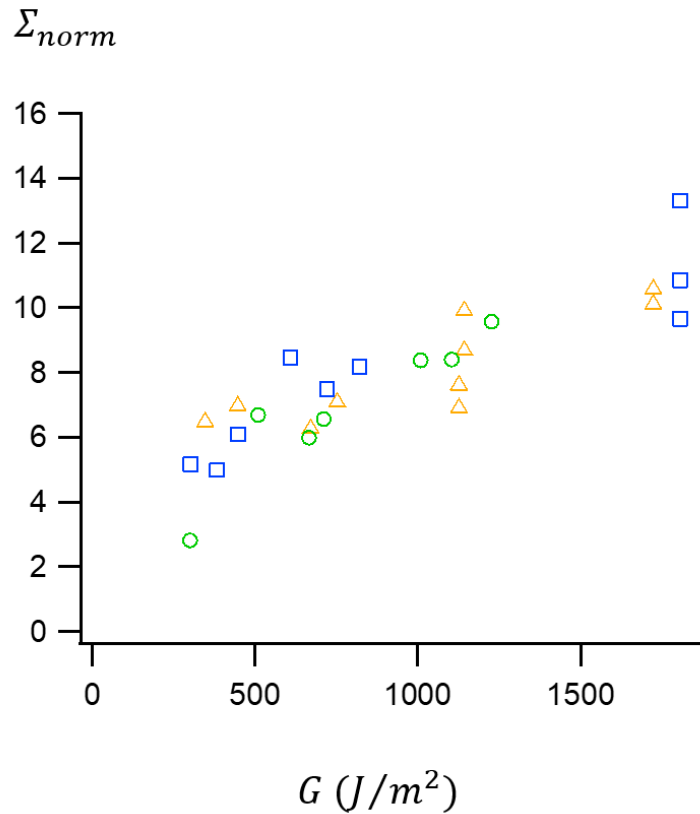


Figure 20 Post-mortem normalized areal number of broken chains  $\Sigma_{norm}$  as a function of the energy release rate  $G$  for samples with various initial notch sizes (blue 1.8 mm, green 1.0, yellow 0.5)

As described in section 1.1.2, we estimated the energy release rate from the model of Liu et al. [5] for each crack tip position during the crack propagation, where  $G$  depends on  $a_{nd}$  in the single-edge notch geometry. We assume that at each moment of the propagation, the fracture energy  $\Gamma$  of the sample (with a propagated crack length  $a_{nd}$ ) is equal to the energy release rate at such crack length ( $a_{nd}$ ).  $\Sigma_{norm}$  measured along the crack propagation path also depends on  $a_{nd}$ .

Figure 20 shows experimentally a small, if any, effect of the initial notch length on the normalized areal density of broken chains  $\Sigma_{norm}$  as a function of the energy release rate  $G$  (calculated as a function of the crack position in section 1.1.2).

Notably, despite the differences in crack propagation rate, critical stretch and stress induced by the variations in initial notch length, the energy release rate  $G$  as defined by Rivlin and using the corrected values of Hui and coworkers [5], remains a good parameter to describe the quantity of broken chains at the crack tip validating directly the fracture mechanics approach for such soft materials.

This result shows experimentally for the first time that even at high deformation, during a crack propagation, the bond breakage at the crack tip is governed by the energy release rate of the sample. As

the probability of bond scission is controlled by local stretch, this confirms the LEFM description of the crack tip field where  $G$  is related to a local stretch and stress.

In a second part of this chapter, we investigate another contribution to the fracture mechanics which is the nucleation of a crack.

## 2. Fracture of unnotched samples

In their real life usage, the failure of materials often comes from the catastrophic propagation of a crack nucleated at one pre-existing defect. If we picture an idealized network, as represented in Figure 21 (A), when stretched all the chains in the direction of deformation will bear the same load. Close to the chains limit of extensibility, when one chain breaks, the stress previously supported by this chain, will be transferred to the surrounding chains which will induce their breakage as well, and a crack will propagate catastrophically. If we picture a real network, as represented in Figure 21 (B), the distribution of chain length and chain conformations should lead to breakage of the shorter and more stretched strands (in the direction of traction) that will be more randomly distributed in the network. The stress previously supported by these chains will be transmitted to the surrounding chains which may lead to clusters of chains breakage macroscopically invisible in the material. These clusters may grow independently, and once one cluster reaches a critical size, the stress concentrates and a crack propagates.

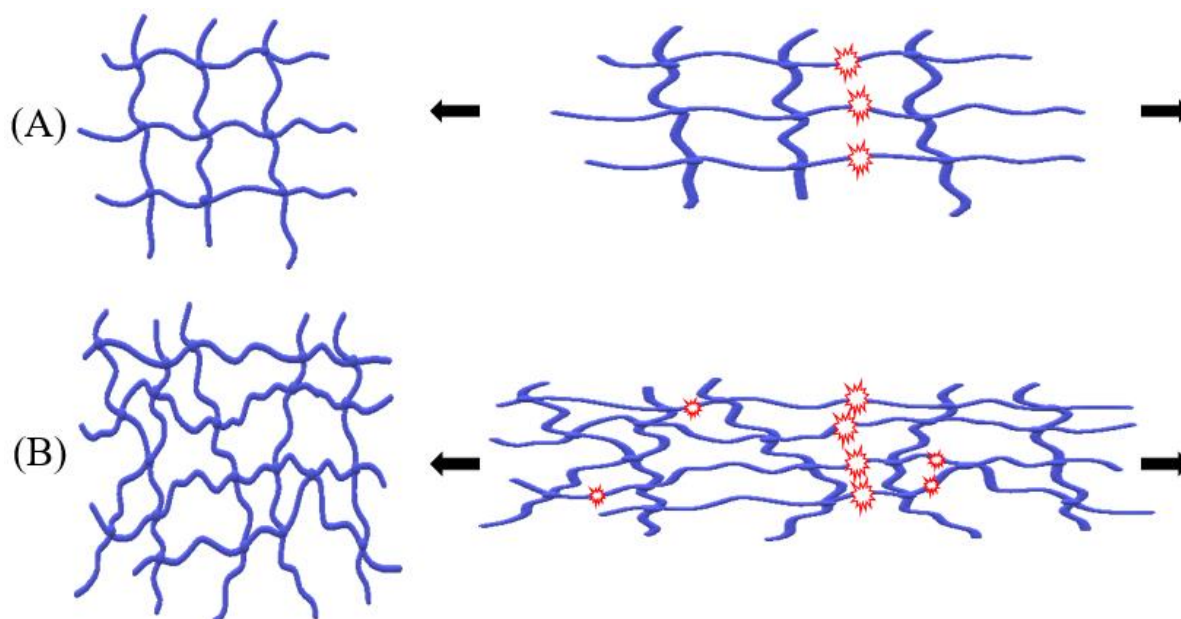


Figure 21 Representation of fracture in a “ideal network” (A) and in a conventional network (B).

We aim at observing these potential clusters of broken chains at the origin of crack propagation. Using mechanochemistry, we stretched samples up to failure and observed post breakage what happened at the crack initiation point at the molecular level. In principle the mechanochemical tool enables us to also

look for other observable clusters of broken bonds elsewhere in the broken sample that may not have evolved into a propagating crack.

## 2.1. Mechanical reproducibility

Before observing chain breakage in a broken single network elastomer, we want to verify the reproducibility of the fracture process. We assume that the way the samples are cut in a dogbone shape prior to deformation will introduce defects at the edges which will be at the origin of crack propagation. The size of these defects should depend on the way the sample is cut.

We usually cut our samples with a punch, but we know this introduces defects at the sample edges. We decided to try another cutting method, using pressurized water, as we believed this would help us achieve a “cleaner” cut with less defects at the edges.

We performed uniaxial extension on SN0.5 dogbone shaped samples cut with a punch (sample 1 to 9) and cut with pressurized water (sample 10 to 12) at constant crosshead speed fixed to  $50 \mu\text{m/s}$  ( $\dot{\lambda} = 3.33 \times 10^{-3} \text{ s}^{-1}$ ).

Stress-stretch curves are summarized in Figure 22. All samples presented below, broke in the region of interest and not under the clamps.

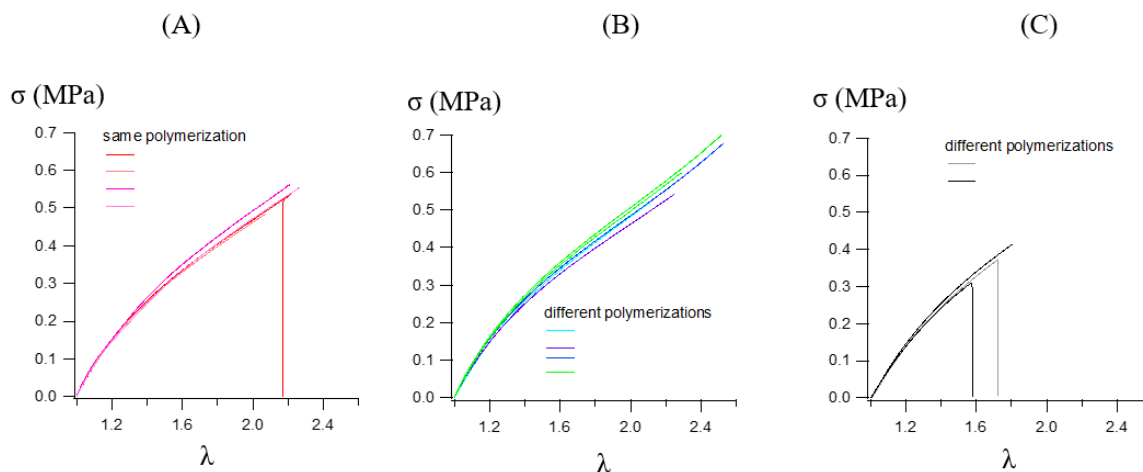


Figure 22 Uniaxial extension of dogbone samples cut with a punch (A) from the same batch or from different batches (B), or samples cut with pressurized water from different batches (C).

For the same type of material, the breakage point (the critical stress and critical strain) varies and highly depends on the way the sample is prepared. The punch seems to introduce the same defect length at the edges of the sample as most samples from the same polymerization batch break at the same critical point in the stress-stretch curve. Unfortunately, the pressurized water seems to introduce a larger defect that

is more random, which is the opposite of what we were looking for. In the following, we only worked with samples cut with a punch for reproducibility and ease of processing.

It is possible to get an estimate of an initial defect size  $c$  from the material's toughness  $\Gamma$  and the elastic energy  $W$  (the area under the stress-strain curve). Depending on the model chosen to estimate  $G$  and  $\Gamma$  (equal to  $G$  at break), we don't find the same numerical value for the defect length.

The Greensmith's formula leads to an averaged defect length of  $100 \mu\text{m}$  and the formula from the work of Liu et al. leads to an averaged defect length of  $250 \mu\text{m}$ .

## 2.2. Direct observation

The fracture of an unnotched polymer network occurs by fast crack propagation. It couldn't be recorded with the extensometer (at  $0.22 \text{ s/frame}$ ) that was used with the tensile test machine. We needed a way to know where the propagation started. It is however possible to identify the crack initiation by looking at the crack surface. It corresponds to the region of sample where the surface is very rough.

We performed conventional microscopy of the crack surface of broken samples to find the region of crack initiation. Figure 23 is an example of what could be observed with the microscope at magnification  $\times 50$ .

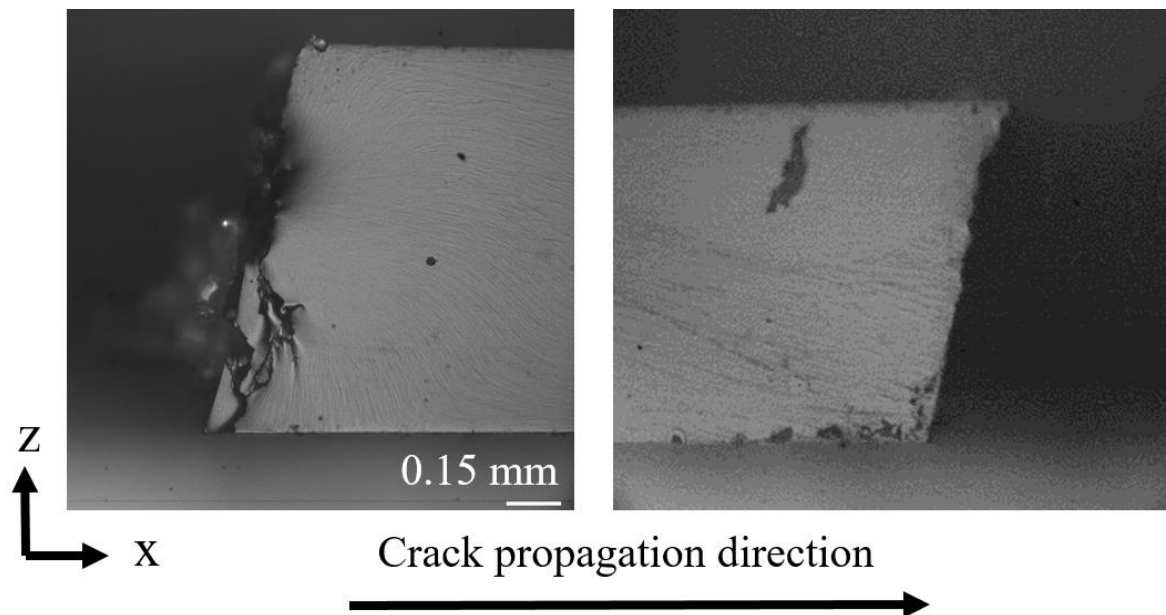


Figure 23 Post-mortem microscope images of the crack surface of propagation at the border of the unnotched samples. The left image corresponds to the crack initiation surface and the right image corresponds to the end of propagation surface.

We can observe a rough surface at the left edge of the left picture in Figure 23. It corresponds to the early stages of propagation where crack bifurcations are observed. Then the crack accelerates and the surface becomes smooth.

Conventional post-mortem microscopy imaging of the surface gives information on the direction of propagation, especially the region where the propagation started. However, surface observations are qualitative and questions remains on the extent of damage and chain breakage occurring deeper in the material. The presence or not of clusters of broken chains which didn't propagate a macroscopic crack remain invisible with conventional optical microscopy, but may become observable with confocal imaging.

Once we know the crack direction of propagation and the region of crack initiation, it is possible to image the crack surface, and volume below the crack surface, following the confocal imaging process, detailed in Chapter 4 section 3, to correlate the quantification of bond breakage with the theoretical crack length (which will be the position along the crack surface where imaging is performed). We performed confocal microscopy to get the best resolution possible.

Confocal imaging microscopy enables us to observe the fraction of broken bonds in depth in the sample at a spatial resolution as good as 1  $\mu\text{m}$ . Zones where crack propagation starts where observed. Images of crack initiation are reported in Figure 24.

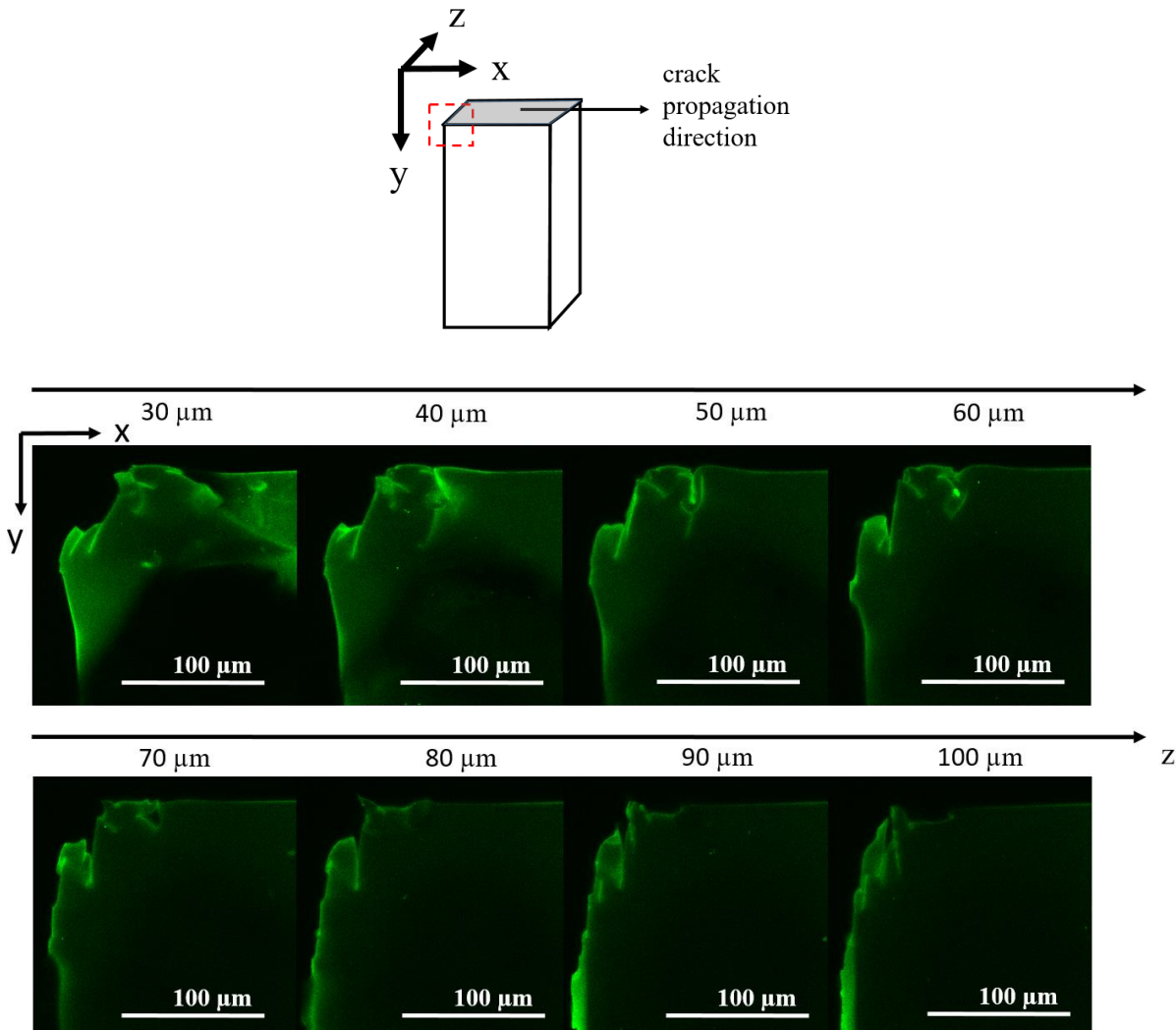


Figure 24 Post-mortem confocal images of crack initiation as a function of depth for one unnotched samples. The red square on the scheme represents the x-y zones images as a function of the depth (z).

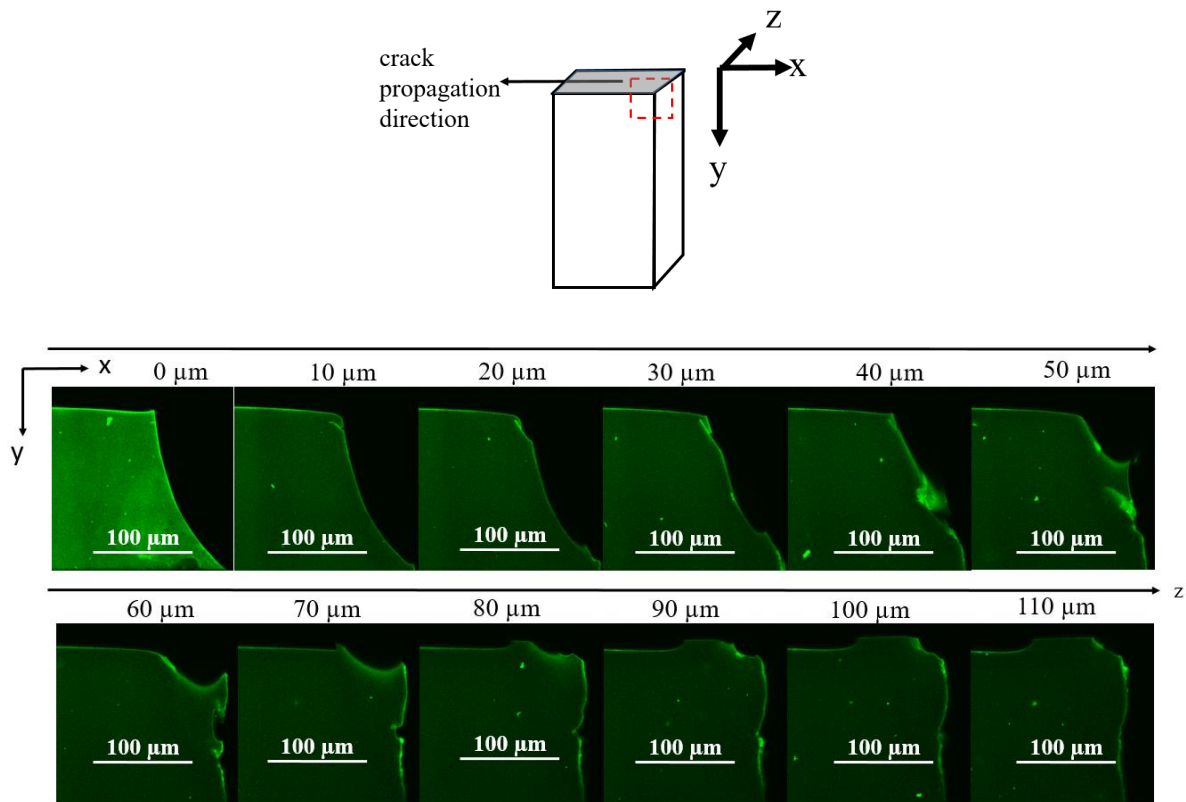


Figure 25 Post-mortem confocal images of crack initiation as a function of depth for another unnotched samples. The red square on the scheme represents the x-y zones images as a function of the depth (z).

We observe bifurcations and mechanophores' activation at the crack initiation point in the volume of the sample. Nucleation of damage in conventional polymer networks is not only a surface process. However, the punch cutting process introduced irregular damage on the edges of the original samples (parallel to the y axis) that activates the mechanophores. Then it becomes difficult to differentiate activation at the border due to nucleation of activation at the border due to cutting.

We looked for other damaged zones elsewhere than the crack propagation region, mostly at the border of the sample. Unfortunately, the way of preparing the sample for mechanical tests activates the mechanophore at the sample edges and makes it difficult to discriminate between activation resulting from tensile test damage and damage from cutting with a punch. No clusters of activation of noticeable activation were observed in the DASN0.5 samples.

The mechanophores activation could be quantified along the crack propagation surface following the strategy presented in Figure 17. If we consider that nucleation is equivalent to a "notch" of a length equivalent to the defects length, then we should obtain the same results as presented in the first section

of this chapter, where the ratio of broken chains increases in the direction of crack propagation. Results are reported in Figure 26.

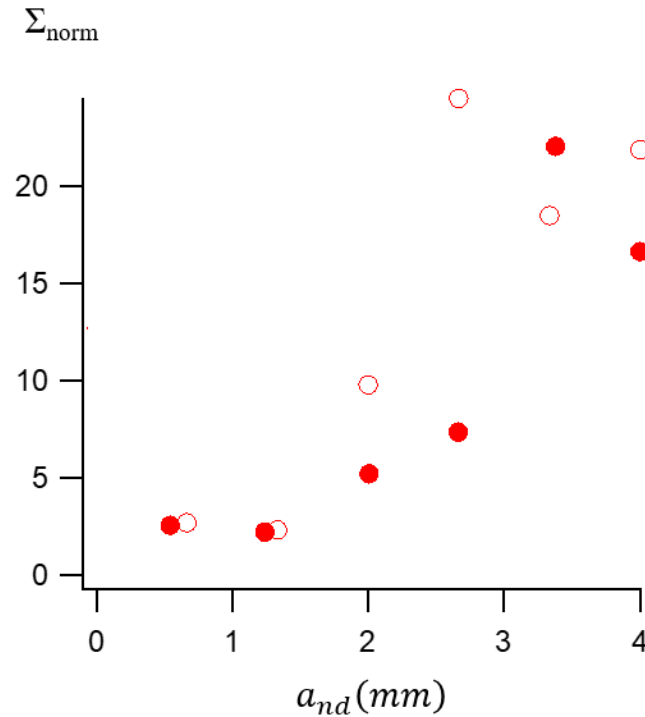


Figure 26 Normalized areal number of broken chains along the crack surface in the direction of propagation)

As expected, the normalized areal number of broken chains increases with the position along the crack surface in the direction of propagation. However, Figure 26 shows that there seems to be two regimes of propagation: a first regime where the activation is low and a second one where the activation is much higher. This should correlate with the propagation speed that increases as the crack propagates. Unfortunately, due to the low frame rate (0.22 s/frame) and the very fast propagation, we couldn't record images of the crack propagation, neither extract the propagation speed.

The fast crack propagation for the unnotched sample made it impossible with our experimental set-up to record enough images of the crack propagation to estimate the local deformation at the crack tip during propagation. Anyway, we made the assumption that the local deformation remains equal to the far field deformation, and estimate an energy release rate during the crack propagation.

We could then compare the variation of the normalized areal density of chain with the estimation of the energy release rate, to the rest of the notched samples analyzed before. The results are shown in the Figure 27.

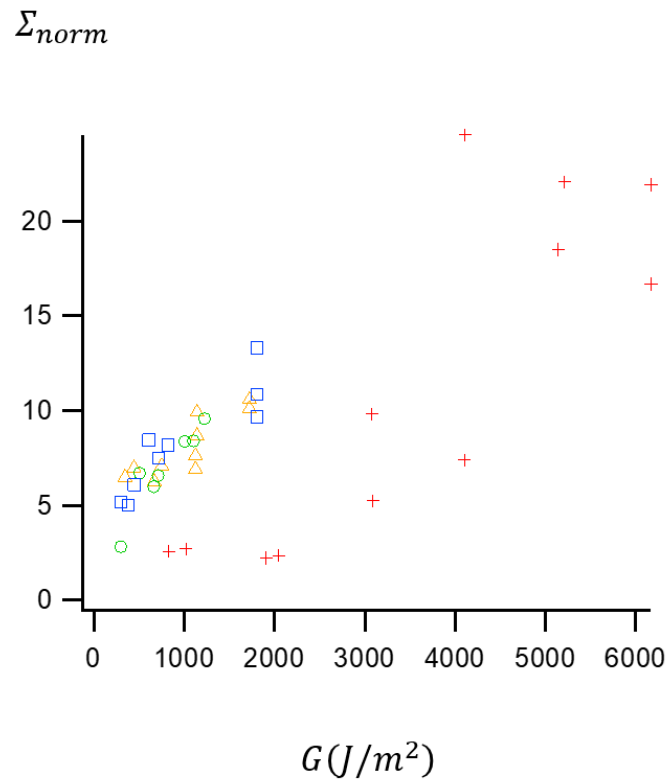


Figure 27 Normalized areal number of broken chains as a function of the energy release rate during the propagation of a crack in an unnotched sample (in red) and three notched samples with different initial notch length (blue 1.8 mm, green 1.0, yellow 0.5).

The results show that the unnotched sample reach much higher energy release rates than the notched samples. This is due to the high deformation reached by the sample before the propagation of a crack. However, interestingly the normalized areal density of broken chains of the unnotched sample does not fall onto the previous trend. In the unnotched sample, the beginning of crack propagation doesn't break as many chain as in the notched samples which suggests the fast propagation of a fairly sharp (closed) crack. It may also be that for this fast crack propagation the assumption of quasi-static propagation does not hold and  $G \gg \Gamma$ .

### 2.3. Effect of the viscoelasticity

As discussed above, in these poly(ethyl acrylate) based DASN0.5 samples we did not observe clusters of activated mechanophores elsewhere in the samples that would have indicated the presence of other clusters of damage that did not lead to crack propagation. . Until now, we have worked with the same network, made of PEA, whose glass transition temperature ( $T_g$  around  $-20$  °C) is well below ambient temperature at which the mechanical tests are performed. We know that materials closer to their  $T_g$  reach higher values of fracture energy, due to the intensification of the viscoelastic dissipative mechanisms,

that slow crack propagation. We believe that working with a network with a higher  $T_g$  should facilitate the observation of clusters of broken chains somewhere where no macroscopic crack occurred.

To do so, we synthesized a crosslinked single network of poly (methyl acrylate) (MA) following the same formulation as for the DASN0.5. We only varied the molar concentration of crosslinker to 0.43 mol% in order to reach similar numbers of monomer units between crosslinks. We performed tensile test experiments on dogbone samples of DASNMA0.4. The glass transition temperature of DASNMA0.4 is approximately  $+18\text{ }^\circ\text{C}$ . The tests were performed at  $22\text{ }^\circ\text{C}$ , which is quite close to the DASNMA0.4  $T_g$  and enhances the viscoelastic effects. The stress-stretch curve of the unnotched MA network is represented in Figure 28, with one typical stress-stretch curve of unnotched DASN0.5.

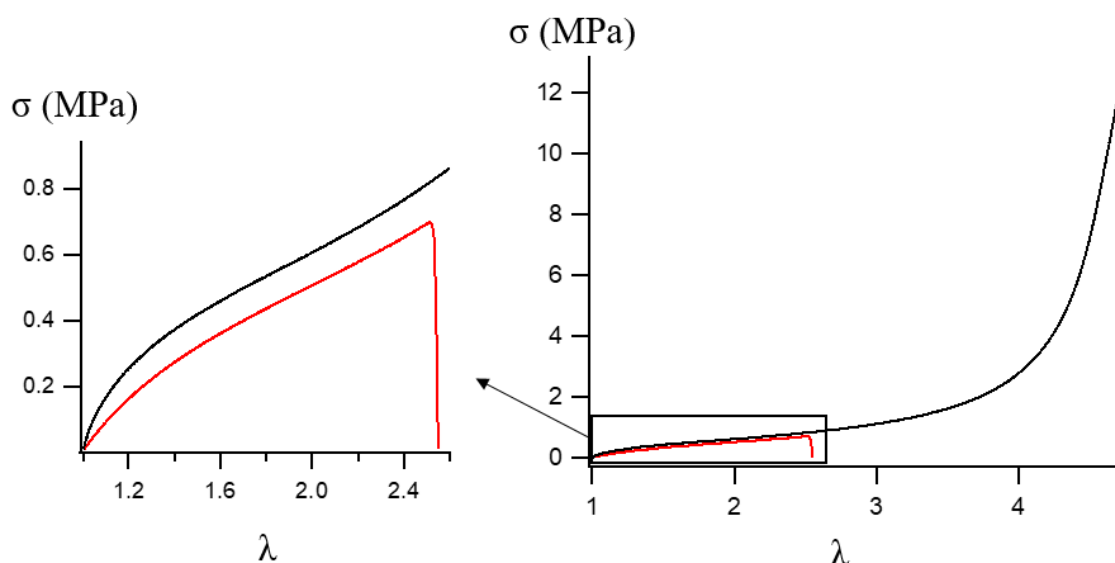


Figure 28 Uniaxial extension of unnotched DASNEA0.5 (red) and DASNMA0.4 (black)

As expected, Figure 28 shows that DASNMA0.4 breaks at a much higher stress and stretch than DASN0.5. The DASNMA0.4 sample demonstrates a significant strain hardening behavior above  $\lambda = 4$ , as it is close to the theoretical limit of chain extensibility. There is a high probability that the shorter chains of the MA network break in the bulk before the macroscopic failure of the sample.

To verify the previous statement, we performed confocal imaging of the broken DASNMA0.4 and looked for clusters of chain scission far from the crack propagation surface.

We noticed first an overall activation in the bulk of the sample. Compared to the activation in the bulk in EA samples,  $\Phi \approx 0.10\%$ , taken as noise, DASNMA0.4 shows a bulk activation three times higher at  $\Phi \approx 0.36\%$ .

We also observe a micrometer crack at the edges of the sample, far from the crack propagation surface, reported in Figure 29. It confirms that clusters of broken chains can exist elsewhere than the crack surface, and it is more easily observable in samples which demonstrate strain-hardening.

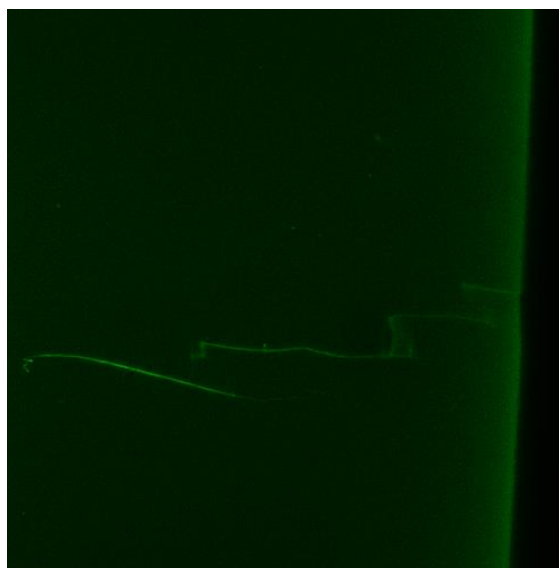


*Figure 29 Localized damage after breakage far from the crack propagation zone in SNMA0.4*

## Conclusion

In this work, the use of a confocal microscope gave us access to a higher image spatial resolution ( $\sim 1 \mu\text{m}$ ). It enabled us to precisely quantify the areal density of broken chains in broken crosslinked single PEA networks, which was not possible with the previous low magnification microscope set-up. Our results show that the density of broken chains, near the crack surface, systematically increases in the direction of propagation.

We then looked into the effect of the initial notch length on the crack propagation from a macroscopic and a microscopic point of view. We initiated cracks, of three different initial lengths, in samples from the same PEA polymer network, tagged with a mechanofluorescent molecule that activates upon breakage.

According to LEFM, the energy release rate is related to the local stretch and stress at the crack tip which controls bond breakage. We could verify experimentally if this statement remains true for highly elastic materials by experimentally checking the dependence of the broken chains density at the crack tip with the energy release rate.

The mechanical study confirmed that the onset of propagation of the crack commonly defining the fracture energy  $\Gamma$  is independent of the variation of critical stress and stretch (far field) with the initial

notch length. From video analysis, we could estimate the crack length in the unloaded state at each step during crack propagation from which we could estimate the energy release rate at all times during the propagation. The post-mortem confocal imaging of the same samples gave microscopic information on the quantity and location of broken chains.

We confirmed experimentally for the first time, from the comparison of the energy release rate  $G$  (estimated by the mechanical data and video analysis) to the normalized areal density of broken chains  $\Sigma_{\text{norm}}$  (estimated by the confocal images analysis), that the ratio of broken chains at the crack tip, during the crack propagation, is governed by the energy release rate of the sample. And this remains true despite the differences in (far field nominal) stress and stretch induced by the variation of initial notch length that could have affected the local viscoelastic dissipation at the crack tip and the ratio of broken chains.

In the second part, we looked into the nucleation of a crack. The mechanical study of unnotched samples highlighted the importance of samples preparation on the creation of defects that would lead to a failure of the material. Confocal imaging showed that nucleation mainly occurred from the edges of the samples. The complexity of the nucleation mechanism could be experimentally visualized. We observed that the chains scission occurs in a volume below a rough surface with various crack bifurcations. Quantification of chain scission in the initiation region (by confocal image analysis) was limited by the mechanophores' activation at the edges coming from the sample preparation.

The crack propagation in an unnotched sample differs from the typical crack propagation behavior in notched sample. The variation of the normalized areal density of broken chains  $\Sigma_{\text{norm}}$  as a function of the energy release rate  $G$  showed that the crack propagation in an unnotched sample break fewer chains at the beginning of the propagation while the sample reaches higher  $G$ .

Due to the stochastic nature of the polymer network, we looked for molecular signs of chain breakage far from the fracture surface, in samples tagged with a mechanofluorescent molecule. No such thing was observed in PEA samples, possibly due to the resolution limits of the confocal microscope.

We then worked with PMA samples also tagged with the mechanofluorescent molecule. This sample, with a  $T_g$  close to ambient temperature, is more viscoelastic than the previously tested sample. Thanks to its dissipative network, the material's breakage point occurred at a much higher extension after a strong strain hardening. The confocal images revealed the existence of non-negligible activation in the bulk of the material and localized correlated mechanophores' activation in the form of micrometer size fracture lines, far from the crack surface, at the edges of the material. This encourages us to believe in a transition between random chain breakage and correlated chain breakage involved in the nucleation of fracture.

## Appendix

### Notched samples

#### Estimations of the deformation

The differences between the average deformation  $\lambda_{avg}$  and the local deformations in front of the crack  $\lambda_{loc}$  estimated from the linear model and the Mooney-Rivlin model are shown in Figure 30, for a sample DASN0.5 with an initial notch length of 0.5 mm. The plot starts when the force reached a maximum as it is considered to be the start of crack propagation and is the range of interest.

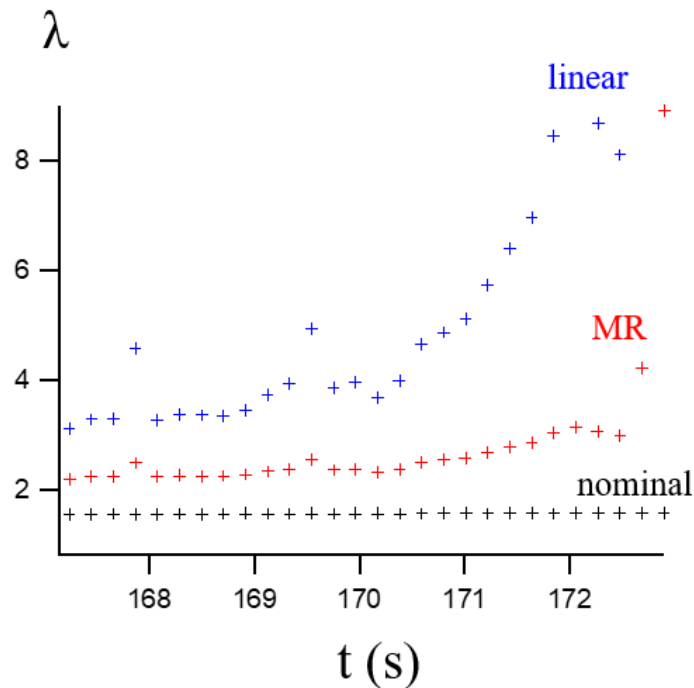


Figure 30 Comparison between experimental estimation of lambda local in front of the crack tip during crack propagation (blue linear model, red model of Mooney-Rivlin) and nominal lambda (black) as a function of time  $t$ .

As expected, the farfield average deformation, in black in Figure 30, is lower than the average local deformation in the crack plane and doesn't seem to vary much as the crack propagates compared to the local deformation. It confirms that the nominal deformation neglects the presence of a crack and the inhomogeneity of stress in the sample. The difference between the nominal deformation and the average local deformation increases as the crack propagates and the remaining section reduces because of stress concentration at the crack tip. The local deformation calculated with the model of linear elasticity (in blue), varies more strongly as the crack propagates than the local deformation calculated with the model of Mooney-Rivlin (in red), which is a softening model.

#### Crack length

Figure 31 represents the crack length estimated using the local deformation from the linear model and from the Mooney-Rivlin model.

When we apply a simple linear model to calculate the crack length, the estimation depends only on  $\frac{F}{F_{max}}$  as:

$$a_{nd}(t) = w_0 \left( 1 - \frac{F}{F_{max}} \right) \quad \text{Eq. 17}$$

And Eq. 17 doesn't take into account the initial notch length as shown in the Figure 31.

The local deformation calculated from the Mooney-Rivlin leads to an estimation of the crack length that takes into account the initial notch length, which is an advantage compared to the value from the linear elastic model, as shown in the Figure 31.

However, the highly stretched section of material, when the crack has almost propagated through the entire sample, doesn't follow linear elasticity and strain hardening may be happening very locally as chains at the crack tip reach their limiting extensibility and then break. Both the linear model and the Mooney-Rivlin model don't describe the strain hardening behavior at high extensions. The model of Arruda-Boyce would have taken the strain hardening into account, but we couldn't fit this model on our experimental stress-stretch curves, so we decided to work with the local deformation as estimated by the model of Mooney-Rivlin (Eq. 9).

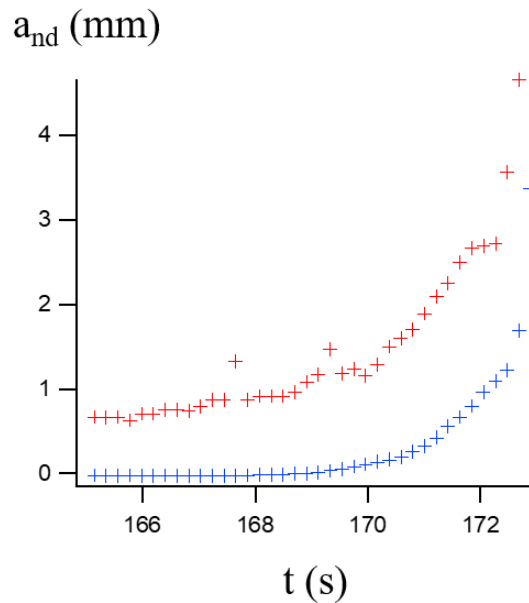


Figure 31 Comparison of crack length estimated from local deformation calculated with the linear model (in blue) or the Mooney-Rivlin model (in red) as a function of time

#### Crack profile as a function of crack length

During the propagation, we estimated the crack profile. The measures are reported in Figure 32.

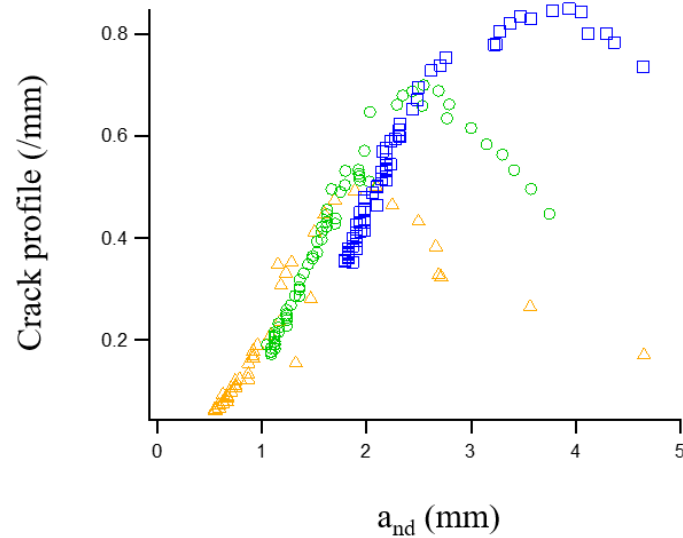
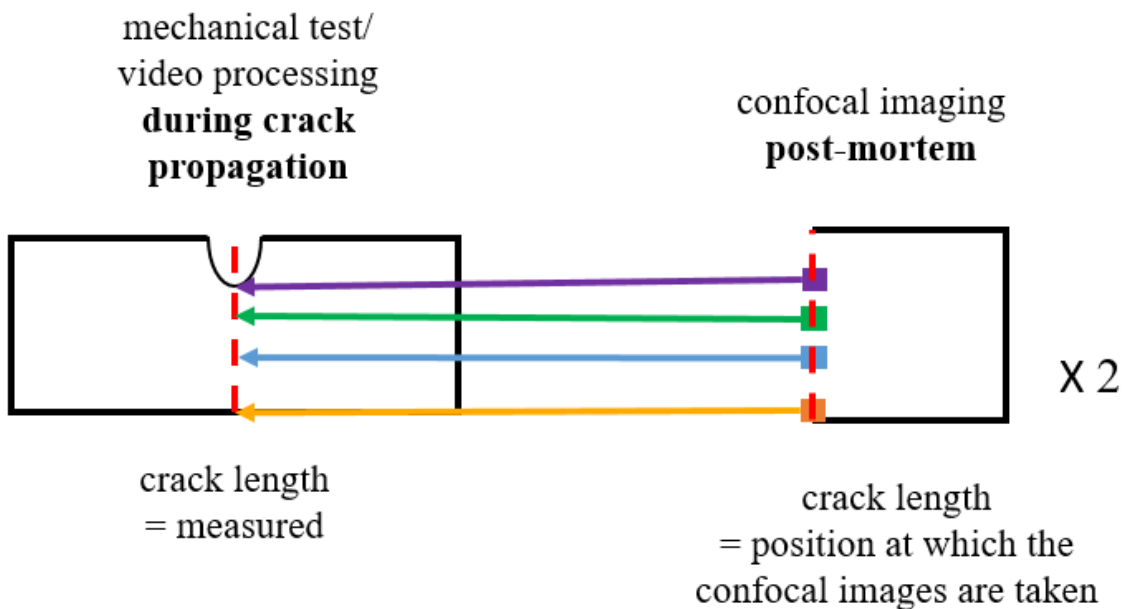


Figure 32 Effect of the initial notch length on the evolution of the crack profile with notch propagation (initial notch length: blue 1.8 mm, green 1.0 mm, yellow 0.5 mm)

The results show that the crack propagation starts with a very open crack profile, then as the crack propagates, the crack becomes pointer and finally it reopens.

### Comparing the data from mechanical and from confocal image analysis

#### Error on the crack length



As shown in the figure above, we need to find the crack length measured from the mechanical test/video processing corresponding to the position at which the confocal images were taken, to compare the data from the mechanical test/video processing to the data from the confocal imaging.

Generally the position on the crack surface where the confocal image was taken does not match exactly the value of crack length of a specific image (of the crack propagation video). Hence, the closest estimated crack length value from the video analysis was selected, to compare the data from confocal

imaging and the data from mechanical test/video processing. This can introduce a small error. This error is shown in Figure 33, where we plot the crack length from confocal imaging minus the crack length from mechanical test/video processing.

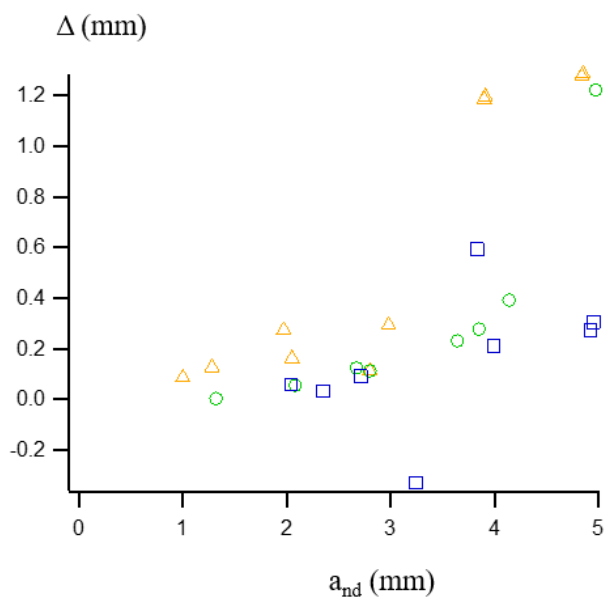


Figure 33 Error  $\Delta$  on crack length from the video analysis as a function of crack length (from confocal imaging). DASNO.5 samples with various initial notch length: blue 1.8 mm, green 1.0 mm, yellow 0.5 mm

Figure 33 shows that the error on the crack length estimated from the video processing is low for the low crack length (below 3.5). At the end of the crack propagation, when the crack length approaches the width of the sample (5), the error increases and the crack length estimated from the video processing tend to underestimate the crack length from the confocal imaging.

### Normalized areal number of broken bonds as a function of mechanical characteristics of crack propagation

If we assume that the crack profile during crack propagation is a good parameter to describe the local deformation of the chains at the crack tip and knowing that chain scission occurs with a higher probability when the chains are extended close to their maximum extensibility, then the crack profile could be a parameter related to the ratio of broken chains. We plot here both the normalized areal density of broken chains as a function of local deformation (Figure 35) and as a function of crack profile (Figure 34).

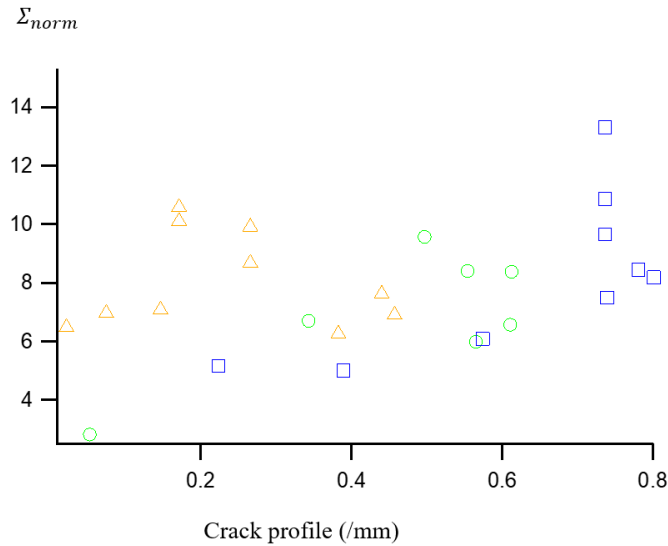


Figure 34 Post-mortem normalized areal number of broken chains  $\Sigma_{norm}$  as a function of the crack profile. DASNO.5 samples with various initial notch length: blue 1.8 mm, green 1.0 mm, yellow 0.5 mm

We believed that the crack profile should give access to the local stress and by extension damage. Figure 34 shows that the normalized areal number of broken chains increases when the crack profile is narrower. However, the precision of our measures of the profile does not enable us to say more on the comparison between samples.

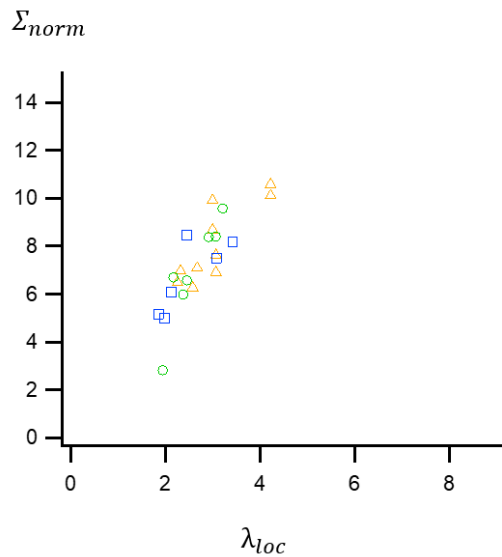


Figure 35 Post-mortem normalized areal number of broken chains  $\Sigma_{norm}$  as a function of the local deformation  $\lambda_{loc}$  for samples with various initial notch sizes (blue 1.8 mm, green 1.0, yellow 0.5)

Based on geometric arguments, the estimated local deformation in front of the crack tip should be a good parameter to describe damage at the crack tip. Varying the initial notch length, when the crack propagates, Figure 35 shows that at similar local deformation, similar normalized areal number of chains are broken.

### Notch cutting

Introducing a notch in a sample is necessary for the study of crack propagation but it is very sensitive to experimental reproducibility and introduces some new molecular defects at the crack tip from the start, that bias the study of nucleation. If we look at the crack tip of a notched samples made with a new sharp razor blade before propagation, we can observe some activation at the very tip, as shown in Figure 36.

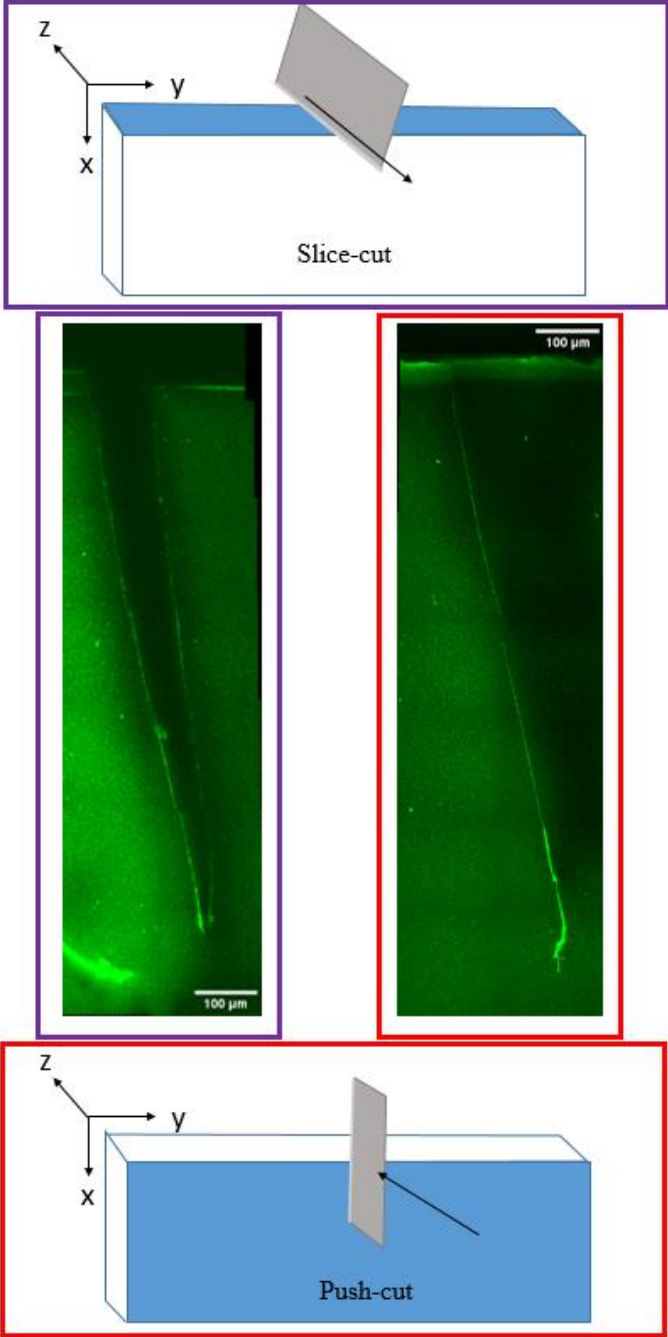


Figure 36 Two notched samples before crack propagation, initial notch made in two different ways: razor blade in the plane  $xz$  pushed in the  $x$  direction to cut through the  $yz$  surface (left) or razor blade in the plane  $xz$  pushed in the  $z$  direction to cut through the  $xy$  surface (right)

## References

1. Creton, C. & Ciccotti, M. Fracture and adhesion of soft materials: a review. *Rep. Prog. Phys.* **79**, 046601 (2016).
2. Tada, H., Paris, P. C. & Irwin, G. R. *The Stress Analysis of Cracks Handbook, Third Edition*. (ASME Press, 2000). doi:10.1115/1.801535.
3. Rivlin, R. S. & Thomas, A. G. Rupture of rubber. I. Characteristic energy for tearing. *Journal of Polymer Science* **10**, 291–318 (1953).
4. Greensmith, H. W. Rupture of rubber. X. The change in stored energy on making a small cut in a test piece held in simple extension. *Journal of Applied Polymer Science* **7**, 993–1002 (1963).
5. Liu, Z., Zakoworotny, M., Guo, J., Zehnder, A. T. & Hui, C.-Y. Energy release rate of a single edge cracked specimen subjected to large deformation. *Int J Fract* **226**, 71–79 (2020).
6. Zhang, W. *et al.* Fatigue of double-network hydrogels. *Engineering Fracture Mechanics* **187**, 74–93 (2018).
7. Gent, A. N. & Schultz, J. Effect of Wetting Liquids on the Strength of Adhesion of Viscoelastic Material. *The Journal of Adhesion* **3**, 281–294 (1972).
8. Sloodman, J. *et al.* Quantifying Rate- and Temperature-Dependent Molecular Damage in Elastomer Fracture. *Phys. Rev. X* **10**, 041045 (2020).

# **Chapter 6**

## **Effect of soft networks structures on fracture studied with mechano- fluorescence**



## Table of contents

Introduction .....	227
1. Experimental methods .....	229
1.1. Materials .....	229
1.2. Mechanical characterization .....	230
2. Results and discussion .....	230
2.1. Mechanical properties .....	230
2.2. Damage quantification .....	237
Conclusion.....	245
Appendix .....	246
References .....	247



## Introduction

In so-called threshold conditions, where no viscoelastic dissipation occurs, the molecular model of Lake and Thomas suggests that when a network breaks, the minimum amount of bond scission and energy dissipation is due to the breakage of a monolayer of bonds crossing the new surface, and each broken strand between crosslink frees an energy which evolves linearly with the strand's length.

Applied to real-life experiments on a given material, this model still predicts the right relation between toughness and the polymer network structure even when viscoelastic dissipation isn't negligible. Up to this day, why this model works so well remains an open question.

The model of Lake and Thomas [1] gives the fracture energy from two main adjustable parameters: the areal number of broken bonds  $\Sigma$  and the energy released per broken strand  $U_{\text{chain}}$ . The areal number of broken bonds can be derived from the network mesh size and the chains' density.

Even in the absence of viscoelasticity, in real-life experience, the stochastic nature of the polymer network inevitably leads to early breakage of shorter strands which encourages us to believe that more than a monolayer of bonds breaks to propagate a crack and create a new surface. It was shown by the work of J. Slotman [2], that bond breakage happens in a volume in front of the crack tip.

Sakai et al. [3] studied the fracture energy of well-controlled tetra-arm PEG gel networks. They found that the model of Lake and Thomas fitted their experimental fracture energy with the introduction of a constant corrective parameter to the mesh size. Their calculations led to estimate the length upon which energy of the bonds should be released which corresponded to 3 times the distance between crosslinks.

Whether it's the areal number of broken chains that is minimized or the energy released by one broken chain that is overestimated, there may be compensating mistakes in the estimations of these adjustable parameters.

The fracture energy, measured experimentally from crack propagation tests, englobes both the number of broken chains and the energy dissipated per chain. Using mechanochemistry, we can have access to the fraction of broken chains alone, and get back to an energy dissipated per chain and per bond.

In previous work [4], J. Slotman tried to investigate the effect of network structure on the fracture energy of soft networks by comparing two PMA samples with different crosslink densities. Her result showed that the relative contribution of chain breakage was lower in the less cross-linked network which couldn't, therefore, explain the increase in fracture toughness with decreasing cross-linking density. She attributed the increase in fracture energy to other dissipative mechanisms such as viscoelastic contribution.

We believe that her analyses can be improved to get clearer results: first, the fluorescent signal was averaged on four images taken in the middle of the crack propagation path which didn't take into account

the evolution of bond scission with crack propagation (shown in Chapter 5) and increases the error bars; secondly, the optical resolution of the confocal microscope is limited, and only PMA samples, which are quite viscoelastic and far from the threshold conditions required by the model of Lake and Thomas, could be imaged.

The use of the confocal microscope enables us to image samples with a higher resolution than with the microscope. Therefore, we will be able to work with Poly(ethyl acrylate) (PEA) samples (far from their glass transition temperature ( $T_g$ ) so less viscoelastic than PMA samples) and image the mechanophore's activation as a function of crack growth.

In this work, we experimentally look into the network structure effects on fracture using mechanochemistry. We synthesize PEA single networks, labeled with mechanophore and with various crosslink densities, and perform notch propagation tests. We follow crack propagation macroscopically and at the micrometer scale. We extract the energy release rate during crack propagation and correlate it to an experimental estimate of the areal number of broken strands.

## 1. Experimental methods

This project aims at investigating the effect of network structure on crack propagation and in particular bond breakage at the crack tip. We work with PEA single networks because they are good model polymer networks previously studied [2,5], and whose synthesis is robust [4,6]. We vary the network structure by varying the molar concentration of crosslinker between 0.25 mol% and 1.5 mol%. Then we performed mechanical tests (uniaxial extension and notch propagation) to verify the network structure effect on the samples' mechanical responses. To couple the mechanical characterization with bond breakage imaging and quantification at the crack tip, we synthesized the same networks with 0.02 mol% of DACL mechanophore introduced as crosslinker (the total concentration of crosslinker remained between 0.25 and 1.5 mol%), performed notch propagation tests, and analyzed the broken samples post-mortem using confocal microscopy. This section focuses on the methods to synthesize and characterize the samples.

### 1.1. Materials

To study the network structure's effect on fracture in bulk material, five PEA single networks were synthesized by UV-induced bulk free radical polymerization (as detailed in Chapter 4 section 1.3) with EA as monomer, BDA as crosslinker, and HMP as UV initiator. The molar concentration of crosslinker was varied between 0.25 mol% and 1.5 mol% as reported in Table 1, to obtain networks with varying chain lengths. The samples are labeled SN<sub>x</sub> where x is the molar concentration of crosslinker.

To be able to observe damage at the molecular scale with the confocal imaging process (detailed in Chapter 4), we incorporated in the networks DACL mechanophore molecules capable of reporting bond breakage. The same UV-induced free radical bulk polymerizations were performed with 0.02 mol% DACL mechanophore as crosslinker, BDA as crosslinker, EA as monomer, and HMP as UV initiator. The total crosslinker molar concentration (BDA and DACL) was varied between 0.25 and 1.5 mol% to obtain the same network structure as the previously synthesized samples without mechanophores. The mechanophore molecules were synthesized by J. Slootman, G. Sanoja, and G. Mellot following a process described in J. Slootman's thesis [4]. The synthesis was quite time-consuming, therefore, the product was carefully used to minimize waste, and the samples containing mechanophores were only used to perform crack propagation, and image and quantify bond breakage. The samples will be labeled DASN<sub>x</sub>, where x is the molar concentration of crosslinker.

For uniaxial extension characterization and rheology, we used samples without mechanophores and assumed that the syntheses were reproducible enough to extend the results to the samples with mechanophores.

## 1.2. Mechanical characterization

Uniaxial extension and notch propagation tests were performed using an Instron tensile setup equipped with a video extensometer that followed marks on the sample and calculated deformation (as detailed in Chapter 2 section 2.3.4). The video extensometer was also used to record images of the sample during the tests, and enable us to perform, later on, video analysis (as detailed in Chapter 5).

We cut with a punch, dumbbell shaped samples (20 mm long and 4 mm wide, with a thickness varying with the sample from 0.4 to 1 mm) for the uniaxial extension tests and rectangular samples (20 mm x 5 mm, thickness between 0.4 and 1 mm and depending on the sample) for the notch propagation tests. Each notch was introduced by hand using a new sharp razor blade in a push-slice motion.

## 2. Results and discussion

### 2.1. Mechanical properties

The network's structure effect on the mechanical behavior in uniaxial extension was verified first, to make sure that the mechanical behavior varied as expected with the crosslinker content. We extracted the contribution of crosslinks ( $E_x$ ) to the Young's modulus  $E$  and estimated the network average chain length ( $N_{cc}$ ) between crosslinks which is expected to increase with decreasing crosslinker content [ref].

#### *Uniaxial extension*

Uniaxial extensions at a stretch rate  $\dot{\lambda} = 3.3 \times 10^{-3} \text{ s}^{-1}$ , at 22°C, were performed on SN<sub>xx</sub> samples (where xx is the crosslink concentration in mol%) with five different crosslink densities between 0.25 and 1.5 mol%. The stress-stretch curves are represented in Figure 1.

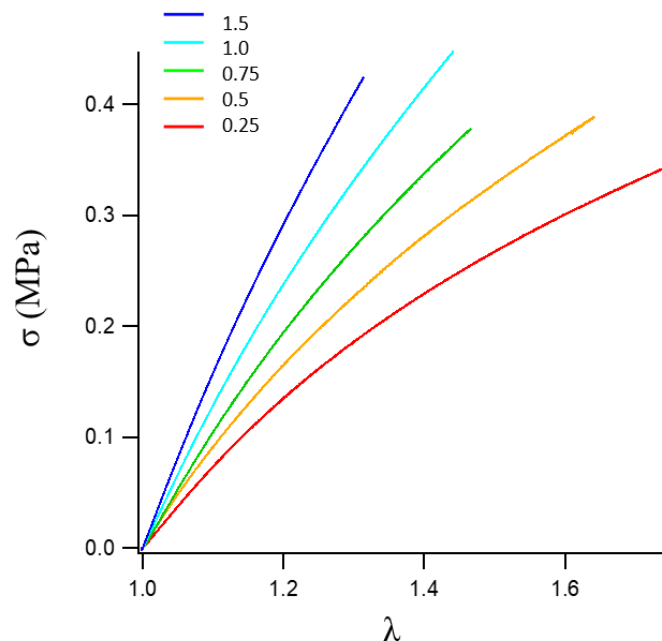


Figure 1 Stress-stretch curves to failure of unnotched single networks with crosslink concentration varying between 0.25 and 1.5 mol%. Stretch rate  $3.3 \times 10^{-3} s^{-1}$ .

From the stress-stretch curves represented in Figure 1, we measured the Young's modulus as the slope of a linear fit to the stress-stretch curve between 1.02 and 1.08. The Young's modulus was found to increase with increasing crosslink concentration. It was to be expected from polymer mechanics as increasing crosslink densities increases chain density, and the low strain modulus is directly related to the number of chains being stretched: so higher chain densities lead to higher modulus. The values are reported in Table 1. It should be noted that the stress and stretch at break, shown in Figure 1, are lower than expected because experimentally the samples broke under the clamps, despite the use of the dogbone shape to limit stress concentration. This happened because the clamps must have been too tight. Anyway, it is shown that increasing crosslink densities reduce the stretch at break. These results are in agreement with what is intuitively to be expected from polymer physics: increasing crosslinker content, increases the chain density ( $v_x$ ), and decreases the average strand length. Shorter chains reach their limit extensibility for lower stretches and should lead to lower extensibilities. Note however that none of these elastomers reach a limiting extensibility of the network (no strain hardening) so that fracture by crack propagation occurs much before the majority of the chains reach their limiting extensibility.

The Young's modulus can be separated into contributions of the crosslinks ( $E_x$ ) and entanglements ( $E_e$ ). We fitted the Rubinstein-Panuykov model [7] to extract the contribution of the crosslinks to the Young's modulus. The entanglements in a polymer network are mainly the results of the monomer side groups. So we fixed the contributions of the entanglement to the numerical values obtained for the best fits

(which were the ones with the largest fit range, equivalent to the larger deformation range, samples SN0.25 and SN0.5). The results are reported in Table 1.

The contributions of crosslinks to the Young's modulus from the Rubinstein-Panuykov model are compared to the Young's modulus in Figure 2. It is shown that the evolution of the Young's modulus evolves linearly with the concentration of crosslinker that was introduced suggesting a relatively constant efficiency, and so is the contribution of the crosslinks to the Young's modulus.

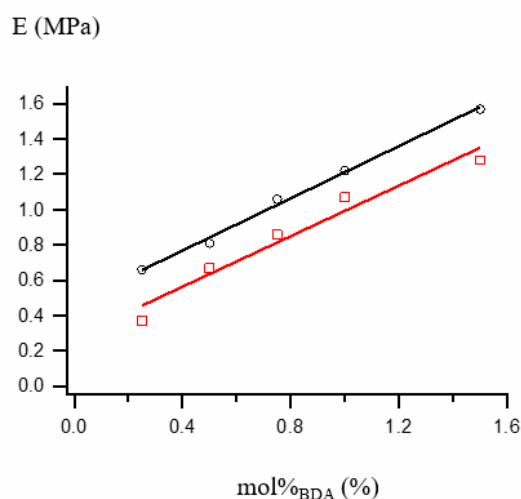


Figure 2 Evolution of the Young's modulus (black) and the contribution of crosslinks to the Young's modulus (from Rubinstein-Panuykov model, in red) as a function of crosslinker molar concentration.

Sample name	mol%BDA <sup>a</sup>	E <sup>b</sup> (MPa)	E <sub>x</sub> <sup>c</sup> (MPa)	E <sub>e</sub> <sup>d</sup> (MPa)	v <sub>x</sub> <sup>e</sup> (/m <sup>3</sup> )	N <sub>cc</sub> <sup>f</sup> (E <sub>x</sub> )	C <sub>1</sub> <sup>g</sup> (MPa)	C <sub>2</sub> <sup>h</sup> (MPa)
SN0.25	0.25	0.66	0.37	0.29	3.00E+25	486	0.095	0.047
SN0.50	0.5	0.81	0.67	0.29	5.43E+25	268	0.124	0.047
SN0.75	0.75	1.06	0.86	0.29	6.97E+25	209	0.179	0.015
SN1.0	1	1.22	1.07	0.29	8.67E+25	168	0.225	0.013
SN1.5	1.5	1.57	1.28	0.29	1.04E+26	140	0.233	0.078

Table 1 Summary of the mechanical characteristic of samples SN. **a.** molar concentration of crosslinker in the single network.

**b.** Young's modulus measured as the slope of the stress-stretch curve in the linear elastic domain. **c and d.** respective contributions of crosslinks and entanglements to the Young's modulus, from the Rubinstein-Panuykov model. **e.** chain density. **f.** Averaged number of carbon-carbon bonds in a network strand between crosslinking points, calculated with Ex. **g and h.** C<sub>1</sub> and C<sub>2</sub> parameters of the Mooney-Rivlin model extracted from fits to the experimental data.

*Notch propagation*

To verify the effect of network structure on the fracture energy of soft networks, notch propagation tests were performed on single edge 1 mm notched samples of DASNxx in the same temperature (22 °C) and stretch rate conditions ( $3.33 \times 10^{-3} \text{ s}^{-1}$ ) as the uniaxial extension tests. The stress-stretch curves are plotted in Figure 3.

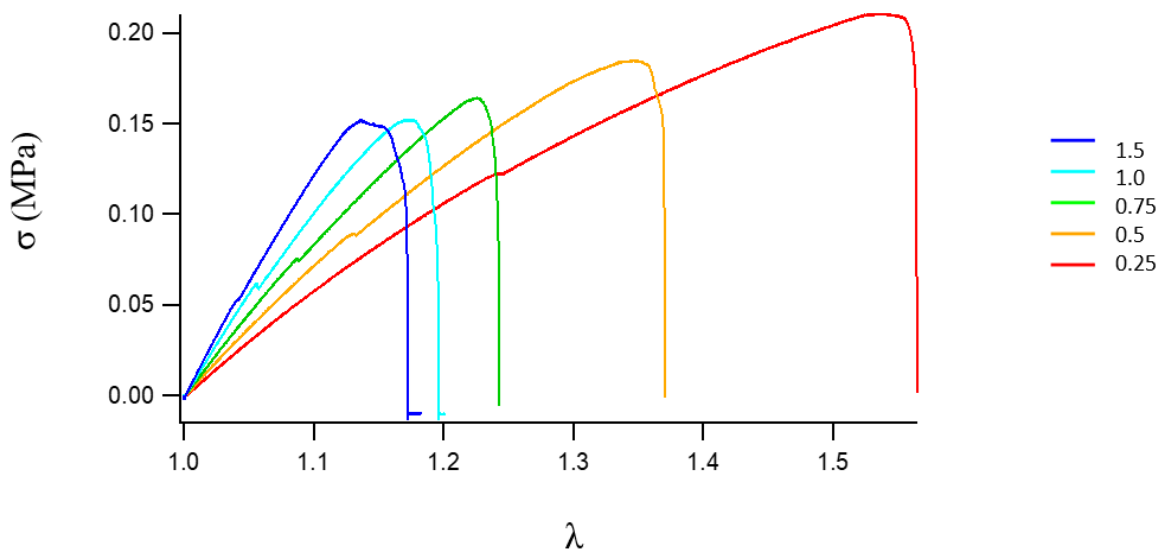


Figure 3 Stretch-stress curves of notched single networks with various crosslink concentrations between 0.25 and 1.5 mol%.  
Stretch rate  $3.3 \times 10^{-3} \text{ s}^{-1}$ .

Figure 3 shows that increasing crosslink densities leads to lower stretches at break. The sample breaks at a lower stretch when the crosslink density increases. As expected by the molecular model of Lake and Thomas, the energy dissipated to propagate a crack increases with increasing chain length.

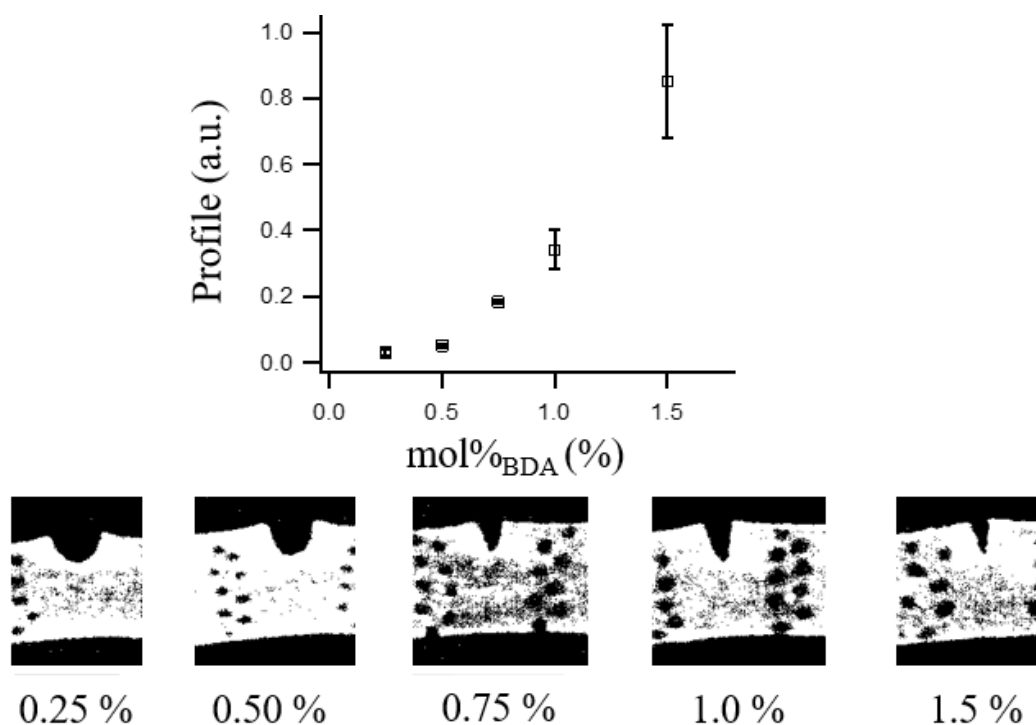


Figure 4 Evolution of the crack profile (corresponding to the maximum force) with the molar concentration of crosslinker

The mechanical data seem in agreement with what is predicted by polymer mechanics. Shorter mesh sizes lead to a lower stretch at break. We verify this by observing and analyzing the crack propagation.

The sample deformation was followed via a video extensometer during the test. The images could be recorded during the test and analyzed after to study the crack propagation characteristics, following the same process as that described in Chapter 5 section 1.1.1. The images give us access to the local deformation, the crack length, the crack propagation speed, and a rough estimation of the crack shape.

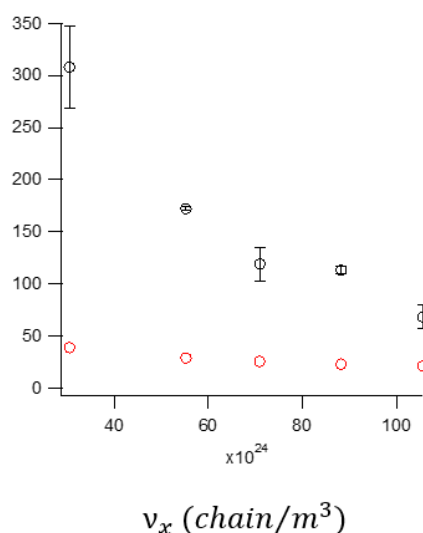
To obtain the crack profile measurement, we decided that the maximum force would be the reference for the start of crack propagation and extracted the image corresponding to the maximum force. Then we binarized it and fitted a parabolic function ( $y=Ax^2+Bx+c$ ) centered at the crack tip, the crack profile corresponding to the coefficient A. The more open the crack profile is, the lower the profile parameter A will be. The results are reported in Figure 4. The images reported show that the crack is more blunted in samples with the lowest crosslink density. The graph translates numerically this observation. This relates with strand length since a lower crosslink density leads to longer chains which extend more before breaking.

%mol <sub>BDA</sub> (%)	$\Gamma$ (J/m <sup>2</sup> )
0.25	308
0.50	172
0.75	119
1.0	113
1.5	68

Table 2 Fracture energy measured experimentally for single networks of varying crosslink concentration between 0.25 and 1.5 mol%, using Greensmith's formula

From the critical stretch at break, we calculated the strain energy by taking the area under the unnotched stress stretch curve. We injected this value into the Greensmith formula [8] to extract the material's fracture energy for each network. Results are reported in Table 2. It shows that the fracture energy decreases with increasing crosslink densities. This is in agreement with the scaling predicted by the model of Lake and Thomas [1]. The experimental values of fracture energies are compared to the theoretical predictions of the Lake and Thomas model in Figure 5. In this figure, we see that there is consequent significant difference between the absolute values of fracture energy from the experimental measurements and from the model of Lake and Thomas, but the trends predicted by the model fit those of experimental values.

$\Gamma$  (J/m<sup>2</sup>)



$\Gamma$  (J/m<sup>2</sup>)

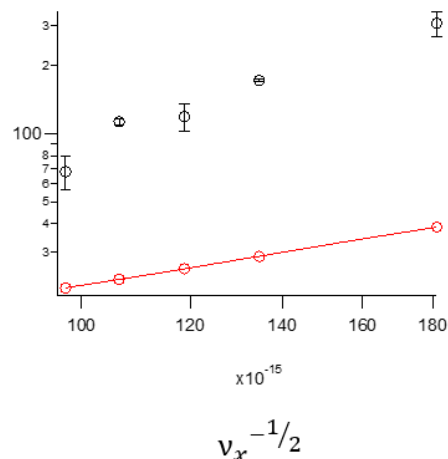


Figure 5 (Left) Fracture energies of single networks with various crosslink concentrations between 0.25 and 1.5 mol%, measured experimentally, using Greensmith formula, (black) and expected from the model of Lake and Thomas (red) as a function of chains density. (Right) Same fracture energies in log-lin axis as a function of the chain density to the power -1/2.

The model of Lake and Thomas predicts that the fracture energy should scale with the inverse of the square root of the chain density [<sup>1</sup>]. So, when the chain density increases, the fracture energy decreases, consistent with Figure 5 (Left). This variation is in agreement with the model. The difference between experimental and theoretical values could be explained by the fact that the fracture energy measured from single edge notch propagation includes also the energy dissipated from viscoelastic dissipation. Somehow, even far from the specific conditions where the model should be valid (no viscoelastic dissipation, only one monolayer of CC bonds break to create the new surface), the scaling relationship between fracture energy and the chain energy density is well described by the model.

Using mechanochemistry coupled with mechanical characterization of crack propagation, our work aims at understanding that the underlying reason for this good agreement.

#### *Energy release rate and crack propagation speed*

The samples are all of the same chemical nature. Though the side groups of the chains remain the same, the efficiency of the crosslinking reaction may lead to more pendant chain population and affect the samples viscoelastic dissipation. The network structure affects the critical stress and stretch at which the crack propagates and the moduli are different, so the elastic energy released by each sample during propagation will also vary with the concentration of crosslinker, which should affect the crack propagation speed. The higher the released elastic energy, the faster the crack should propagate.

A simple way to approximate crack propagation velocity consists in describing crack propagation with an averaged crack propagation speed and an initiation fracture energy. The averaged crack propagation speed is taken equal to the length of the unnotched width filament over the time required for the force to go from its maximum value to zero.

$$v_m = \frac{b_0}{t(F = 0) - t(F = F_{max})} \quad \text{Eq. 1}$$

Unfortunately, we already know that it doesn't explain the discrepancy between the Lake and Thomas model and the reality. So, we decided to follow the crack propagation speed more precisely. To obtain a measure of the crack speed, we fitted the curve of crack length as a function of time and extracted the slope at each time. We also decided to estimate the energy release rate during the crack propagation using the model of Liu et al. [<sup>9</sup>] (as in Chapter 5 section 1.1). The Mooney-Rivlin model was fitted to the plots in Figure 1 to extract the  $C_1$  and  $C_2$  parameters (reported in Table 1) and used in the energy release rate formula given by Liu et al. Crack propagation speeds and energy release rates are reported as a function of position along the crack in Figure 6.

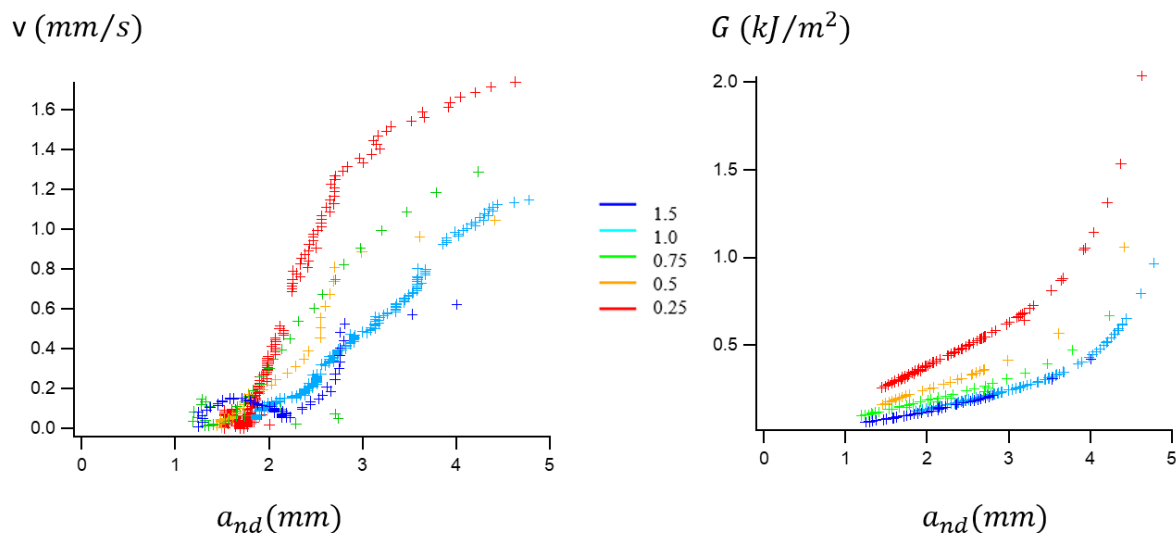


Figure 6 Crack propagation speed as a function of crack length (left) and energy release rate calculated from Liu et al. model as a function of crack length (right) for samples with crosslink densities between 0.25 and 1.5 mol%.

Figure 6 (left) confirms that the crack propagates faster in samples with lower crosslinker concentrations. This is due to the energy release rates  $G$ , represented in Figure 6 (right). The energy release rate is higher in samples with lower crosslinker concentrations. The energy release rate increases as the crack length increases, which explains why once the crack starts propagating, it accelerates, the propagation becomes catastrophic and leads to the fracture of the sample. Note that in this analysis we implicitly assume that we remain in quasi-static conditions and the elastic energy released is dissipated at the tip of the propagating crack, i.e.  $G = \Gamma$  for all points.

## 2.2. Damage quantification

During crack propagation, the dynamic fracture energy includes multiple dissipation mechanisms and can be divided into two main contributions: the energy dissipated from molecular damage (bond scission) and the energy dissipated from viscoelastic friction.

The mechanochemistry tool gives us access to bond breakage quantification as a function of position along the crack and enables us to separate the contribution of damage to the energy release rate.

### *Efficiency of the crosslinking reaction*

In this chapter, for the first time, we want to compare the mechanophore's activation in networks of various structures. Because the mechanophore is incorporated as a crosslinker and the total amount of crosslinker is varied to get different structures, it is important to take into account the efficiency of the crosslinking reaction.

The efficiency of the crosslinker incorporation into the network during the polymerization affects the chain density and the contribution of the crosslinks to the Young's modulus. The crosslinkers may not be homogeneously incorporated into the network or create loops or dead-ends in the network, which would decrease the theoretical density of elastically active chains. As the mechanophore is integrated into the network as a crosslinker, the crosslinking reaction efficiency can affect the ability of the mechanophore to be activated. The mechanophore needs to be attached to the network at both ends to be able to stretch when the sample stretches and break and activate. This aspect was not discussed in the previous chapter because the network structure was constant, so the effect of the crosslinking distribution would have affected all data in the same way, which wouldn't have changed our conclusions. In this work, the variation of structure may affect the crosslinkers' distribution in the network and as a consequence the areal density of broken chains quantified.

Therefore, we focus on the crosslinker concentration's effect on the crosslinking reaction's efficiency. We estimate the reaction efficiency,  $R$ , as the ratio of experimental and theoretical chain densities (respectively  $\nu_x$  and  $\nu_{xth}$ ), in the affine model:

$$\nu_x = \frac{E_x}{3kT} \quad \text{Eq. 2}$$

Where  $E_x$  is the contribution of crosslinks to the Young's modulus from the Rubinstein-Panuykov model (presented in section 1.2).

$$R = \frac{\nu_x}{\nu_{xth}} = \frac{E_x}{E_{xth}} \quad \text{Eq. 3}$$

And it is possible to estimate  $E_{xth}$  from:

$$E_{xth} = \frac{3\rho RT}{M_0 / (2 \times \text{mol}\%_{BDA})} \quad \text{Eq. 4}$$

If the reaction is fully efficient, we expect  $R = 1$ .

Otherwise,  $R < 1$ . Assuming that the mechanophore is statistically distributed in the network as is the conventional crosslinker BDA, the total activatable mechanophore's concentration,  $C_{tot\_act}$ , corresponds to:

$$C_{tot\_act} = R \times C_{tot} \quad \text{Eq. 5}$$

Where  $C_{tot}$  is the total mechanophore concentration and R is the crosslinking reaction's efficiency.

Thus, the ratio of broken mechanophores is also affected by R as:

$$\Phi_R = \frac{C_{act}}{C_{tot\_act}} = \frac{C_{act}}{R \times C_{tot}} = \frac{1}{R} \times \Phi \quad \text{Eq. 6}$$

Where  $\Phi_R$  is the ratio of activated mechanophores corrected by the crosslinking reaction's efficiency and  $\Phi$  the ratio of activated mechanophores where all the mechanophores are supposed activatable.

This correction on the ratio of activated mechanophores affects the areal number of broken chains estimated from confocal images:

$$\Sigma_R = 2 \times \nu_x \times \int \Phi_R(y) dy \quad \text{Eq. 7}$$

Where  $\Sigma_R$  is the areal number of broken chains which takes into account the crosslinking reaction's efficiency.

$$\Sigma_R = 2 \times \nu_x \times \int \left( \frac{1}{R} \times \Phi(y) dy \right) = \frac{1}{R} \times \Sigma_{exp} \quad \text{Eq. 8}$$

Where  $\Sigma_{exp}$  is the areal number of broken chains without taking into account the crosslinking reaction's efficiency, as described in Chapter 4, section 3.3.2.

The reaction's efficiency ratios are reported in Table 1Table 3. It decreases with increasing crosslinker concentration. More crosslinker increases the probability to create loops in the network or dead-ends.

% mol <sub>BDA</sub> (%)	E <sub>x</sub> (MPa)	E <sub>xth</sub> (MPa)	Reaction's efficiency ratio
0.25	0.37	0.41	0.90
0.50	0.67	0.82	0.81
0.75	0.86	1.23	0.70
1.0	1.07	1.65	0.65
1.5	1.28	2.47	0.52

Table 3 Experimental and theoretical contribution of crosslinks to the Young's modulus, and crosslinking reaction efficiency ratio as a function of the total molar concentration of crosslinker initially added

### Areal density of broken chains

We now investigate the effect of network structure on bond breakage occurring near the crack surface during fracture propagation. Following the same procedure described in Chapter 4, section 3 on our series of samples mechanically characterized in section 1.2, mechanochemistry enables us to access the fraction of broken bonds, post-mortem, at different positions along the crack surface, noted  $a_{conf}$ .

Confocal images were collected along the crack surface, post-mortem, as represented in Figure 7. The results are reported in Figure 8.

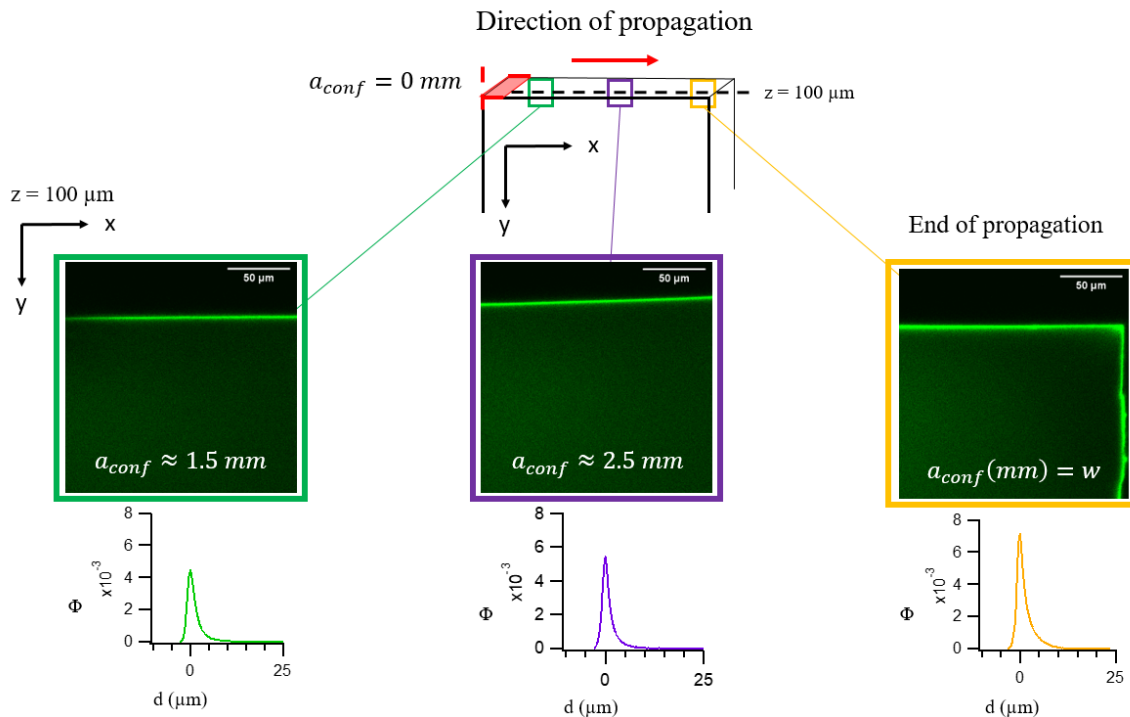


Figure 7 Representation of the confocal images collection process along the crack surface  $a_{conf}$ . The edge is taken as the beginning of the axis  $a_{conf}$ .

As expected from the results presented in Chapter 5, Figure 8 shows that the measured areal density of broken chains on the fracture surface increases along the crack propagation direction for all the samples. However, the concentration of crosslinker seems to affect the variation of each data set. To compare this from numerical parameters, we fitted a linear model to each set of data and extracted the slope of the curve. The results are reported in Figure 9.

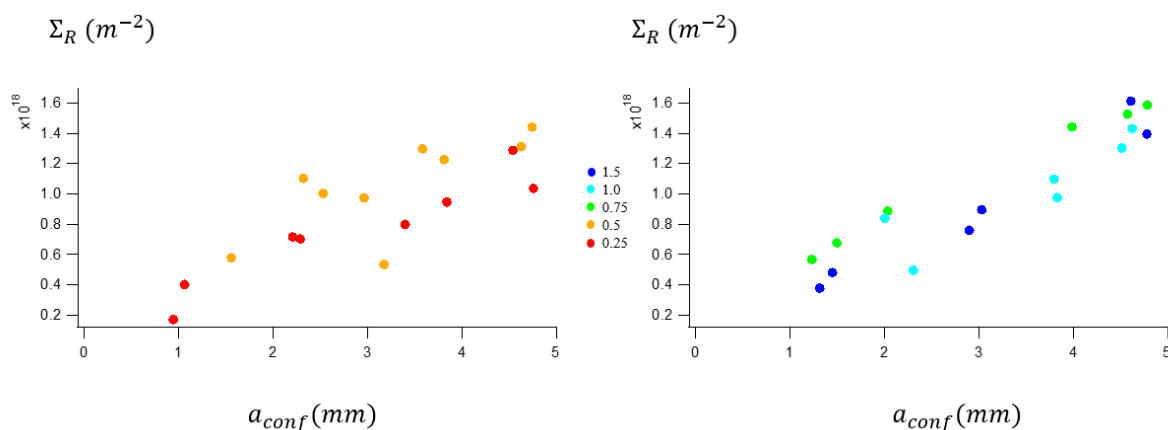


Figure 8 Effect of chain density on the areal density of broken chains as a function of the crack length  $a_{conf}$ . For more clarity, the left graph reports the data of SN0.25 and SN0.5, and the graph on the right reports the data of SN0.75, SN1.0, and SN1.5.

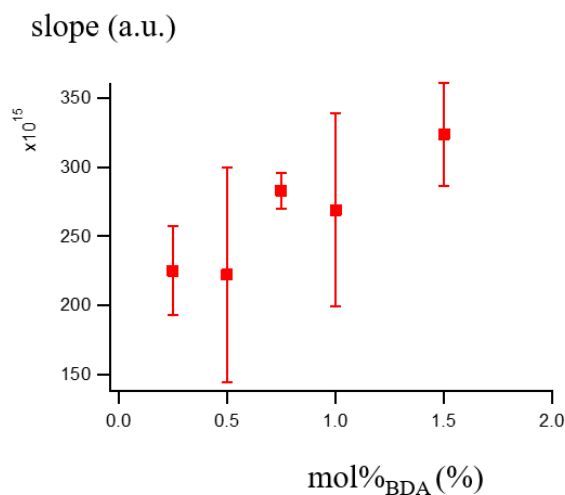


Figure 9 Slope of the linear fit for each set of data represented in Figure 8, as a function of the crosslinker molar concentration.

Figure 8 and Figure 6 show that there is both an increase in  $G$  and an increase in  $\Sigma_R$  along the crack propagation direction. Figure 9 represents the slope of the data of Figure 8 and shows that more crosslinked networks, where crack propagate slower typically break more chains

This goes against intuition. If we consider that increasing crack speed would increase the viscoelastic dissipation at the crack front, then, faster crack propagation speed should lead to higher dissipation in a small volume in front of the crack tip. Or maybe it is the opposite: the crack propagates faster because the viscoelastic dissipation at the crack tip is lower in samples with low crosslink density. Therefore, less dissipation and bond breakage occurs in a small volume in front of the crack tip of samples with low crosslinker density.

It is now interesting to plot  $\Sigma_R$  as a function of  $G$  for the materials with different crosslink densities. Interestingly, Figure 10 shows that chain breakage increases faster with  $G$  for the more crosslinked samples.

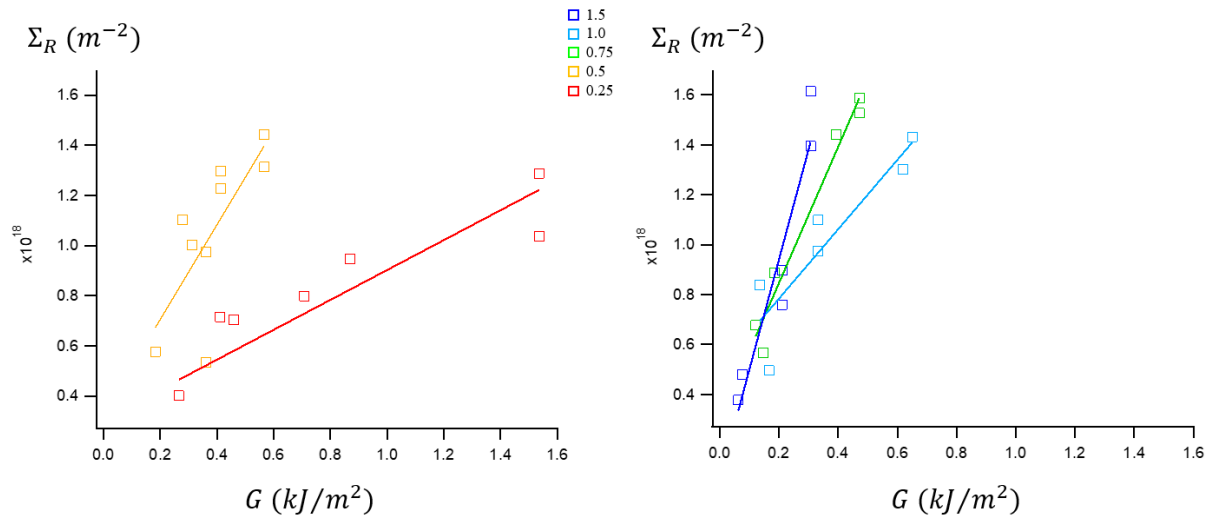


Figure 10 Effect of the crosslink density on the variation of the areal density with the energy release rate.

As shown in Chapter 5, Figure 10 shows that the areal densities of broken chains increase linearly with the energy release rate. But the figure also demonstrates that the network structure affects the extent of chain scission for the same applied  $G$ . At similar values of  $G$ , more chains are broken in materials with higher crosslinker contents. From the slope  $p$  of the linear fit represented in Figure 10, we can extract an energy dissipated per chain, calculated as Eq. 9 and represented in Figure 11:

$$G = \frac{1}{p} \Sigma_r \quad \text{Eq. 9}$$

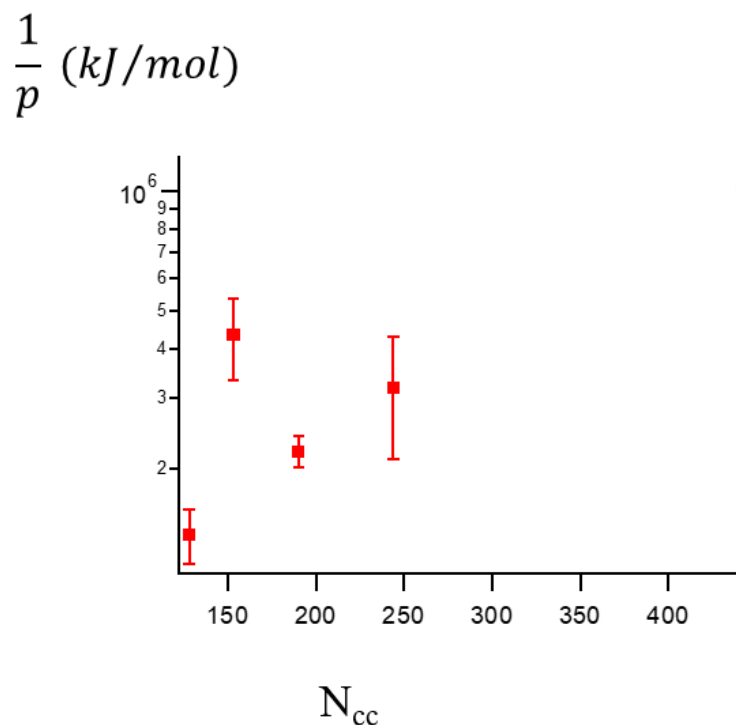


Figure 11 Energy dissipated per chain as a function of the number of CC bonds in the chain backbone ( $N_{cc}$ ), log-lin axis.

With the exception of the SN1.0 samples, Figure 11 shows clearly that the energy dissipated per broken chain increases with chain length, as expected from the need to stretch all the CC bonds composing the chain before actually breaking the chain. However, the dependence on chain length appears to be significantly stronger than linear: the energy increases with the number of CC bonds to the power 2.4.

#### *Energy dissipated for molecular damage*

The areal density of broken chains is measured independently of the crosslinks concentration in our experiments. To create a new surface, we know that it is required to break at least the chains crossing the new surface. This means that a sample with a high areal chain density (and a high concentration of crosslinks) will require more chain breakage than a sample with a low areal chain density. The contribution of chain scission to the energy release rate can be estimated by multiplying the areal density of broken chains by the theoretical amount of energy released to break one chain (equal to the number of CC bonds in the chain multiplied by the energy of a CC bond dissociation according to the model of Lake and Thomas [<sup>1,10</sup>]). Therefore, the chain density (and the crosslink density) is taken into account to estimate the contribution of the damage to the fracture energy. The damage energy  $G_{damage}$  is reported

as a function of the applied energy release rate  $G$  (or the total fracture energy  $\Gamma$ ) in Figure 12 for all the different networks

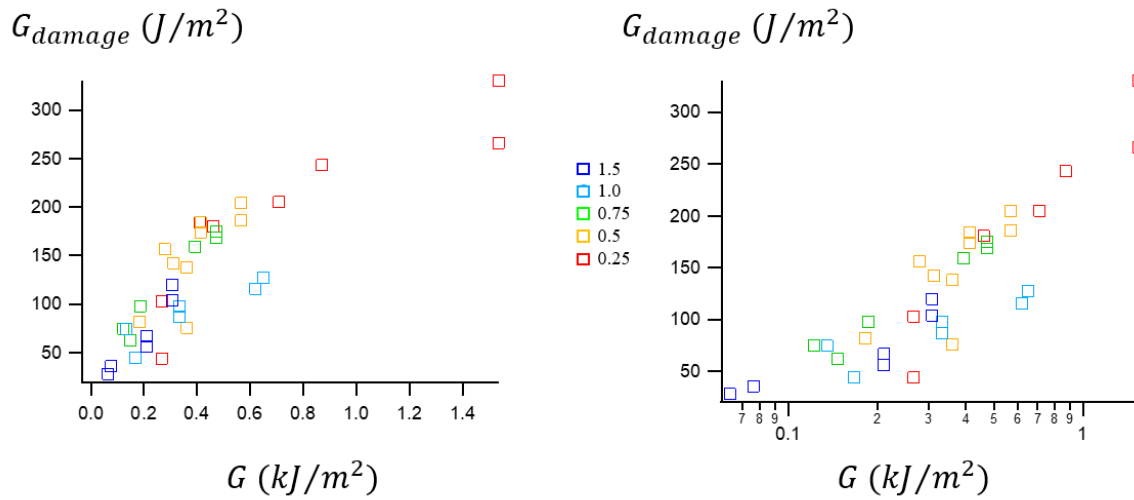


Figure 12 Effect of the network structure on the variation of fracture energy (from bond breakage) with the energy release rate  $G$ . Left plot linear axis and right plot lin-log axis.

Figure 12 shows the variation of the energy dissipated by bond scission  $G_{damage}$  as a function of the released elastic energy during crack propagation. Although there is some scatter in the data, it is reasonable to say that  $G_{damage}/G$  doesn't depend much on the sample structure despite the variation of the viscoelastic dissipation with network structure (see Appendix). This is an important result showing that the number of broken chains and their length is directly related to the total energy dissipated and is not a constant value even close to threshold conditions. This result brings an experimental explanation to why the model of Lake and Thomas predicts relatively well the variations of fracture energy with network structure even in the presence of viscoelasticity: it is because the energy release rate during propagation is directly related to the energy dissipated per broken chain despite the existence of bulk viscoelastic dissipation. There maybe two types of rate dependent dissipation, one in small strain acting relatively far from the crack and only important close to  $T_g$ , and another type of rate dependent dissipation directly related to bond scission.

## Conclusion

In this work, we studied the effect of network structure on the crack propagation process macroscopically and at the molecular scale.

Macroscopically, we recorded the crack propagation initiated from a hand-made 1 mm notch and performed video analysis to estimate the local deformation, crack propagation speed, and energy release rate during the propagation.

We got access to molecular-scale information of bond breakage using networks tagged with a mechano-fluorescent molecule which reports for bond breakage, and we imaged and quantified activation with confocal microscopy as a function of crack growth.

We could then link the estimated areal density of broken chains with the energy release rate and found that the areal density of broken chains increases linearly with the energy release rate. The variation of the energy release rate as a function of the areal density of broken chains is non-linear. It led to an estimation of an energy dissipated per chain which increases with chain length to the power 2.4.

We found that the network structure didn't affect much the fraction of energy dissipated by bond scission during the propagation. This suggests that the number of broken chains is a major factor controlling the energy dissipated during the crack propagation in samples, despite the possible variation in bulk viscoelastic dissipation with the network structure. This experimental observation brings light to why the molecular model of Lake and Thomas predicts that well the variation of fracture energy with network structure even when the numerical value underestimates the experimental ones by orders of magnitude (because of the viscoelastic contributions to the fracture energy).

## Appendix

### Rheology

#### Methods

The temperature and frequency dependence of the samples were tested with an RDAII parallel plate rheometer (Anton Paar, Physica MCR 501). The samples were cut in disk shape using an 8 mm diameter puncher. To avoid slippage from the geometry, samples were glued using Loctite 406. A frequency sweep was then applied from 0.063 to 63 rad.s<sup>-1</sup> every 1.5 °C between 15 °C and 70 °C. The strain was fixed at 0.02 % to be in the linear regime. Using the time-temperature superposition principle, data taken at different temperatures were manually shifted to construct a master curve at a reference temperature of 22 °C. The tan δ data obtained for each temperature are first horizontally shifted one by one by a factor U) until the best fit is achieved. Generally, in the vicinity of the glass transition, the shift factors are related to the applied temperature by the Williams-Landel-Ferry (WLF) relation [ref].

$$\log(a_T) = \frac{-C_1(T - T_{ref})}{C_2 + (T - T_{ref})}$$

Where  $C_1$  and  $C_2$  are constants,  $T_{ref}$  is the reference temperature (in K),  $T$  is the measurement temperature (in K).

To improve the quality of superposition of the master curve, a vertical shift of  $b_T$ ) was also applied taking into account the temperature and density dependence of the entropic modulus.

$$b_T = \frac{\rho T}{\rho_{ref} T_{ref}}$$

Where  $\rho$  and  $\rho_{ref}$  are the network density at  $T$  and  $T_{ref}$  respectively.

#### Results

Storage modulus  $G'$  and loss modulus  $G''$  master curves at 22 °C for SN1.5 and SN0.25 are represented in Figure 13. The correction of the raw data in the vertical direction is a little off. However, this shouldn't change our conclusion. As expected,  $G'$  scales with  $E/3$ .  $G''$  increases on one order of magnitude with frequency for both SN1.5 and SN0.25. The loss modulus is slightly higher for the more crosslinked sample SN1.5. The viscoelastic dissipation is affected by the network structure.

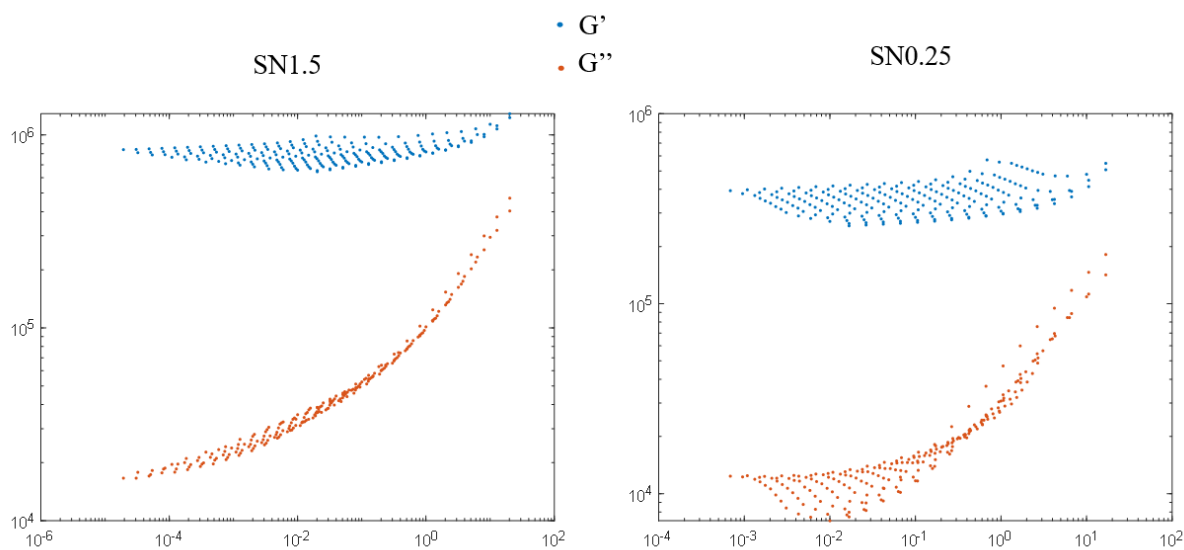


Figure 13 Master curves at 22 °C of  $G'$  and  $G''$  for SN1.5 and SN0.25 as a function of frequency.

## References

1. Lake, G. J. & Thomas, A. G. The Strength of Highly Elastic Materials. *Proceedings of the Royal Society A: Mathematical, Physical and Engineering Sciences* **300**, 108–119 (1967).
2. Sloodman, J. *et al.* Quantifying Rate- and Temperature-Dependent Molecular Damage in Elastomer Fracture. *Phys. Rev. X* **10**, 041045 (2020).
3. Akagi, Y., Sakurai, H., Gong, J. P., Chung, U. & Sakai, T. Fracture energy of polymer gels with controlled network structures. *The Journal of Chemical Physics* **139**, 144905 (2013).
4. Sloodman, J. Détection quantitative de l'endommagement moléculaire, par mécano-fluorescence, dans les matériaux mous. (PSL, 2019).
5. Millereau, P. *et al.* Mechanics of elastomeric molecular composites. *Proceedings of the National Academy of Sciences* **115**, 9110–9115 (2018).
6. Chen, Y. Cartographie quantitative de la contrainte dans les matériaux mous par mécano-chimie. (PSL, 2018).
7. Rubinstein, M. & Panyukov, S. Elasticity of Polymer Networks. *Macromolecules* **35**, 6670–6686 (2002).

8. Greensmith, H. W. Rupture of rubber. X. The change in stored energy on making a small cut in a test piece held in simple extension. *Journal of Applied Polymer Science* **7**, 993–1002 (1963).
9. Liu, Z., Zakoworotny, M., Guo, J., Zehnder, A. T. & Hui, C.-Y. Energy release rate of a single edge cracked specimen subjected to large deformation. *Int J Fract* **226**, 71–79 (2020).
10. Wang, S., Panyukov, S., Rubinstein, M. & Craig, S. Quantitative Adjustment to the Molecular Energy Parameter in the Lake–Thomas Theory of Polymer Fracture Energy. *Macromolecules* **52**, (2019).

## **Chapter 7**

# **Quantitative study of molecular bond breakage and load transfer during the necking of multiple network elastomer**



## Table of contents

Introduction .....	253
1. Materials and methods.....	254
1.1. Chemicals and reagents .....	254
1.2. Single network synthesis .....	255
1.3. Multiple network synthesis.....	255
1.4. Mechano-fluorescent network synthesis .....	256
1.4.1. DACL incorporation.....	256
1.4.2. SP incorporation.....	257
2. Confocal imaging of stretched samples.....	257
2.1. Home-made tensile test set up.....	258
2.2. Confocal imaging .....	259
2.3. Systematic image analysis.....	260
3. Necking in multiple networks .....	269
3.1. Mechanical characteristics of necking.....	269
3.2. Damage quantification bulk vs neck regions (in the bulk and the matrix).....	271
3.3. Load transfer between the filler and the bulk (SP in the matrix).....	275
4. What parameters control the necking process? .....	277
4.1. Effects of the pre-stretch .....	277
4.2. Effects of the filler network crosslinking content .....	282
5. Effect of the connectivity between filler and matrix networks .....	287
5.1. SNHMA synthesis .....	287
5.2. Necking in HMA multiple networks .....	289
6. Discussion .....	293
Conclusion.....	294
Appendix .....	296
References .....	300



## Introduction

Multiple networks are interesting model materials in which a first crosslinked network is pre-stretched by the successive polymerization of matrix networks. These materials benefit from the early rupture of the filler network short and pre-stretched chains, which are called sacrificial bonds, as they dissipate energy before the macroscopic failure of the material [1,2]. This specific network architecture enables to stretch the filler network to extension that could not be reached by the network alone, due to its catastrophic fracture. Therefore, the filler network chains will reach high extensions and break, before the failure of the multiple network. In a way, the extension reached by the filler network mimics the extension that happens very locally at the crack tip, during the crack propagation of the filler network alone.

Remarkably, some of multiple networks demonstrate a particular behavior called necking [3], which is typically attributed to ductile materials. This untypical behavior, for elastomers, consists in the localization of deformation to highly strained regions in the sample, which propagate stably in the sample upon further elongation.

Interestingly, the group of Gong already reported, in 2002, the occurrence of this necking behavior in double network hydrogels with similar material designs [4]. The necked region softened to an elastic modulus and tensile behavior similar to the second network alone. They proposed a mechanism for the transfer of load from the filler network to the second network [5]: in their picture, the filler network breaks into isolated clusters that are linked between each other through the remaining continuous matrix network.

They investigated the structure in the necked region by Small Angle Neutron Scattering of samples with deuterated second network and found typical second network concentration inhomogeneities with a characteristic length around 1.5  $\mu\text{m}$  [6]. These observations support their plausible necking mechanism where the filler network breaks into separate clusters that are physically connected by the second network, implying that [7] most of the filler network chains in the clusters should be unloaded after necking.

Different conclusions were obtained in our group, by the work of Y. Chen [8], regarding necking of multiple network elastomers. In this study, spiropyran (SP), a stress-sensing molecule, was introduced in the filler network or the matrix network of multiple network elastomers. His results showed that necking is accompanied by significant localized stress in the filler network and in the matrix network in the necked region, that results in a softening of the necked regions. Careful analysis of the SP adsorption, showed that after necking, the load was shared by both the filler and the matrix networks, with 90 % of the activated SP in the filler still under load in the necked region. These observations suggest the formation of microcracks in the filler network in the necked phase, rather than islands or clusters, as described by Gong in double network gels.

Mechanochemistry is a great tool to localize and quantify the rupture of chains during the necking process. Spiropyran and dioxetane has been used in our lab in the study of necking in a standard quadruple network elastomer. Nevertheless, spiropyran isn't representative for the breakage of C-C chains and it has not been adapted to perform real-time imaging yet. The dioxetane mechanophore, which gives dynamic information of bond breakage, is not adapted to precisely quantify and localize bond breakage, due to a low emission signal and a low spatial resolution.

In this study, we aim at getting real-time and quantitative information on the fraction of broken chains in the filler network, as well as stress transfer to the second matrix network, upon necking. We aim at understanding the parameters that control the necking of multiple network elastomers, by changing the structure or chemistry of the multiple network.

To do so, we used two mechanochemical tools to tag the first and second network of our samples with two mechanophores, reporting for either chain scission (DACL) or stress transfer (SP). We combined in-situ tensile test with direct observation with a confocal microscope, to quantify and observe in real-time the molecular state (damage or stress) of the material during necking. We varied the filler network pre-stretch, the filler network crosslinking density and the filler network chemical composition to investigate these parameters on the necking process.

The work presented in this chapter was done in collaboration with Jean Comtet.

## 1. Materials and methods

We present here materials and methods, regarding material synthesis and incorporation of the two mechanophores in the material.

### 1.1. Chemicals and reagents

Ethyl acrylate (EA, Aldrich, 99%), 1,4-butanediol diacrylate (BDA, Aldrich, 90%), 2-hydroxy-2methyl propiophenone (HMP, Aldrich, 97%), hexyl methacrylate (HMA, Aldrich, 98%).

EA or HMA, BDA, HMP were used as monomers, crosslinker, and UV initiator, respectively. An aluminum oxide column was used to purify and remove additives contained in as-received EA, HMA and BDA. Acetone was used without further purification, in some of the polymerizations, to enhance the solubility of  $\pi$ -extended anthracene (DACL) mechanophore (synthesized in the lab by J. Sloodman, G. Mellot and G. Sanoja) in HMA.

## 1.2. Single network synthesis

Single networks were prepared as previously presented in Chapter 4 section 1.1.3. They were obtained through UV induced free radical bulk polymerization.

PEA and PHMA samples will be respectively labeled according to the following formulas:

SNEA $x$  and SNHMA $x$  where  $x$  represents the molar content of crosslinker.

## 1.3. Multiple network synthesis

Double networks are synthesized in a sequential process. A filler network synthesized as presented above is put into a bath containing a mix of EA monomer (19.5 mL), BDA crosslinker (0.01 mol%,  $17.9 \times 10^{-3}$  mmol, 3.37  $\mu$ L) and HMP initiator (0.01 mol%,  $17.9 \times 10^{-3}$  mmol, 2.73  $\mu$ L). The sample is kept in the bath until swelling equilibrium (2 h). The swollen sample is then removed from the bath and put under UV for 2h at low intensity ( $<10 \mu\text{W}/\text{cm}^2$ ) to polymerize the monomers trapped inside the filler network into a network called the matrix network. Finally, the sample is put under vacuum overnight at room temperature to remove the eventually remaining unreacted volatile species and the final double network is obtained.

To make a triple (and quadruple) network, these steps are repeated using a double network (respectively a triple network) as the network to swell.

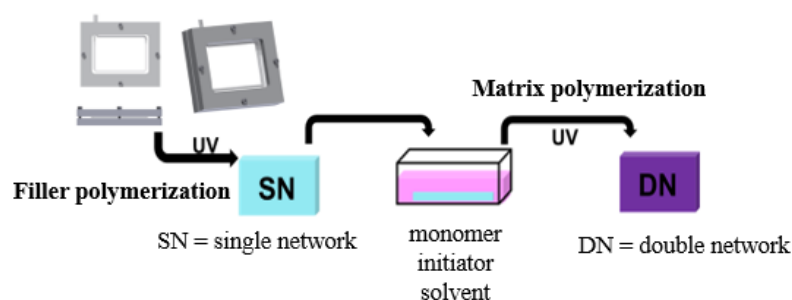
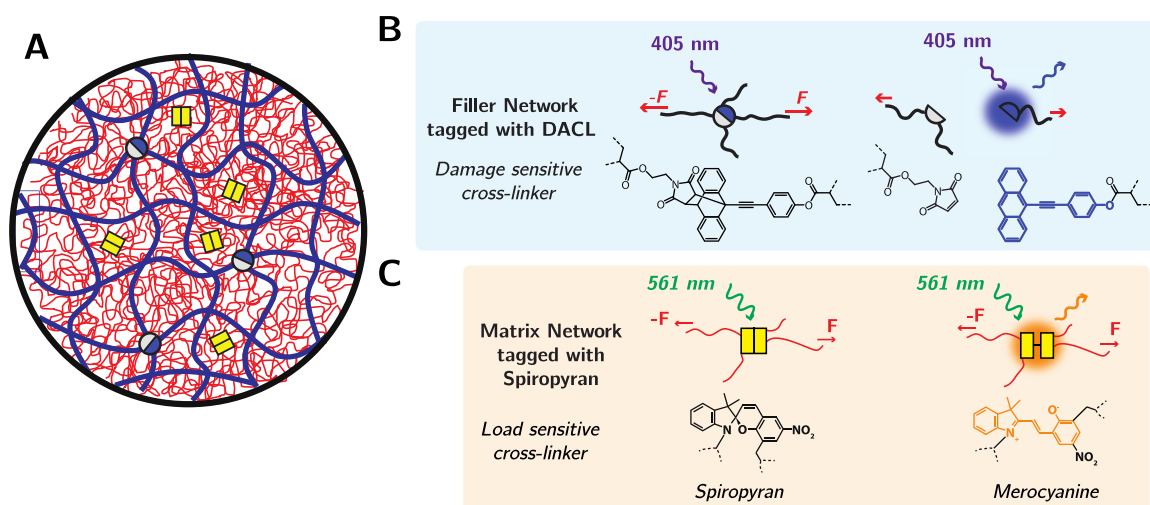


Figure 1 Representation of the multiple-step process to synthesize a double network

Multiple network samples will be labeled TN $m$  $x$  and QN $m$  $x$  respectively for triple network and quadruple network,  $m$  being the filler network monomer's initials (EA or HMA) and  $x$  being the molar concentration of crosslinker in the filler network.

## 1.4. Mechano-fluorescent network synthesis



**Figure 2** Representation of the incorporation of the different mechanophores in the filler network and in the matrix network.

As shown in Figure 2, two types of mechanophores were used to tag the multiple networks and follow damage and stress transfer in these networks following deformation.

The first mechanophore is the  $\pi$ -extended anthracene (Diels Alder Cross-Linker, DACL), which acts as a fluorescent reporter for bond scission and is incorporated in the first (filler) network. This mechanophore becomes fluorescent upon irreversible scission and enables the quantitative measurement of damage in this filler network (see [9], Chapter 4 and paragraph 1.4.1 below for details).

The second mechanophore used is spiropyran. Above a critical stress, spiropyran opens into merocyanine, a colored and fluorescent isomer of spiropyran [10,11]. Spiropyran is a mechano-chromic molecule (which means it changes color upon its force-induced isomerization into merocyanine) and was previously used by Y. Chen [8,12] to map stress in multiple networks by monitoring the change in sample adsorption through RGB video analysis. It is also a mechano-fluorescent molecule, as merocyanine, the stress-induced open isomeric form of spiropyran is fluorescent (this conformation change is reversible). We incorporated spiropyran in the second network (the matrix), where it acts as a force sensor, enabling us to probe the local stress of this network (see details below, in paragraph 1.4.2).

### 1.4.1. DACL incorporation

Mechano-fluorescent single networks were synthesized by incorporating  $\pi$ -extended anthracene mechano-fluorescent molecules (DACL) as crosslinker inside the network.

The single network was synthesized as describe in Chapter 4 section 1.1.3 keeping the global amount of crosslinker constant to 0.5 mol% with DACL (0.02 mol%,  $7.34 \times 10^{-3}$  mmol), BDA (0.48 mol%, 0.176 mmol, 33.20  $\mu$ L), EA (4 mL, 36.7 mmol) and HMP (1.16 mol%, 0.425 mmol, 64.86  $\mu$ L).

These filler networks were used as filler networks for the polymerization of multiple networks tagged with DACL.

Samples containing DACL will be indicated with **DA** at the beginning of the sample name. For example, a quadruple network of PEA with a filler network containing 0.5 mol% crosslinker and functionalized with DACL will be labeled **DAQNEA0.5**.

### 1.4.2. SP incorporation

Spyropiran was incorporated in the first matrix network of the multiple network. It was used as a crosslinker and replaced all the crosslinkers in the previous bath mix presented above. EA (19.5 mL, 0.1788 mol), SP (0.01 mol%,  $17.9 \times 10^{-3}$  mmol, 9.3 mg) and HMP (0.01 mol%,  $17.9 \times 10^{-3}$  mmol, 2.73  $\mu$ L).

Assuming that the diffusion of all the compounds present in the bath into the network was homogeneous, the matrix network is composed of EA and 0.01 mol% SP.

Samples containing SP in their first matrix network will be indicated with **sp** at the end of their name. For example, a quadruple network with a filler network containing DACL and crosslinked with 0.5 mol% crosslinker, containing SP in its first matrix network will be labeled **DAQNEA0.5sp**.

## 2. Confocal imaging of stretched samples

To visualize molecular-scale processes such as damage in the filler network and stress-transfer to the matrix network during the necking process, we developed a home-made tensile test set-up, which allows to stretch the sample while simultaneously imaging it with the confocal. This section presents the tensile set-up, the specifications of the sample size, and the systematic data correction and analysis done to each image to quantify damage and stress transfer in the deformed sample.

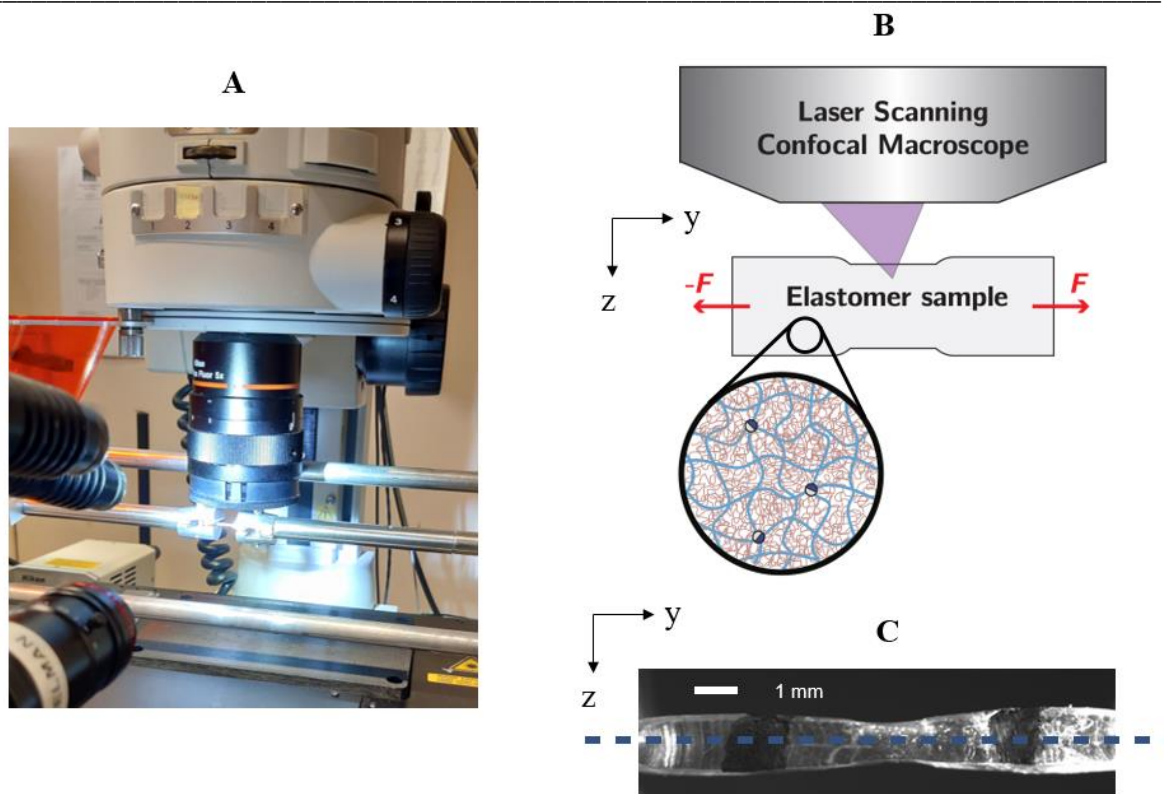


*Figure 3 A. Photo of the setup composed of the confocal microscope, under which a multiple network sample is being stretched by a homemade tensile test set up. To correct for slippage during the tensile test an additional camera on the side can record pictures of the stretched sample. B. Schematic representation of the sample during the test. C. Side view of the stretched sample from the additional camera. The dotted line represents the center plane of the sample*

## 2.1. Home-made tensile test set up

A homemade tensile set-up was specifically designed (by Bruno Bresson and Jean Comtet) to perform tensile tests under the confocal microscope and image sample in their deformed state (Figure 3).

The set-up was composed of a load cell (s-form load sensor KD40s, ME-Meßsysteme, 50 N and 500 N, precision 0.1 %) which measured the force applied on the sample and two linearly translating arms (PI L-239.033232 linear actuators and C-884.4DC motion controller), controlled with LabView, which were used to deform the samples.

The sample was cut from multiple network sheets with a specific dumbbell-shaped punch of gauge length 1 mm, width 1 mm (Figure 3 C.). The dumbbell shape of the sample is required to avoid stress concentration and breakage of the sample under the clamps. The sample was purposely small so it could fit in the image frame of the confocal microscope at the beginning of the test (maximal field of view of approximately 4x4 mm, with 1x magnification). During the tensile test, the sample deforms and becomes

too long to fit completely within the confocal frame. However, we could pause the mechanical test and image the entire sample by simultaneously shifting the arms of the tensile set-up to one side or the other.

We were particularly interested in imaging the region of necking nucleation and the necking fronts.

The confocal acquisitions could be precisely synchronized to the mechanical data by also recording the trigger signal of the confocal, which trigs each time a frame is taken.

## 2.2. Confocal imaging

The main interest of this method is the possibility to image neck nucleation in a multiple network elastomer and take images of the necked and unnecked regions at the same time. To do so, it is important to be able to image as much of the sample as possible in a single frame. This is why, in this project, we choose to work with a confocal microscope with low magnification, as we could obtain a field of view of 4.2x4.2 mm, sufficient to image dogbone samples of gauge length 1 mm and width 1 mm. Sample thickness varies between 2 to 3 mm depending on the sample.

The conditions to image DACL activation are the same as the ones used in Chapter 4 section 3:

Confocal images were taken with a customized Nikon AZ-100/C2+ confocal microscope. The objective used was an AZ Plan Fluor 5x, with a focal length of 15 mm. The objective was used with a 1x zoom for quantitative image analysis. Pixel size corresponds to 8.15  $\mu\text{m}$  and image size was 512x512 px (4.2x4.2 mm).

To measure the fluorescence of DACL, a 405 nm excitation wavelength was used and the emission rays were recorded between 450 and 550 nm. DACL activation was stable during the experiment, no photobleaching was noticed at the working laser intensities.

As presented earlier, we also worked spiropyran (SP). This mechanophore will be presented more in details later in this section (section quantification). Here, we focus on the setup settings. To measure SP activation, a 561 nm excitation wavelength was used and the emission rays were recorded between 570 and 670 nm.

SP activation is sensitive to mechanical stress but also to light. SP can be activated with UV but also with the 405 nm laser used to excite the activated DACL moiety. Thus, for all samples containing DACL and SP, SP was always imaged before DACL. SP also suffers from deactivation with white light and bleaching upon exposure to the 561 nm laser. Only few image of SP activation were thus taken for quantification, in order to prevent bleaching of SP.

### 2.3. Systematic image analysis

To be able to compare quantitatively the fluorescent intensities measured between samples, it was necessary to perform some correction to the images, namely flatfield correction, thickness correction, etc... They are presented in this section.

#### *Flatfield correction*

If we image a sample with a homogeneous distribution of fluorescent molecules as represented in Figure 4, we would expect a homogenous signal over the entire image. However, we clearly observe that the intensity in the image is not constant and the corners are not showing any signal at all. This is a typical optical aberration called vignetting. The inhomogeneous illumination can be corrected as a post-treatment and the corners shouldn't be considered in the rest of the analysis.

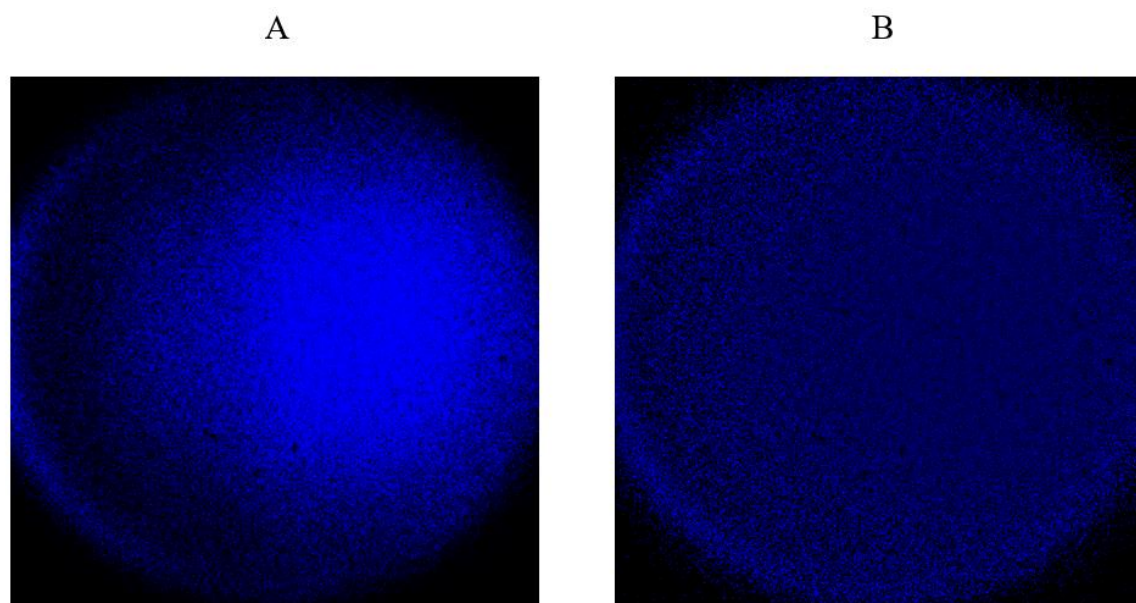


*Figure 4 A. Confocal image of sample homogeneously distributed in fluorescent molecules before flatfield correction. B. Image of the same sample after flatfield correction.*

To correct for the vignetting, a sample with a homogeneous distribution of fluorescent molecules is imaged in the same conditions as the rest of the samples studied (zoom, laser intensity and gain). From this image, a correction factor can be calculated for each pixel. For a given pixel, the correction factor is equal to the ratio between the mean intensity of a region of homogeneous signal, over the pixel intensity.

Then for a given sample image, the corrected intensity is given by multiplying each pixel's intensity by the correction factor previously described. These results are reported in Figure 5. Fig. 4A corresponds

to the image before flatfield correction, where the mechanophore's activation seems less intense on the left side of the image than on the right side. However, the material is stretched homogeneously and the distribution of mechanophores is supposed to be homogeneous, so we expect a homogeneous signal. Once we apply the flatfield correction, represented in Figure 5 B, the mechanophore's activation appears indeed homogeneous.

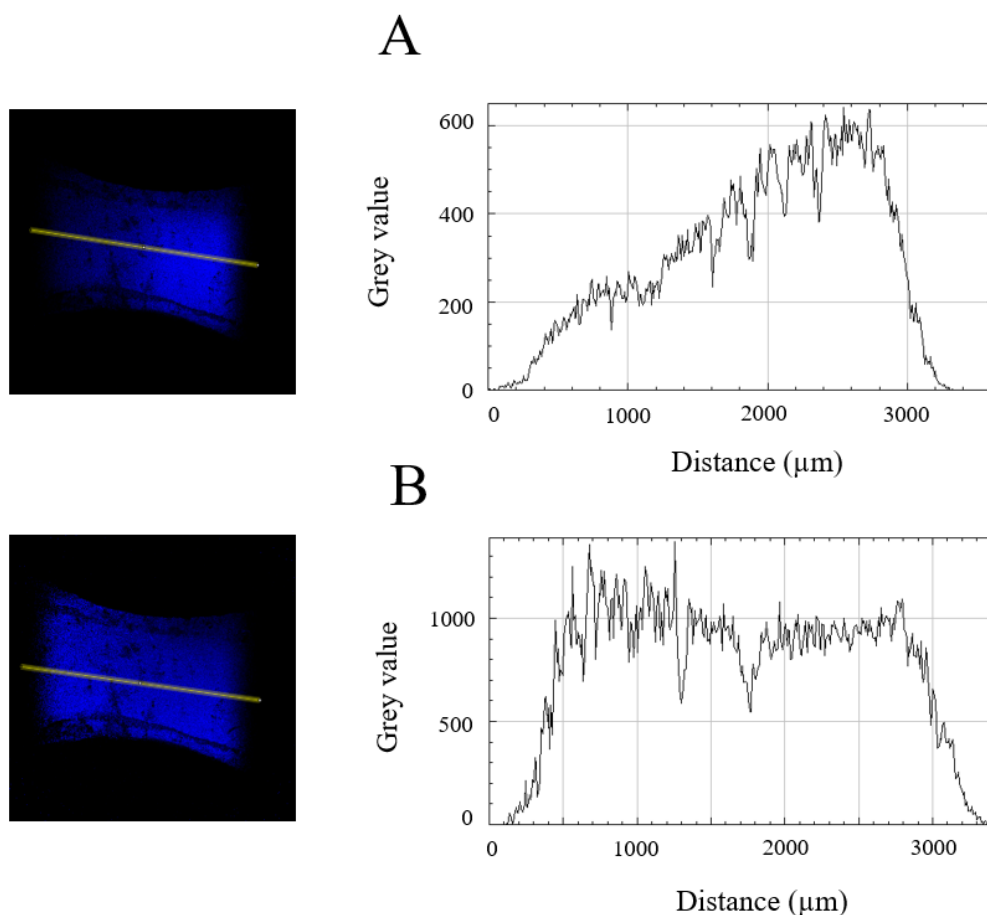


*Figure 5 A* Confocal image of a sample before flatfield correction and the intensity measured along the yellow line. *B* Same image after flatfield correction and the intensity measured along the yellow line.

### Thickness correction

Most of the previous work of the team using this mechanophore was done in the context of fracture, where a localized fluorescent signal is observed at the edge of the sample. Instead, we were here interested in quantifying bulk activation of the material, which required to develop a new methodology. Images were taken while the sample was stretched. Because of the incompressibility of the sample, when stretched in one direction, the sample is compressed in the two other directions. This means that the thickness of the sample varies during the tensile test. Thus it is not so relevant anymore to image at a constant depth like what was done for post mortem analysis. Instead, the samples was imaged in volume

from the top surface to the bottom surface, by taking a set of images at constant (x,y) positions but different depth (z) positions, the distance between adjacent images is well controlled (we chose a 20  $\mu\text{m}$  step), and then stacking all these images (the process will be called a z-scan).

As shown in Figure 6 B, in a stretched DAQNEA0.5, we observe a decrease in intensity with depth. This is because the material absorbs light. This decrease can be described with an exponential as given in the following equation:

$$I(z) = I_0 \times \exp\left(-\frac{z}{z_0}\right) \quad \text{Eq. 1}$$

where  $z = 0$  corresponds to the sample surface,  $z_0$  is the typical decay length for intensity which depends on the material.

As shown in Figure 6, this decay could be experimentally corrected to get to the intensity in the bulk  $I_0$ .

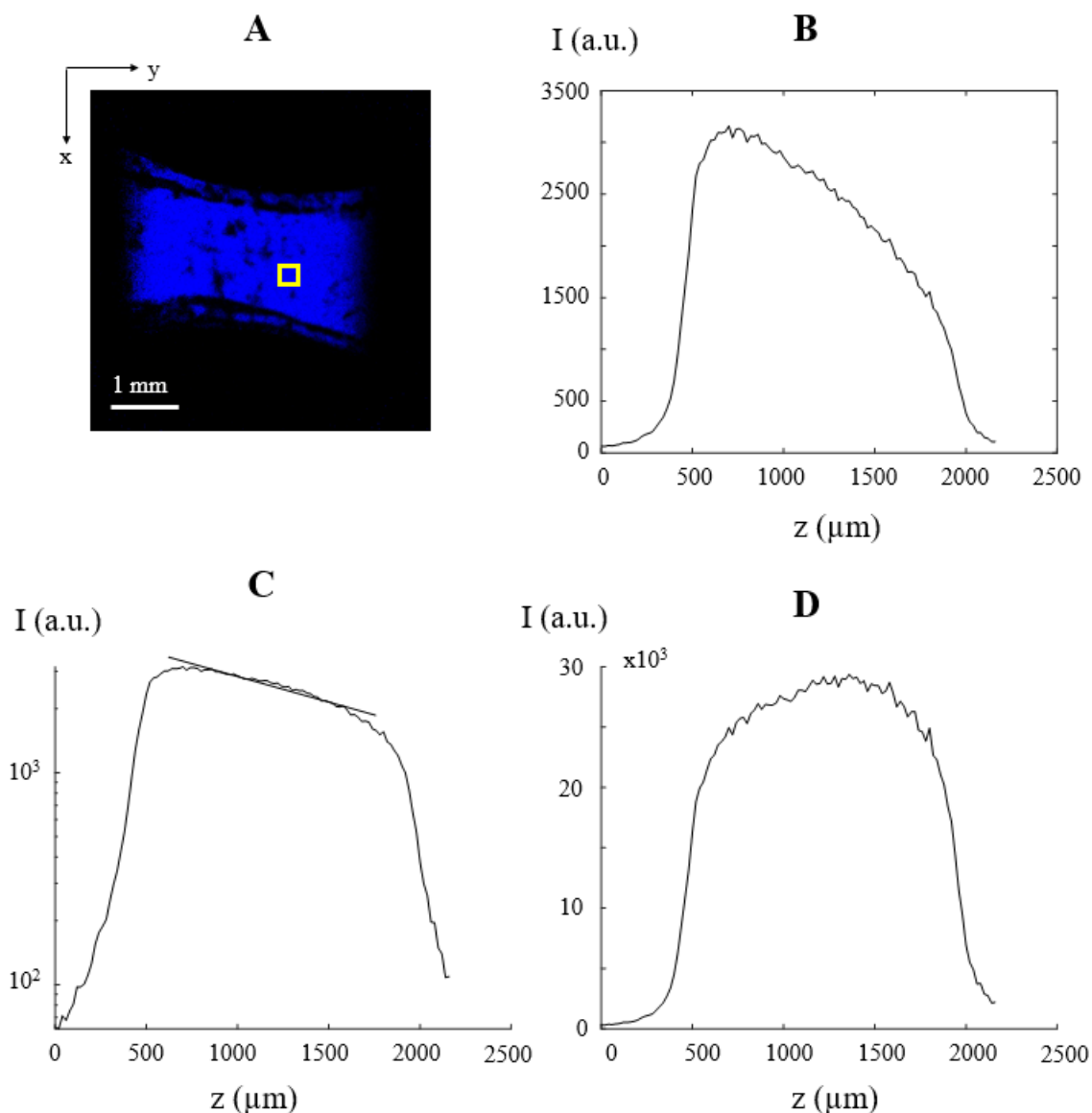


**Figure 6** A. Multiple network sample DAQNEA0.5 in the deformed state. The yellow square corresponds to the zone where the average intensity is measured as a function of depth. B. Intensity as a function of depth. The intensity decreases with depth because the sample absorbs light. C. Same plot in log-lin axis to fit the Eq. 1 D. Intensity  $I_0$  corrected by the material's light absorption properties as a function of depth. The intensity  $I_0$  appears more constant with depth.

In this chapter, we worked with two image collection modes: a static one (describes previously in Chapter 4 and section 2.2 of this chapter) which is quantitative, and a dynamic one that gives real-time information but is not quantitative. The dynamic mode will be detailed in the following section.

#### *Specificities of real-time imaging*

The set-up combines tensile test and confocal imaging, which makes it possible to image a sample in real-time during its deformation. Real-time imaging requires fast images collection, while z-scans image of the sample in depth can take several minutes. To allow for real-time imaging, only xy-scans at one

position in depth were recorded with time. We choose the depth position as the middle of the sample because this plan should remain the same independently of sample deformation.

The middle of the sample was found by performing a z-scan of the sample, then identifying the top surface and bottom surface of the sample, and setting the position in between these surfaces.

The thickness of the sample will decrease as the sample is stretched (due to the material's incompressibility). This means that, during the tensile test, the measured fluorescent signal will go through decreasing material thicknesses and will be less absorbed overall before reaching the confocal objective. This is a limitation to the quantification of the fraction of broken chains. Therefore, when real-time confocal imaging is performed, the description of the mechanophore activation will remain qualitative.

#### *Quantification of mechanophores activation*

Quantification of the mechanophores' activation is possible in static mode as it has been presented in Chapter 4.

The mechano-fluorescent molecules used activate either upon bond scission for DACL, or force threshold for spiropyran. The measured intensities in the sample report for the information provided by the mechanophores activation (damage or force). To get quantitative measurements (on bond breakage or force), it is interesting to quantify the fluorescent signals (in terms of ratio of broken bonds for DACL or force for SP). The following section details how DACL and spiropyran activation are quantified.

- DACL

The quantification of activated DACL has already been detailed in Chapter 4 section 3. The following section is a summary of the DACL activation calibration process.

To convert a measured intensity into a concentration of activated DACL, we build a calibration curve using samples with known concentrations of activated fluorescent molecules: the 9-((4-anisyl)ethynyl)anthracene, a reference fluorophore, synthesized by J. Sloodman [<sup>13,14</sup>], which corresponds to the activated DACL fluorescent moiety. The fluorescent molecules were dispersed in linear PEA and imaged with the confocal in the same conditions (zoom, laser intensity and gain) as the rest of the sample studied.

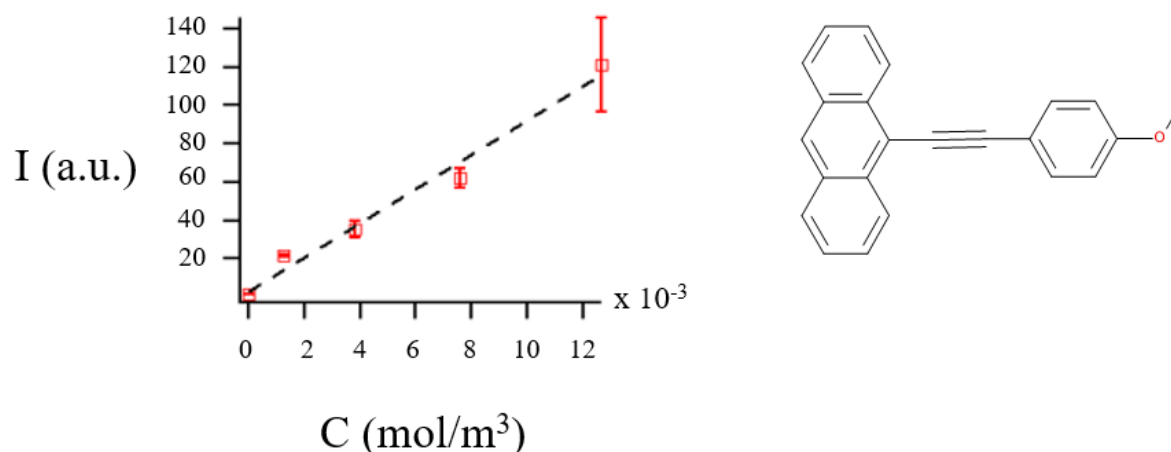


Figure 7 Calibration curve with the confocal microscope and representation of 9-((4-anisyl)ethynyl)anthracene, fluorescent reference for DACL activation used in the calibration samples.

- SP

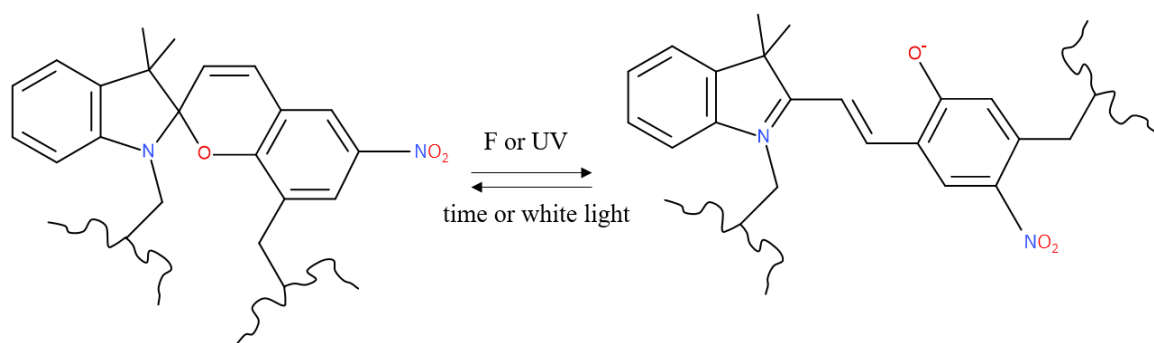


Figure 8 Spiropyran incorporated in the polymer network as a crosslinker and its isomerization into the fluorescent merocyanine form upon force or UV.

Spiropyran is a mechanosensitive molecule, represented in Figure 8, when pulled with or above a certain force, it opens into an unstable form, called merocyanine, which is fluorescent and adsorbs light, giving a coloration to the sample. When the sample is in the unloaded state, with time, the unstable merocyanine form goes back to SP. Previous work of Y. Chen <sup>[8,12]</sup> has mainly used the variation of light absorption and change in color of samples tagged with spiropyran/merocyanine to map stress in elastomer samples. Using RGB analysis, he calibrated the signal by activating all SP manually with UV, then deactivated the molecule with white light and performed mechanical tests where he quantified the activation of SP with color variations. He could thus get to a ratio of activated SP. Although images of the fluorescent signal of merocyanine were taken to follow crack propagation and map stress concentration at the crack

tip, no quantitative analysis of the activated SP fluorescence could be performed due to the absence of calibration. In this work, we focus on the quantification of SP fluorescence, and, we develop a calibration method for quantifying spiropyran's activation.

Single network PEA with SP concentrations of respectively 0.73, 0.37, 0.19 and 0.09 mM were used as calibration samples to extract quantitatively the activation of SP. The mechanophore in these samples was manually activated with UV. Because of SP sensitivity to photobleaching, a small untested piece of calibration sample was used for each calibration. For each concentration, the calibration sample was exposed to UV (350 nm) while performing a time scan. Once the recorded intensity reached a plateau, 100% of the SP was considered activated and a z-scan was performed, as represented in Figure 9 for the calibration sample with 0.73 mM SP.

The intensity measured at the same depth for each calibration sample could be plotted as a function of the concentration of activated SP.

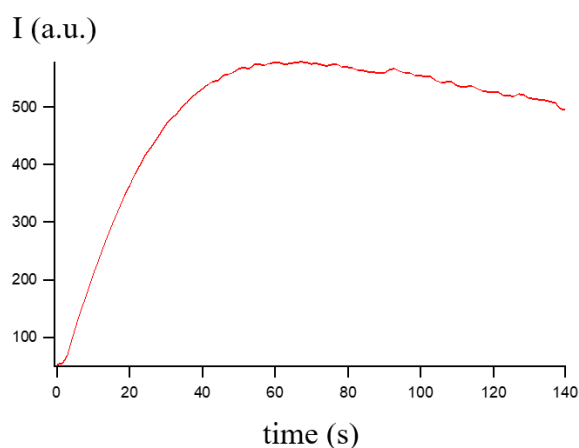


*Figure 9 Intensity as a function of time of calibration samples containing 1 mol% of SP under UV.*

From the calibration curves, the intensities (a.u.) were converted into concentrations of activated molecules ( $\text{mol.m}^3$ ). This concentration is used to calculate a ratio of activated molecule  $\Phi$  as given by the following equation:

$$\Phi = \frac{C_{\text{act}}}{C_{\text{tot}}} \quad \text{Eq. 2}$$

Where  $C_{\text{act}}$  and  $C_{\text{tot}}$  are respectively the concentration of activated mechanophore and the total concentration of mechanophore.

Assuming that:

- DACL activates close to the breakage point of any other polymer chain in the polymer network
- The mechanophores are statistically distributed in the polymer network
- Breakage of the network happens with the same probability at crosslinking points as within chains

We extrapolate and say that the ratio of activated DACL molecules represents the ratio of broken chains in the polymer network.

Assuming that:

- SP activates above a force threshold in the polymer network
- The mechanophores are statistically distributed in the polymer network
- Force in the network is similar within the chains and at crosslinking points

The ratio of activated SP represents the ratio of polymer chains pulled by a force above the SP force threshold (240 pN detected by Craig's group with AFM single molecular force spectrum [<sup>15</sup>]).

*Correction with the concentration of crosslinks*

In multiple networks, the dilution of both the filler network and the matrix network should be considered to account respectively for the dilution of DACL and SP within the whole sample and properly quantify respectively damage and stress distribution in the material.

- For the DACL in the filler network:

The fraction of SN in the whole sample corresponds to:

$$\Phi_{SN} = \frac{V_{SN}}{V_{tot}} = \frac{1}{\lambda_0^3} \quad \text{Eq. 3}$$

Where  $V_{SN}$  is the filler network's volume,  $V_{tot}$  is the multiple network's volume and  $\lambda_0$  is the filler network pre-stretch.

This gives the corrected fraction of broken chains in the filler network  $\Phi_{filler}$ :

$$\Phi_{filler} = \frac{\phi}{\Phi_{SN}} \quad \text{Eq. 4}$$

This corrective factor will be taken into account to estimate the DACL's activation in the filler network.

- For the SP in the matrix network:

SP in the matrix network is only present in the second network. This second network is diluted into the filler network and the third and fourth network (respectively for triple and quadruple networks).

For a multiple network, the fraction of matrix network is given by:

$$\Phi_m = 1 - \Phi_{SN} \quad \text{Eq. 5}$$

The second network is a part of this matrix network, and this part can be estimated by  $\Phi_{1m}$ :

$$\Phi_{1m} = \frac{\Phi_m}{\lambda_{1m}^3} \quad \text{Eq. 6}$$

Where  $\lambda_{1m}$  is the second network pre-stretch.

In a double network, the second network isn't diluted in the matrix:

$$\lambda_{1m} = 1$$

In a triple network, the second network is diluted in the matrix by a factor  $\Phi_{matrix}$ :

$$\lambda_{1m} = \frac{\lambda_{TN}}{\lambda_{DN}} \quad \text{Eq. 7}$$

Where  $\lambda_{DN} = \frac{V_{DN}}{V_{SN}}$  and  $\lambda_{TN} = \frac{V_{TN}}{V_{SN}}$  are respectively the filler network pre-stretch in the double and the triple network ( $\lambda_{DN} = \lambda_0$  of the DN network and  $\lambda_{TN} = \lambda_0$  of the TN network,  $V_{SN}$  is the filler network's volume,  $V_{DN}$  is the double network's volume and  $V_{TN}$  is the triple network's volume).

In a quadruple network, the second network is pre-stretched by a factor  $\lambda_m$  given by:

$$\lambda_m = \frac{\lambda_{QN}}{\lambda_{DN}} \quad \text{Eq. 8}$$

Where  $\lambda_{QN} = \frac{V_{QN}}{V_{SN}}$  is the filler network pre-stretch in the quadruple network ( $\lambda_{QN} = \lambda_0$  of the QN network).

This gives the corrected fraction of activated mechanophores in the second network:

$$\Phi_{matrix} = \frac{\Phi}{\Phi_{1m}} \quad \text{Eq. 9}$$

This corrective factor will be considered when estimating the ratio of activated SP in the matrix network.

## 3. Necking in multiple networks

### 3.1. Mechanical characteristics of necking

In this section, we report on the behavior of quadruple network elastomers in uniaxial extension. These materials undergo a necking transition. We specify the mechanical signature of such behavior and highlight its characteristics.

Macroscopically, necking corresponds to the mechanical analogy of a phase separation. After an initial localization of the deformation, two stable zones coexist in series in the sample carrying the same load but different deformations. As the macroscopic displacement increases (at fixed load) the relative proportion of the high stretch region increases while that of the low stretch region decreases. The existence of a stable necking requires the existence of a strong softening followed by a stiffening. Necking in multiple network elastomer has been shown to occur only for materials with a filler network of pre-stretch equal to or higher than 3 [3,16] and therefore a very dilute network. We thus performed tensile tests on a quadruple network DAQNEA0.25 with a pre-stretch of 3.4.

As can be seen on the stress-stretch curve in Fig. 10, these materials are linearly elastic at low stretches and show a non-linear elastic behavior at larger stretches ( $\lambda > 1.3$ ). This behavior is known as strain hardening: in the filler network, at such extension ( $\lambda \times \lambda_0$ ), Gaussian elasticity breaks down and finite chain extensibility described by the Langevin relation becomes dominant. However, no residual deformation remains when the material is unloaded.

Then the material reaches a maximum stress, after which it softens. In these materials this softening corresponds macroscopically to the nucleation of a necked region that is softer and deforms more than the rest of the material. Note that, when the material is unloaded, no residual deformation can be seen and one cannot visually distinguish between a region that was part of the neck or that was not part of the neck. This is a key difference with plasticity related necking where the neck is permanent.

Upon further deformation, the nominal stress remains constant with stretch as the necked region propagates along the sample. This regime is fairly short for our small sample, as shown in Figure 10. During this stress plateau, the local deformations in the necked region and in the other parts of the sample

also called the un-necked regions, stay constant. The overall sample deformation corresponds to an average of the local stretches of these different regions and evolves as the necked region grows.

Once the whole sample has been fully necked, the stress increases again and overpass the previous local maximum stress (right before necking). A second strain hardening can be observed which corresponds to the chains of the matrix getting closer to their limit extensibility. It is not visible in Figure 10 A, but can be extrapolated on plot B. Plot B corresponds to the second load of the same sample after a neck has propagated. We observe a strong hysteresis between the first loading and the second loading due to structural changes within the multiple network. The Young's modulus of the necked samples appears a lot lower than the original Young's modulus of the unnecked sample. The necked region is the first one being deformed when the necked sample is stretched again because it is softer. Then the necked sample demonstrates a strong strain hardening behavior as the chains of the broken filler network get closer to their limit extensibility.

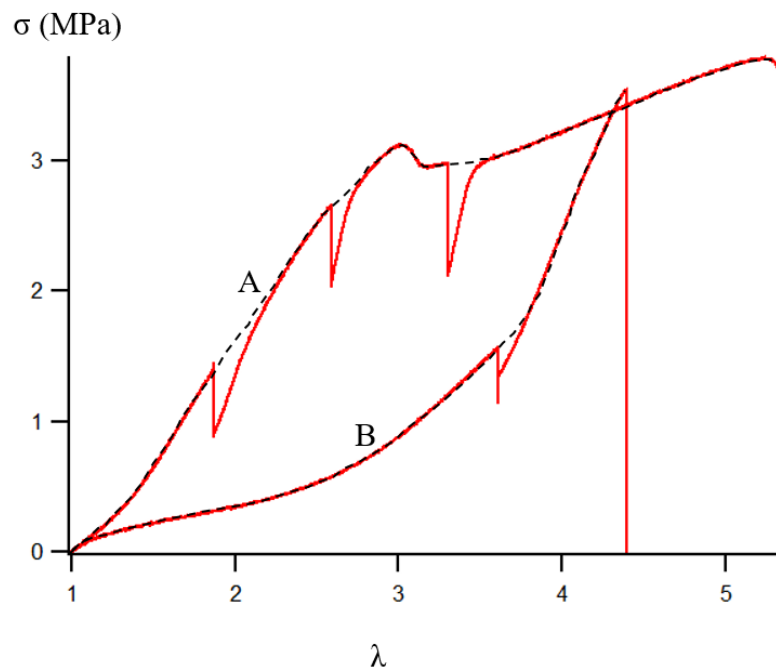


**Figure 10** Tensile test of a DAQNEA0.25 elastomer sample with a filler network pre-stretch equal to 3.4. **Plot A** corresponds to the first loading. **Plot B** corresponds to the second loading. Drops in the curve are due to the relaxation of the samples when the test was stopped to tighten the clamps. The samples were held by mechanical clamps which needed to be tightened during the test to prevent slippage (if the clamps became too loose due to the sample deformation) or early breakage (due to stress concentration under the clamps). The deviation of the experimental plots from the dotted lines comes from the relaxation of the samples when the test was stopped to tighten the clamps. Dotted lines are only here to guide the eye.

### 3.2. Damage quantification bulk vs neck regions (in the bulk and the matrix)

In multiple networks, the filler network is mainly responsible for the stiffness of the material [3]. The extension and early random breakage of the filler network chains reaching their finite extensibility dissipate energy. This translates mechanically by a first stiffening of the material, followed by a softening.

To observe the spatial extension of damage in the sample before and after necking, we synthesized a quadruple network elastomer containing the damage reporting DACL mechanochemical probe in its filler network.

With the help of the tensile test set-up under the confocal microscope, we could perform real-time in-situ imaging of the mechanophores' activation. Activation and stress as a function of stretch are represented in the figure below.

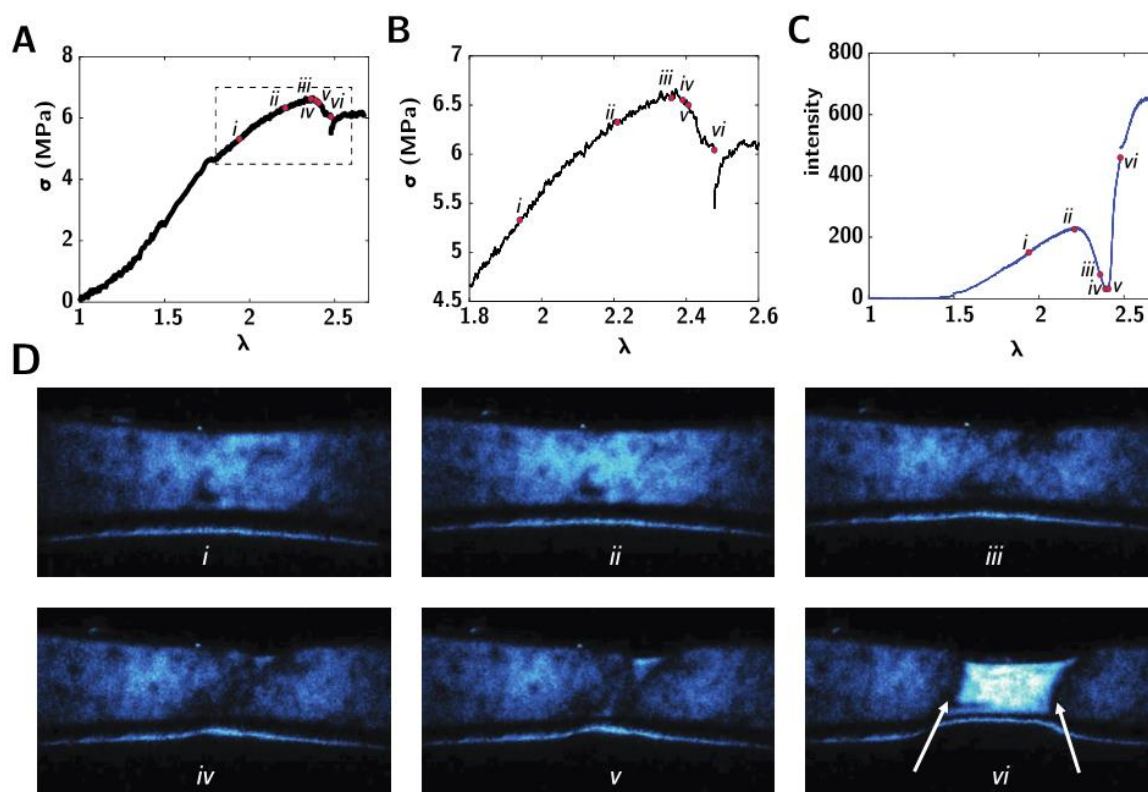


*Figure 11* Confocal images of the sample during the tensile test at a constant depth. Plots represent the stress-stretch curve (on the left) and the averaged measured intensity as a function of stretch (on the right).

At the beginning of the tensile test (Figure 11 A. for  $\lambda < 1.5$  and Figure 11C.), the sample demonstrates almost no fluorescent signal, meaning no significant level of mechanophore was activated at this level

of sample deformation. The stress increases linearly for low stretches. During this linear phase, low activation can be measured.

Note that low intensities spots exist before any mechanophore's activation and remain during the whole test (they move as the sample is stretched). These spots of low intensity are due to defects at the sample surface forming shadows.

For higher stretches (Figure 11 A. strain above 1.5), we can see a non-linear evolution of the stress with the stretch, resulting in an increase in the slope of the stress-stretch curve also known as strain-hardening. This behavior is due to elastically active chains getting closer to their limiting extensibility. This mechanical behavior is accompanied by a noticeable increase in the fluorescence signal (Figure 11 D. i and C.) without any localization. This means that a significant fraction of chains has been broken at this point. This suggests that the shorter chains close to their limit extensibility break randomly in the sample without correlations.

Just before the necked region becomes macroscopically visible (Figure 11 D. iii), the stress-stretch curve reached a stress threshold (Figure 11 B. iii). This happens at the same time as a decrease in the measured intensity (Figure 11 C. iii). Such loss in fluorescence signal in real time cannot be due to deactivation of the fluorophore since the scission reaction is irreversible in those conditions, but can probably be explained by the nucleation of defects which modify locally the sample density. This would result in light diffusion, hence a loss of measured intensity [4].

Note that shadows or regions of lower intensities appeared on Figure 11 image D. iii. If we follow these zones in images D. iv and D. v, the former regions of low intensities transform into the regions of higher intensities where the necked region starts (D. vi).

During the softening of the material (Figure 11 B. ii to v), the measured intensity decreases as the material softens (Figure 11 C. ii to v).

The nucleation of defects is localized and chains breakage in the filler network becomes correlated and may form microcracks or more probably microstructures of contrasting densities.

At the stress plateau (Figure 11 A. vi), a macroscopic zone of higher deformation can be observed (Figure 11 D. vi). This zone corresponds to the necked region of the material and is associated with higher activation of the mechanophores which means that a higher fraction of chains has been broken to nucleate this necked phase.

At this stage, the necked phase doesn't diffuse light as much which means that the sizes of the defects are either smaller or bigger than the excitation wavelength. We think that the defects are possibly smaller, as breakage continues to happen from the un-necked to the necked phase.

At each border of the necked phase, we can observe a darker transition zone (Figure 11 D. vi). This zone corresponds to a zone of homogeneous defects, whose size is close to the excitation wavelength, and which scatter light. At the neck front, the distribution of broken chains transitions from a random distribution (defects of various sizes) to a more homogeneous distribution (with defects sizes in the range of the excitation wavelength). Then the neck propagates and the defects in the necked phase become smaller than the excitation wavelengths, the light isn't scattered anymore, the intensity measured increases. As light scattering implies differences in refractive index, we believe that these defects could be very localized and dispersed variation of the density within the multiple network.

The quantification of the fraction of broken chains exactly at the necking front is impossible to get with this technique because of the shadow induced by the defects scattering light.

Nevertheless, this method enables us to access the damage either in the necked (N) or in the unnecked (UN) regions as can be seen in Figure 12 (see Figure 26 for a 3D image of the stacked images and the regions of analysis in the sample).

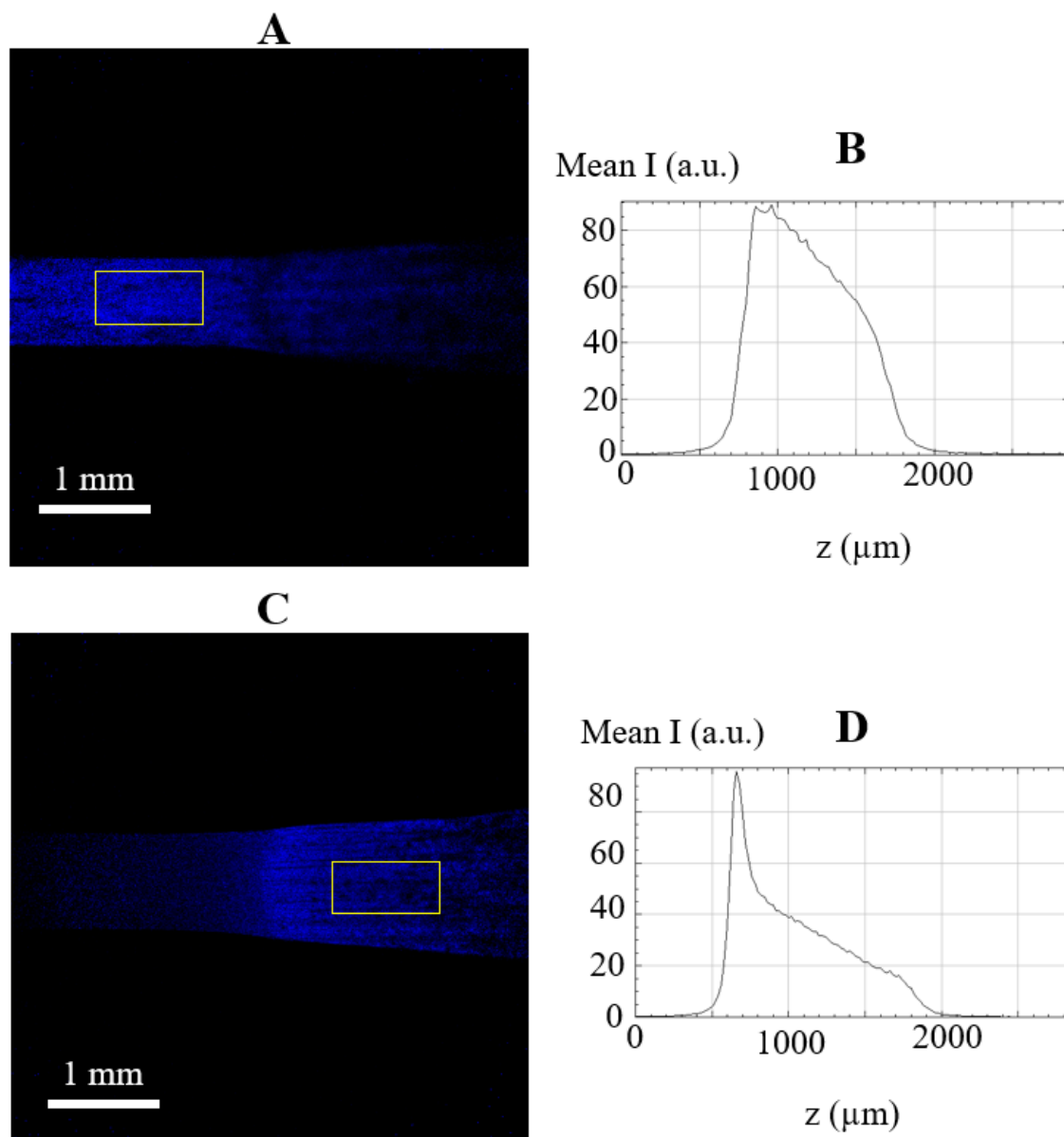


*Figure 12 A and C. Confocal images of a stretched necked DAQNEA0.5 at two different depths extracted from the same z-scan. The yellow rectangle corresponds to the zone used to measure the intensity in the necked region (A) and the unnecked region (C). B and D. Respectively averaged measured intensity in the necked and unnecked region as a function of depth.*

The first pic that can be seen in the Figure 12 D is an artefact of the materials surface and the differences in the optical indexes of the sample and air. It is not relevant and was not considered in the quantitative analysis.

From the raw intensity data presented in Figure 12, we extracted the fraction of broken chains of the filler network, in the necked (N) and unnecked (UN) regions. We measure approximately that 20 % of the chains of the filler network are broken in the UN region and around 30 % of the chains of the filler network are broken in the N region. These values seem quite high if we consider that the network exists

in 3 D and the chains should break only in the tensile direction (one third of the total number of chains would potentially break). Therefore, 30 % of breakage of the filler network corresponds to the breakage of almost all the filler network chains in the tensile direction. Values reported in Figure 13 show that the neck region is more damaged than the unnecked region. This corroborates the fact that the necked region is softer than the unnecked region as more of the filler network is broken in the necked region, the force is probably transferred from the filler network to the matrix network.

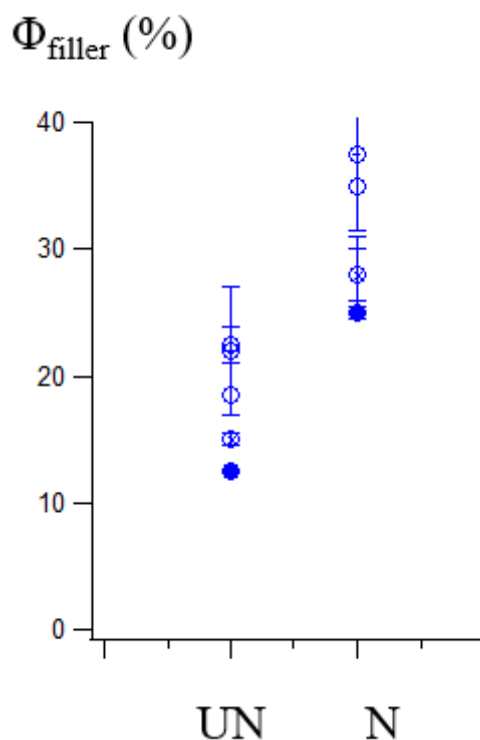
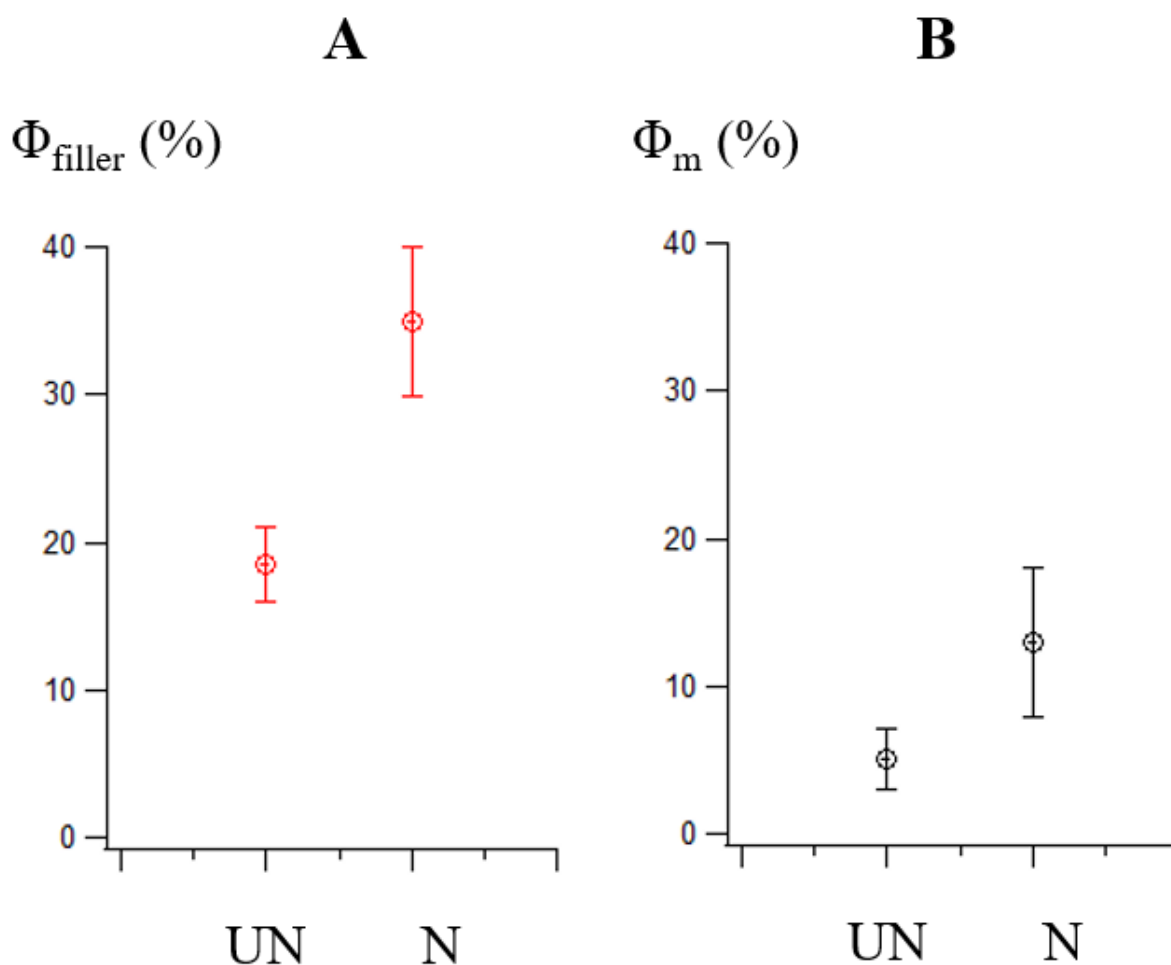


Figure 13 Damage fraction in the unnecked (UN) and necked (N) regions of DAQNEA0.5 samples at the neck plateau.

### 3.3. Load transfer between the filler and the bulk (SP in the matrix)

The large damage evidence in the filler network raises the question of how does the material retains its macroscopic integrity. Such large damage suggests that the matrix network takes part of the load. We aim at characterizing this transfer of stress between the filler network and matrix network. To do so, we measured the evolution of damage in the filler network and stress in the matrix at the same time by working with multiple network samples marked with two mechanophores, one in the filler network and another one in the matrix network. Specifically, we synthesized a quadruple network elastomer from a filler network containing DACL and incorporated spiropyran in the first matrix network only. The sample was then stretched while being imaged with the confocal. Results are reported in the following figure.



*Figure 14* Quantification of mechanophores' activation ratio in DAQNEA0.5sp, with DACL in the filler network (A) and SP in the first matrix network (B) in the unnecked (UN) and necked (N) regions.

The fraction of broken chains in the filler network and the fraction of activated SP in the matrix network, reported in Figure 14, show that for both mechanophores, the activation is always higher in the necked region than in the unnecked region.

More activation is measured in the filler network than in the matrix network for both the unnecked and necked regions of the sample. In the material, the filler network is more stretched than the matrix, hence the stress is focused on the filler network.

The ratio of chains in the matrix that are pulled by a force superior to the SP force threshold (Figure 14 B.) in the unnecked region is around 5 % and is considered negligible and within the noise from the self-activation of the SP (possibly induced by the light of the laboratory where we performed the experiments). Once the region is necked, SP activates in the matrix.

SP activation is measured to be around 14 %, of the matrix chains, in the necked region. This shows that there is a significant transfer of stress between the filler and the matrix during the necking propagation, which results in higher forces applied to the matrix network.

## 4. What parameters control the necking process?

The previous chapter focused on the characterization of necking in one type of sample with a given structure. In the following section, we try to understand the parameters that govern necking by investigating the effect of filler pre-stretch and network structure on the necking transition and on the amount of damage in necked samples.

### 4.1. Effects of the pre-stretch

Considering filler networks with constant crosslinking density, previous work by the group [3] has shown that it was possible to build a master curve of the stress-strain behavior of multiple network elastomers based on the dilution of the first filler network in the overall sample and a corrected deformation corresponding to the effective deformation experienced by the first pre-stretched network. This rescaling demonstrates that the mechanical properties of the material are controlled by the effective stress  $\sigma \cdot \lambda_0^2$  carried by the filler network chains and the effective deformation  $\lambda \lambda_0$  of the filler network.

In this section, we compare the necking behavior in uniaxial tension of a triple network (TN) ( $\lambda_0 = 2.4$ ) and a quadruple network (QN) ( $\lambda_0 = 3.0$ ) made from the same filler network DASN0.5 (containing 0.5 mol% crosslinker) and we study the mechanical response upon necking and the effective damage in these two materials. Specifically, we performed tensile tests of these samples under the confocal microscope and imaged the necked and unnecked regions. We quantified damage following the same analysis as described in section 2.3.

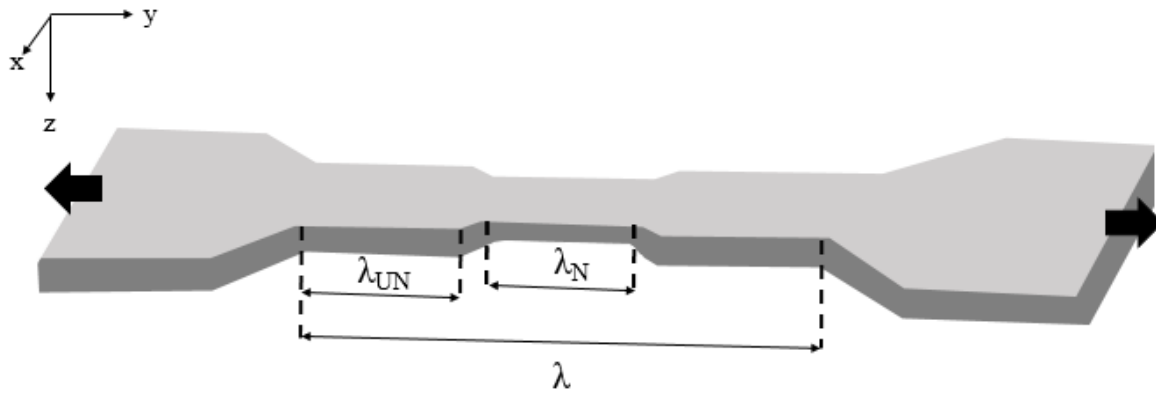


**Figure 15** Representation of the stretched necked sample and the deformation  $\lambda$  measured as if the deformation was homogeneous in the sample and the deformation  $\lambda_{UN}$  and  $\lambda_N$  which corresponds respectively to the local deformation in the unnecked and necked regions.

To compare these samples, we also extracted the local deformations  $\lambda_{loc}$  of the necked ( $\lambda_N$  in the Figure 15) and unnecked ( $\lambda_{UN}$  in the Figure 15) regions. Assuming that the material is incompressible, we can estimate the local deformation in the direction of traction  $\lambda_{loc}$ , if we know the deformations in the width and thickness directions as  $\lambda_{loc} = \lambda_y = 1/\lambda_x\lambda_z$ . Using the confocal images, the deformations  $\lambda_x$  and  $\lambda_z$  were estimated from the width and thickness of the sample in the loaded state, divided respectively by the initial width and thickness.

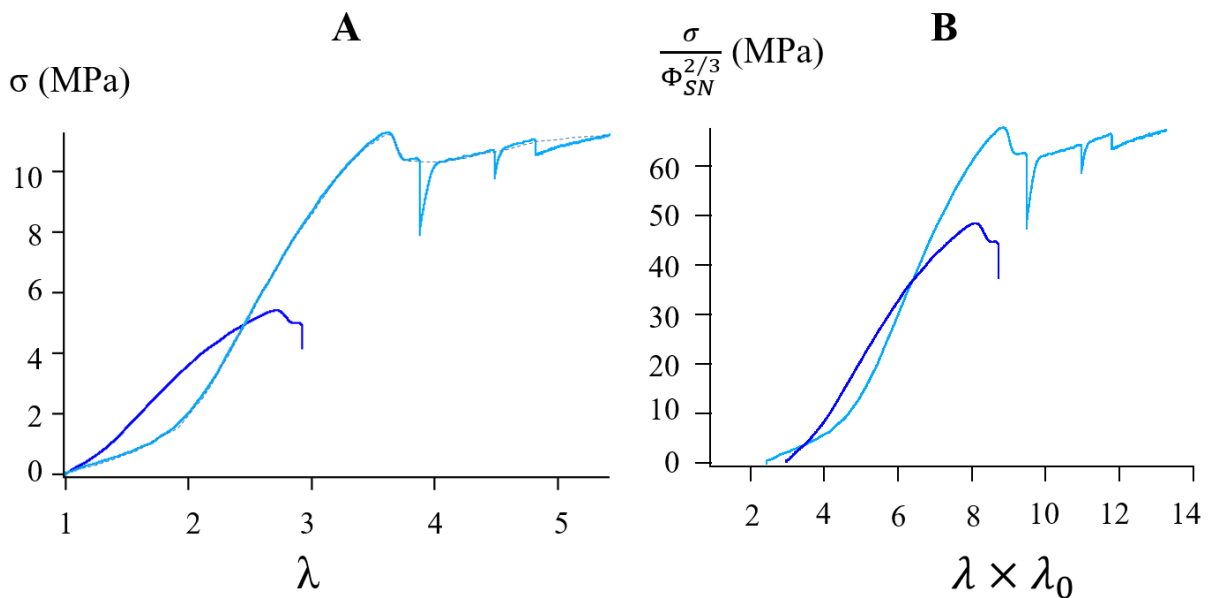


**Figure 16 A.** Stress-stretch curves of DATNEA0.5 and DAQNEA0.5. Drops in the curve are due to the relaxation of the sample happening when the test was stopped to tighten the mechanical clamps. The dotted line serves only as a guide for the eye. **B.** Nominal stress renormalized by  $\phi_{SN}^{2/3} = \lambda_0^{-2}$  as a function of the deformation corrected by the filler network pre-stretch  $\lambda_0$  for the stress-strain curves of A.

We should note that it was very difficult to observe necking in the TN, most samples either broke or slipped under the mechanical clamps, and only one necked TN could be analyzed. The results are reported in Figure 16 and Figure 17.

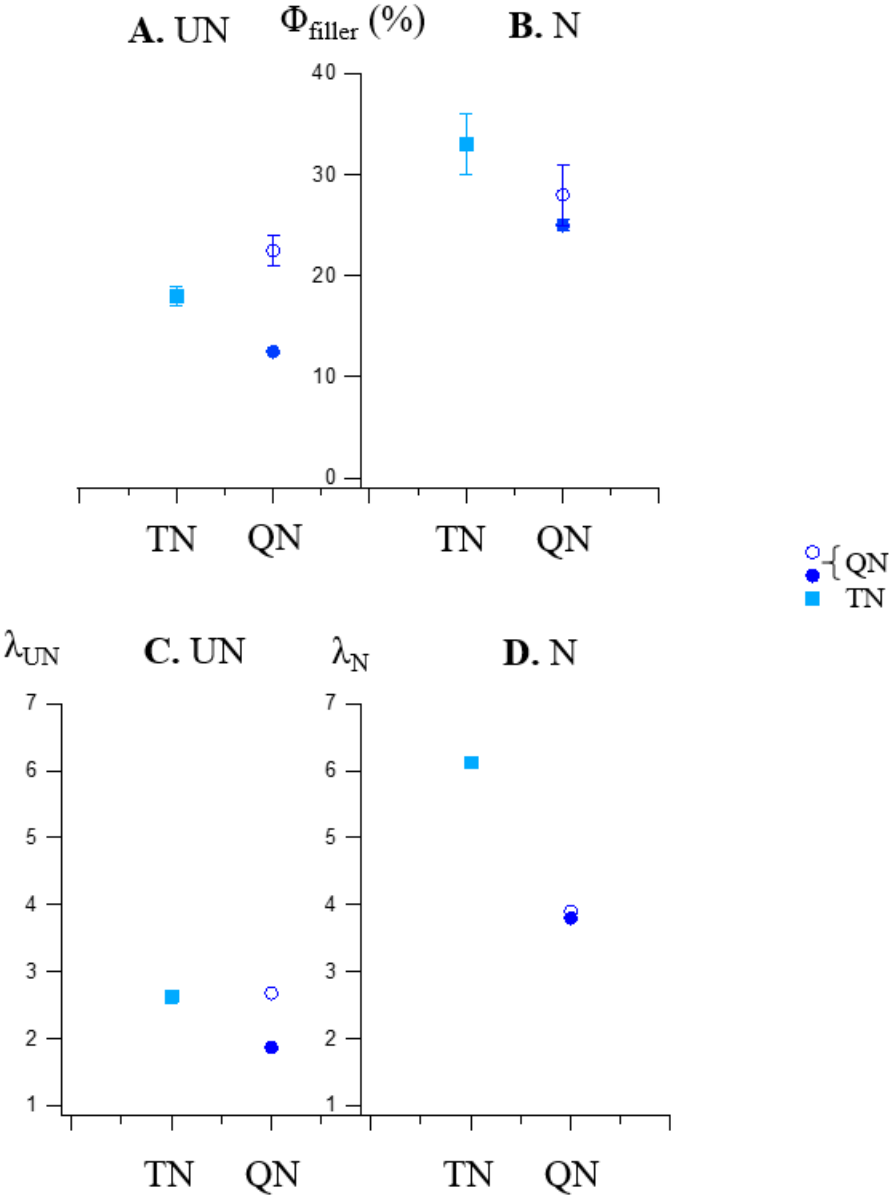


Figure 17 Quantification of damage in the filler network in the unnecked (A.) and necked (B.) regions, and local deformations in the unnecked (C.) and necked (D.) regions in DATNEA0.5 and DAQNEA0.5.

By looking at the mechanical test results in the Figure 16, two observations can be made. First, the TN deforms more before necking than the QN. Second, the stress threshold reached by the TN is higher than the one reached by the QN.

These observations can be explained by the dilution and the pre-stretch of the filler network in the multiple network. The filler network is pre-stretched by the different networks composing the matrix: it is more pre-stretched in the QN than in the TN. Therefore, the chains of the filler network, are less diluted in the TN than in the QN.

As the material's modulus is a function of the areal density of elastically active chains, the maximum stress of the TN is logically higher than the one of the QN. The chains of the TN are also less pre-stretched which means they are further away from their limit extensibility, so the TN can deform more than the QN before nucleating a neck.

The stress-stretch behavior of a series of multiple network samples from the same filler network fit into a master curve [3] if we plot the normalized stress (corrected by the filler network dilution) as a function of the normalized deformation (corrected by the pre-stretch of the filler network), represented in Figure 16 B.

These differences in the mechanical response can also be seen in Figure 17, where we plot the local deformation  $\lambda_{loc}$  in the neck and in the unnecked phase. The local deformation in the unnecked region is a little lower in the QN than in the TN. The difference is more noticeable in the necked region, where the local deformation is approximately 4 in the QN and 6 in the TN.

It should be discussed that the local deformations might seem a little off with the mechanical results in the unnecked region: from section 3.1, we explained that once the neck has nucleated, the local deformation in the unnecked and necked regions should remain constant, and that the averaged deformation of the macroscopic sample was only the result of the neck propagation. This means that the local deformation of the unnecked region should remain at 3.6 for the TN and at 2.7 for the QN. The calculated local deformations, reported in Figure 17 B, underestimates the local deformation for the TN and overestimates it for the QN. The error can be due to slippage of the sample during the tensile test (which overestimates the measured macroscopic deformation) or due to the way the local deformation is indirectly measured:

The width and thickness, used to estimate the local deformation, and measured in the loaded state, suffer from experimental errors: as the material's width and thickness are not constant between the clamps because of the sample's dogbone shape and the applied pressure at the clamps (as shown in Figure 3 C). To minimize the experimental error, in the necked region, we measured the width and thickness at what seemed to be the minimum, and in the unnecked region, we measured the width and thickness at what seemed to be the maximum.

We didn't perform step-cycles of loading on our materials to quantify the mechanical hysteresis in each cycle as was done by Millereau et al. [3], but, assuming that the mechanical behavior of necking samples follows the same pattern in terms of mechanical hysteresis as those tested by Millereau et al., we estimate the hysteresis directly from our uniaxial extension test until failure, as detailed in the Appendix.

The hysteresis between the loading and unloading path of the tensile test [3] is equivalent to an work done by the sample. This work is due to the damage of the filler network and structural modification of the multiple network which translates macroscopically into a deformation. This gives an estimate of the energy dissipated before the nucleation of the necked region occurs and of the same quantity once the whole gauge length has undergone necking, i.e; once the necked region has propagated to the whole sample.

Our results are shown in Table 1. As expected from the high levels of stress reached by the TN at the onset of necking, hysteresis is much higher for the TN than for the QN sample.

We can then study the evolution of the fraction of broken filler network crosslinkers, expressed as a fraction of the filler network  $\Phi_{\text{filler}}$  (Eq. 4), for both types of samples (detailed values are summarized in Table 7, in the Appendix for all samples). As shown in Figure 17 A., The damaged fraction appears of the same order of magnitude, with a slightly larger damage for the TN: in the necked region:  $\phi_{\text{filler}} = 33\%$  for the TN and  $\phi_{\text{filler}} = 26\%$  for the QN.

Given the large differences in mechanical properties for these two materials, in particular with respect to the local deformation in the necked phase, this result is unexpected. However, we have to remember that the density of elastically active chains of the filler network are different in the TN and QN. Comparing the effective strain  $\lambda_{10c}\lambda_0$  in the necked phase in TN and QN, we obtain approximately similar values of respectively 15 and 13, consistent with the similar damaged fraction of filler network in the two materials.

Though the damaged fractions of filler network are similar between TN and QN, if we now consider the concentration of broken chains (of the filler network, in the overall multiple network), we need to take into account the dilution of the filler network. In the TN, the filler network is less diluted than in the QN, therefore, the concentration of broken chains is actually higher as shown in Table 1.

From the analysis of the stress-strain curves as described in the Appendix, the energy dissipated in the process of necking of the TN is higher than that dissipated during the necking of the QN. Yet, more chains are also broken per unit volume in the TN than in the QN. From the energy dissipated (U) and

the concentration of broken chains ( $C$ ), we estimate the energy dissipated per broken chain ( $Q$ ) and results are summarized in Table 1. The most obvious result is the difference in energy dissipation before and during necking. Clearly the formation of the neck, that involves a large increase in macroscopic stretch, occurring in the transition region between unnecked and necked region, dissipates much more energy while the additional number of broken chains remains small.

If we compare materials, the results show that more energy per chain is dissipated by the breakage of the filler network in the QN than in the TN both before and after necking. In terms of energy dissipation, the damage of the filler network is more efficient in multiple network with increasingly pre-stretched filler network.

*Table 1 Effect of the filler network pre-stretch on the concentration of broken chains ( $C_i$ ), the energy hysteresis ( $U_i$ ) and the energy dissipated per mol of broken chains ( $Q_i$ ), in the unnecked ( $i=UN$ ) and necked ( $i=N$ ) regions.*

sample name	$C_{UN}$ (mol/m <sup>3</sup> )	$C_N$ (mol/m <sup>3</sup> )	$\Delta C$ $= C_N - C_{UN}$ (mol/m <sup>3</sup> )	$U_{UN}$ (MJ/m <sup>3</sup> )	$U_N$ (MJ/m <sup>3</sup> )	$Q_{UN}$ (MJ/mol)	$Q_N$ (MJ/mol)
DATNEA0.5	1.17	2.16	0.98	3.5	29.6	3.0	30.2
DAQNEA0.5	0.33	0.54	0.21	1.5	8.5	4.5	40.5
	$\pm 0.17$	$\pm 0.17$	$\pm 0.17$			$\pm 0.8$	$\pm 0.6$

#### 4.2. Effects of the filler network crosslinking content

In this section, we investigate the effect of network structure on the necking process by varying the chain length of the filler network. We compare two quadruple networks with filler networks of different crosslink densities (DAQNEA0.5 and DAQNEA0.25) and characterize the damage threshold required to nucleate a neck in regards to the molar concentration of crosslinker in their filler network.

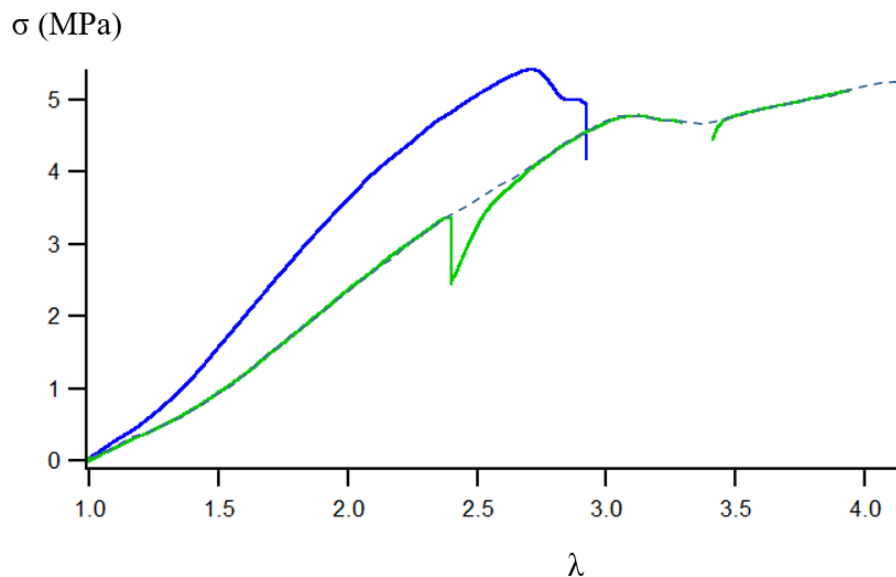


Figure 18 Effect of the filler network crosslinker molar content on the stress-stretch curve of quadruple networks whose filler network contains 0.5mol% (blue) or 0.25mol% (green) crosslinker.

From the tensile tests on DAQNEA0.5 and DAQNEA0.25, we can spot three differences between these samples. First at low strain, DAQNEA0.5 is stiffer than DAQNEA0.25. Second the maximum stress at which the samples neck is higher in DAQNEA0.5 than in DAQNEA0.25. Finally, the deformation at which the samples nucleate a neck is lower in DAQNEA0.5 than in DAQNEA0.25.

The low strain stiffness is in agreement with the expected effect of the filler network on the mechanical properties of the multiple network. The work of P. Millereau has shown that the yield stress is an increasing function of the areal chain density of the filler network [3]. The filler network DASNEA0.5 has a higher chain density than DASNEA0.25. This is exacerbated by the successive swelling of these networks to obtain a quadruple network, as lower crosslink content in the filler network results in higher swelling [17] and increased dilution of chains.

The latter argument also explain the maximum stress reached by the samples before necking. With a higher chain density of filler network, DAQNEA0.5 reaches a higher stress than DAQNEA0.25.

Finally, on average the strands between crosslinks of the filler network are longer in a less crosslinked network (SN0.25). This means that to reach its finite extensibility, SN0.25 will deform more than SN0.5. This effect still applies to the network when embedded in the matrix, therefore, DAQNEA0.25 nucleates a neck at higher deformation than DAQNEA0.5.

Sample	DASN0.5	DASN0.25
Young's modulus (MPa)	0.81	0.66
Toughness (J/m <sup>2</sup> )	172	308
E <sub>x</sub> (MPa)	0.67	0.37
E <sub>e</sub> (MPa)	0.29	0.29
N <sub>x</sub>	268	486

Table 2 Mechanical characteristics of DASNEA0.5 and DASNEA0.25 from uniaxial extension tests (chapter 6)

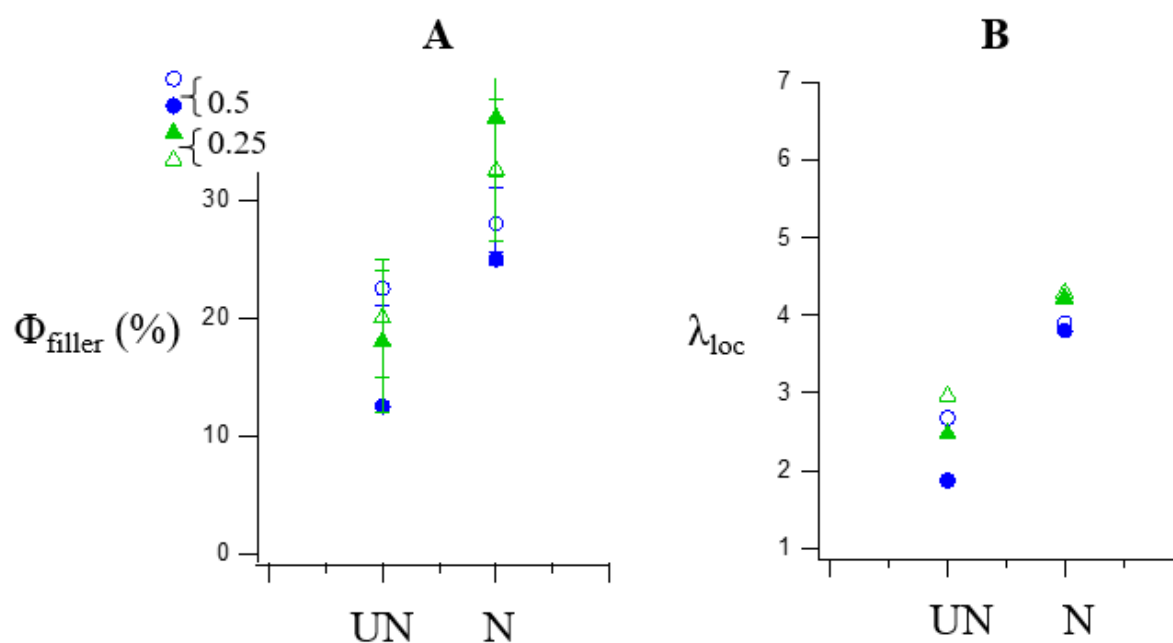


Figure 19 A. Quantification of damage and B. local deformation in DAQNEA0.25 and DAQNEA0.5 in the unnecked and necked regions.

If we look at the local deformation (reported in Figure 19 B.), we notice that the local deformations are slightly higher for DAQNEA0.25 than DAQNEA0.5 in both unnecked and necked regions.

Estimations of the energy dissipation induced by the structural modification within the multiple networks, as detailed in the Appendix, are shown in the Table 3. In the unnecked region, the energy

dissipated is similar in DAQNEA0.25 and DAQNEA0.5. In the necked region, a little more energy is dissipated in DAQNEA0.5 8.5 MJ/m<sup>3</sup> compared to 7.8 MJ/m<sup>3</sup> for DAQNEA0.25.

Table 3 Effect of the filler network crosslink density on the concentration of broken chains ( $C_i$ ), the energy hysteresis ( $U_i$ ) and the energy dissipated per mol of broken chains ( $Q_i$ ), in the unnecked ( $i=UN$ ) and necked ( $i=N$ ) regions.

sample name	$C_{UN}$ (mol/m <sup>3</sup> )	$C_N$ (mol/m <sup>3</sup> )	$\Delta C$ $= C_N - C_{UN}$ (mol/m <sup>3</sup> )	$U_{UN}$ (MJ/m <sup>3</sup> )	$U_N$ (MJ/m <sup>3</sup> )	$Q_{UN}$ (MJ/mol)	$Q_N$ (MJ/mol)
DAQNEA0.5	0.33	0.54	0.21	1.5	8.5	4.5	40.5
	$\pm 0.17$	$\pm 0.17$	$\pm 0.17$	$\pm 0.3$	$\pm 0.1$	$\pm 0.8$	$\pm 0.6$
DAQNEA0.25	0.23	0.42	0.19	1.5	7.8	6.5	41.1
	$\pm 0.02$	$\pm 0.05$	$\pm 0.05$	0.2	0.7	$\pm 0.9$	$\pm 3.8$

The fractions of filler network damage (reported in Figure 19 A.) are within the same order of magnitude in the unnecked region despite the differences in stress and deformation. The fraction of damage is slightly higher in the necked region for DAQNEA0.25 than DAQNEA0.5. It correlates with the slightly higher local deformation of the necked region in DAQNEA0.25 than DAQNEA0.5.

If both samples show the same fractions of filler network damage, considering the dilution of the filler network, as the filler network is more diluted DAQNEA0.25 than in DAQNEA0.5, the concentration of broken chains is higher in DAQNEA0.5 than in DAQNEA0.25, as shown in the Table 3.

The energy hysteresis is higher in DAQNEA0.5 but the concentration of broken chains is also higher in DAQNEA0.5. The results in Table 3 show that the fracture of filler network chains induces more energy dissipation per chain in DAQNEA0.25 ( $Q_{UN} = 42.6$  MJ/mol and  $Q_N = 44.1$  MJ/mol) than in DAQNEA0.5 ( $Q_{UN} = 29.9$  MJ/mol and  $Q_N = 39.4$  MJ/mol). In terms of energy dissipation, the damage of the filler network is therefore more efficient per sacrificial bond broken as the crosslink density of the filler network decreases.

Finally, we probed the effect of structure on stress transfer from filler network to matrix network during necking. To do so, SP was incorporated in the first matrix network of a quadruple network from a filler

network functionalized with DACL and containing either 0.25 mol% or 0.5 mol% total crosslinker. These DAQNEA0.5sp and DAQNEA0.25sp were tested in tensile tests under the confocal, and quantification of damage in the filler and the matrix is reported in Figure 20.

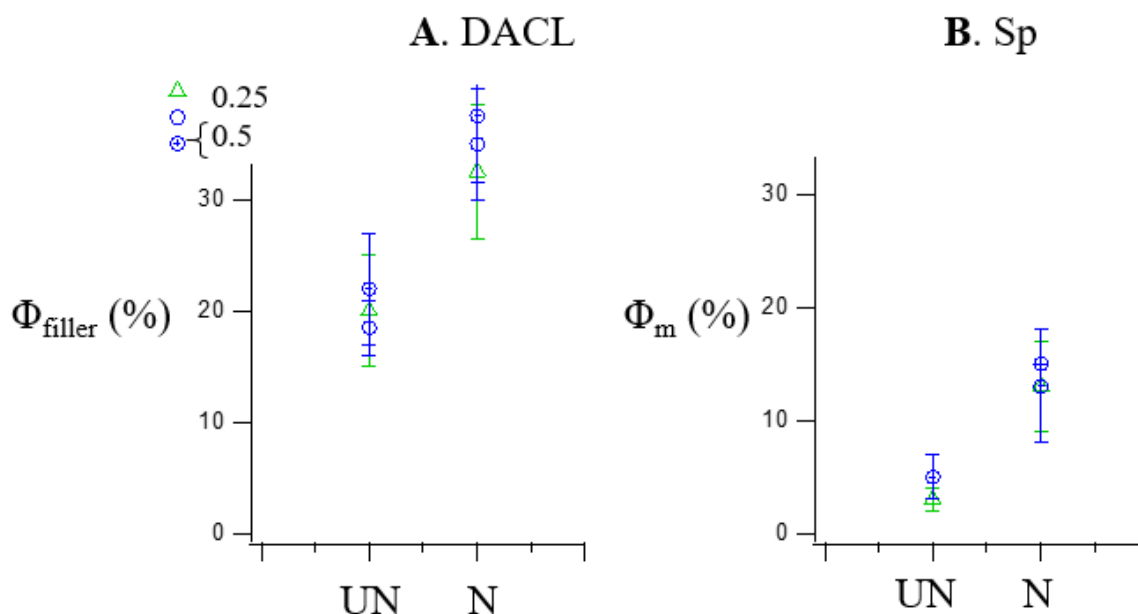


*Figure 20* Effect of the network structure on stress transfer during the necking process on DAQNEA0.25sp and DAQNEA0.5sp. **A.** damage fraction of the filler network from DACL activation and **B.** fraction of matrix network loaded with a force above 240 pN from SP activation, in the necked and unnecked regions of DAQNEA0.25sp and DAQNEA0.5sp

For both samples, the damage fractions of filler network  $\Phi_{\text{filler}}$  measured in the necked and the unnecked regions are similar within the experimental error. The fraction of matrix network which is loaded with a force above the force threshold of SP activation  $\Phi_m$ , is also similar between DAQNEA0.5sp and DAQNEA0.25sp in the necked regions. The values in the unnecked regions aren't considered as SP activation because they correspond to the same levels of noise in the un-tested samples.

The matrix network has the same composition in both samples and the stress levels reached by DAQNEA0.5sp at the necking plateau is very close to the one of DAQNEA0.25sp. The force distribution measured seems in agreement with the similarities of the macroscopic mechanical properties.

## 5. Effect of the connectivity between filler and matrix networks

In this section, we focus on the effect of connections between the filler network and the matrix in the fraction of damage in the filler network during necking. Uncontrolled transfer reactions during the polymerization of EA can connect a PEA chain with a growing chain. This is due to the presence of labile hydrogen in the PEA chain. These reactions randomly connect the successive networks.

To avoid these uncontrolled connections, we worked with a methacrylate monomer that doesn't contain the labile hydrogen required for the transfer reactions, such that no connections can happen between the filler methacrylate network and the acrylate matrix.

### 5.1. SNHMA synthesis

The filler network is very important to the properties of the final multiple network as previously explained in Chapter 1 section 3.5.3. We choose to work with hexyl methacrylate as monomer because its glass transition temperature is quite low ( $-5\text{ }^{\circ}\text{C}$ ) compared to other methacrylate monomers.

PHMA samples will be labeled SNHMA $x$  where  $x$  is the molar content of crosslinker.

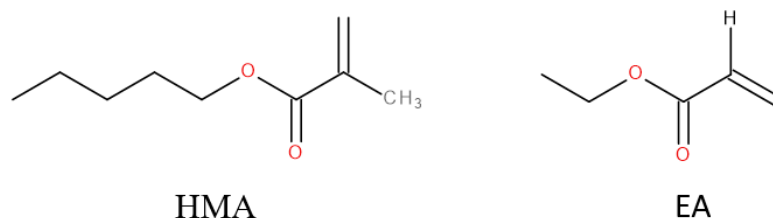


Figure 21 Representation of HMA and EA monomers

To compare the HMA and EA networks, we decided to reach comparable molecular weight between crosslinks. This led us to choose a total molar crosslinker concentration equal to 0.85 mol%, so a theoretical molecular weight between crosslink equal to approximately 10 000 g/mol, similar to what is theoretically expected for SNEA0.5. However, the side chain of HMA is very big compared to EA, this affects the number of monomer units between crosslinks which corresponds to 59 for SNHMA0.85 and 100 for SNEA0.5 (Table 4). Shorter chains and longer side groups should affect the mechanical properties of the network because of differences in the chains limit extensibility and entanglements.

Methacrylate monomers do not have the same reactivity as acrylates. Therefore, we needed to adapt the polymerization process to reach high conversions. The modified polymerization process will be detailed

below, the main changes were the polymerization time, which lasted 3 times longer than the polymerization of EA, and the initiator amount, which was increased 10 times.

The DACL mechanophore is not as easily soluble in HMA as it is in EA. To enhance the dispersion of DACL in HMA, we dissolved DACL (0.0022 g, 0.02 mol%) first in acetone (0.45 mL) before mixing it with HMA (4.05 mL, 20.5 mmol), BDA (32.03  $\mu$ L, 0.170 mmol, 0.83 mol%) and HMP (312  $\mu$ L, 2.05 mmol, 10.00 mol%). The mix was then injected into molds and irradiated with low intensity UV ( $< 10 \mu\text{W}/\text{cm}^2$ ) for 6 h.

We synthesized a filler network of Poly(hexyl methacrylate) (PHMA) and characterized its mechanical properties. The results of the tensile test are represented in the Figure 22.

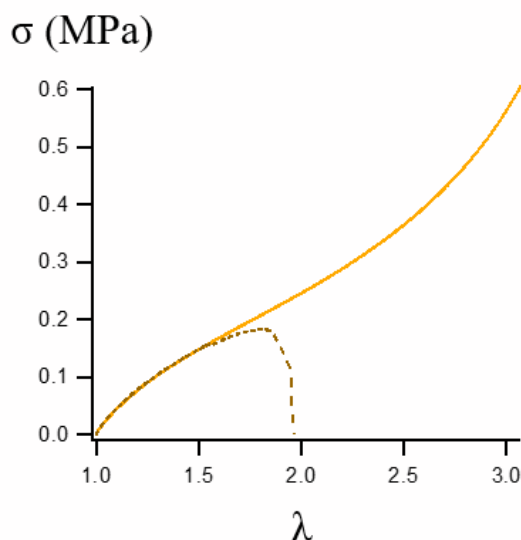


Figure 22 Stress-stretch curve of a DASNHMA0.85 unnotched (full line) and notched (dotted line)

Sample	DASNHMA0.85	DASN0.5	DASN0.25
Young's modulus (MPa)	0.42	0.81	0.66
Toughness ( $\text{J}/\text{m}^2$ )	443	172	308
$E_x$ (MPa)	0.39	0.67	0.37
$E_e$ (MPa)	0.04	0.29	0.29
$N_x$	271	268	486

Table 4 Summary of the mechanical properties of DASNHMA0.85, DASNEA0.5 and DASNEA0.25

The Young's modulus of the DASNHMA0.85 is low compared to both EA single networks crosslinked with 0.5 and 0.25 mol% BDA. From the Rubinstein-Panuykov fit, we could extract the contributions of the entanglements and crosslinks in the Young's modulus. As expected from the length of the side chain and the use of solvent during the polymerization process, the contribution of the entanglements in DAQNHMA0.85 is very low compared to PEA networks. This results in similar contributions of crosslinks in the Young's modulus between DASNHMA0.85 and DASN0.25. Finally, the theoretical number of monomer units between crosslinks, calculated using the contribution of crosslinks to the Young's modulus, results in similar numbers of monomer units in DASNHMA0.85 and DASN0.5.

From the modulus perspective, it makes sense to compare the quadruple networks from DASNHMA0.85 and DASN0.25 in the following sections. And from a chain length perspective, it makes sense to compare the quadruple networks from DASNHMA0.85 and DASN0.5.

## 5.2. Necking in HMA multiple networks

To study the effect of connections between filler and matrix network during the necking of multiple network elastomer, we worked with quadruple networks with either PEA or PHMA as filler network and PEA as matrix network. We deformed them under the confocal microscope and imaged them to quantify damage in the necked and unnecked regions.

The DASNHMA0.85 network is used as filler network in the process of making multiple network as described in section 1.3. The sample is mechanically tested and results are reported in Figure 23.

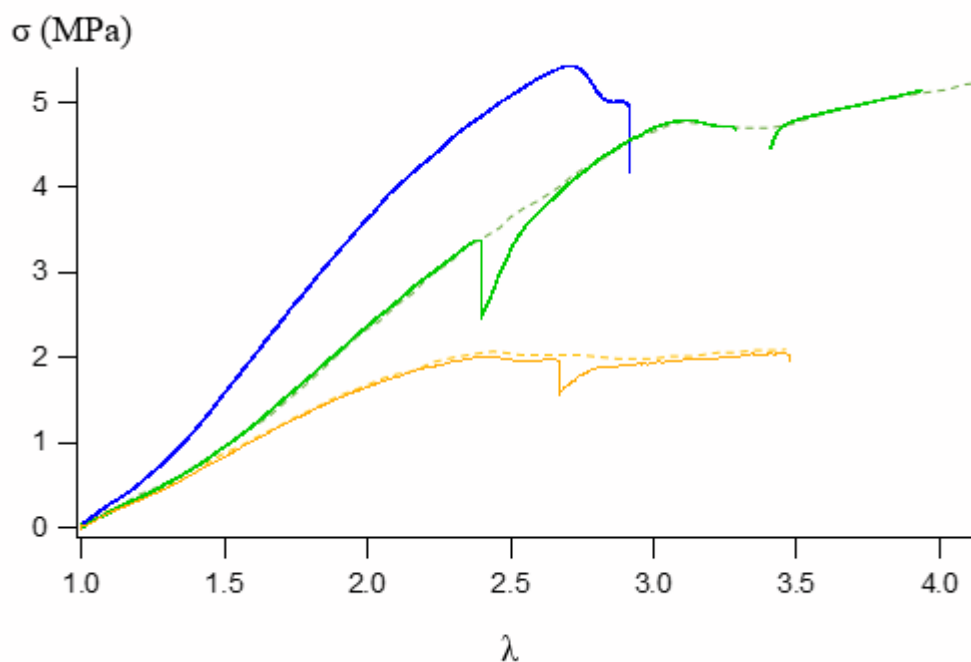


*Figure 23* Stress-stretch curve of DAQNHMA0.85 (yellow), DAQNEA0.5 (blue) and DAQNEA0.25 (green)

From the mechanical test (Figure 23), we can see that DAQNHMA0.85 and DAQNEA0.25 have similar Young's modulus. However, at higher stretches, their mechanical behavior differs. DAQNEA0.25 becomes stiffer than DAQNHMA0.85. DAQNHMA0.85 also nucleates a neck for a much lower stress and deformation than DAQNEA0.25.

The mechanical behavior of DAQNHMA0.85 and DAQNEA0.5 are quite different in terms of stress and modulus. DAQNHMA0.85 is softer than DAQNEA0.5. Finally, DAQNHMA0.85 nucleates a neck for slightly lower deformation than DAQNEA0.5, even though their theoretical chain length were similar.

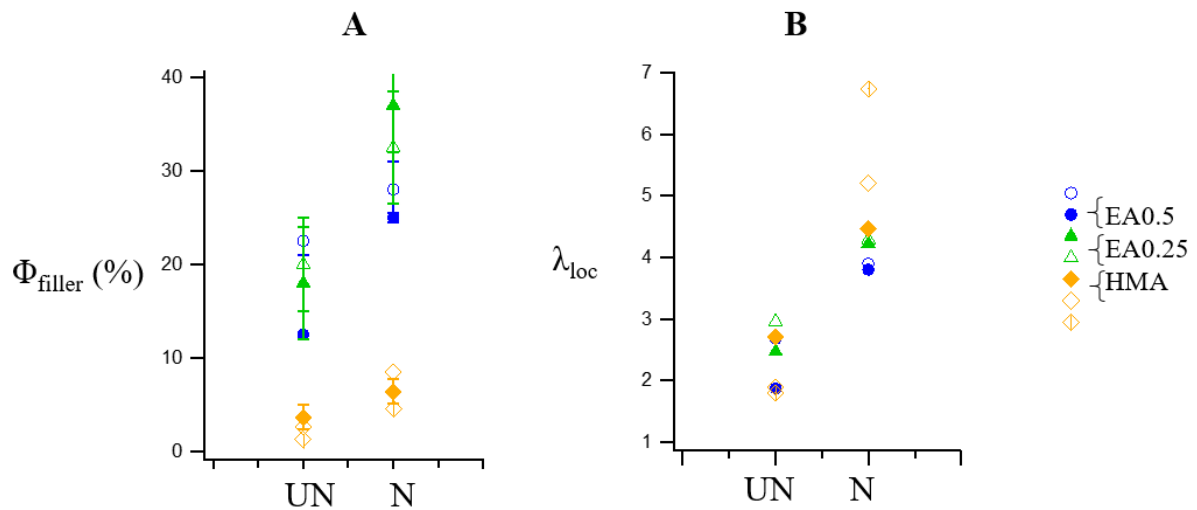


Figure 24 A. Quantification of damage and B. local deformation in necked samples of DAQNHMA, DASN0.5 and DASN0.25

The measured local deformation (Figure 24 B.) is higher in the necked region of DAQNHMA0.85 than in the other samples. In the unnecked region, the measured local deformations are similar in all samples despite the difference in the stress-stretch curves.

As expected from the mechanical curves and the lower levels of stress reached by DAQNHMA0.85, the estimations of the energy hysteresis  $U$  (as detailed in the Appendix) show that less energy is dissipated in the necking process of DAQNHMA0.85 than in any of the other EA samples (results reported in Table 5).

## Chapter 7: Quantitative study of molecular bond breakage and load transfer during the necking of multiple network elastomer

Table 5 Effect of the connections between the filler and the matrix networks on the concentration of broken chains ( $C_i$ ), the energy hysteresis ( $U_i$ ) and the energy dissipated per mol of broken chains ( $Q_i$ ), in the unnecked ( $i=UN$ ) and necked ( $i=N$ ) regions.

sample name	$C_{UN}$ (mol/m <sup>3</sup> )	$C_N$ (mol/m <sup>3</sup> )	$\Delta C$ $= C_N - C_{UN}$ (mol/m <sup>3</sup> )	$U_{UN}$ (MJ/m <sup>3</sup> )	$U_N$ (MJ/m <sup>3</sup> )	$Q_{UN}$ (MJ/mol)	$Q_N$ (MJ/mol)
DAQNHMA0.85	0.05	0.08	0.03	0.6	3.7	12.0	123.3
DAQNEA0.5	0.33	0.54	0.21	1.5	8.5	4.5	40.5
	$\pm 0.17$	$\pm 0.17$	$\pm 0.17$	$\pm 0.3$	$\pm 0.1$	$\pm 0.8$	$\pm 0.6$
DAQNEA0.25	0.23	0.42	0.19	1.5	7.8	6.5	41.1
	$\pm 0.02$	$\pm 0.05$	$\pm 0.05$	$\pm 0.2$	$\pm 0.7$	$\pm 0.9$	$\pm 3.8$

About damage quantification, as reported in Figure 24 A., the damage in DAQNHMA0.85 in the necked and the unnecked regions are very low (around 4 % in the unnecked region and 7 % in the necked region) compared to EA samples. The material becomes ductile and nucleates a neck with much fewer broken chains when samples have no connection between the filler network and the matrix compared to samples whose filler and matrix are connected.

Finally, we showed that a multiple network whose filler network is not connected to the matrix network breaks less chains and dissipates less energy than a multiple network where the filler network is connected to the matrix network. However, in terms of energy dissipation, the damage of the filler network in DAQNHMA0.85 is a lot less efficient in the unnecked region ( $Q_{UN} = 12.0$  MJ/mol) and surprisingly a lot more efficient in the necked region ( $Q_N = 123.3$  MJ/mol) than any of the two QN EA samples, as shows Table 5. This interesting result suggests that although all sacrificial bonds are equal (the DA adduct or the C-C bond) their potential for energy dissipation and hence for toughening seems to be dependent on their local environment.

Energy dissipation induced by the damage of the filler network may be enhanced by the absence of connection between the filler and the matrix networks, because the structural changes in the multiple network are possibly exacerbated in the absence of connection between filler and matrix networks.

## 6. Discussion

From the previous results, we can plot the damage fraction of filler network as a function of the corrected local deformation (which corresponds to the local deformation multiplied by the filler network pre-stretch). The data are gathered in Figure 25.

Figure 25 shows that the damage fraction of the filler network seem to evolve linearly with the renormalized filler network deformation. With the exception of the samples containing HMA, all the “all acrylate” samples fit into a similar curve. The damage fraction of filler network increases linearly with the corrected local deformation of the filler network up to what looks like a plateau value around 35 %. More data at higher corrected local deformation should be added to confirm this pioneer observation.

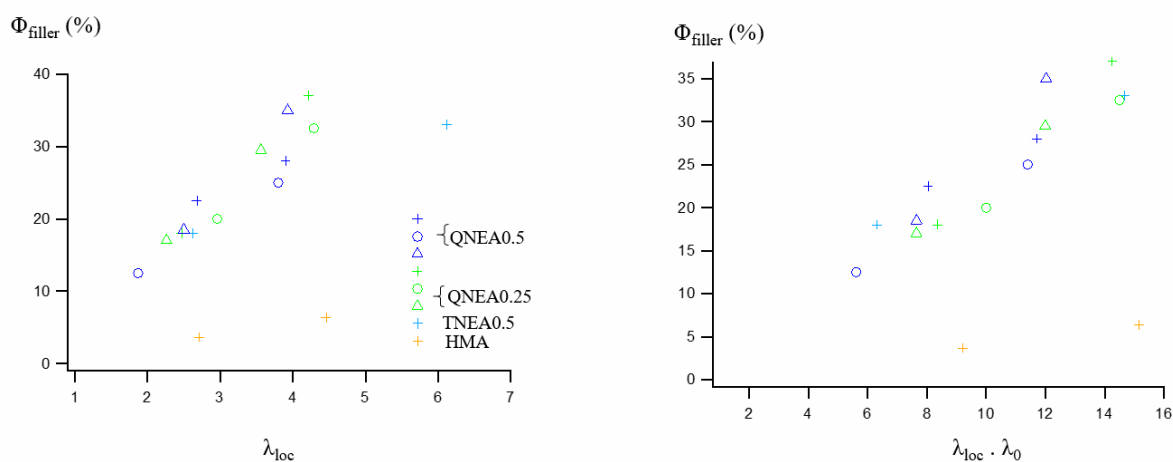


**Figure 25** Damage fraction of the filler network as a function of the local deformation  $\lambda_{\text{loc}}$  (left) and the corrected local deformation  $\lambda_0 \times \lambda_{\text{loc}}$  (right)

## Conclusion

The fracture of multiple network elastomer can be pictured to happen in a two-step process where, in order to propagate a crack, the filler network breaks, first, at the crack tip, prior to the matrix network. Experiments on double network hydrogels have shown experimentally that such yielding occurred at the crack tip of the double network gels [18]. The study of necking is a way to investigate at a bigger scale (in the bulk) the mechanism that happens, very locally, at the crack of multiple networks, during a crack propagation.

We designed a coupled tensile test/confocal set-up, to observe the fluorescent signal in stretched materials and synthesized multiple network elastomers functionalized with mechanophores, that become fluorescent upon breakage (DACL) or force threshold (SP). Together, these gave new insights on the damage process and stress transfer between filler network and matrix network upon necking. Using these coupled methods, we could reveal in real-time, previously invisible bond scission, building in the material, as it is being stretched. With the addition of another mechano-fluorophore, that reports for stress in the material, and its quantification, our method enables to access, the stress transfer from the damaged filler network to the matrix network, in a quantitative manner.

In conclusion, we used damage sensitive and load sensitive mechanophores to obtain novel insights into the necking process which can be observed in multiple network elastomers.

Using these local probes, we saw that the necking occurs in three stages, first a diffuse and delocalized damage in the filler network, which can reach up to 15 to 20% of broken chains.

Past this level of damage, we note that to transition from the unnecked region to the necked region only few more percentage (~ 10%) of chains are broken. Most damage happens before the nucleation of a neck. This suggests that in the neck propagation, the breakage of few bonds triggers a large energy dissipation by macroscopic deformation. Mostly occurring locally at the neck fronts, we have seen the material becoming more diffusive due to the apparition of heterogeneities in the materials. From there, a highly damaged necked phase propagates and the damaged filler network partially transfers stress to the matrix network.

We varied the filler network pre-stretch, the filler network structure and the filler network chemical nature to study respectively the effect of filler-prestretch, the effect of chain length and the effect of connections between filler and matrix on the nucleation of a neck and on the fraction of bond scission in the filler network in the unnecked and necked regions.

Our results show that the energy dissipated per moles of broken chains increases, in both the necked region and the unnecked region, when the filler network crosslink density decreases and the fraction of filler network in the matrix decreases (increasing filler pre-stretch). The absence of connections between

the filler and the matrix networks tend to enhance the energy dissipated per broken chains in the necked region due to an exacerbated macroscopic deformation of the sample.

Our results (Figure 25) show that the fraction of damage in the filler network varies linearly with the “real” local deformation of the filler network (which takes into account the filler network pre-stretch and the local deformation).

There could be a plateau value of the filler network damage fraction around 35 %, more tests and data are needed to confirm this observation.

## Appendix

### 3D view of damage in a necked sample

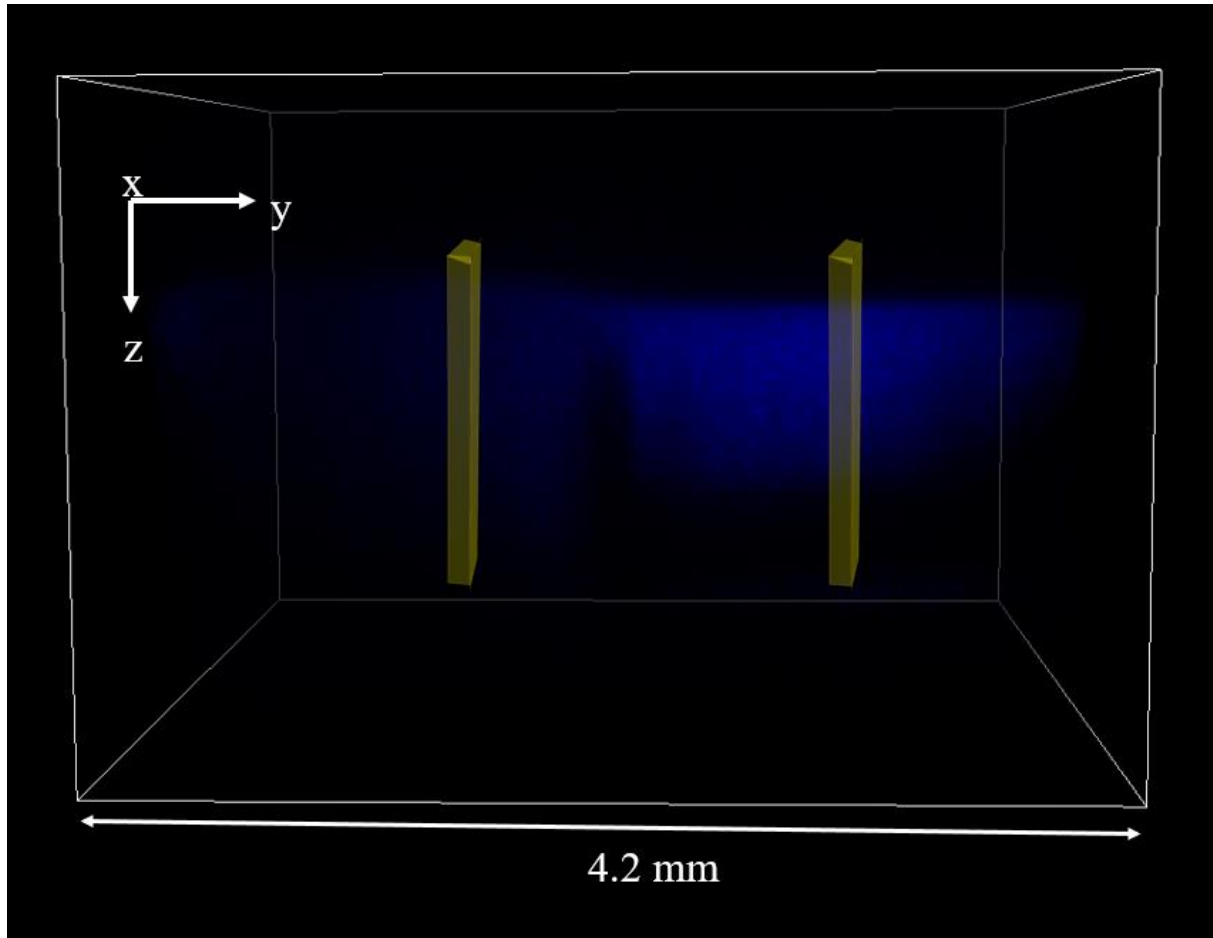


*Figure 26 3D image of the depth scan of a necked sample (without flatfield correction). The direction  $y$  is the direction of traction.  $z$  is the depth direction. The yellow parallelepipeds correspond to two zones of analysis: the left one is the unnecked region of the sample and the right one is in the necked region.*

We should note the 3D observations could only be performed on the raw confocal images. This means that the light absorption of the sample was not taken into account, nor the flatfield correction in the figure above.

### Summary of the differences in the multiple network materials synthesized

Multiple network samples with different compositions have been synthesized. They are all reported in the table below.

Table 6 Description of the materials used in the study of necking

Sample name	filler network	$\lambda_0$	SN wt%	number of polymerization step
DATNEA0.5	SN0.5	2.4	7.2	3
DAQNEA0.5	SN0.5	3	3.7	4
DAQNEA0.25	SN0.25	3.4	2.5	4
DAQNHMA0.85	SNHMA0.85	3.4	2.5	4

### Effect of network structure on energy dissipation

The different samples were not tested in cyclic loading. So we do not have access experimentally to the exact measurements of the energy dissipated as a function of  $\lambda$ . But we can estimate the hysteresis from the uniaxial extension tests.

Assuming that the stress-stretch curve of necking follows the general pattern represented in Figure 27. From the cyclic loading experiments of P. Millereau [3], we can extract the fraction ( $f$ ) of the work done on the sample ( $W$ ) which corresponds to the mechanical hysteresis ( $U_{UN}$  before necking and  $U_N$  during the necking plateau).

Before the neck, the work done  $W_{UN}$  must scale with:

$$W_{UN} \approx \sigma_y \times \lambda_{UN} \quad \text{Eq. 10}$$

Where  $\sigma_y$  and  $\lambda_{UN}$  are the yield stress and the deformation at which the neck nucleates.

And at the end of the neck plateau when the whole gauge length is necked,  $W_N$  is given as:

$$W_N \approx \sigma_y \times \lambda_N \quad \text{Eq. 11}$$

Where  $\lambda_N$  is the local deformation of the necked region.

Then, the fraction of elastic energy which corresponds to the mechanical hysteresis can be obtained from the data of Millereau et al. and will be given by:

$$f_i = \frac{U_i}{W_i} \quad \text{Eq. 12}$$

Where  $i$  is either UN or N, to describe respectively before the sample's necking and at the end of the neck plateau.

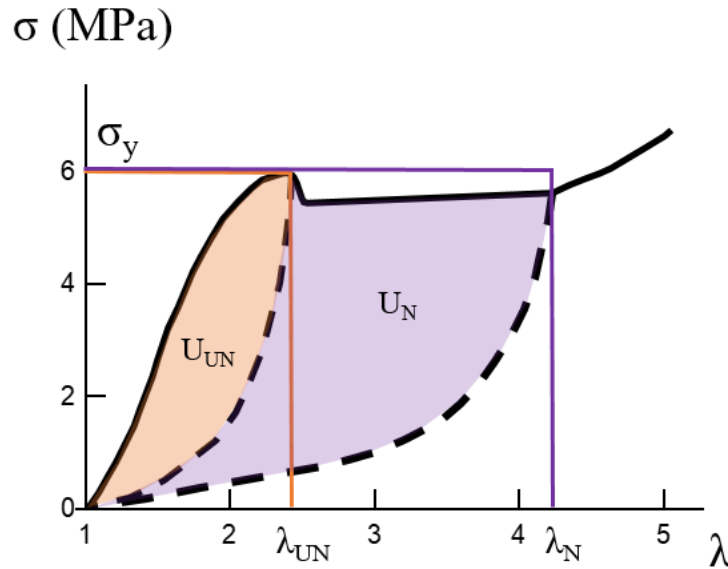


Figure 27 Schematic representation of the stress-stretch curve of the necking of a multiple network elastomer and the mechanical hysteresis before necking  $U_{UN}$  and the mechanical hysteresis during necking  $U_N$

Experimentally, we found  $f_{UN} \approx 12\%$  and  $f_N \approx 41\%$ . The fraction of the work done to the material that is dissipated is 4 times higher during the formation of the neck than before the neck. This is due to the permanent structural change of the filler network occurring during the necking process.

Then from our uniaxial extension tests, we can access the work done  $W_{UN}$  and  $W_N$  as given by Eq. 10 and Eq. 11. Finally, we multiply this value by the percentage found above (from the experimental data of P. Millereau) to get an estimate of the hysteresis due to  $U_{UN}$  and  $U_N$  from Eq. 12.

The confocal data gives in parallel an information on the concentration of broken chains (from the filler network in the multiple network), these are reported in the Table 7.

Table 7 Summary of the quantification of damage from confocal imaging

sample name	$\lambda_0$	$\Phi_{\text{filler}}$		$\Phi$		Concentration of broken chains (mol/m <sup>3</sup> )		
		UN	N	UN	N	$C_{UN}$	$C_N$	$\Delta C = C_N - C_{UN}$
DATNEA0.5	2.4	18%	33%	1.30%	2.39%	1.17	2.16	0.98
DAQNEA0.5	3	18% $\pm 5\%$	29% $\pm 5\%$	0.66% $\pm 0.19\%$	1.09% $\pm 0.19\%$	0.33 $\pm 0.17$	0.54 $\pm 0.17$	0.21 $\pm 0.17$
DAQNEA0.25	3.4	18% $\pm 2\%$	33% $\pm 4\%$	0.47% $\pm 0.04\%$	0.84% $\pm 0.10\%$	0.23 $\pm 0.02$	0.42 $\pm 0.05$	0.19 $\pm 0.05$
DAQNHMA0.85	3.4	4%	6%	0.10%	0.15%	0.05	0.08	0.03

Then, with the estimate of the mechanical hysteresis, we can obtain an approximation of the energy dissipated per mole of broken chains (noted  $Q_{UN}$  and  $Q_N$ ) just before necking (at the neck nucleation) and during necking, as shown in Table 8.

Before the neck,  $Q_{UN}$  is given by:

$$Q_{UN} = \frac{U_{UN}}{C_{UN}} \quad \text{Eq. 13}$$

For the neck plateau,  $Q_N$  is given by:

$$Q_N = \frac{U_N}{\Delta C} \quad \text{Eq. 14}$$

Where  $\Delta C$  is the concentration of broken chains that were not broken before the neck propagated, and is equal to the concentration of broken chains in the necked region  $C_N$  minus the concentration of chains broken before the neck formation  $C_{UN}$ .

Table 8 Summary of the hysteresis estimated from the mechanical data in before the neck and at the neck plateau

sample name	$\lambda_{UN}$	$\lambda_N$	$\sigma_y$ (MPa)	$U_{UN}$ (MJ/m <sup>3</sup> )	$U_N$ (MJ/m <sup>3</sup> )	$Q_{UN}$ (MJ.m <sup>3</sup> /mol)	$Q_N$ (MJ.m <sup>3</sup> /mol)
DATNEA0.5	2.6	6.1	11.3	3.5	29.6	3.0	30.2
DAQNEA0.5	2.4	3.9	5.4	1.5	8.5	4.5	40.5
	$\pm 0.4$	$\pm 0.1$		$\pm 0.3$	$\pm 0.1$	$\pm 0.8$	$\pm 0.6$
DAQNEA0.25	2.6	4.0	4.8	1.5	7.8	6.5	41.1
	$\pm 0.4$	$\pm 0.4$		$\pm 0.2$	$\pm 0.7$	$\pm 0.9$	$\pm 3.8$
DAQNHMA0.85	2.7	4.5	2	0.6	3.7	12.0	123.3

## References

1. Zhao, X. *et al.* Soft Materials by Design: Unconventional Polymer Networks Give Extreme Properties. *Chem. Rev.* **121**, 4309–4372 (2021).
2. Ducrot, E., Chen, Y., Bulters, M., Sijbesma, R. P. & Creton, C. Toughening Elastomers with Sacrificial Bonds and Watching Them Break. *Science* **344**, 186–189 (2014).
3. Millereau, P. *et al.* Mechanics of elastomeric molecular composites. *Proceedings of the National Academy of Sciences* **115**, 9110–9115 (2018).
4. Na, Y.-H. *et al.* Necking Phenomenon of Double-Network Gels. *Macromolecules* **39**, 4641–4645 (2006).
5. Gong, J. P. Why are double network hydrogels so tough? *Soft Matter* **6**, 2583 (2010).
6. Tominaga, T. *et al.* The molecular origin of enhanced toughness in double-network hydrogels: A neutron scattering study. *Polymer* **48**, 7449–7454 (2007).
7. Na, Y.-H. *et al.* Structural Characteristics of Double Network Gels with Extremely High Mechanical Strength. *Macromolecules* **37**, 5370–5374 (2004).
8. Chen, Y., Sanoja, G. & Creton, C. Mechanochemistry unveils stress transfer during sacrificial bond fracture of tough multiple network elastomers. *Chem. Sci.* 10.1039/D1SC03352B (2021) doi:10.1039/D1SC03352B.
9. Göstl, R. & Sijbesma, R. P.  $\pi$ -extended anthracenes as sensitive probes for mechanical stress. *Chemical Science* **7**, 370–375 (2016).
10. Klajn, R. Spiropyran-based dynamic materials. *Chem. Soc. Rev.* **43**, 148–184 (2014).
11. Zhang, H. *et al.* Spiropyran as a Mechanochromic Probe in Dual Cross-Linked Elastomers. *Macromolecules* **47**, 6783–6790 (2014).
12. Chen, Y. Cartographie quantitative de la contrainte dans les matériaux mous par mécano-chimie. (PSL, 2018).
13. Slooman, J. Détection quantitative de l'endommagement moléculaire, par mécano-fluorescence, dans les matériaux mous. (PSL, 2019).

14. Sloodman, J. *et al.* Quantifying Rate- and Temperature-Dependent Molecular Damage in Elastomer Fracture. *Phys. Rev. X* **10**, 041045 (2020).
15. Gossweiler, G. R., Kouznetsova, T. B. & Craig, S. L. Force-Rate Characterization of Two Spiropyran-Based Molecular Force Probes. *J. Am. Chem. Soc.* **137**, 6148–6151 (2015).
16. Millereau, P. M. Large Strain and Fracture of Multiple Network Elastomers. (Paris 6, 2017).
17. Flory, P. J. & Rehner, J. Statistical Mechanics of Cross-Linked Polymer Networks II. Swelling. *The Journal of Chemical Physics* **11**, 521–526 (1943).
18. Tanaka, Y. *et al.* Localized Yielding Around Crack Tips of Double-Network Gels. *Macromolecular Rapid Communications* **29**, 1514–1520 (2008).



# General conclusion



## Design of novel soft materials

The double network concept has been discovered on hydrogels in 2003 by the group of Gong [1] and successfully applied to elastomers at the SIMM lab in 2014 [2]. It is based on a particular interpenetrated structure, in which a first crosslinked soft network is pre-stretched in a second sparsely crosslinked and softer network. Although this strategy leads to a mechanical improvement of both the strength and the toughness of the materials, the process to synthesize them remains inapplicable at an industrial scale. In the first part of the present work, two new material's designs have been developed, both inspired by the double network structure. The aim of the proposed novel syntheses is to overcome the limitations of the conventional bulk synthesis process, which are long swelling times with a volatile monomer and the poor control of the shape.

First, we successfully synthesized nanocomposite elastomers filled with soft crosslinked particles. The microstructure of these materials resembles that of double network particles embedded in a continuous soft matrix, as represented in Figure 1. Compared to conventional nanocomposite elastomers filled with hard particles, these materials present the advantage of being transparent in both the undeformed and the deformed state (no whitening). Compared to the conventional bulk synthesis of double networks, this new process permits to control the final shape of the sample (and as an added bonus, no excess chemicals were required to swell the filler network particles). The volume fraction of fillers as well as the crosslinking density of the filler particles was varied to understand the effect of these parameters on the materials' mechanical properties. Mechanical characterizations of these nanocomposites filled with soft particles (in uniaxial extension, cyclic loading and notch propagation) showed that the materials remain highly elastic and their modulus was not much affected by the concentration of fillers. In contrast, interestingly, we could tune the materials' strain hardening by changing the fillers' volume fraction. However, the maximal volume fraction of filler in the matrix is limited by the increased viscosity in the filler/ monomer mixture. Above a threshold value, the mix was not injectable anymore in the polymerization mold, and we could not control the material's shape anymore. Finally, the effect of the filler particles on the fracture energy remained low probably due to the absence of connections (chemical or physical) between filler particles.

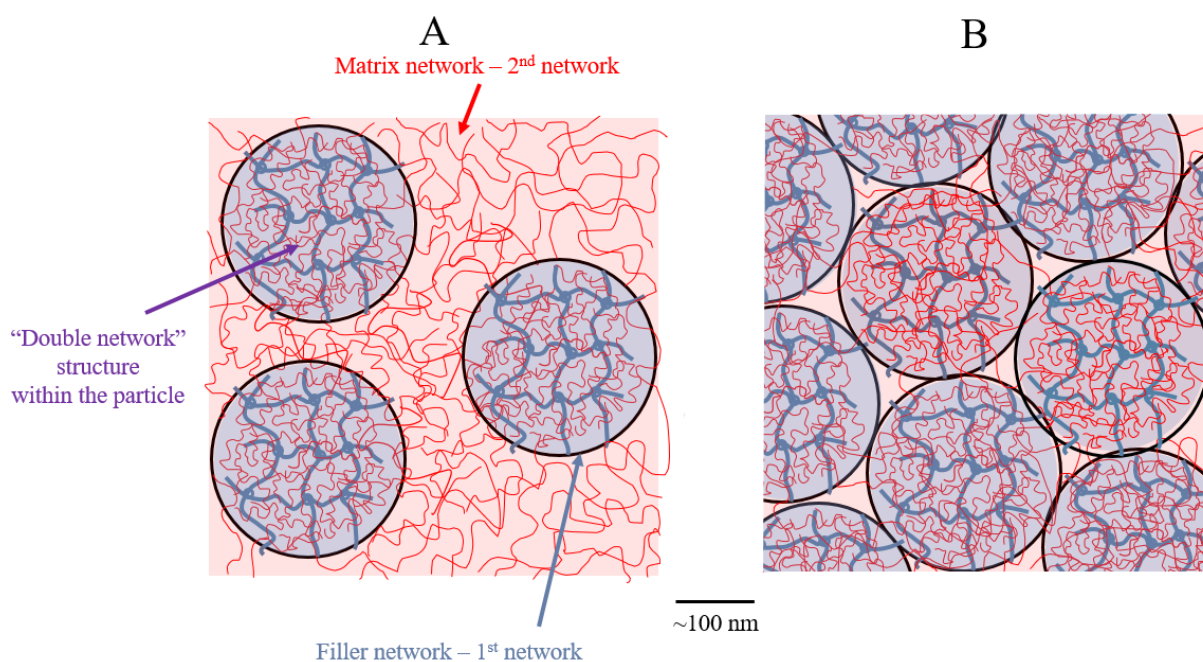


Figure 1 Schematic representation of the networks' "double network" structure (A) obtained from the nanocomposite strategy or (B) from the emulsion strategy. The 1<sup>st</sup> network particles are pre-stretched with the 2<sup>nd</sup> network.

In our second "all-water" synthesis strategy, we synthesized double network particles directly in water, using emulsion polymerization. In the developed process, we synthesized in a first emulsion polymerization step slightly crosslinked particles (first network), that we thereafter used as seeds in a second polymerization step, in which – after monomer swelling of the seed latex in water – the second network is polymerized within the first particles (still in water). This process overcomes the two main limitations of the conventional bulk synthesis of double networks, as the swelling of nanoparticles is fast and it is possible to control the shape of the final material. However, the synthesis of double particles is challenging: the second network may polymerize partially or completely outside of the first network particles, which would then fail to pre-stretch the first network, therefore not activating the sacrificial bond reinforcement mechanism.

We tested the mechanical properties of dried films of double network particles and highlighted the importance of the particles interfaces. This led us to functionalize the double network particles (either in their first or second network) with a reactive monomer, namely DAAM. The DAAM's ketone functions could be connected during the drying step through reaction with a dihydrazide, ADH. Applied to the first network, the final material was more elastic than the previous DAAM-free materials. Finally, when the particles were connected through their second network, the mechanical properties led us to conclude that the structure of the material should be similar to the material obtained with the previous strategy (represented in Figure 1). Compared to the previous process, the new one presents the advantage to

reduce the swelling time and enables us to reach a higher volume fraction of filler particles. It should be noted that the second “all-water” process should be easily scalable and compatible with commonly used processes in the industry.

To conclude, we successfully designed two soft materials inspired by the double network structure, in a more versatile way. Though, these materials do not present the same improved mechanical properties as conventional bulk double networks, their structure proved to have a positive effect on the stress-stretch response of the materials compared to the first and second network components alone. These new processes are of great interest for the production of soft materials with tunable strain-hardening, at large scales, and in particular for industrial applications like paints and coatings.

### Understanding how soft networks break using mechano-fluorescence

To guide the materials chemists in their design of stronger and tougher elastic materials, it is important to understand the fracture process of soft materials and how it relates to the network molecular structure. However, how soft networks break is a multi-scale process (Figure 2), which is not well understood. This is due to the complexity of the dissipation mechanism involved in front of the crack tip, that remained a complete black box, until the recent work of J. Sloopman [3,4]. She used mechanochemistry coupled with confocal imaging to observe and quantify damage in soft materials. Her mechanofluorescent tool opened a new window for the comprehension of chain scission in the fracture of soft materials. The present project logically continues her pioneering work.

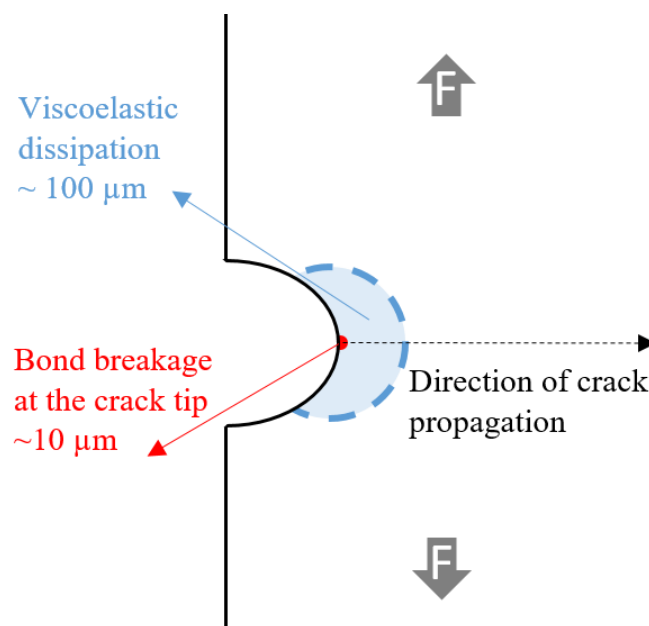


Figure 2 Schematic representation of the dissipation mechanisms involved in the fracture of soft materials (bond breakage at the crack tip, viscoelastic dissipation in a bigger zone around the crack tip)

We started by questioning the representativity of the DACL mechanophore to report for the homolytic rupture of a C-C bond. Though the DACL mechanophore activates at a lower force threshold than the breakage of C-C bond, our results showed that, at our working concentrations of mechanophores, the mechanophore over-activate only slightly. We found little to no effect of the stretch rate (between  $3.33 \times 10^{-4}$  and  $3.33 \times 10^{-2} \text{ s}^{-1}$ ) and only a slight effect of the temperature (between 25 and 80 °C) on the mechanophore's activation. Therefore, we concluded that the DACL mechanophore is a good candidate to report for bond breakage in soft materials.

We adapted the confocal imaging process (from J. Sloodman's work [3]) to the use of a confocal microscope, in order to get images of the fracture surfaces at a higher spatial resolution, and access weak and localized activation signals that were not detected with the previous microscope set-up. We were able to work with samples of crosslinked PEA single networks (that are less viscoelastic than the poly(methyl acrylate) samples previously studied [3]) and studied their fracture in conditions where viscoelasticity is not dominant. Our results show that the fraction of broken chains increases along the crack surface in the direction of propagation.

From there, combining mechanochemistry with mechanical tests, we examined the applicability of the LEFM relationship between critical energy release rate and critical crack tip stress and strain field. In one crosslinked PEA single network, varying the initial notch length, we performed crack propagation tests and recorded videos of the crack propagation. From the video analysis, we extracted the crack length (in the unloaded state) during the propagation. Then, by using a recently published mechanical model [5], we estimated the evolution of the energy release rate at the crack tip during the propagation and compared it to the areal density of broken chains, measured *via* the confocal imaging process on the fracture surfaces. Our experimental results confirmed that the bond scission at the crack tip is governed by the energy release rate. Since the damage at the crack tip is a function of the local stress (and stretch), we conclude that the LEFM relationship between the energy release rate and the critical crack tip stress and strain field is valid in these highly elastic materials.

Following the same procedure, we varied the structure of the crosslinked PEA single network to address experimentally the model of Lake and Thomas. Our results showed that the network structure affects the linear relationship between the damage at the crack tip and the energy release rate. In other terms, our results show that the energy dissipated per broken chain increases non-linearly with the chain's length. Surprisingly, no effect of the network structure was found on the fraction of energy dissipated by bond scission, during the propagation. This suggests that the number of broken chains is a major factor controlling the energy dissipated during a crack propagation, despite the possible variation in bulk viscoelasticity. This is a first experimental observation that brings light to why the molecular model of Lake and Thomas predicts that well the variation of fracture energy with the network structure, even

when the numerical value underestimates the experimental one by orders of magnitude (because of the viscoelastic contributions to the fracture energy).

Finally, in the last chapter, we studied bond scission and energy dissipation during the formation of a necked region in uniaxial tensile tests of multiple network elastomers. Yielding has previously been observed at the crack tip of double network hydrogels [6]. This observation gave an important insight on the physical picture of fracture in double network hydrogels and, by extension, multiple network elastomers, in which breakage of the filler network happens prior to the breakage of the material. The study of necking, in multiple network elastomers, enables to observe at a bigger scale (in the bulk) the yielding that happens locally at the crack tip of double network elastomers [7].

We developed a new set-up to couple tensile tests with confocal microscope imaging. Therefore, we could observe, qualitatively, bond scission in real-time as a sample is stretched and nucleates a neck. We observed a characteristic signal decrease right before the nucleation of the neck. We believe this transient decrease in intensity results from an opacification due to a specific micro-structuration induced by the damage in the filler network: As the filler network breaks, defects in the network are created randomly at first and then transition to a more homogenous distribution of defects, which may locally scatter the light.

In a more static mode, when the stretching was stopped, we could get quantitative information on the broken fraction of filler network in the unnecked and necked region of the sample. In a necked sample, our results show that approximately 20% of the filler network is broken in the unnecked region, and 30% of the filler network is broken in the necked region. This means that in the necked region, the quasi entirety of the filler network chains in the direction of traction are broken. However, networks are 3D object, though almost all the chains in one direction are broken, we should picture chains in the cross directions of traction and chains entanglements keeping the filler network crosslinking point under load [7].

We should also note that only 10 more percent of the filler network should break to trigger a large energy dissipation induced by a macroscopic deformation. These results support the picture of a random distribution of defects in the material before necking, that transition to a more homogenous distribution of defects responsible of a macroscopic deformation of the material. This macroscopic deformation is associated to a stress transfer to the matrix network, measured with the use of a second mechanophore in the first matrix network.

To conclude, the use of mechanochemistry in model PEA single networks coupled with confocal microscopy made it possible to revisit old questions of soft polymer mechanics. Furthermore, the use of mechanochemistry in multiple network elastomers coupled with a new set up combining confocal microscopy with a tensile set-up. This enabled us to observe and quantify damage occurring during the

necking process. Our results improved the understanding of the role of chain scission in the picture of soft networks' fracture.

The recent adaptations and improvements of the mechanical tool paved the way to even more possibilities of investigations and should lead to more future experiments. In particular, more experiments are required to understand how damage occurs at the point of nucleation of a crack, and a more refined image analysis process should be developed to quantify damage during the nucleation mechanism (which occurs over a volume). The activation induced at the edges of the sample (due to the punch cutting) may be avoided by molding the sample directly into a dumbbell shape. Additionally, using the tools developed in this project, the effect of the filler/matrix network connections on the stress transfer in the necking process of multiple network elastomer could be easily accessed with complementary experiments.

1. Gong, J. P., Katsuyama, Y., Kurokawa, T. & Osada, Y. Double-Network Hydrogels with Extremely High Mechanical Strength. *Advanced Materials* **15**, 1155–1158 (2003).
2. Ducrot, E., Chen, Y., Bulters, M., Sijbesma, R. P. & Creton, C. Toughening Elastomers with Sacrificial Bonds and Watching Them Break. *Science* **344**, 186–189 (2014).
3. Sloomman, J. Détection quantitative de l'endommagement moléculaire, par mécano-fluorescence, dans les matériaux mous. (PSL, 2019).
4. Sloomman, J. *et al.* Quantifying Rate- and Temperature-Dependent Molecular Damage in Elastomer Fracture. *Phys. Rev. X* **10**, 041045 (2020).
5. Liu, Z., Zakoworotny, M., Guo, J., Zehnder, A. T. & Hui, C.-Y. Energy release rate of a single edge cracked specimen subjected to large deformation. *Int J Fract* **226**, 71–79 (2020).
6. Tanaka, Y. *et al.* Localized Yielding Around Crack Tips of Double-Network Gels. *Macromolecular Rapid Communications* **29**, 1514–1520 (2008).
7. Chen, Y., Sanoja, G. & Creton, C. Mechanochemistry unveils stress transfer during sacrificial bond fracture of tough multiple network elastomers. *Chem. Sci.* 10.1039.D1SC03352B (2021) doi:10.1039/D1SC03352B.

## Résumé en français

Les matériaux élastiques désignent les matériaux capables de se déformer, de plusieurs fois leur taille initiale, de façon réversible. Cette particularité leur offre une large gamme d'utilisation des pneus, aux joints d'étanchéité. Les matériaux élastiques sont naturellement souples et mous. Certaines utilisations hautes performances requièrent un renforcement du module d'Young tout en gardant les mêmes performances de déformabilité. Cependant, cela n'est pas si facile à faire, car il existe un compromis entre la rigidité des matériaux élastiques et leur déformabilité. De nouveaux matériaux élastiques sont donc synthétisés pour répondre aux critères (module d'Young, extensibilité et résistance à la fracture) des nouvelles applications.

La déformabilité des matériaux élastiques est limitée par la présence de défauts qui entraînent la propagation d'une fissure de façon catastrophique. Les grandes déformations auxquelles un défaut microscopique devient critique dans la rupture macroscopique du matériau, complique la modélisation et la prédiction de la rupture. En effet, contrairement à la rupture des matériaux fragiles dont la mécanique linéaire décrit bien la fracture, les matériaux élastiques se déforment de façon non linéaire bien au-delà d'un petit volume en pointe de fissure. Cela rend non négligeables des mécanismes de dissipation tels que la friction entre les monomères, la relaxation des chaînes pendantes ainsi que la rupture de chaînes du réseau loin de la pointe de fissure.

Le travail effectué dans le cadre de cette thèse se divise en deux grandes parties.

### **I. Nouvelles synthèses de matériaux mous**

La première partie se concentre sur le renforcement des élastomères. La stratégie la plus utilisée industriellement dans le renforcement des élastomères est celle des composites. Il s'agit d'incorporer des renforts durs dans une matrice élastomère pour obtenir un matériau qui bénéficie d'un compromis des propriétés mécaniques des composants. Ces matériaux ont cependant leur limite, ils sont notamment opaques.

Une nouvelle stratégie a été appliquée aux élastomères en 2014 au laboratoire SIMM : il s'agit des réseaux doubles. Ces matériaux sont composés de réseaux polymères interpénétrés de même nature chimique. Le premier réseau doit être réticulé, il joue le rôle de renfort. Il est composé de chaînes courtes, mais reste mou et déformable.

Le deuxième réseau est moins réticulé que le premier réseau, il est composé de chaînes plus longues, est plus mou et déformable que le premier réseau. Il joue le rôle de matrice. Le deuxième réseau préétire le premier réseau. La quantité de matrice est donc d'intérêt dans le degré de pré-étirement du renfort. Lors de la déformation de ce matériau, les chaînes courtes et préétirées du renfort atteignent leur extensibilité limite avant celles de la matrice. Ces chaînes cassent de façon aléatoire dans le matériau avant sa rupture macroscopique. On parle de liaisons sacrificielles : elles dissipent de l'énergie et retarde

la propagation macroscopique d'une fissure (qui est le résultat d'une rupture corrélée des chaînes du réseau interpénétré). Ces réseaux doubles sont obtenus en laboratoire au prix d'une synthèse inadaptée aux grandes échelles de production. Le premier réseau doit être gonflé dans un bain de monomère, cette étape prend un temps conséquent selon la taille du réseau initial, la taille du bain limite la taille du matériel final et la forme du premier réseau détermine la forme du matériel final. Enfin le monomère est utilisé en excès dans le bain, il doit être de petite taille pour diffuser dans le réseau et est donc volatil et pose des questions de toxicité. Nous nous sommes donc inspirée du renforcement structurel de ces matériaux pour développer de nouvelles synthèses, moins restrictives, d'élastomères renforcés.

### 1. Nanocomposites à charges molles

Nous avons d'abord choisi de synthétiser des composites à charges molles et inter-pénétrables, dans lesquels les particules et la matrice sont de même nature chimique. Ainsi les particules se dispersent facilement dans la matrice et le composite finale reste transparent même largement déformé.

Les particules ont été synthétisées en émulsion puis dispersées dans le monomère (Figure 1). Le mélange a été injecté dans un moule pour polymériser la matrice sous UV. La structure de réseau interpénétré dans ces composites se trouve localement au sein des particules molles et inter-pénétrables, comme représenté en Figure 1.

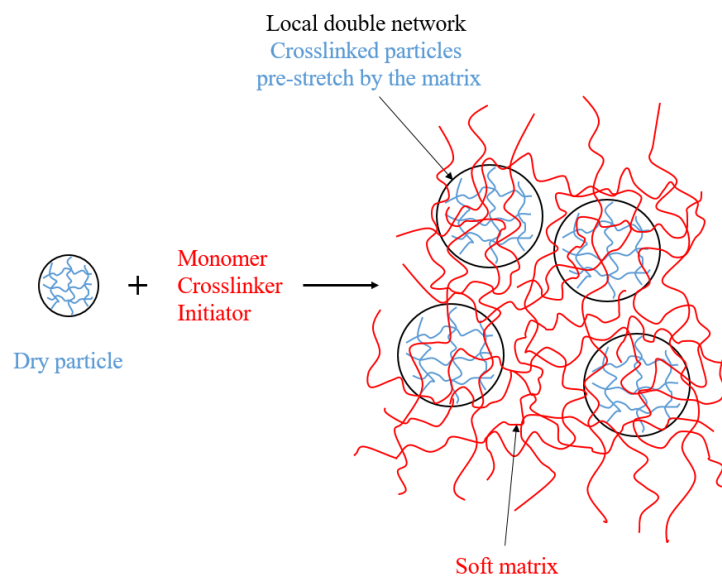


*Figure 1 Nanocomposite à charge molle: représentation schématique du procédé de synthèse et de la structure obtenue.*

Nous avons étudié les propriétés mécaniques de ces matériaux en fonction du pourcentage volumique de particules dans la matrice et en fonction du taux de réticulation des particules. Peu d'effets ont été observés sur la résistance à la propagation de fissure probablement à cause de l'absence de connexions entre les particules. Mais les matériaux obtenus sont tous très déformables et cassent à des contraintes

supérieures à celle de la matrice seule. La présence de particules a permis de retarder la rupture du matériau. De plus, avec cette synthèse, il est possible de contrôler la déformation à partir de laquelle le matériau se durcit en traction à partir de la fraction volumique de particules dans le composite, comme le montrent les résultats de la Figure 2.

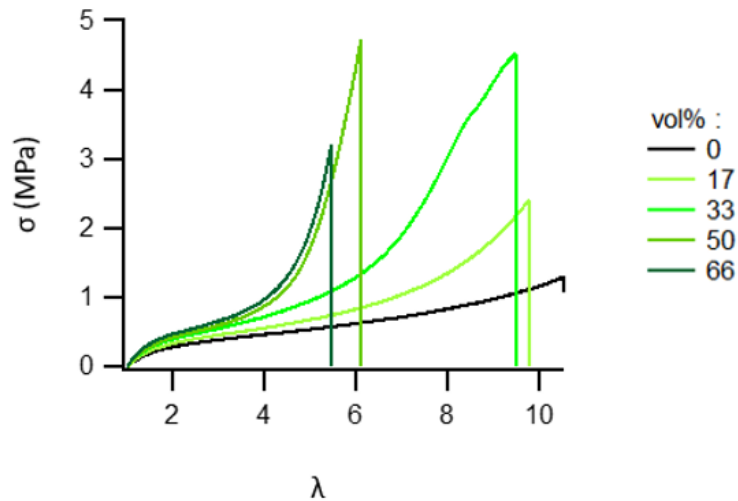
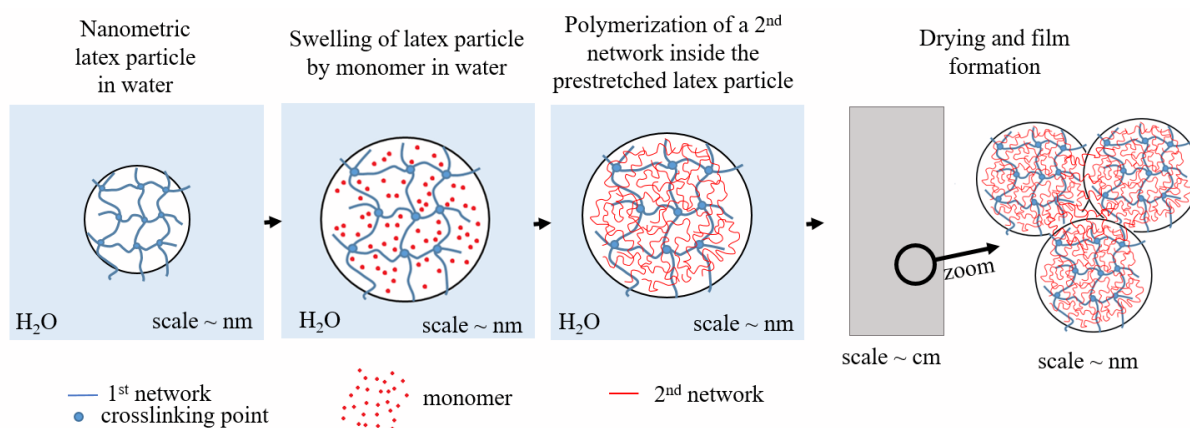


Figure 2 Effet de la fraction volumique de particules molles sur les propriétés mécaniques (contrainte nominale/déformation) des nanocomposites à charge molles

## 2. Synthèse de particules doubles par polymérisation en émulsion et étude de la réponse mécanique des films issus de ces latex

La synthèse précédente présente des limites : la concentration des particules en volume dans la matrice est limitée par la viscosité du mélange et l'étape d'injection dans les moules, l'absence de connexions entre les particules et la difficulté de les connecter par cette synthèse. Nous avons donc décidé d'explorer une voie toute en émulsion pour la synthèse de particules double réseau et la fabrication de revêtements aux propriétés comparables au réseau double en masse. Nous avons ainsi synthétisé des particules réticulées (premier réseau) en émulsion puis introduit le monomère et l'amorceur au réacteur, pour synthétiser dans une deuxième étape en émulsion, le deuxième réseau non réticulé.



*Figure 3 Procédés en émulsion de synthèse des réseaux doubles*

L'émulsion de particules doubles séchées forment un film qui a été testé mécaniquement. Les films de particules doubles, transparents, ont montré une meilleure cohésion que les films de particules réticulées seules (particule type premier réseau).

## II. Étude de la fracture dans les réseaux polymères déformables

La seconde partie est dédiée à la compréhension de la fracture dans les matériaux élastiques à l'aide d'une nouvelle méthode de visualisation et de quantification de la rupture de chaînes de polymères grâce à l'activation d'un signal fluorescent lors de la rupture moléculaire.

### 1. Visualisation et quantification de la rupture de chaînes à l'aide de la mécanofluorescence

Mon travail fait suite à la thèse de J. Sloopman qui a développé au sein du laboratoire SIMM une méthode permettant de visualiser et de quantifier la rupture de chaînes dans les matériaux polymères à l'aide de la mécanofluorescence et de l'imagerie confocale. Cette méthode va être utilisée dans les chapitres de cette partie, et comme elle n'est pas triviale, ce chapitre se concentre sur la présentation de cette méthode et de ses spécificités.

Le terme mécanofluorescence décrit l'émission d'un signal fluorescent qui fait suite à un stimulus mécanique. La molécule mécanofluorescente utilisée par J. Sloopman est le Pi-extended anthracene, incorporé dans les réseaux polymères en tant que réticulant (il est appelé DACL). Cette molécule a l'avantage de se casser par une réaction de rétro Diels-Alder lorsqu'elle est soumise à des déformations proche de la déformation maximale d'une liaison simple carbone-carbone, et une fois cassée, elle libère une moitié anthracène qui émet un signal fluorescent stable. Combiné à de l'imagerie confocale, cet outil permet donc d'imager les mécanofluorophores activés en volume dans l'échantillon.

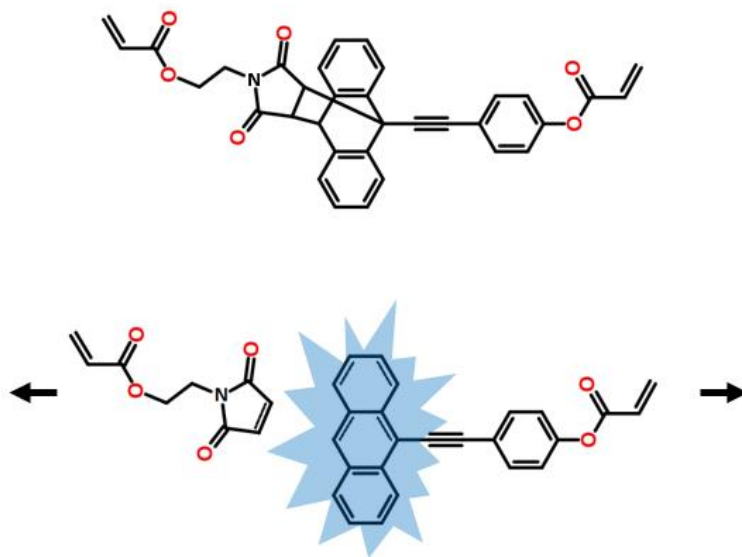


Figure 4 DACL mécano-fluorophore à l'état inactivé (non fluorescent) et à l'état activé après traction (fluorescent)

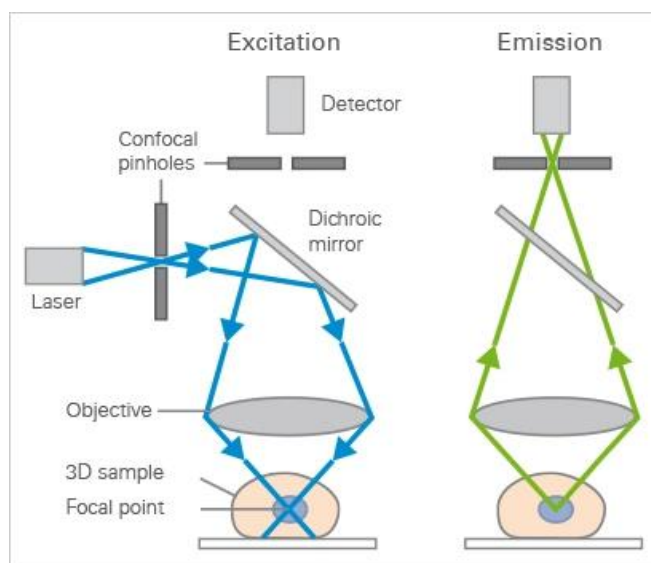


Figure 5 Principe de l'imagerie confocale

Pour affiner la méthode développée par J. Sloodman, nous avons vérifié la représentativité de l'activation du mécano-fluorophore vis-à-vis de la rupture d'une chaîne du réseau polymère et montré que la molécule ne surestimait pas drastiquement la rupture de chaînes dans le réseau, pour les concentrations de ces molécules auxquelles nous travaillons.

Nous avons également vérifié les effets des conditions de tests mécaniques (températures et vitesse de déformation) sur l'activation du mécano-fluorophore et nous avons montré que les conditions n'avaient que peu d'effet sur l'activation du DACL.

Pour pouvoir imager et quantifier la rupture de chaînes dans des échantillons post-fracture avec une meilleure résolution que celle du confocal microscope, nous avons enfin adapté la méthode d'imagerie et de quantification (utilisée par J. Sloodman avec un microscope confocal) à un microscope confocal à objectif inversé. Pour cela, nous avons produit des échantillons de calibration adapté au microscope confocal à objectif inversé, en utilisant la même molécule de calibration 9-((4-anisyl)ethynyl)anthracene synthétisé par J. Sloodman, dans du poly(acrylate d'éthyle) (PEA) linéaire, sur des plaques minces de verre.

## **2. Mécanique de la rupture dans les réseaux mous étudié par mécanofluorescence**

Nous avons utilisé la méthode d'imagerie et de quantification des chaînes cassées, précédemment présenté, pour étudier la rupture des chaînes lors de la propagation d'une fracture dans des réseaux simples de PEA réticulés à 0.5 mol% de réticulant.

Nous avons synthétisé ces échantillons avec 0.02 mol% de DACL, les avons entaillés avec un rasoir pour créer un défaut qui initiera la propagation d'une fracture lorsque l'échantillon sera mis sous traction.

La propagation de la fracture lors des tests mécaniques a été filmé et grâce à l'analyse des images nous avons pu remonter à la longueur de la fissure si l'échantillon était non-déformé et à la déformation locale en front de fissure. Ces données nous ont permis d'estimer le taux de restitution d'énergie de déformation  $G$  à tout moment de la propagation de la fissure.

En corrélant le taux de restitution d'énergie de déformation  $G$  avec la densité surfacique de chaînes cassées  $\Sigma$  mesurée grâce aux analyses confocal le long de la fissure dans la direction de propagation.

La mécanique de la fracture élastique linéaire prédit que l'énergie de fracture  $\Gamma$  (équivalent à  $G$  au moment où la fissure se propage) contrôle la déformation locale et ainsi la rupture des chaînes en pointe de fissure.

En variant la taille de défaut initial différents échantillons du même réseau de polymère, nous avons accès à différentes contraintes et déformations critiques de propagation de fissures et ainsi différents  $G$  lors de la propagation. Grâce à l'analyse confocal des échantillons post fracture, nous avons une mesure de  $\Sigma$ . Ainsi, nous pouvons comparer pour chaque échantillon  $G$  et  $\Sigma$ .

Nos résultats ont montré que pendant la propagation, il y a une relation linéaire en le taux de restitution d'énergie de déformation  $G$  et la densité surfacique de chaînes cassées  $\Sigma$ , qui confirme les prédictions du modèle de la fracture linéaire élastique.

## **3. Effet de la structure du réseau sur la fracture observée à l'aide de la mécanofluorescence**

Dans des conditions dites de seuil, où aucune dissipation viscoélastique ne se produit, le modèle moléculaire de Lake et Thomas suggère que lorsqu'un réseau se rompt, la quantité minimale de scission

de liaisons et de dissipation d'énergie est due à la rupture d'une monocouche de liaisons traversant la nouvelle surface, et chaque brin rompu entre les réticulations libère une énergie qui évolue linéairement avec la longueur du brin.

Appliqué à des expériences réelles sur un matériau donné, ce modèle prédit toujours la bonne relation entre la ténacité et la structure du réseau polymère, même lorsque la dissipation viscoélastique n'est pas négligeable. À ce jour, la raison pour laquelle ce modèle fonctionne si bien reste une question ouverte.

Le modèle de Lake et Thomas donne l'énergie de rupture à partir de deux paramètres ajustables principaux : le nombre surfacique de liaisons cassées  $\Sigma$  et l'énergie libérée par brin cassé  $U_{\text{chain}}$ . Le nombre surfacique de liaisons brisées peut être dérivé de la taille de la maille du réseau et de la densité des chaînes.

Même en l'absence de viscoélasticité, dans la réalité, la nature stochastique du réseau polymère conduit inévitablement à une rupture précoce des brins les plus courts, ce qui nous incite à penser que plus d'une monocouche de liaisons se rompt pour propager une fissure et créer une nouvelle surface. Il a été démontré par les travaux de J. Slootman, que la rupture des liaisons se produit dans un volume situé devant la pointe de la fissure.

Que ce soit le nombre surfacique de chaînes brisées qui soit minimisé ou l'énergie libérée par une chaîne brisée qui soit surestimée, il peut y avoir des erreurs de compensation dans les estimations de ces paramètres ajustables.

L'énergie de rupture, mesurée expérimentalement à partir d'essais de propagation de fissures, englobe à la fois le nombre de chaînes brisées et l'énergie dissipée par chaîne. En utilisant la mécano-chimie, nous pouvons avoir accès à la seule fraction de chaînes brisées, et revenir à une énergie dissipée par chaîne et par liaison.

Dans un travail précédent, J. Slootman a essayé d'étudier l'effet de la structure du réseau sur l'énergie de rupture des réseaux mous en comparant deux échantillons de PMA avec différentes densités de réticulation. Son résultat a montré que la contribution relative de la rupture de la chaîne était plus faible dans le réseau moins réticulé, ce qui ne pouvait donc pas expliquer l'augmentation de la résistance à la rupture avec la diminution de la densité de réticulation. Elle a attribué l'augmentation de l'énergie de rupture à d'autres mécanismes dissipatifs tels que la contribution viscoélastique.

Nous pensons que ses analyses peuvent être améliorées pour obtenir des résultats plus clairs : premièrement, le signal fluorescent a été moyenné sur quatre images prises au milieu du chemin de propagation de la fissure, ce qui ne tient pas compte de l'évolution de la scission des liaisons avec la propagation de la fissure (montrée au chapitre 5) et augmente les barres d'erreur ; deuxièmement, la résolution optique du microscope confocal est limitée, et seuls les échantillons de PMA, qui sont assez

viscoélastiques et loin des conditions de seuil requises par le modèle de Lake et Thomas, ont pu être imagés.

L'utilisation du microscope confocal nous permet d'imager les échantillons avec une résolution plus élevée qu'avec le microscope. Ainsi, nous pourrions travailler avec des échantillons de Poly(éthyl acrylate) (PEA) (loin de leur température de transition vitreuse donc moins viscoélastique que les échantillons de PMA) et imager l'activation du mécanophore en fonction de la croissance de la fissure.

Dans ce travail, nous examinons expérimentalement les effets de la structure du réseau sur la fracture en utilisant la mécanochimie. Nous synthétisons des réseaux simples de PEA, marqués avec le mécanophore et avec différentes densités de réticulation, et réalisons des tests de propagation d'entailles. Nous suivons la propagation des fissures de manière macroscopique et à l'échelle micrométrique. Nous extrayons le taux de libération d'énergie pendant la propagation des fissures et le corrélons à une estimation expérimentale du nombre surfacique de brins cassés.

#### **4. Etude quantitative de la rupture de chaînes et du transfert de contraintes lors du necking des réseaux multiple élastomères**

Les réseaux multiples sont des matériaux modèles intéressants dans lesquels un premier réseau réticulé est pré-étiré par la polymérisation successive de réseaux matriciels. Ces matériaux bénéficient de la rupture précoce des chaînes courtes et pré-étirées du réseau de charge, appelées liaisons sacrificielles, car elles dissipent l'énergie avant la rupture macroscopique du matériau. Cette architecture de réseau spécifique permet d'étirer le réseau de charge jusqu'à une extension qui ne pourrait être atteinte par le réseau seul, en raison de sa rupture catastrophique. Par conséquent, les chaînes du réseau de charge atteindront des extensions élevées et se briseront, avant la rupture du réseau multiple. D'une certaine manière, l'extension atteinte par le réseau de remplissage imite l'extension qui se produit très localement à la pointe de la fissure, pendant la propagation de la fissure du réseau de remplissage seul.

De manière remarquable, certains réseaux multiples démontrent un comportement particulier appelé necking, qui est typiquement attribué aux matériaux ductiles. Ce comportement atypique, pour les élastomères, consiste en la localisation de la déformation à des régions fortement déformées dans l'échantillon, qui se propagent de manière stable dans l'échantillon lors d'un allongement supplémentaire.

Il est intéressant de noter que le groupe de Gong a déjà signalé, en 2002, l'apparition de ce comportement de rétrécissement dans des hydrogels à double réseau avec des conceptions de matériaux similaires. La région rétrécie s'est ramollie pour atteindre un module élastique et un comportement à la traction similaires à ceux du second réseau seul. Ils ont proposé un mécanisme pour le transfert de la charge du réseau de remplissage au second réseau : dans leur image, le réseau de remplissage se brise en grappes isolées qui sont reliées entre elles par le réseau matriciel continu restant.

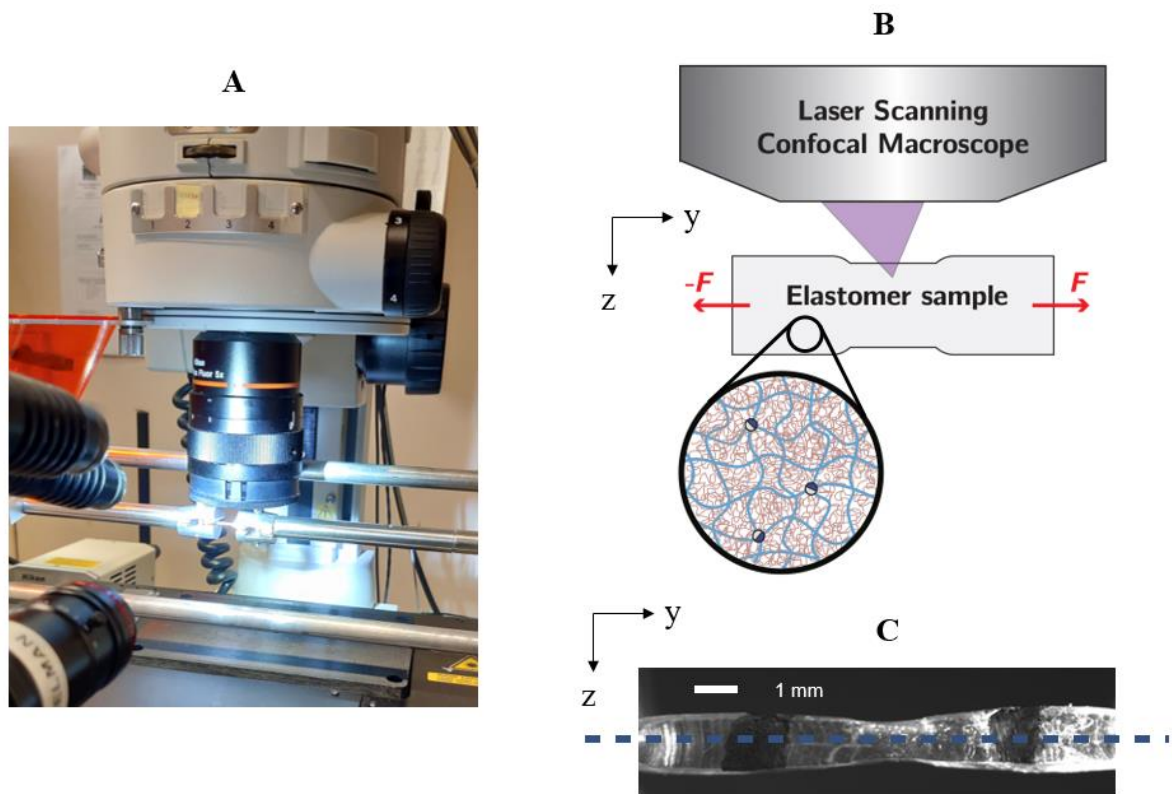


Figure 6 A Montage expérimental microscope confocal/traction. B Schema de l'expérience. C Vue transverse de l'échantillon en traction

Ils ont étudié la structure de la région rétrécie par diffusion de neutrons aux petits angles sur des échantillons avec un second réseau deutéré et ont trouvé des inhomogénéités de concentration typiques du second réseau avec une longueur caractéristique d'environ  $1,5 \mu\text{m}$ . Ces observations soutiennent leur mécanisme de rétrécissement plausible dans lequel le réseau de charge se brise en clusters séparés qui sont physiquement connectés par le second réseau, ce qui implique que la plupart des chaînes du réseau de charge dans les clusters devraient être déchargées après le rétrécissement.

Des conclusions différentes ont été obtenues par notre groupe, par le travail de Y. Chen, concernant le rétrécissement des élastomères à réseaux multiples. Dans cette étude, le spiropyran (SP), une molécule détectant les contraintes, a été introduit dans le réseau de la charge ou le réseau de la matrice des élastomères à réseaux multiples. Ses résultats ont montré que le rétrécissement est accompagné d'une contrainte localisée significative dans le réseau de la charge et dans le réseau de la matrice dans la région rétrécie, ce qui entraîne un ramollissement des régions rétrécies. Une analyse minutieuse de l'adsorption des PS a montré qu'après le rétrécissement, la charge était partagée par les réseaux de la charge et de la matrice, avec 90 % des PS activés dans la charge encore sous charge dans la région rétrécie. Ces observations suggèrent la formation de microfissures dans le réseau de la charge dans la phase rétrécie, plutôt que d'îlots ou de grappes, comme décrit par Gong dans les gels à double réseau.

La mécanochimie est un excellent outil pour localiser et quantifier la rupture des chaînes pendant le processus de rétrécissement. Le spiropyrane et le dioxétane ont été utilisés dans notre laboratoire pour étudier le rétrécissement dans un élastomère standard à réseau quadruple. Néanmoins, le spiropyran n'est pas représentatif de la rupture des chaînes C-C et il n'a pas encore été adapté pour réaliser des images en temps réel. Le mécanophore dioxétane, qui donne une information dynamique de la rupture des liaisons, n'est pas adapté pour quantifier et localiser précisément la rupture des liaisons, en raison d'un faible signal d'émission et d'une faible résolution spatiale.

Dans cette étude, nous cherchons à obtenir des informations quantitatives et en temps réel sur la fraction de chaînes cassées dans le réseau de la charge, ainsi que sur le transfert de contraintes vers le second réseau de la matrice, lors du rétrécissement. Nous cherchons à comprendre les paramètres qui contrôlent le rétrécissement des élastomères à réseaux multiples, en changeant la structure ou la chimie du réseau multiple.

Pour ce faire, nous avons utilisé deux outils mécanochimiques pour marquer le premier et le second réseau de nos échantillons avec deux mécanophores, signalant soit la scission de la chaîne (DACL) soit le transfert de contrainte (SP). Nous avons combiné un test de traction in-situ avec une observation directe à l'aide d'un microscope confocal, afin de quantifier et d'observer en temps réel l'état moléculaire (dommage ou contrainte) du matériau pendant le rétrécissement. Nous avons fait varier le pré-étirement du réseau de charge, la densité de réticulation du réseau de charge et la composition chimique du réseau de charge pour étudier ces paramètres sur le processus de rétrécissement.

## RÉSUMÉ

---

Les matériaux élastiques peuvent se déformer de façon réversible de plusieurs fois leur taille initiale. Leur faible résistance à la fracture provient de la présence de défauts, qui lors de la déformation, entraînent la nucléation et propagation catastrophique d'une fissure, mécanisme qui reste mal compris. Cette thèse s'organise autour de deux axes : (i) le développement de nouvelles stratégies de synthèse de renforcement des élastomères, et (ii) l'étude, plus fondamentale, de la fracture dans des matériaux contrôlés modèles. Inspiré du renforcement structurel des réseaux multiples, nous avons développé deux nouvelles voies de synthèse d'élastomères renforcées : des composites à charges molles et inter-pénétrables de même nature chimique que la matrice, et des films de particules à réseaux interpénétrés synthétisés par polymérisation en émulsion. Nous avons obtenu des composites dont le durcissement à la déformation est contrôlable par la fraction volumique de particules dans la matrice. Les particules à réseaux interpénétrés obtenues par polymérisation en émulsion ont pu être fonctionnalisées pour pouvoir être connectées lors du séchage. Dans un second temps, nous avons travaillé sur des réseaux élastomères modèles contenant des mécanophores pour étudier leur fracture. Nous avons notamment amélioré une nouvelle méthode permettant la visualisation et quantification par microscopie confocale de rupture des chaînes du réseau, basée sur une activation de fluorescence lors de la rupture de liaison chimique. En variant la longueur initiale de l'entaille dans des échantillons du même réseau polymère, nous avons pu discuter les prédictions de la mécanique de rupture élastique au regard de l'endommagement par rupture de chaînes en pointe de fissure. En variant la maille des réseaux polymères, nous avons pu étudier les effets structurels du réseau sur la rupture de chaînes en pointe de fissure et discuter le modèle moléculaire de Lake et Thomas. Enfin nous avons observé in situ la formation d'une striction élastique dans des réseaux multiples. Nous avons quantifié localement la rupture de liaisons et le transfert des contraintes du premier réseau vers le deuxième. Ces nouveaux résultats seront utiles au développement de nouveaux modèles réalistes de la fracture des matériaux élastiques.

## MOTS CLÉS

---

Elastomère – Fracture – Renforcement mécanique – Réseau multiple

## ABSTRACT

---

Elastic materials can deform reversibly by several times their initial size. Their low resistance to fracture is due to the presence of defects, which during deformation, lead to the still poorly understood catastrophic propagation of a crack. This thesis is organized around two axes: (i) the development of new elastomers designs for toughening, and (ii) the more fundamental study of fracture in more conventional elastomeric networks. Inspired by the structural reinforcement of multiple networks, we have developed two new ways of synthesizing reinforced elastomers: firstly, composites with soft and interpenetrable fillers of the same chemical nature as the matrix and secondly, films made from particles of interpenetrated networks synthesized by emulsion polymerization. We obtained composites with tunable strain-hardening according to the volume fraction of particles in the matrix. The double network particles obtained by emulsion polymerization could be functionalized chemically, which allowed their connection by covalent bonds during the drying process. In a second stage, we investigated the mechanisms of fracture of model elastomeric networks with a newly developed method allowing the mapping and quantification of network damage by fluorescence confocal microscopy. By varying the initial notch length in samples of the same polymer network and quantifying chain scission at the crack tip, we were first able to discuss the validity of the predictions of elastic fracture mechanics. Then, by varying the chain length in the polymer networks, we were able to investigate the effects of changing the network structure on chain scission at the crack tip and discuss the molecular model of Lake and Thomas. Finally, we observed in situ the necking process in multiple networks and quantified the local bond scission accompanying the stress transfer from the first to the second network. These new results will be useful for the development of new molecular models of fracture of elastic materials.

## KEYWORDS

---

Elastomer – Fracture – Mechanical reinforcement – Multiple network

